VILNIUS UNIVERSITY
CENTER FOR PHYSICAL SCIENCES AND TECHNOLOGY

Maliha Parvin

Photoelectrochemical Synthesis of Strong Oxidants Using Tungsten (VI) Oxide

DOCTORAL DISSERTATION

Natural sciences,
Chemistry (N 003)

VILNIUS 2022

The dissertation was prepared between 2018 and 2022 at the State research institute Center for Physical Sciences and Technology.

Academic supervisor – Dr. Jurga Juodkazytė (State research institute Center for Physical Sciences and Technology, Natural Sciences, Chemistry – N003)

This doctoral dissertation will be defended in a public meeting of the Dissertation Defence Panel:

Chairman - Prof. Dr. Rasa Pauliukaitė (State research institute Center for Physical Sciences and Technology, Natural Sciences, Chemistry - N003)

Members:
Doc. Dr. Renata Butkutė (State research institute Center for Physical Sciences and Technology, Natural Sciences, Physics - N002)
Prof. Dr. Henrikas Cesiulis (Vilnius University, Natural Sciences, Chemistry - N003)
Habil. Dr. Zenonas Jusys (Ulm University, Natural Sciences, Chemistry - N003)
Prof. Habil. Dr. Eimutis Juzeliūnas (State research institute Center for Physical Sciences and Technology, Natural Sciences, Chemistry - N003)

The dissertation shall be defended at a public meeting of the Dissertation Defence Panel at 14:00 on September 16, 2022 in meeting room E302 of the State research institute Center for Physical Sciences and Technology .
Address: Saulėtekio av. 3, LT-10257, Vilnius, Lithuania.
Phone +370 5 264 8884, fax +370 5 264 9774, e-mail office@ftmc.lt.
The text of this dissertation can be accessed at the libraries of Center for Physical Sciences and Technology and Vilnius University, as well as on the website of Vilnius University:
www.vu.lt/lt/naujienos/ivykiu-kalendorius

VILNIAUS UNIVERSITETAS
FIZINIŲ IR TECHNOLOGIJOS MOKSLŲ CENTRAS

Maliha Parvin

Fotoelektrocheminė stiprių oksidatorių sintezė naudojant volframo (VI) oksidą

DAKTARO DISERTACIJA

Gamtos mokslai,
Chemija (N 003)

VILNIUS 2022

Disertacija rengta 2018–2022 metais Valstybiniame mokslinių tyrimų institute (VMTI) Fizinių ir technologijos mokslų centre.

Mokslinė vadovė – dr. Jurga Juodkazytė (VMTI Fizinių ir technologijos mokslų centras, gamtos mokslai, chemija – N003)

Gynimo taryba:

Pirmininkė - Prof. dr. Rasa Pauliukaitė (VMTI Fizinių ir technologijos mokslų centras, gamtos mokslai, chemija - N 003)

Nariai:
Doc. dr. Renata Butkutė (VMTI Fizinių ir technologijos mokslų centras, gamtos mokslai, fizika - N 002)
Prof. dr. Henrikas Cesiulis (Vilniaus universitetas, gamtos mokslai, chemija - N 003)
Habil. dr. Zenonas Jusys (Ulmo Universitetas, gamtos mokslai, chemija - N 003)
Prof. habil. dr. Eimutis Juzeliūnas (VMTI Fizinių ir technologijos mokslų centras, gamtos mokslai, chemija - N 003)

Disertacija ginama viešame Gynimo tarybos posėdyje 2022 m. rugsėjo mėn. 16 d. 14 val. VMTI Fizinių ir technologijos mokslų centro E302 posėdžių salėje. Adresas: Saulėtekio al. 3, LT-10257, Vilnius, Lietuva. Tel. +370 5 264 8884, faksas +370 5 264 9774, el. paštas: office@ftmc.lt.

Disertaciją galima peržiūrėti Vilniaus universiteto, Fizinių ir technologijos mokslų centro bibliotekose bibliotekose ir VU interneto svetainėje adresu:
https://www.vu.lt/naujienos/ivykiu-kalendorius

LIST OF ABBREVIATIONS

ABPE	Applied bias photon-to-current conversion efficiency
BuOH	Butanol
CA	Chronoamperometry
CBD	Chemical bath deposition
CB	Conduction band
CV	Cyclic Voltammetry / Voltammogram
EASA	Electrochemically active surface area
EIS	Electrochemical impedance spectroscopy
EtOH	Ethanol
FTO	Fluorine-doped tin oxide
HER	Hydrogen evolution reaction
IsoPrOH	Isopropanol
MeOH	Methanol
NHE	Normal hydrogen electrode
OER	Oxygen evolution reaction
PEC	PhotoElectroChemical
PL	Photoluminescence
PTA	Peroxotungstic acid
RCS	Reactive chlorine species
SEM	Scanning electron microscopy
STH	Solar-to-hydrogen conversion efficiency
UV	Ultraviolet light
VB	Valence band
XRD	X-ray diffraction

TABLE OF CONTENTS

1. INTRODUCTION

In an ongoing effort to decrease air pollution and prevent global warming European Commission has announced European Green Deal - an action plan with a major goal to reach zero emissions of greenhouse gases by 2050. Chemical industry is among the most polluting as well as energy- and resource-intensive sectors. Therefore new, environmentally friendly and economically efficient technologies, which would exploit renewable energy sources are sought. Photoelectrochemical (PEC) processes, which convert solar energy into chemical energy and therefore are referred to as artifical photosynthesis have been attracting increasing attention recently. PEC splitting of water for sustainable production of hydrogen as fuel of the future is one of the most intensively investigated processes of artificial photosynthesis. However, as demonstrated recently, this technology has great potential in the synthesis of other high added-value chemicals, especially strong oxidants ($HClO$, H_2O_2, $H_2S_2O_8$, etc.), which are suitable for water treatment and disinfection. The global demand for disinfectants has been increasing continuously due to growing efforts to prevent the spread of infectious diseases. PEC synthesis of strong oxidants is rather new area of research, therefore, new data on efficient systems and the mechanism of the processes are very important for the further development of the field. Deliberate choice of PEC system (photoelectrode + electrolyte) is required in order to achieve high efficiency of the process. Tungsten (VI) oxide as a photoanode material is of special interest due to its moderate band gap (2.6 – 2.8 eV), relatively large hole-diffusion length (150 - 500 nm) as well as deep valence band position (~ 3 V vs. NHE), rendering high oxidizing power to photogenerated holes. Photoelectrochemical reactions as multistep processes, involving light absorption, charge carrier generation, separation, transport and transfer across electrode/electrolyte interface, are strongly dependent on the structural properties, crystallinity and morphology of the semiconductor photoelectrodes. To ensure the efficient generation of desired product, careful engineering of semiconductor/electrolyte interface is required.

The aim of this PhD thesis was to synthesize photoelectrochemically active WO_3 layers of different morphology and thickness and to investigate their performance in PEC synthesis of strong oxidants in sulfate and chloride electrolytes. To achieve this, following tasks were formulated:

1. To investigate how different alcohols (methanol, ethanol, isopropanol and butanol) used as reductants in chemical bath deposition as well as annealing temperature influence the crystallization of WO_3 phase, morphology of the coatings and their PEC activity;
2. To synthesize highly porous nanostructured WO_3 layers of increasing thickness (from ~ 0.5 up to ~ 10 µm) and investigate their PEC activity;
3. To investigate the energy conversion efficiency of PEC generation of reactive chlorine species ($ClO^- + ClO_2^-$) and persulfate ($S_2O_8^{2-}$) on WO_3 coatings having different thickness and morphology;
4. To investigate the competition between photoanodic oxidation of water and anions as well as stability of different WO_3 coatings under conditions of photoelectrolysis in sulfate and chloride electrolytes;
5. To test the antimicrobial effect of photoelectrochemical generation of strong oxidants using WO_3 photoanode.

The novelty and originality of PhD thesis:

- The coating morphology-dependent competition between the photoanodic oxidation of water molecules and anions, which occurs on the surface of tungsten (VI) oxide photoelectrodes in sulphate and chloride electrolytes, is investigated for the first time.
- Photoelectrochemical behavior of WO_3 photoelectrodes in H_2SO_4 and NaCl electrolytes is analysed on the basis of novel approach in which PEC processes are treated as electrode potential assisted photochemical reactions involving hole-mediated formation of radical intermediates.
- Significant role of specific adsorption of chloride ions as well as intermediate products of their oxidation ($Cl\bullet$, $Cl_2^-\bullet$) in lowering the photocurrent onset potential, trapping the photogenerated charge carriers as well as protecting WO_3 surface from deleterious accumulation of peroxo species is revealed.

2. LITERATURE REVIEW

2.1. Harnessing solar energy

Having sufficient energy is one of the main challenges to the world's population in the twenty-first century. Annual energy consumption is predicted to be about 27 TW and 43 TW by 2050 and 2100, respectively [1]. Fossil fuels like oil, gas, and coal contribute approximately equally to this demand. However, the availability of fossil fuels decreases, whereas their burning causes the emission of CO_x and other greenhouse gas like NO_x, SO_x, which are responsible for global climate change. Therefore, growing environmental concerns and increasing energy demand drive to search for new, sustainable sources of energy [2]. Solar energy is considered as a great source of renewable energy. About 7.6 PW of solar power strikes just the Earth's desert per year. Conversion of only 6% of this desert solar resource would enable humankind to meet the energy demand forecasted for the year 2100 [3,4]. There are several ways to harness solar power, e.g. i) collecting thermal energy (solar water heating), ii) converting light into electricity (photovoltaics), iii) converting light into chemical energy and storing it in the form of fuels (hydrogen, methane, methanol, etc. [4]). The latter process is called artificial photosynthesis.

2.2. Artificial photosynthesis

2.2.1. Solar water splitting

Collecting and conserving solar energy in chemical bonds as a chemical fuel is one of the most fascinating possibilities to harness the energy of light. Chemical fuels have higher energy densities compared to batteries, mechanical or gravity-based storage systems like flywheels and pumped water reservoirs. Required energy for many chemical syntheses in the form of visible-light is only 1 - 3 eV or 100–300 kJ mol^{-1}. Light-driven water splitting intended for the sustainable production of H_2 as a fuel of the future is one of the most investigated processes of artificial photosynthesis. At present, 96% of hydrogen are produced from fossil fuels (petroleum, coal and natural gas) and the rest is mainly derived from renewable energy as depicted in Fig.1 [5,6].
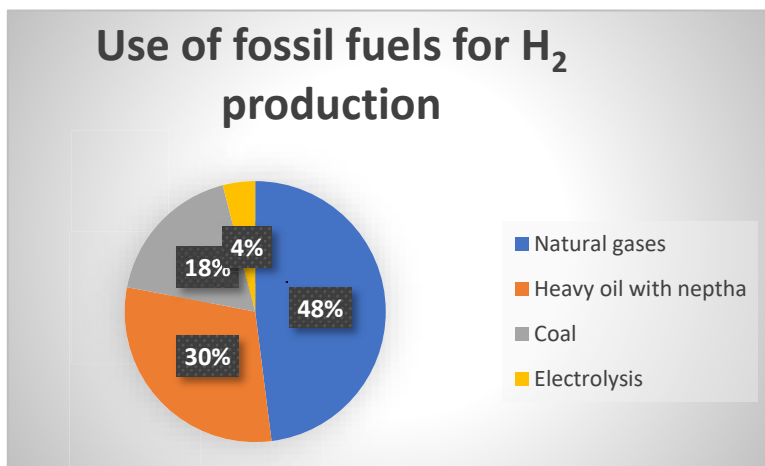
Figure 1. Fossil fuels used in world H_2 production. The figure is redrawn based on reference [5]

Photoelectrochemical (PEC) water splitting has been attracting continuous interest since Fujishima and Honda reported their pioneering work in 1972, where decomposition of water into hydrogen and oxygen under irradiation with ultraviolet (UV) light and without any applied electric power was achieved using n-type TiO_2 anode and Pt cathode [6]. This discovery triggered intensive search for semiconductor electrode materials, which would ensure high energy conversion efficiency and would be resistant to photocorrosion [7,8]. In a PEC water splitting cell at least one electrode is made of a semiconductor material that is able to absorb light. In general, there are three possible setups: 1) photoanode made of n-type semiconductor and metal cathode, 2) photocathode made of p-type semiconductor and metal anode and 3) both electrodes are light sensitive, i.e. n-type semiconductor photoanode and p-type semiconductor photocathode [9]. An ideal photoelectrode requires good light absorption (the band gap energy should be around 2 eV to ensure optimal absorption of the solar light), efficient charge separation and transport along with sufficiently fast kinetics of hydrogen or oxygen evolution reactions (HER and OER) at its surface. To make PEC technology commercially viable, the targeted solar to hydrogen energy conversion efficiency should exceed 10% [9].

2.2.2. Photoelectrochemical production of high value-added chemicals

Investigations on solar water-splitting systems are focused on the production of H_2, whereas simultaneous evolution of O_2 attracts almost no interest because market price of O_2 is significantly lower [10,11] . Recently, it has been suggested that in PEC systems oxygen evolution reaction can be replaced with light-driven synthesis of other high value-added oxidants such as reactive chlorine species (RCS), hydrogen peroxide (H_2O_2), persulfates ($H_2S_2O_8$), tetravalent cerium (Ce^{4+}), periodate (IO^{4-}), Mn^{7+}, Cr^{6+}, etc [12–14]. Coupling the PEC production of valuable oxidants on photoanode with generation of hydrogen on (photo)cathode can make the technology more advantageous.

Among other high value-added oxidants, photoelectrochemical generation of reactive chlorine species (HOCl, OCl^-, Cl_2) attracts special attention due to several reasons. Firstly, active chlorine and its compounds are widely used for the production of polymers, disinfection of drinking water, waterworks and swimming pool systems, treatment of dye wastewater, bleaching, etc [12,15]. Secondly, in industry, RCS are produced by electrolysis of chloride solutions, known as the chloralkali process, which is the second highest energy consuming technology among the electrolytic processes after aluminum manufacturing [16,17]. Therefore, more sustainable and less energy-intensive technologies for production of RCS are sought. Another important aspect related to photoelectrochemical production of RCS is the possibility to exploit vastly abundant seawater. Compared to scarcely available freshwater, seawater is available in sufficient quantities on earth and geographically is distributed homogeneously. Therefore, using seawater as an electrolyte is an attractive alternative for solar-driven PEC systems [18]. Though many electrocatalytic systems were explored in acidic, alkaline, or buffered aquoeus solutions over the past decades [19], significantly less attention has been devoted to the issues of using seawater in electrochemical [20,21] and photoelectrochemical water splitting [22] systems so far.

PEC production of strong oxidants can find applications in such areas as water disinfection, wastewater treatment, organic pollutant degradation [23]. Moreover, it offers the possibility to generate chemicals on-demand and on-site without the need of storage and handling of hazardous species. These alternative photo-oxidation processes represent rather new area of research compared to PEC water splitting. Profound understanding of the mechanisms of these reactions is crucial for development of efficient energy conversion devices, what motivated our research in this field.

2.3. Photoelectrode materials

As mentioned above, the essential aspect of PEC energy conversion systems is to find the right electrode materials. According to molecular bonding theory, bonding and anti-bonding levels are formed by combination of atomic orbitals of several atoms. Bonding and anti-bonding energy levels correspond to the valence band, VB, or the highest occupied molecular orbital (HOMO) and conduction band, CB, or the lowest unoccupied molecular orbital (LUMO), respectively. Difference between HOMO and LUMO is called bandgap (E_g). Under appropriate illumination, an electron in the VB is excited and transferred to CB, creating a hole in the VB. These photogenerated charge carriers initiate the PEC synthesis. The feasibilty of a certain photo-induced reaction depends on the arrangement of CB and VB energy levels with respect to oxidation/reduction potentials of solution species, which participate in charge transfer processes. For a water splitting reactions to occur, the valence band potential of semiconductor should be more positive than the thermodynamic potential of OER ($E(O_2/H_2O)$ = 1.23 V vs. Normal Hydrogen Electrode (NHE)), while the potential of conduction band should be more negative than the thermodynamic potential of HER ($E(2H^+/H_2)$ = 0 V (NHE)). Hence, a theoretical minimum of 1.23 eV energy is needed for light-driven water splitting corresponding to wavelength, λ, of 1008 nm. Considering the thermodynamic losses and overpotential requirement for surface reaction kinetics, minimum bandgap of ~ 1.8 eV is required, corresponding to λ ~ 690 nm. Because of the rapid drop in sunlight intensity below 390 nm in the solar spectrum, the maximum limit of semiconductor bandgap energy is 3.2 eV. Therefore, E_g between 1.8 and 3.2 eV is desirable for a single semiconductor material [24]. Fig. 2 illustrates the bandgaps and band positions of typical photoelectrodes used in PEC water splitting. It is noteworthy that metal oxide semiconductors are very attractive due to low cost, ease of preparation, the flexibility of forming different nanostructures, lattice manipulation as well as higher resistance to photocorrosion in aqueous solutions compared to nitrides, phospides, sulfides or selenides [25–27]. For the PEC production of strong oxidants, semiconductors with deep VB positions are of special interest, because such position renders high oxidizing power to photogenerated holes. In the sections below metal oxide materials, which are the most commonly used as photoanodes and have sufficiently positive valence band potentials (2.5 – 3.5 V (NHE)), are briefly reviewed.
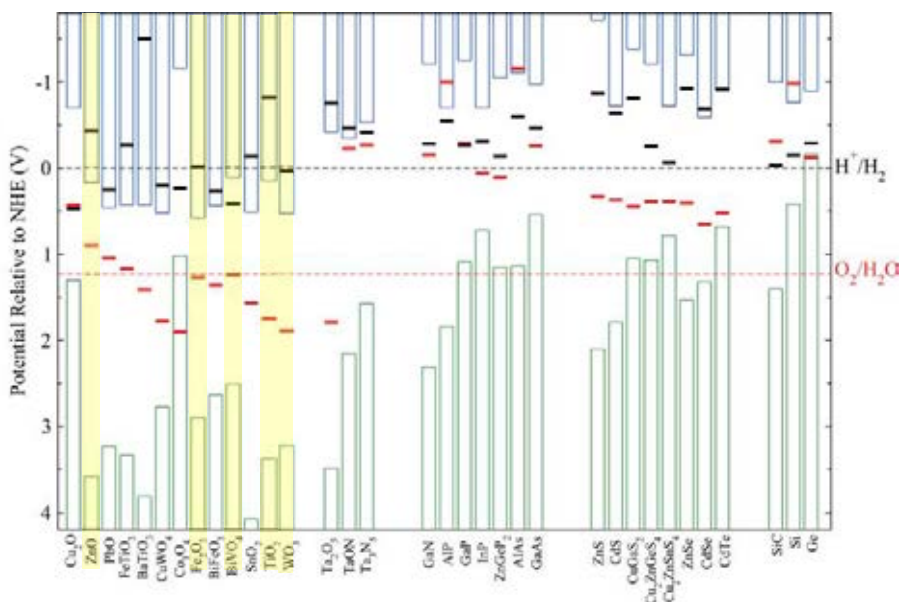
Figure 2. Bandgap energies, conduction, and valence band positions (vs. NHE) of different semiconductors with respect to redox potentials of water [28]; yellow background highlights semiconductors which are discussed in the following sections

2.3.1. Titanium dioxide (TiO$_2$)

TiO$_2$ has been intensively studied since 1972 due to its earth-abundance, availability, low cost, nontoxicity as well as resistance to photocorrosion [29,30]. When the surface of TiO$_2$ photoanode is illuminated with absorbable light at the band gap frequency (3.2 eV for anatase and 3.0 eV for rutile), O$_2$ is released from water solutions as a product of photoelectrochemical water splitting. Competitive PEC oxidation of other solution species, including halide or SO$_4^{2-}$ ions from supporting electrolytes has also been reported [31]. However, only a small percentage of solar spectrum in UV region can be absorbed by TiO$_2$ due to its wide bandgap, which leads to very low solar-to-hydrogen conversion efficiency (STH) [32,33].

2.3.2. Hematite (Fe$_2$O$_3$)

Iron (III) oxide has been considered a promising photoanode material due to its thermal stability, natural abundance, low cost, low toxicity, chemical stability in a wide range of pH solutions, suitable valence band position, etc. Moreover, it has relatively narrow bandgap (1.9 - 2.32 eV corresponding to

14

652 - 530 nm), which allows visible light absorption with maximum theoretical STH efficiency of 7.7% [34]. Furthermore, Fe_2O_3 is an electrocatalyst of oxygen evolution reaction [35]. However, hematite has significant disadvantages as a material for PEC energy conversion, such as short charge carrier lifetime (3×10^{-12} s) [36], fast charge carrier recombination in the bulk, low absorption coefficient (10^3 cm^{-1}), which requires at least 400-500 nm thick film for optimal light absorption, slow hole mobility ($0.2 – 0.5$ cm^2 V^{-1} s^{-1}), which causes a very short hole diffusion length (2-4 nm) and poor electronic conductivity, which requires high doping levels [37–39].

2.3.3. Zinc oxide (ZnO)

Zinc oxide (ZnO) as a photoanode with a wide bandgap of 3.37 eV [40] has drawn extensive interest owing to its low cost, wide availability, low toxicity, ease of preparation, excellent optical properties, fast electron and hole mobility, favorable environmental compatibility etc. [41,42]. Despite these excellent properties, ZnO-based photoanodes have several limitations. Most importantly, photo-corrosion is observed in aqueous solutions, which is caused by trapping of holes on ZnO surface under UV illumination. Besides, under dark conditions, if solution pH is too low or high, decomposition of ZnO is detected. These disadvantages have hindered the development of ZnO-based photoanodes in PEC water splitting applications [43].

2.3.4. Bismuth Vanadate ($BiVO_4$)

Bismuth vanadate possesses three crystal forms: tetragonal (zircon), monoclinic (scheelite) and tetragonal (scheelite) structured systems. Among these three structures, monoclinic $BiVO_4$ shows good visible light response [44]. As a photoanodic material it has attracted considerable attention due to its moderate band gap (2.4 eV), positive position of VB edge (~2.5 V (NHE)) [36] and conduction-band edge potential close to 0 V (NHE) (pH 0), good visible light absorption, stability, nontoxicity, low cost, high theoretical solar-to-hydrogen efficiency of 9.2% [45]. However, slow charge transport (electron diffusion length is only 10 nm), fast charge carrier recombination and slow water oxidation kinetics significantly limit the efficiency of $BiVO_4$ [46]. Nevertheless, application of $BiVO_4$ photoanodes for PEC production of reactive chlorine species has been gaining more and more interest recently [47]. In this regard formation of $BiVO_4/WO_3$ heterojunctions looks especially promising [48].

2.3.5. Tungsten (VI) oxide (WO$_3$)

Tungsten (VI) oxide has a band gap of 2.5 - 2.8 eV and can absorb ~12% of solar light; its' theoretical STH conversion efficiency is 6.3% [49]. WO$_3$ is one of the few metal oxides which exhibits high stability in acidic environment [50] and possesses long hole diffusion length (150 - 500 nm) [36], which can reduce bulk recombination of photogenerated charge carriers resulting in high incident photon to current efficiencies (IPCEs) [51,52]. Therefore, research interest in WO$_3$ as photoanodic material has been growing steadily [53–55], as reflected by the sharp increase in the number of publications and citations since 2000 (Fig. 3). From basic electronic structure of WO$_3$, it is proposed that WO$_3$ display good oxidation abilities because of the low valence band position determined by the O 2p orbitals [56], whereas its conduction band consists of empty W 5d orbitals [57]. Valence band edge of WO$_3$ is located at ~3.0 V (NHE), which provides sufficient potential for oxidation of water, generation of strong oxidants and degradation of organic wastes [58,59]. Although conduction band is not negative enough for hydrogen evolution reaction [60], it is possible to overcome this disadvantage by applying external bias, doping or coupling with p-type photocathode. Though vast majority of papers on PEC performance of tungsten (VI) oxide are devoted to water splitting issues, it is well known that the products of photoanodic reactions taking place on WO$_3$ electrodes strongly depend on the composition of electrolyte [61,62] and there is a competition between PEC oxidation of water molecules and anions present in the solution. The processes of PEC formation of strong oxidants on WO$_3$ photoanodes have been significantly less explored so far. Thus, PEC performance of WO$_3$ in chloride and sulphate electrolytes was selected as an area of our research. These electrolytes are of particular interest because of the possibility to photoelectrochemically produce reactive chlorine and sulphate species, which are strong oxidants used for disinfection. It is very important to identify the factors, which determine the efficiency of the photoanodic reactions and affect the competition between them as well as to understand the mechanism of the processes involved. Photoelectrochemical reactions are complex multi-step processes, which include light absorption, electron-hole pair generation, separation, transport, and transfer across electrode/solution interface. Therefore, phase purity, crystallinity as well as morphology of the photocatalysts play crucial role in determining the kinetics and efficiency of these processes. It is well known that structure and morphology of semiconductor layers can be controlled by synthesis route, additives as well as annealing conditions. To date, a great variety of

nanostructured forms of WO$_3$ have been reported [63–68] including nanoplates, nanosheets, 3D nano-urchins, nanoflakes, nanorods, nanowires, etc. Synthesis routes applied for WO$_3$ photoelectrode preparation are discussed in the next section.
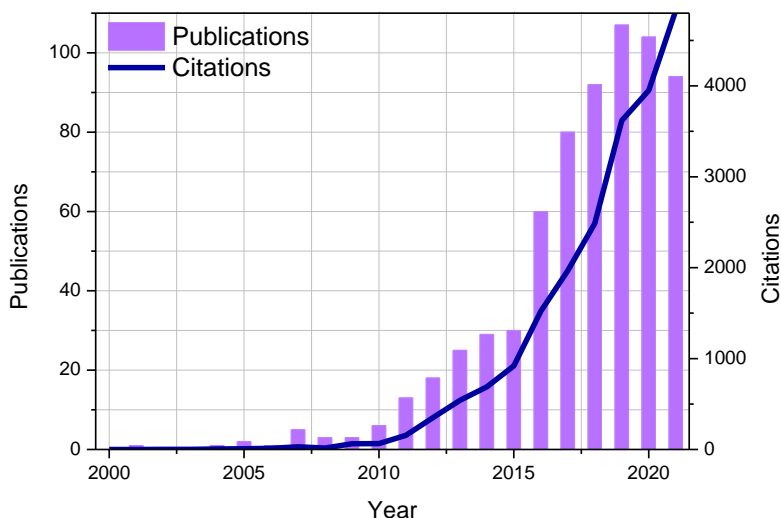
Figure 3. Number of publications and citations per year as reported by Web of Science (https://apps.webofknowledge.com) when using keywords "WO$_3$ photoanode" in the search engine.

2.4. Methods of synthesis of WO$_3$ layers

Various methods such as sol-gel synthesis [69], chemical bath deposition [70], solvo/hydrothermal synthesis [71], electrodeposition [72], anodization [73], etc are used to synthesize WO$_3$. Each of these methods has its own impact on the structure and, hence, photoelectrochemical properties of the synthesized material. Various factors should be considered in the process of photoelectrode preparation, i.e. good ohmic contact between the semiconductor and substrate, thickness and morphology of the layer for optimal light absorption, crystallinity, surface area, etc. Further, the most commonly used synthesis methods for the preparation of light sensitive WO$_3$ layers are discussed.

17

2.4.1. Solvothermal synthesis

Solvothermal method is used to synthesize compounds with good homogeneity from simple and extremely complex liquids at high temperature and pressure. In general, H_2WO_4 [74], WCl_6 [75], and Na_2WO_4 [76] solutions are used as starting materials in this process. Appropriate capping reagents [77] are then added to the precursor, which is followed by autoclaving at a certain temperature and time to allow the nucleation and growth of the crystallites. Different morphologies, sizes or phases of WO_3 can be achieved via solvo/hydrothermal synthesis by changing the concentration of solutes and additives, reaction temperature, reaction time, solution pH, etc. [75,76]. Solvothermal synthesis is an effective method to produce metal oxides, but it has several disadvantages related to difficulties of controlling the processes involved in the synthesis. Besides, this process requires expensive autoclaves to conduct the experiments.

2.4.2. Electrochemical deposition

Electrochemical deposition is a promising coating technique due to several advantages such as low cost, large area coating ability, etc [72]. The setup consists of a two (or three) electrode cells. Deposition is usually performed using peroxo-tungstic-acid (PTA) solution as electrolyte to produce W_2O_5 by an electroreduction process in acidic conditions, which is later converted to WO_3 by means of annealing at high temperature. The process requires only small applied voltage and deposition duration ranges between 1 to 30 minutes since excessive applied voltage and longer duration time will result in the formation of compact film with low porosity [78]. By tuning the process parameters and the electrolyte composition, electrodeposited WO_3 films are easily modified and controlled [79,80]. Although electrochemical deposition is rather simple and one of the cheapest methods, but it is difficult to maintain the uniformity of the prepared films, therefore, reproducibily is quite challenging.

2.4.3. Sol-gel synthesis

The sol-gel method is considered to be the most attractive process among wet chemistry coating technologies due to the production of solid-state material from chemically homogeneous precursors, formation of complex inorganic materials at lower temperatures and shorter synthesis times. It allows to easily control phase composition, particle morphology and size. Additional

advantages are low-cost and possibility of scaling-up for large area coating preparation [81]. Therefore sol-gel is an attractive method for commercial applications.

As a starting material, tungsten alkoxides $(W(OR)_6)$ or tungsten oxyalkoxides $(WO(OR)_4, WO_2(OR)_2)$ are not stable towards hydrolysis or condensation. Besides, these precursors need some stabilizers that may affect the desired crystalline phase of WO_3 layer. Therefore, stable inorganic salts, such as tungstates are used as molecular precursors in sol-gel synthesis, which usually starts form precipitation of tungstic acid and its dissolution in aqueous solution of H_2O_2 [82]. On the other hand, if metal alkoxide is used as a starting material in the sol-gel process, it needs to be dissolved in appropriate organic solvent, e.g. ROH [83].

After the formation of sols, layers are deposited onto the substrate by dip-coating [82], spin-coating [84] or spray pyrolysis [85] techniques, followed by drying and annealing processes to achieve stoichiometric and crystalline WO_3 films. PEC properties and photoactivity can be tuned by using different stabilizers [86], capping agents [87], varying the annealing temperature [88], etc.

2.4.4. Chemical bath deposition

Chemical bath deposition (CBD) is another attractive method among wet chemical methods, also known as solution growth, electroless plating, controlled precipitation or simply chemical solution deposition. The idea for the chemical bath deposition is based on controlled performing of the precipitation process. The reaction is conducted with dissolved precursors (in aqueous solution) at a low temperature (30 - 80 °C). CBD method attracts considerable attention as it does not require any advanced equipment. Besides, a large number of substrates can be coated at once with proper holder design unlike in the electrodeposition method. Most importantly, starting materials are cheap and available. Uniform and stoichiometric deposition is obtained easily under low-temperature deposition conditions. Also, preparative parameters are easily controllable, and improved grain structure can be easily achieved. Precipitation onto substrate mainly depends on the nucleation in solution. Depending upon the deposition conditions, such as the bath temperature, stirring, rate, pH, solution concentration, etc., the film growth can take place by ion-by-ion condensation of the materials or by adsorption of colloidal particles from the solution on the substrate [70,89]. From the

industrialization point of view, chemical bath deposition of WO_3 has been demonstrated to be effective in the fabrication of large-area devices [90].

We have followed two different CBD procedures to obtain WO_3 layers with different morphology and thickness. Further in the text these procedures are reffered to as "peroxotungstic acid route" and "tungstic acid route".

3. EXPERIMENTAL

3.1. Working electrode preparation

3.1.1. Formation of WO_3 layers by „peroxotungstic acid" route

All chemicals were of analytical grade and were used as received from suppliers without any further purification. WO_3 thin films on conducting glass (fluoride doped tin oxide - FTO) substrate were prepared using chemical bath deposition method following the slightly modified procedure described in [52]. FTO coated glass substrates (6 - 9 Ω/sq) were cut into fixed 2.5 x 1 cm^2 slides and washed consecutively in acetone (Reachem), isopropanol (Reachem) and deionized water under ultrasonication for 15 minutes in each solvent. At first, 0.8 g of $Na_2WO_4 \cdot 2H_2O$ (Carl Roth, 99% purity) and 0.3 g of $(NH_4)C_2O_4$ (Chempur, 99.7% purity) as capping agent were dissolved in 66 ml of distilled water and 18 ml of HCl (37%) (Chempur) were added to this solution under continuous stirring for 10 min at 50 °C to get tungstic acid (H_2WO_4). Subsequently, 16 ml of H_2O_2 were added into the suspension to form peroxotungstic acid (PTA) and the solution was stirred for 10 min. Next, 60 ml of reductant (methanol (MeOH), ethanol (EtOH), isopropanol (IsoPrOH) or butanol (BuOH)) were added, and after 10 min, 8 pieces of cleaned FTO substrates were dipped into the solution in an FTO-side-down position and kept for 180 min under water bath conditions at 85 °C. After that samples were rinsed in distilled water for 1 min and dried in the drying oven at 50 °C for 12 h. Finally, the coatings were annealed in ambient atmosphere at 400 °C or 500 °C for 2 h with heating rate of 1 °C min^{-1} to remove residual carbon and to obtain crystalline WO_3 films. Further in the text WO_3 coatings prepared using different reductants are denoted as $MeOH\_WO_3$, $EtOH\_WO_3$, $IsoPrOH\_WO_3$, and $BuOH\_WO_3$.

3.1.2. Formation of WO_3 layers by "tungstic acid" route

WO_3 photoanodes with highly porous morphology were prepared employing slightly modified procedure described in [70]. 0.9 g of $Na_2WO_4 \cdot 2H_2O$ was

dissolved in 90 ml of deionized water under constant stirring at 50 °C, which was followed by the addition of 1.8 g of anhydrous citric acid (C_6H_8O, 99.7% purity). After mixing properly, 18 ml of 3 M HCl were added to this solution. 10 min later cleaned FTO substrates were immersed into the solution and the deposition was allowed to proceed for two hours at 50 °C. After that the as-prepared films were collected and washed with water. Crystalline WO_3 film was obtained by annealing the as-prepared film in an ambient atmosphere at 400 °C for 2 h. The same procedure was repeated up to four times to obtain WO_3 layers with increasing thickness.

3.2 Structural, morphological and optical characterization

The surface morphology of tungsten oxide layers on FTO substrate was investigated by means of scanning electron microscopy (SEM) using a Helios NanoLab dual-beam workstation equipped with X-Max 20 mm^2 energy dispersion spectrometer (Oxford Instruments, Oxford, UK). The cross-sections of the samples were produced applying focused ion beam (FIB) technique. Pt layer of 0.7 μm thickness was e-beam deposited on the sample surface before sectioning with Ga^+ focused beam.

Texture of WO_3 coatings deposited on the FTO substrate was analyzed by creating 3D surface plots of SEM micrographs using ImageJ software (https://imagej.nih.gov/ij/). Dimensions of morphological features of WO_3 films were determined using the same software.

The crystalline structure of WO_3 films was characterized by means of X-ray diffraction (XRD) analysis using an X-ray diffractometer SmartLab (Rigaku) equipped with a 9 kW rotating Cu anode X-ray tube. Grazing incidence (GIXRD) method was used in 2θ range 20 – 60°. An angle between a parallel beam of X-rays and a specimen surface was adjusted to 0.5 °C. Phase identification was performed using Match software and Crystallography Open Database (COD). The average crystallite size, D, of WO_3 coatings was calculated using the Debye-Scherrer formula [91]:

$$D = \frac{k\lambda}{\beta \cos\theta} \tag{1}$$

Dislocation density (δ) was calculated using Williamson and Smallman relation:

$$\delta = \frac{1}{D^2} \tag{2}$$

where k is the Scherrer constant (predictable shape factor of 0.9 was used), λ is the wavelength of the X-ray used (0.15406 nm), θ is the Bragg diffraction angle (in degrees) and β is the full width at half maximum (FWHM) of the

diffraction peak (in radians). For calculations, all reflections within a 2θ range from 20 to 60° were used.

Stacking fault (SF) values were determined using the following equation [92]:

$$SF = [\frac{2\pi^2}{45(3tan\theta)^{1/2}}]\beta \tag{3}$$

The phase composition was investigated by Fourier Transform Infrared spectroscopy using a PerkinElmer spectrophotometer, with a resolution of 4 cm^{-1} over a wavenumber range of 450 - 4000 cm^{-1}.

Phase evolution of the tungsten oxide upon heat treatment was studied using thermogravimetric analysis (TGA) (PerkinElmer STA6000) and differential thermal analysis (DTA) (PerkinElmer STA6000). Samples were annealed at temperature from 30 to 500 °C with 10 °C min^{-1} heating rate. Air flow was 20 cm^3 min^{-1}.

To evaluate the optical properties of WO$_3$ coatings as a function of thin-film morphology, photoluminescence (PL) spectroscopy was used. Optical characterization was performed using a time-correlated single-photon counting Edinburgh-F900 spectrophotometer (Edinburgh Instruments Ltd., Livingston, UK). The photoluminescence spectra were excited by a solid-state laser with an excitation wavelength of 375 nm (the average pulse power was about 0.15 mW mm^{-2}, the pulse duration was 76 ps) and measured in the range of 400 to 600 nm. All photoluminescence spectra were corrected for the instrument sensitivity.

The diffuse reflectance spectra of WO$_3$ films were measured in the spectral range from 300 to 1100 nm using the Avantes spectrometer (AvaSpec-HS-TEC) equipped with an integrating sphere (Labsphere). Avantes Xenon lamp (AvaLight-XE) was used as the light source for sample excitation. Optical bandgap energies (E$_g$) of the prepared films were determined by extrapolating the linear region of the (αhυ)^2 vs hυ plots.

3.3. Photoelectrochemical measurements

Photoelectrochemical measurements (cyclic voltammetry (CV), chronoamperometry (CA), and electrochemical impedance spectroscopy (EIS)) were performed using three-electrode cell and potentiostat/galvanostat AUTOLAB 302 (Ecochemie, Utrecht, The Netherlands). Tungsten (VI) oxide films on FTO substrates were used as working electrodes. Silver/silver chloride electrode with saturated KCl solution (E = 0.197 V (NHE)) and Pt plate (1 x 1 cm^2) were used as reference and counter electrodes, respectively. All potential values in the text refer to Ag/AgCl scale unless noted otherwise.

The surface of working electrodes was illuminated with a high-intensity discharge Xe lamp with 6000 K spectrum and calibrated with a silicon diode to simulate AM 1.5 illumination ($\sim$100 mW cm^{-2}) at the sample surface. Current density values were calculated based on the geometric area of the working electrode. CV experiments were carried out in 0.5 M H$_2$SO$_4$, 0.5 M NaCl and mixed (0.5 M H$_2$SO$_4$ + 0.5 M NaCl) electrolytes.

EIS measurements were conducted under continuous illumination. The spectra were recorded under the open-circuit potential in potentiostatic mode with the AC voltage amplitude of $\pm$ 10 mV. The frequency range from 10^5 to 0.01 Hz was explored. The fitting of EIS data was performed using ZSimpWin software.

Mott-Schottky measurements were performed in dark at a fixed frequency of 1000 Hz with an AC voltage amplitude of $\pm$ 10 mV. Donor density, N_D, was evaluated from the slope of $1/C^2$ - E plots according to the following equation (4):

$$\frac{1}{C^2} = \frac{2}{\epsilon\epsilon^0 A^2 e N_D}\left(E - E_{FB} - \frac{K_B T}{e}\right) \tag{4}$$

where C is the specific capacitance (F cm^{-2}), ε is the relative permittivity of semiconductor (50 for WO$_3$ [93] and ε^0 is the permittivity of vacuum (8.854 $\times$ 10^{-14} F cm^{-1}), A is the area of electrode (cm^2), e is the electron charge (1.60 $\times$ 10^{-19} C), N_D is the donor density (cm^{-3}), E is the applied electrode potential, E_{FB} is the flat band potential, K_B is the Boltzman constant and T is the temperature in absolute scale.

Applied bias photon-to-current efficiency (ABPE) or light-to-electrical energy conversion efficiency in PEC systems investigated was calculated from photocurrent-potential characteristics using equation:

$$ABPE(\%) = j_{ph}\left[(E^0_{rev} - |E_{app}|)/I_0\right] \times 100 \tag{5}$$

where j_{ph} is the photocurrent density (mA cm^{-2}), E^0_{rev} is the thermodynamic potential of a reaction (V), E_{app} is applied potential (V), and I_0 is the power density of incident light (100 mW cm^{-2}) [94].

To determine the Faradaic (FE) or electrical-to-chemical energy conversion efficiency of photoelectrochemical generation of RCS (ClO$^-$ + ClO$_2$$^-$) and S$_2O_8$$^{2-}$, photoelectrolysis experiments were performed in 0.5 M NaCl and 0.5 M H$_2$SO$_4$ solutions, respectively, in a two-electrode cell with Pt cathode. The anodic and cathodic compartments of the cell were separated with a glass frit. Cell voltage of 1.8 V in 0.5 M H$_2$SO$_4$ or 1.6 V in 0.5 M NaCl

was applied. Under such conditions, the photocurrent was sufficiently high, whereas the dark current was still negligible. Photoelectrolysis with a particular WO_3 photoelectrode was performed 3 to 5 times with periods of increasing duration. After each period, solution from the anodic compartment of the cell was collected and subjected to titrimetric analysis to determine the amount of photoelectrochemically formed $S_2O_8^{2-}$ or $ClO^- + ClO_2^-$ (m_{exp}). For determination of persulfate, dichromatometry was used, whereas the amount of RCS was quantified with the help of iodometric titration in slightly alkaline acetate medium (for ClO^-) and acidic sulfuric acid medium (for $ClO^- + ClO_2^-$). The FE (%) of the photoelectrochemical generation of active chlorine and sulfate species was evaluated as the ratio m_{exp}/m_{theor}, where m_{theor} is the theoretical mass calculated according to Faraday's law assuming two-electron transfer in $Cl^- \rightarrow ClO^-$, $ClO^- \rightarrow ClO_2^-$ and $2SO_4^{2-} \rightarrow S_2O_8^{2-}$ transitions.

3.4. Evaluation of antimicrobial effect of photoelectrolysis with WO₃ photoanodes

Bacillus sp. and *E.coli* C41(DE3) were selected as the biological objects to evaluate the antimicrobial effect of photoelectrolysis with synthesized WO_3 photoelectrodes. Bacterial strains were cultured in Lysogeny broth at 37 °C for 6 h with shaking 180 rpm. The cells were harvested by centrifugation at 3000 rpm for 15 min, washed twice with 0.9% NaCl and then suspended in 50 cm³ of either 0.5 M NaCl or 0.1 M Na_2SO_4. Samples of 10 cm³ were taken for bacterial disinfection experiments, which were conducted under photoelectrochemical (electrolysis at cell voltage of 1.6 V under illumination), electrolytic (electrolysis at 1.6 V without illumination) and photolytic (illumination without electrolysis) conditions. The experiments were performed in a two-compartment quartz cell. The compartments were separated with Millipore membrane filter (0.22 μm pore size). Pt plate (1 × 1 cm²) served as cathode and WO_3 samples were used as photoanodes. The cathodic compartment of the cell was filled with 0.5 M NaCl or 0.1 M Na_2SO_4, whereas the anodic one was filled with suspension of cells in corresponding solution. After each experiment, 1.5 cm³ aliquots of anolyte were acquired for the analysis of bacterial survival by doing serial dilutions with sterile physiological solution. From that, 0.1 cm³ of the diluted sample was spread on plate count agar plates which were incubated at 37 °C for 16 h. The formed colonies were counted before and after the disinfection experiments.

4. RESULTS AND DISCUSSION

4.1. WO$_3$ coatings prepared via "peroxotungstic acid" route

In this synthesis, WO$_3$ formation conditions were modified by using four different alcohols (methanol, ethanol, isopropanol, and butanol) as reductants and two different annealing temperatures, T$_{anneal}$, i.e. 400 °C and 500 °C. Influence of these factors on PEC performance of the films was analyzed.

4.1.1. Morphological, structural and optical properties of WO$_3$ coatings

SEM images of the surface morphology and cross-sections of WO$_3$ coatings formed in four different solutions and annealed at different T$_{anneal}$ are shown in Fig. 4. The main difference between the morphology of WO$_3$ films, deposited using different alcohols consists in the size and shape of the particles forming the coating. MeOH_WO$_3$ layers are composed of 400 - 600 nm circle shaped plates. EtOH_WO$_3$ and IsoPrOH_WO$_3$ films consist of rather large 700 - 1200 nm and 800 – 1500 nm rectangular-shaped plates, whereas BuOH_WO$_3$ layers – of 600–700-nm square-shaped particles. The influence of annealing temperature is more vivid in SEM images of EtOH_WO$_3$ and BuOH_WO$_3$ films, where a considerable increase in particle size after annealing at 500 °C can be observed (Fig.4 c,d,g,h). From cross-sectional SEM images of the coatings (insets in Fig. 4), it is observed that the thickness of the layers varies between 0.5 and 0.7 μm and is practically independent of the reductant and T$_{anneal}$. The plate-like array films showed good adhesion to the FTO substrate.

Significant differences in morphology of WO$_3$ films can be explained considering the colloidal stability of the oxide particles in different solvents as well as the reducing ability of primary alcohols. The reducing ability of alcohols increases with decreasing carbon chain length, due to higher electron density on the hydroxyl group of alcohol [95, 96]. During synthesis, stronger reductant should initiate faster reduction of peroxotungstic acid leading to lower stability of solution and precipitation of WO$_3$·nH$_2$O particles. In general, addition of alcohols with lower dielectric constant to aqueous solution leads to supersaturation and precipitation of dissolved substances because of a decrease in their solvation energy [97,98]. Furthermore, dielectric constant is temperature dependent, it decreases with an increase in temperature and this
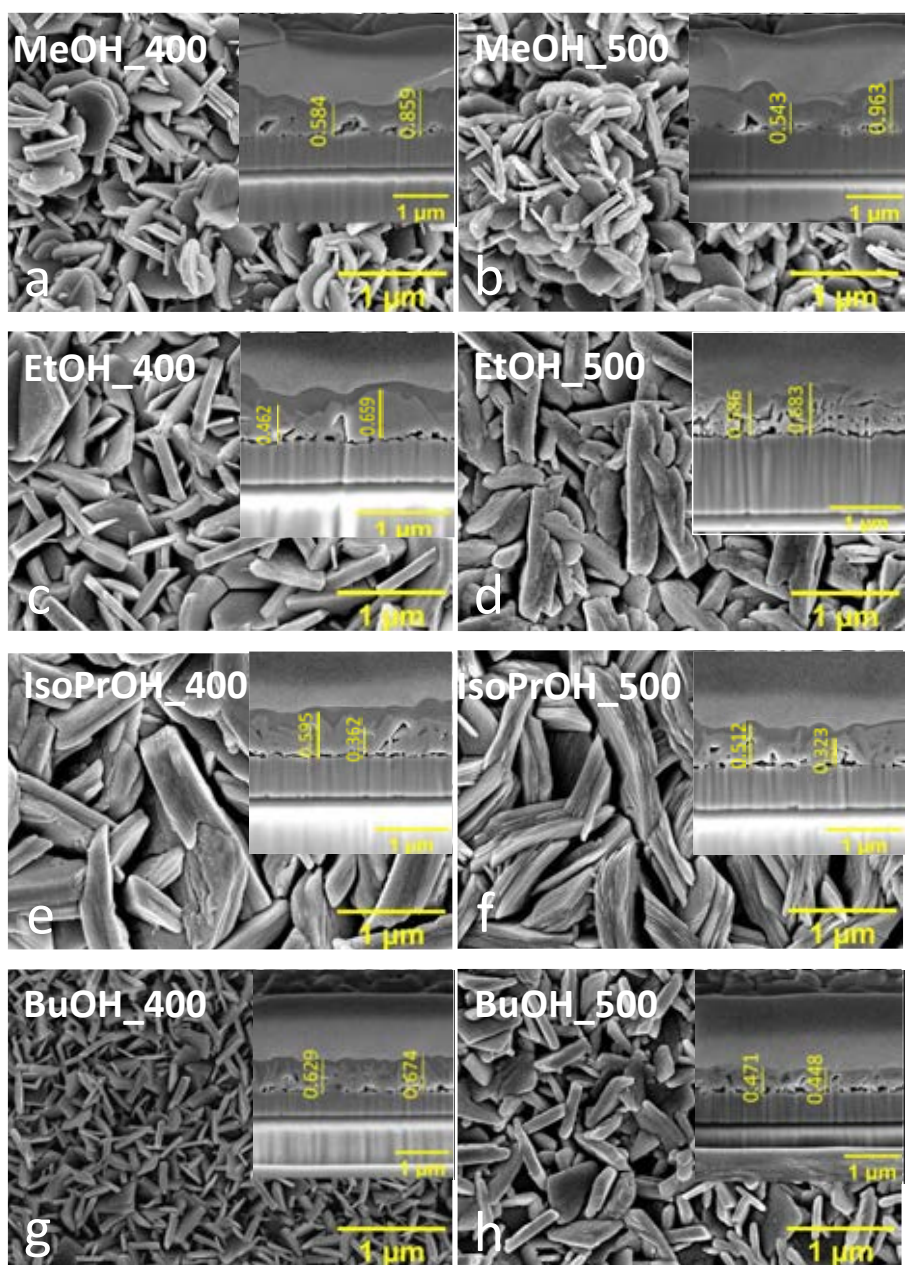
Figure 4. Top view and cross sectional (insets) SEM images of WO₃ samples formed using MeOH (a, b), EtOH (c, d), IsoPrOH (e, f) and BuOH (g, h) and annealed at 400 °C (a, c, e, g) or 500 °C (b, d, f, h)

is why precipitation occurs faster at higher temperatures. On the other hand, the energy barrier which inhibits the agglomeration of the particles is known to be directly proportional to dielectric constant of the liquid medium and the surface potential [99]. In the reduction process, when the dielectric constant of the solution is relatively high, the energy barrier between a particle and solution is high enough. Therefore, the primary oxide particles precipitated from such solution are stable and do not agglomerate, what leads to the formation of smaller units. Dielectric constants of water and alcohols used in the synthesis are listed in Table 1. The trend of increasing size of plate-shaped particles with a decrease in dielectric constant of alcohol is clearly observed in series: MeOH_WO$_3$ < EtOH_WO$_3$ < IsoPrOH_WO$_3$. BuOH_WO$_3$ coatings do not follow the tendency. This could be explained by the lowest reduction ability of butanol among the alcohols-reductants investigated and, consequently, sluggish kinetics of the process. Moreover, steric barriers related with dimensions of 1-butanol and its oxidation products such as butyralaldehyde or butan-1-carboxylic acid can play a crucial role in the formation of WO$_3$·nH$_2$O colloids with oxalate anion. All these factors may contribute to the formation of small particles.

Table 1. Dielectric constant values of water and alcohols used in the synthesis of WO$_3$ films

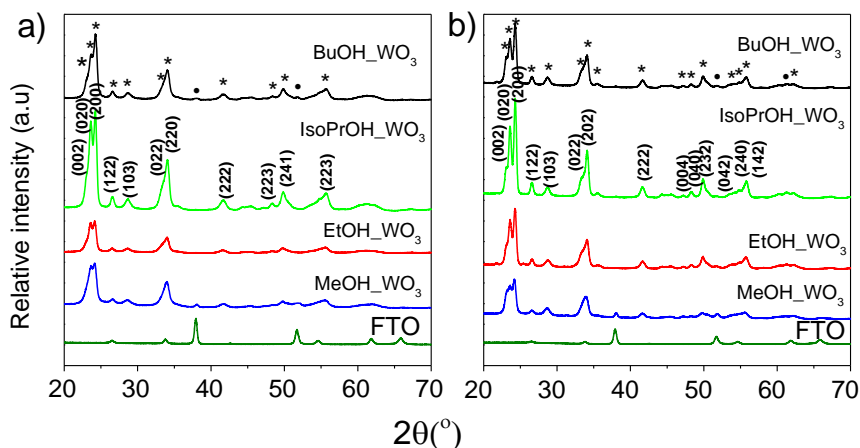| Reductant	Dielectric constant at 20 °C	Dielectric constant at 80 °C	Reference
H$_2$O	80.37	60	[100-101]
MeOH	32.35	28.24	[100,102-105]
EtOH	25.0	19.45	[100,102,104-105]
IsoPrOH	18.62	11.82	[105]
BuOH	17.43	11.4	[100,103-105]

Figure 5. XRD patterns of FTO substrate and WO₃ films deposited from solutions prepared with MeOH, EtOH, IsoPrOH, and BuOH as reductants and aneealed at a) 400 °C and b) 500 °C. Notations: * - WO₃ [COD: 2311041], ● - SnO₂ [COD: 2101853].

Fig. 5 shows XRD patterns of coatings synthesized using MeOH, EtOH, IsoPrOH, and BuOH and annealed at 400 °C or 500 °C. It is evident that different reductants and annealing temperatures influence the crystallinity of the samples. All diffractograms have clusters of three peaks at $2\theta = 23.20°$, $23.60°$, and $24.29°$, which are, respectively, attributed to (002), (020), and (200) facets of monoclinic WO₃. The results of annealed samples indicate preferential growth of WO₃ along (020) and (200) crystal planes. The narrowest diffraction peaks corresponding to (020) and (200) facets are observed in the samples synthesized with IsoPrOH, implying that crystallinity of these WO₃ coatings is the highest. Due to lower crystallinity, all samples annealed at 400 °C (Fig. 5a) have slightly broader peaks compared to their counterparts heated at 500 °C (Fig. 5b).

Another important feature to be noted is that (002) facet at $2\theta = 23.20°$ is not clearly expressed in all the coatings investigated (Fig. 5). The very low intensity of this peak may indicate the perpendicular position of the facet to the substrate, and the higher intensity of (020) and (200) peaks suggests parallel orientation of the facets with respect to substrate. Preferential growth of (200) and (020) planes in the synthesis adopted can be explained by preferential adsorption of oxalate ions as a capping agent onto (002) plane. According to theoretical calculations [106], a surface energy order of the facets is as follows: 1.56 J m⁻² (002) > 1.54 J m⁻² (020) > 1.43 J m⁻² (200),

indicating that (200) is the most stable facet. Thus, the synthesis conditions used in this study are favorable for the formation of thin films with preferential growth of the more stable crystal facets of monoclinic WO_3.
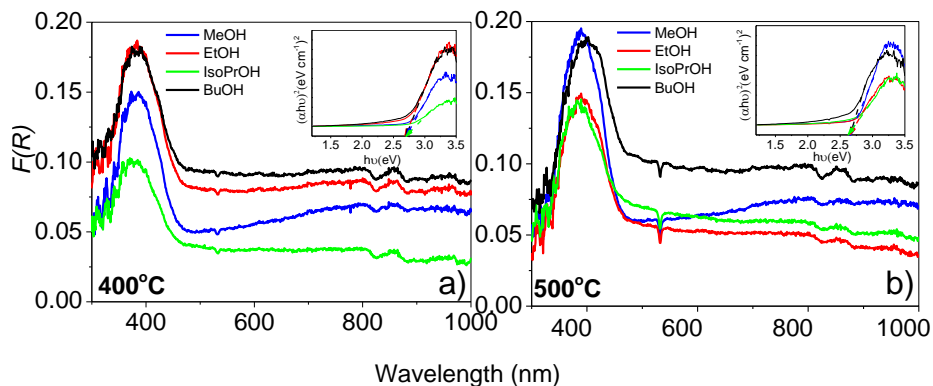

Figure 6. Diffuse reflectance spectra of WO_3 coatings formed with methanol (1), ethanol (2), isopropanol (3), and butanol (4) as reductants and annealed at a) 400 °C and b) 500 °C

The diffuse reflectance spectra of WO_3 films are shown in Fig.6. Direct band gap values determined from Tauc plots shown in the insets in Fig. 6 were close to 2.7 eV irrespective of the reductant used in the synthesis and annealing temperature. This is a typical value for WO_3 [107,108].

4.1.2. Photoelectrochemical performance of WO_3 layers in 0.5 M H_2SO_4: influence of annealing temperature

Photoelectrochemical activity of WO_3 films deposited on FTO substrate was characterized using cyclic voltammetry in the solution of 0.5 M H_2SO_4 in dark and under illumination. The results are presented in Fig. 7. The voltammetric response of WO_3 coatings can be divided into two parts as described further. Within the E range below 0.5 V the electrochemical behavior of the electrode is illumination independent, as can be seen from the comparison of CVs recorded in dark and under illumination (Fig. 7). Nearly symmetric anodic and cathodic peaks correspond to reversible redox transition between W (VI) and W (V) oxygen species:
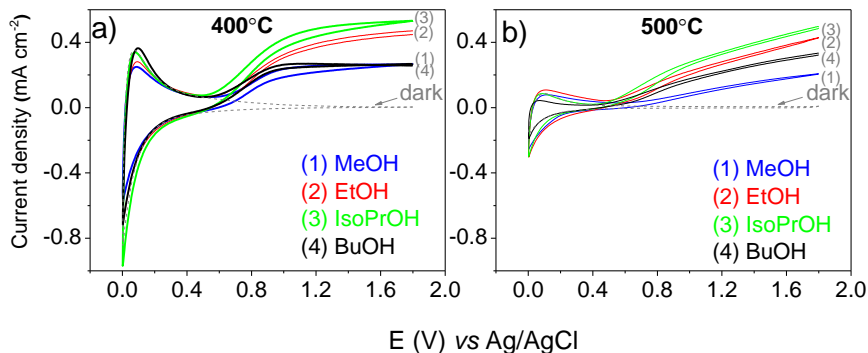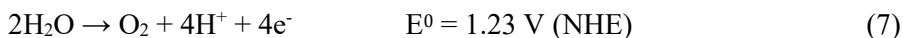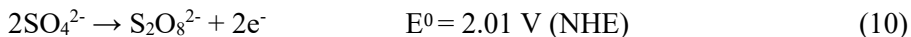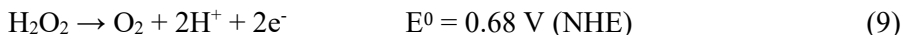
$$WO_3 + xe^- + xH^+ \rightleftarrows H_xWO_3 \qquad (6)$$

Figure 7. Cyclic voltammograms of WO_3 coatings formed with MeOH (1), EtOH (2), IsoPrOH (3), and BuOH (4) as reductants and annealed at a) 400 °C or b) 500 °C; 0.5 M H_2SO_4, potential scan rate 50 mV s^{-1}, intensity of illumination ~ 100 mW cm^{-2}. Curves recorded in dark are those of samples prepared with isopropanol

This electrochemical process, involving participation of protons from the solution, takes place at electrode/electrolyte interface as well as in the bulk of the oxide layer [109, 110]. The kinetics of this process depends on diffusivity of protons within film, which, in turn, is dependent on the structural and morphological characteristics of WO_3 layers. Consequently, the area under the voltammetric peaks within 0 - 0.5 V, which is equivalent to charge consumed in reaction (6), can be treated as a relative measure of the electrochemical activity of WO_3 films.

The region above 0.5 V is the range of photocurrent, $j_{ph,}$ where no electrochemical reactions occur in dark (zero current), whereas under illumination anodic current is observed. Such behavior is consistent with n-type conductivity of WO_3 layers. The photoanodic current results from the interaction of solution species with photogenerated holes, which form in the valence band of semiconductor. Possible processes can be described by the following reactions:

$$2H_2O \rightarrow O_2 + 4H^+ + 4e^- \qquad E^0 = 1.23 \text{ V (NHE)} \qquad (7)$$

$$2H_2O \rightarrow H_2O_2 + 2H^+ + 2e^- \qquad E^0 = 1.77 \text{ V (NHE)} \qquad (8)$$

$$H_2O_2 \rightarrow O_2 + 2H^+ + 2e^- \qquad E^0 = 0.68 \text{ V (NHE)} \qquad (9)$$

$$2SO_4^{2-} \rightarrow S_2O_8^{2-} + 2e^- \qquad E^0 = 2.01 \text{ V (NHE)} \qquad (10)$$
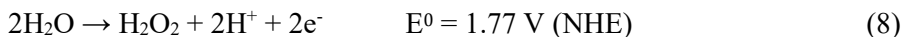
where E^0 is the standard potential. It can be seen in Fig. 7 that samples annealed at 400 °C exhibit significantly faster increase and saturation of j_{ph} than those annealed at 500 °C. This implies more efficient generation, separation, transport as well as transfer of the photogenerated charge carriers in the films annealed at lower temperature. A very distinct feature of the coatings annealed at 500 °C is significant decrease in illumination-independent currents at $E < 0.5$ V (Fig. 7). It means that rearrangement of crystalline structure of WO_3, which takes place during annealing in the range between 400 °C and 500 °C as revealed by XRD and FTIR investigations [111], leads also to a decrease in electrochemical activity of the oxide films. The total charge corresponding to cathodic and anodic current peaks within E range from 0 to 0.45 V decreased from 2 to 3 times upon annealing at 500 °C. This points to a significant restructuring of WO_3 layers, as a result of which the insertion and extraction of protons according to reaction (6) become hindered. This explains the deterioration of photoelectrochemical performance, because these structural rearrangements hamper the movement of photoinduced charge carriers as well. Similar effect of sintering accompanied by deterioration of PEC activity with increase in annealing temperature of WO_3 films was reported in [112]. It should be noted, however, that the optimal annealing temperature depends on synthesis method used. Though majority of the studies report that annealing of WO_3 at 500°C gives the best results in terms of PEC activity, our findings demonstrate that in the case of synthesis adopted in this study, heat treatment at 400°C was the most optimal in terms of crystallinity and morphology of the coatings. Therefore, further investigations were performed with samples annealed at 400°C.

4.1.3. Evaluation of charge transfer resistance, donor density and charge carrier lifetime in WO₃ films using EIS and PL
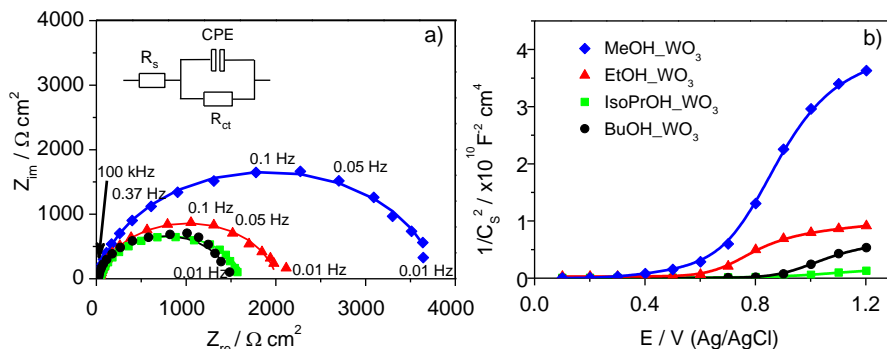

Figure 8. a) Nyquist plots of WO$_3$ coatings formed using MeOH, EtOH, IsoPrOH, and BuOH as reductants: symbols represent the experimental points and lines represent the fitting data; inset shows the equivalent circuit used for fitting; illumination intensity ∼100 mW cm^{-2}; b) Mott-Schottky plots of the same samples obtained at 1000 Hz in 0.5 M H$_2$SO$_4$ solution in dark.

The structural defects, present in the bulk of the synthesized layers, can affect the mobility of photo-generated charge carriers by hindering their transport within the crystal lattice. The influence of these defects on charge transfer resistance of WO$_3$ layers was evaluated using electrochemical impedance spectroscopy. The EIS data were fitted using Randles circuit, which consists of a charge transfer resistance (R_{ct}) that is connected with a constant phase element (CPE) in parallel and solution resistance (R_s) in series (inset in Fig. 8a). Smaller arc radius in Nyquist plots (Fig. 8a) is associated with more efficient separation, transport as well as interfacial transfer of photoinduced charge carriers, whereas larger radius suggests a more hindered photoelectrochemical process [113,114]. There is obviously a large gap between R_{ct} of MeOH_WO$_3$ and those of other samples, which can be understood considering the results of morphological and structural observations: MeOH_WO$_3$ composed of the smallest plates with the smallest crystallite size and having the highest dislocation density (all parameters are summarized in Table 2) showed inferior characteristics of charge transport, because high concentration of structural defects provided resistance for migration of charge carriers. Further clues to understanding the EIS results can be obtained from evaluation of the donor density, N$_D$, from Mott-Shottky plots (Fig. 8b). It is important to note that these measurements were performed

without illumination, which means that no anodic current flows in the range of potentials where ascending parts in C^{-2} vs. E plots are observed (see Fig. 7), therefore capacitive behavior should be related with the charge change within space charge region. The values of donor density, N_D, evaluated from the slope of Mott-Schottky plots are on the order of 10^{19} to 10^{20} (Table 2), which is similar to previously reported data for WO_3 [115,116]. N_D of MeOH_WO_3 was the lowest, which also was a contributing factor to higher R_{ct}, whereas the high donor density and low degree of structural disorder of IsoPrOH_WO_3 resulted in lower charge transfer resistance (Table 2). Determined values of N_D are rather high, characteristic to heavily doped semiconductor. According to literature[117], when the doping level is 10^{19}, the voltage drop in the space charge region is very small, on the order of millivolts, and most of the potential drop occurs in the Helmholtz layer. This introduces certain error to determination of flat band potential (V_{fb}) by extrapolation of C^{-2} vs. E plots [118], therefore this evaluation was not performed.

The n-type doping of metal oxides is ascribed mainly to the presence of oxygen vacancies [119]. It can be seen from Table 2, that higher donor density correlated with larger average crystallite size in WO_3 films.

Table 2. Summary of results of XRD, EIS, and PL analysis of WO_3 coatings formed using different reductants.

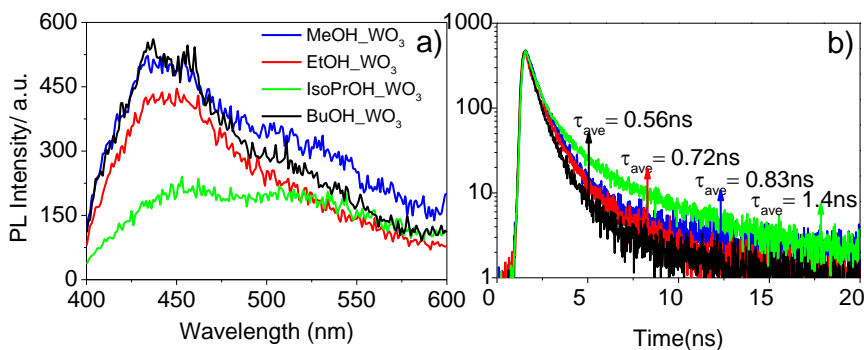| Sample	Average crystallite size D, nm	Dislo-cation density $\partial \times 10^{16}$, lines m^{-2}	Charge transfer resistance R_{ct}, Ω cm^2	Donor density N_D, cm^{-3}	Average decay time τ_{ave}, ns
MeOH_WO_3	8.2 ± 2.8	1.5	3712	1.7×10^{19}	0.83
EtOH_WO_3	9.4 ± 3.0	1.1	2004	7.4×10^{19}	0.72
IsoPrOH_WO_3	11.3 ± 3.3	0.8	1592	4.4×10^{20}	1.4
BuOH_WO_3	9.5 ± 3.2	1.1	1495	9.2×10^{19}	0.56

Figure 9. Room-temperature photoluminescence spectra of WO_3 coatings formed using MeOH, EtOH, IsoPrOH, and BuOH as reductants; excitation wavelength 375 nm; b) time-resolved photoluminescence decay kinetics of the same samples; excitation wavelength 430 nm; values of average decay time are indicated in the figure.

In PEC systems, the most important processes occur at the electrode/electrolyte interface, where defects and surface states can act as recombination centers for electrons and holes and usually govern the kinetics of interfacial charge transfer. The presence of point defects in the interfacial region of the synthesized WO_3 films was probed with the help of photoluminescence spectroscopy. PL spectra in Fig. 9a exhibit two broad bands within 400 - 600 nm. In accordance with literature [120,121], the so-called blue emission band with maximum at 435 - 450 nm is attributed to radiative recombination of photo-induced charge carriers. The green emission band at $\lambda > 500$ nm is due to oxygen vacancies, localized states and defects present within the band gap [122–125] Considering the whole range of wavelengths shown in Fig. 9a, it can be seen that PL intensity decreases in the sequence $MeOH\_WO_3 > BuOH\_WO_3 > EtOH\_WO_3 > IsoPrOH\_WO_3$, which is consistent with transition from the finest to the coarsest morphology of WO_3 layers (Fig. 4). Moreover, the decrease in PL intensity correlates with decrease in degree of structural disorder evaluated from XRD investigations (Table 2). The lower PL emission intensity implies suppressed recombination rate of photoinduced charge carriers. The significantly lower intensity of blue emission peak (at 450 nm) of $IsoPrOH\_WO_3$ compared to other samples suggests that rapid band to band recombination is suppressed due to trapping of charge carriers by oxygen vacancies or some other structural defects of crystal lattice. This is consistent with the highest N_D of $IsoPrOH\_WO_3$ as well as the results of time-resolved photoluminescence decay measurements shown

in Fig. 8b. It can be seen that the average decay time, which is equivalent to lifetime of charge carriers, τ_{ave}, was significantly longer in the case of IsoPrOH_WO$_3$, i.e. 1.4 ns, compared to other samples (Fig. 8b). It is important to note that in order to have efficient PEC performance, the number of defects in the interfacial region of a semiconductor should be sufficient to facilitate charge separation, but not too large to impede PEC reactions due to trap-mediated recombination of electrons and holes [119]. This is supported by much longer τ_{ave} values (4.5 – 11 ns) found in our study for WO$_3$ coatings annealed at 500 °C [126].

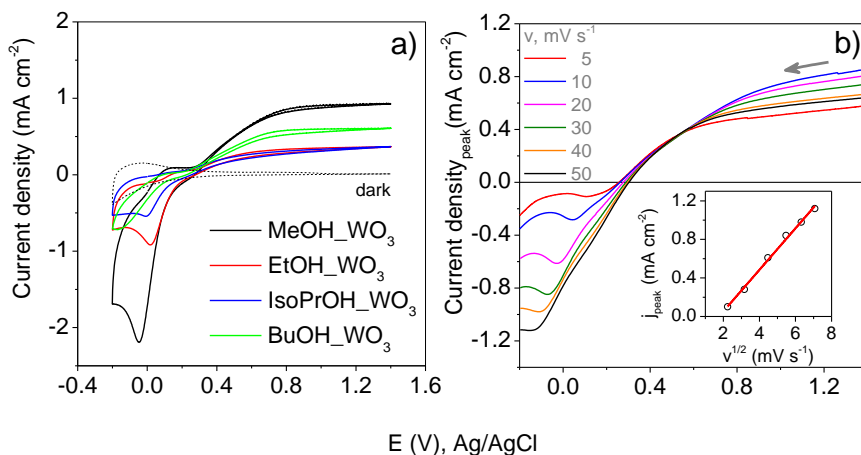### 4.1.4. Photoelectrochemical performance of WO$_3$ layers in 0.5 M NaCl

Figure 10. a) Cyclic voltammograms of WO$_3$ coatings formed using MeOH, EtOH, IsoPrOH and BuOH as reductants, 0.5 M NaCl, 50 mV s^{-1} b) Linear sweep voltammograms of MeOH_WO$_3$ electrode in 0.5 M NaCl recorded at different potential scan rates after polarizing the electrode at 1.4 V for 5 min under illumination (100 mW cm^{-2}). Inset: dependence of cathodic peak current on $v^{1/2}$.

Cyclic voltammograms of WO$_3$ films recorded in 0.5 M NaCl solution are shown in Fig. 10. The illumination-independent region of CVs recorded in chloride medium (Fig. 10a, E < 0.3 V) is different in shape compared to that of CVs in 0.5 M H$_2$SO$_4$ (Fig. 7, E < 0.5 V). The reduction currents here increased proportionally to time the photoelectrode was polarized at 1.4 V under illumination, which implies that there is a causal relationship between the photoanodic and subsequent cathodic processes. To investigate the origin of cathodic current increase in chloride solution at E < 0.3 V, the sample was

35

polarized for 5 min at 1.4 V under illumination and then the electrode potential was swept towards -0.2 V at different scan rates, v, ranging from 5 to 50 mV s^{-1}. The cathodic peak current densities, j_{peak}, were plotted against $v^{1/2}$ (Fig. 10b). Linear dependence of peak current on $v^{1/2}$ (inset in Fig. 10b) points to diffusion-controlled process, implying that cathodic current arises from the reduction of the products of photoanodic reaction, which are released to solution rather than adsorbed on the photoelectrode surface. In addition to photoanodic oxidation of water molecules (reactions (8)-(10) indicated above), hole-induced oxidation of chloride anions can take place:

$$2Cl^- \rightarrow Cl_2 + 2e^- \qquad\qquad E^0 = 1.39 \text{ V} \qquad\qquad (11)$$

$$Cl^- + H_2O \rightarrow HClO + H^+ + 2e^- \quad E^0 = 1.50 \text{ V} \qquad\qquad (12)$$
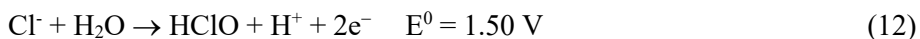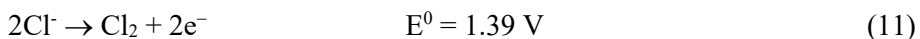
Results of the analysis of the products and Faradaic efficiency of photoanodic reactions in 0.5 M H_2SO_4 and 0.5 M NaCl electrolytes are disscussed further.

4.1.5. Analysis of the products and energy conversion efficiency of photoanodic reactions in 0.5 M H_2SO_4 and 0.5 M NaCl electrolytes
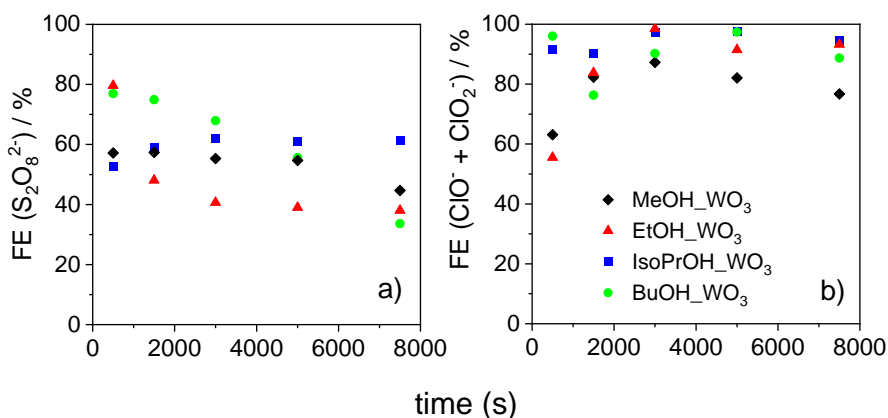
Figure 11. Variation of Faradaic efficiency of photoelectrochemical generation of $S_2O_8^{2-}$ (a) and reactive chlorine species ($ClO^- + ClO_2^-$) (b) on indicated WO_3 coatings during photoelectrolysis in the solutions of 0.5 M H_2SO_4 and 0.5 M NaCl, respectively.

The products of PEC processes occurring on WO_3 surface, that were analysed in this study, were persulfate ($S_2O_8^{2-}$) in 0.5 M H_2SO_4 and reactive chlorine species ($ClO^- + ClO_2^-$) in 0.5 M NaCl. Formation of Cl_2 was not considered based on the thermodynamic stability of various chloride oxidation products

in neutral 0.5 M NaCl [127,128]. The values of Faradaic efficiency are summarized in Fig. 11. Rather wide scattering of experimental points was observed in both solutions: FEs varied between 35 and 80 % for $S_2O_8^{2-}$ (Fig. 11a) and between 50 and 99 % for RCS (Fig. 11b). The remaining charge was assigned to oxidation of H_2O (to O_2 or H_2O_2). While no clear correlation of FE values with sample morphology was observed, these results show that the competition between the photoanodic oxidation of anions and water molecules on the surface of WO_3 electrodes is significant and will be discussed further. Overall, the contribution of anion oxidation into the total photocurrent was markedly higher in chloride medium with FEs reaching nearly 100 % (Fig. 11b). Therefore, the above discussed increase in cathodic current seen in voltammograms of WO_3 photoelectrodes in 0.5 M NaCl (Fig. 10 a, b) is most likely related with reduction of RCS, though the possibility of reduction of H_2O_2 cannot be excluded.
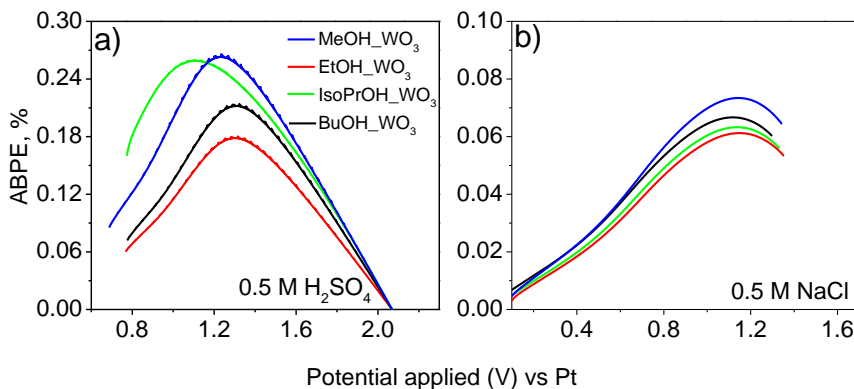
Figure 12. Applied bias photon-to-current efficiency (ABPE) plots in 0.5 M H_2SO_4 (a) and 0.5 M NaCl (b) for WO_3 photoanodes prepared using four different reductants, 50 mV s^{-1}, intensity of illumination 100 mW cm^{-2}

Plots of applied bias photon-to-current conversion efficiency calculated according to eq. (5) from linear sweep voltammograms run at 50 mV s^{-1} are shown in Fig.12. Values of E_{rev}^0 used for calculations were 2.069 V and 1.713 V for in 0.5 M H_2SO_4 and 0.5 M NaCl, respectively. They were evaluated presuming that anodic reactions were (10) and (12), whereas the cathodic one was hydrogen evolution on Pt counter electrode, and taking into consideration the pH-dependence of E values. One can see that ABPE values in both electrolytes were rather low – significantly below 1 %.

4.1.6. Stability of WO$_3$ photoanodes during photoelectrolysis in 0.5 M H$_2$SO$_4$ and 0.5 M NaCl electrolytes

Variation of photocurrent of WO$_3$ films during photoelectrolysis in 0.5 M H$_2$SO$_4$ and 0.5 M NaCl electrolytes is compared in Fig. 13. It is obvious that photocurrents in 0.5 M NaCl were more stable, i.e. less decreasing with time than those in 0.5 M H$_2$SO$_4$ for all WO$_3$ coatings investigated, implying that either charge transfer was more efficient in chloride medium or the degradation/passivation of the photoelectrode was less. In literature, the decay in photocurrent of WO$_3$ electrodes is usually ascribed to formation and accumulation of peroxo species [62, 129, 130] in the process of photoanodic oxidation of water molecules. If so, the stability of j$_{ph}$ suggests that chloride ions in some way prevent the accumulation of peroxo species on the photoanode surface. The reasons of such behavior are analysed further.
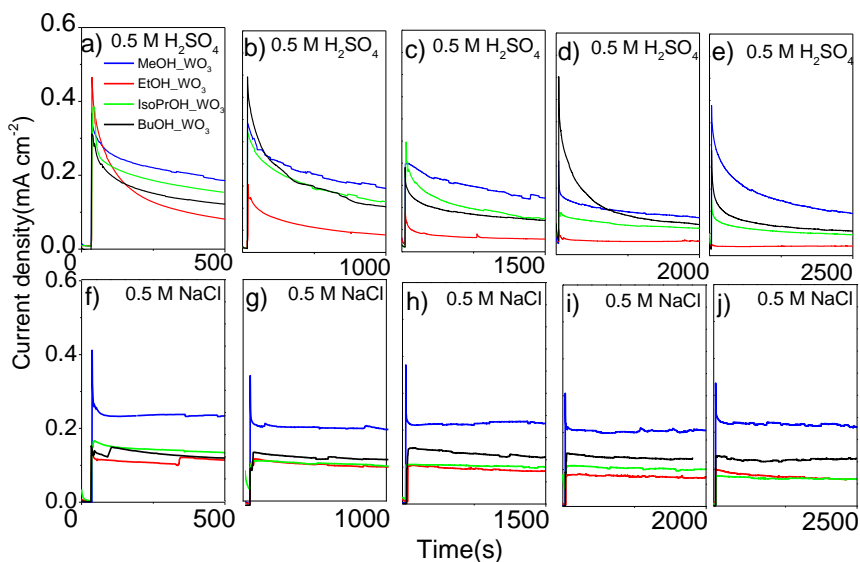

Figure 13. Chronoamperograms of WO$_3$ films prepared using different alcohols. CAs were recorded during five consecutive photoelectrolysis experiments with increasing duration in 0.5 M H$_2$SO$_4$ at cell voltage of 1.8 V (a-e) and 0.5 M NaCl (f-i) at cell voltage of 1.6 V, intensity of illumination $\sim$ 100 mW cm^{-2}.

4.1.7. Analysis of the competition between the photoanodic reactions on WO$_3$ surface

The photoelectrochemical activity of WO$_3$ samples in sulfate and chloride medium was compared in chronoamperometric measurements under potentiostatic conditions and chopped illumination. It is important to note, that the electrode used for CA measurements in both electrolytes was the same, which implies no changes in N$_D$, structure of defects and morphology. The potential of WO$_3$ photoanodes was set to 0.7 V in 0.5 M H$_2$SO$_4$ and 0.4 V in 0.5 M NaCl. These E values are close to the photocurrent onset potential and correspond to the rising part of CVs (Figs. 7a, 10a), implying that under such conditions the electron-hole recombination is not fully suppressed by the applied bias, therefore the influence of morphology and/or presence of defects should be more pronounced (as opposed to the photocurrent saturation region, where practically all photogenerated holes reaching electrode/electrolyte interface participate in charge transfer reactions).
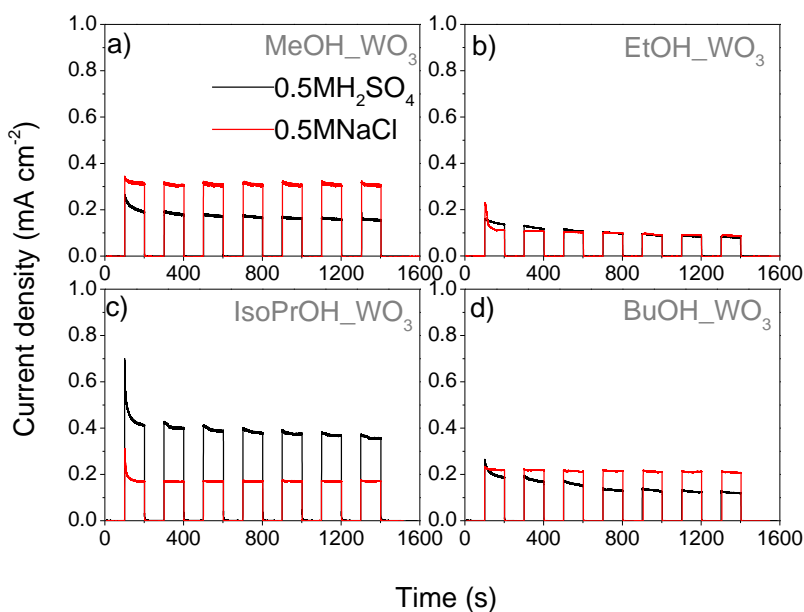

Figure 14. Chronoamperograms of WO$_3$ photoanodes formed using MeOH (a), EtOH (b), IsoPrOH (c) and BuOH (d) as reductants, under chopped illumination in 0.5 M H$_2$SO$_4$ (black lines) and 0.5 M NaCl (red lines) at 0.7 V and 0.4 V, respectively; the same electrode was used in both solutions

It can be seen that the photocurrents in 0.5 M NaCl were higher (Fig. 14a, d) or almost equal (Fig. 14b) to those in 0.5 M H_2SO_4 for all samples except IsoPrOH_WO_3 (Fig. 14c). In terms of morphology, MeOH_WO_3 and BuOH_WO_3 (Fig. 4 a and g) composed of small plates exhibited higher PEC activity in chloride medium, whereas the photocurrent of IsoPrOH_WO_3 electrode with large-plate morphology was significantly higher in 0.5 M H_2SO_4. PEC activity of EtOH_WO_3 was almost the same in both electrolytes, which is consistent with intermediate dimensions of plate-like units forming the film. The competition between photoanodic processes was further investigated by comparing the photoelectrochemical responses of the four electrodes in sulfuric acid solution in the absence and presence of chloride ions (Fig. 15).
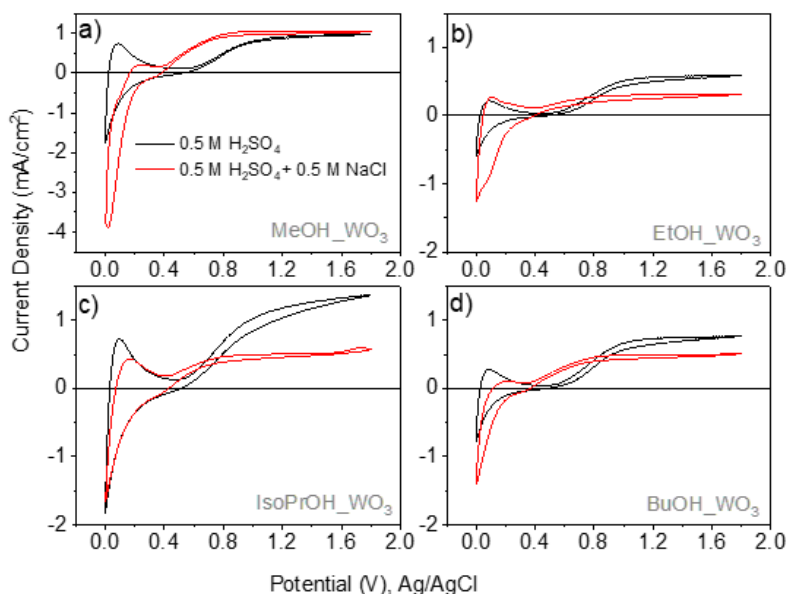
Figure 15. Cyclic voltammograms of WO_3 photoanodes formed using MeOH (a), EtOH (b), IsoPrOH (c) and BuOH (d) as reductants in solutions of 0.5 M H_2SO_4 (black curves) and 0.5 M H_2SO_4 + 0.5 M NaCl (red curves), the same electrode was used in both solutions, illumination intensity 100 mW cm^{-2}, potential scan rate 50 mV s^{-1}

It is clearly seen that in chloride-containing electrolytes the onset of j_{ph} is shifted towards more negative potentials, though pH of 0.5 M H_2SO_4 should not be affected by addition of 0.5 M NaCl. Most likely, chloride ions adsorb specifically on the semiconductor surface [131, 132] leading to an increase in

the electric field strength within the semiconductor space charge layer, and, consequently, increase in band bending. This helps to suppress electron-hole recombination at semiconductor/electrolyte interface, therefore the onset of photoanodic current in chloride containing solution shifts towards lower E values compared with sulfuric acid medium[133].

Though addition of NaCl to sulfuric acid solution depolarized the onset of j_{ph}, it also led to a decrease in photocurrents for all the electrodes except MeOH_WO$_3$ (Fig. 15a). The most significant decrease was observed for IsoPrOH_WO$_3$, the photoelectrochemical activity of which in pure 0.5 M H$_2$SO$_4$ was the highest (Fig. 15c). This implies that addition of chlorides suppressed the rate of hole transfer, whereas the extent of this decrease in j_{ph} correlated with morphological features of WO$_3$ layers.

In order to understand the observed phenomena, possible photoanodic processes occurring in the system under investigation were analyzed. In mixed sulfate-chloride electrolyte the species that can undergo photoanodic oxidation are H$_2$O molecules, Cl$^-$ and SO$_4^{2-}$ ions. The common approach is to compare the electrochemical potentials of possible oxidation processes (eqs. 7-12). The electrode potential, however, is a measure of the energy of electrons, whereas in photoanodic processes the photogenerated holes from the valence band play the key role and their energy depends on the nature of the semiconductor. In the case of WO$_3$, potential of the valence band is around + 3.0 V (NHE) [134], which means that photoholes of tungsten (VI) oxide are strong oxidizers and have enough energy to drive the oxidation of solution species via pathways involving formation of highly reactive intermediates such as free radicals. There is a growing amount of scientific evidence which supports this assumption. It has been demonstrated recently [47,135–137] that hydroxyl radicals are formed during photoelectrocatalytic oxidation of water on WO$_3$. Generation of chlorine radical species on WO$_3$ photoanodes in chloride solutions was experimentally detected in [138,139]. Effective photoelectrochemical inactivation of various bacterial strains with WO$_3$ electrodes in chloride-containing medium was also ascribed to high bacteria killing power of photoanodically formed reactive chlorine radicals [140], [141]. Photo-assisted formation of sulfate radicals, SO$_4^{-\cdot}$, was shown to be the main cause of degradation of refractory organics using WO$_3$ photoelectrode at pH 2 [142]. Therefore, the electrochemical potentials of the reactions involving formation of radicals should, in fact, be considered when analyzing the probability of one or another photoanodic reaction. According to [143] the E^0 values of hydroxyl, chlorine, hypochlorite and sulfate radicals formation are as follows:
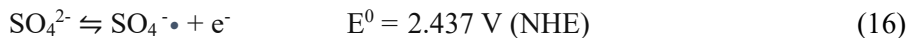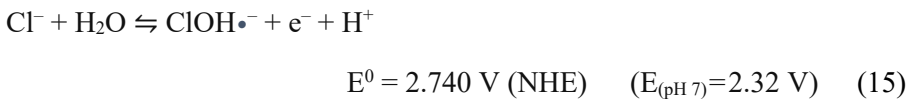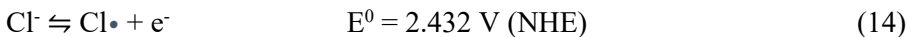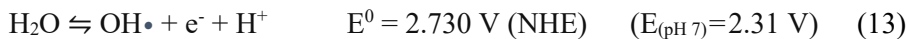
$$H_2O \leftrightharpoons OH\bullet + e^- + H^+ \qquad E^0 = 2.730 \text{ V (NHE)} \qquad (E_{(pH\,7)}=2.31 \text{ V}) \qquad (13)$$

$$Cl^- \leftrightharpoons Cl\bullet + e^- \qquad E^0 = 2.432 \text{ V (NHE)} \qquad (14)$$

$$Cl^- + H_2O \leftrightharpoons ClOH\bullet^- + e^- + H^+$$

$$E^0 = 2.740 \text{ V (NHE)} \qquad (E_{(pH\,7)}=2.32 \text{ V}) \qquad (15)$$

$$SO_4^{2-} \leftrightharpoons SO_4^-\bullet + e^- \qquad E^0 = 2.437 \text{ V (NHE)} \qquad (16)$$

$$SO_4^-\bullet + SO_4^{2-} \leftrightharpoons S_2O_8^{2-} + e^- \quad E^0 = 1.44 \text{ V (NHE)} \qquad (17)$$

Such arrangement of E^0 values implies that in acidic medium formation of $Cl^\cdot$ and $SO_4^{\cdot-}$ is thermodynamically favored over the formation of hydroxyl and hypochlorite radicals, whereas in neutral medium the latter processes have certain thermodynamic advantage. Moreover, formation of OH• according to reaction (13) should not have kinetic limitations inherent to OER due to complexity of its mechanism involving transfer of 4 electrons (eq. (7)).

Another important inference that can be drawn from the reactions (14) and (16) is that thermodynamically oxidation of chloride and sulfate anions is almost equally probable, therefore the competition between these two processes should be governed by the kinetic factors. Since photoanodic reactions are limited to the interface between the photoelectrode and electrolyte, adsorption of solution species should play an important role in determining the occurrence of one or another process. The above discussed shift of the onset of photocurrent to lower potentials upon addition of NaCl to 0.5 M H_2SO_4 means that holes primarily oxidize those species, which are adsorbed on the electrode surface, i.e. Cl^- ions, even though thermodynamic likelihood for oxidation of SO_4^{2-} is the same. Specific adsorption of chloride ions also explains high Faradaic efficiencies of RCS formation found in neutral 0.5 M NaCl (Fig. 11b), though oxidation of water molecules is the thermodynamically favoured process in this case (reaction (13) *vs* (14)).

4.1.8. Influence of WO$_3$ film morphology on PEC performance: potential-assisted photochemical approach

Further the influence of WO$_3$ film morphology on the competition between photoanodic processes in the systems investigated is discussed. Though the dimensions of structural features of WO$_3$ films range between 400 - 1500 of nanometers and are by several orders of magnitude larger than anions and water molecules, the size of slits or cavities between the protruding elements in oxide layer are roughly 10 - 100 times less. Furthermore, the processes

under investigation occur at rough electrified interfaces, where distribution of electric fields as well as the structure of electric double layer and the dynamics of water and ions are rather complex and such parameters as electrolyte concentration, ion charge and size play an important role [144].

In the case of chronoamperometric experiment shown in Fig. 14, competition between the photoanodic oxidation of SO_4^{2-} vs H_2O or Cl^- vs H_2O should be considered. Since the electrode used for CA measurements in both electrolytes was the same, which implies no changes in N_D, structure of defects and morphology, the differences in stationary photocurrent should be attributed to loss of photogenerated charge carriers by recombination, which is affected by the solution species. The results obtained with samples MeOH_WO$_3$ and BuOH_WO$_3$ (Fig. 14 a and d) show that recombination rate in 0.5 M H_2SO_4 is higher than in 0.5 M NaCl. Given the small-plate morphology of MeOH_WO$_3$ and BuOH_WO$_3$, the accessibility of the electrode/solution interface for bulkier, more strongly hydrated sulfate ions [145] should be lower. Sulfate ions compete with H_2O molecules for active sites to combine with holes on photoelectrode surface, thus altering the potential distribution as well as the electronic structure of the electrode at the interfacial region, which probably leads to situation that large fraction of photogenerated charge carriers is lost due to recombination. On the contrary, the large-plate morphology of IsoPrOH_WO$_3$ is more favourable for photoanodic reactions in 0.5 M H_2SO_4 than in 0.5 M NaCl (Figs. 14c, 15c). Most likely, steric hindrance for sulfate ions in this case is lower and formation of persulfate proceeds according to reactions (16) and (17). Stability of Faradaic efficiency of photoelectrochemical formation of $S_2O_8^{2-}$ on IsoPrOH_WO$_3$ (Fig. 11a) corroborates this assumption.

Lower photocurrents observed for IsoPrOH_WO$_3$ in the presence of chlorides (Figs. 14c, 15c) can be understood considering the following possible processes. Photoanodically formed $Cl\bullet$ radicals are known to undergo rapid complexation by excess Cl^- ions [132, 146–148] to form anion radicals:

$$Cl\bullet + Cl^- \rightarrow Cl_2\bullet^- \tag{18}$$

The equilibrium constant of this reaction is $(1.4 \pm 0.2) \times 10^5$ M^{-1} [143], implying that product is strongly favoured over the reactants. Negatively charged $Cl_2^{\cdot-}$ radicals should be electrostatically attracted to positively polarized WO_3 surface, thus blocking the access for water molecules or other anions. Moreover, these adsorbed species can act as surface recombination

centres reacting with photogenerated electrons from the conduction band [128,131]:
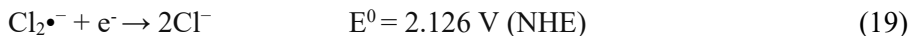
$$Cl_2\bullet^- + e^- \rightarrow 2Cl^- \qquad\qquad E^0 = 2.126 \text{ V (NHE)} \qquad\qquad (19)$$

Chloride ions formed in the above process can again participate in hole scavenging. Thus, the loop of reactions (14), (18) and (19) can account for lower photocurrents observed in the case of IsoPrOH_WO$_3$ in chloride containing electrolytes (Figs. 14, 15). Such surface-charge recombination mechanism or quenching of photogenerated charge carriers by chloride ions has been also suggested in [149] to explain the mechanism of photocatalytic degradation of 4-ethylphenol on TiO$_2$ surface. It is plausible that specific adsorption of Cl$^-$ ions and Cl$_2\bullet^-$ anion radicals prevents formation of peroxo species on WO$_3$ surface in chloride solutions, thus preserving the stability of WO$_3$ photoanodes in neutral medium.

When the dimensions of plate-shaped particles forming WO$_3$ films are smaller, the conditions for adsorption of chlorine species presumably become less favorable due to repulsive interactions between the adsorbates, what leads to a more dynamic exchange of ions or radicals with solution and lower contribution of recombination due to reaction (19). Morphology of EtOH_WO$_3$, which is intermediate between IsoPrOH_WO$_3$ and MeOH_WO$_3$ or BuOH_WO$_3$ in terms of size of plate-like units forming the coating, most likely, provides analogous conditions for the photoinduced charge transfer in both electrolytes (Fig. 14b).

Significant deterioration of PEC activity of WO$_3$ layers in 0.5 M H$_2$SO$_4$ can be ascribed either to photocorrosion/dissolution or to surface passivation of photoactive layer. Dissolution of WO$_3$ during photoanodic reactions in H$_2$SO$_4$ has been evidenced recently in [150–152]. The mechanism of this process is still unclear. Since tungsten in WO$_3$ is in its highest oxidation state, formation of surface peroxo species, induced by H$_2$O$_2$ and OH• as by-products of the water oxidation, is considered to be the main cause of material degradation [152]. The results of our study suggest that photocurrent decay is also significant when oxidation of SO$_4^{2-}$ (not H$_2$O) is dominating photoanodic reaction (Fig. 11, 13). In [153] the degradation of H$_x$WO$_3$ photoelectrodes was explained by recombination of holes with W^{5+} donors, which can be prevented by efficient hole scavenging by solution species. We hypothesize that holes, which are not scavenged by solution species, can destructively oxidize WO$_3$ to more soluble and photoelectrochemically inactive surface peroxotungstate compounds as shown in Fig. 16. Oxidative cleavage of W-O-W bond with

formation of surface peroxo species can also occur as a result of light-induced interaction of WO₃ with radical species ($SO_4^-\bullet$ or $OH\bullet$) leading to deterioration of PEC activity of the samples even though thermodynamically their stability in acidic medium should be higher than in neutral NaCl electrolyte [127].
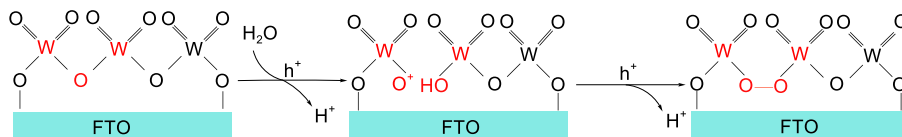

Figure 16. Mechanism of hole-induced formation of peroxo-species on the surface of WO₃ film

The above presented interpretation of possible reaction pathways invokes the mechanisms of photochemical processes, which to a certain extent are governed by the electrostatic interactions, conditioned by the electrode potential. Therefore, such treatment of photoelectrochemical processes can be termed as a potential-assisted photochemical approach.

4.2. WO₃ coatings prepared via "tungstic acid" route

4.2.1. Morphological, structural and optical properties of WO₃ films
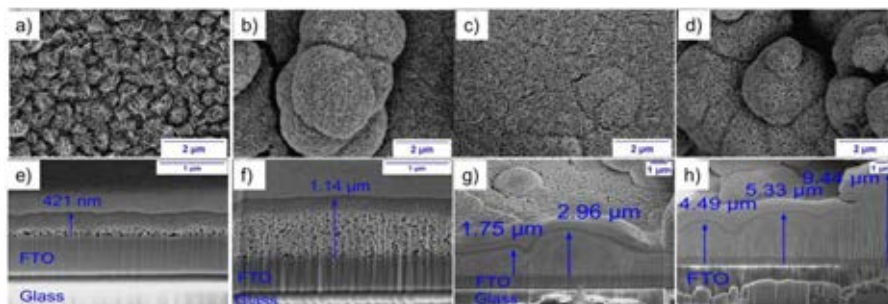
Figure 17. Top-view (a–d) and cross-sectional (e-h) SEM images of one- (a, e), two- (b ,f), three- (c, g) and four-layered (d ,h) WO₃ coatings

SEM analysis (Fig. 17) revealed that WO₃ coatings formed via „tungstic acid route" are composed of clusters of randomly oriented nanosheets (10 – 20 nm thick), which tend to agglomerate into highly porous microspheres. As the number of deposition cycles increased from 1 to 4, the thickness of WO₃ films increased from ~ 0.4 μm to 5 - 10 μm (Fig. 17 e – h).
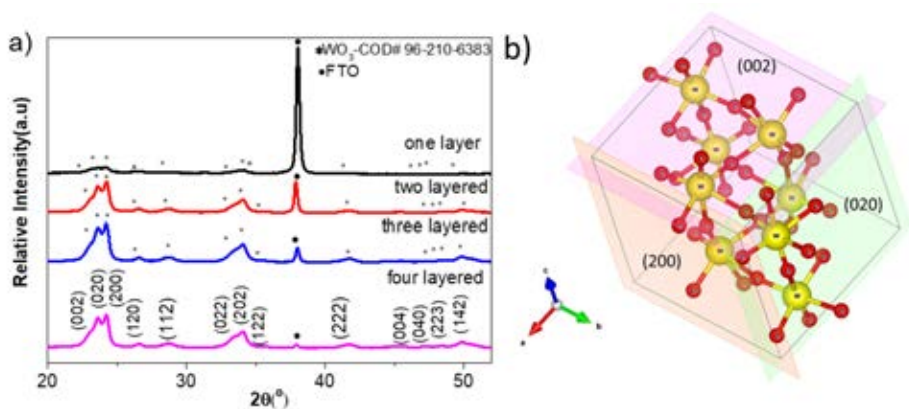
Figure 18. a) XRD spectra of 1-, 2-, 3-,and 4-layered WO$_3$ films, b) crystal structure of monoclinic WO$_3$ (space group P 1 21/n 1) with highlighted (200), (020) and (002) planes

The results of XRD investigations are presented in (Fig. 18). The obvious diffractive peaks within 2θ range from 22 to 26° correspond to (002), (020), (200) crystal planes of the monoclinic phase of WO$_3$ with lattice parameters a = 7.30, b = 7.54, and c = 7.69 Å (COD: 2106383). The intensity of the FTO peaks from substrate decreased consistently with increase in WO$_3$ layer thickness. Similar to WO$_3$ coatings prepared via „peroxotungstic acid route", the intensity of (002) planes was the lowest (Fig. 5). The average size of crystallites was about 14 nm, which is slightly larger compared to previously described coatings (Table 2).

Porous morphology of WO$_3$ samples shown in Fig. 17 suggests that coatings have highly developed surface. Evaluation of relative electrochemically active surface area (EASA) was performed on the basis of double-layer capacitance measurements. Cyclic voltammograms of 1 to 4-layered WO$_3$ films were measured at 5 – 100 mV s^{-1} potential scan rates in 0.5 M H$_2$SO$_4$ in dark within E range from 0.5 to 0.7 V, where no redox processes occur and current is attributed to double-layer charging only. The slope of the current vs. scan rate plots corresponds to double layer capacitance (in farads), which is proportional to EASA [154]. As shown in Fig. 19, the capacitance of four-layered WO$_3$ coating is almost 70 times higher than that of the one-layered film, indicating a good permeation of the electrolyte into the porous structure of the oxide layer.

The diffuse reflectance spectra of 1 to 4-layered WO$_3$ films are shown in Fig. 20. Significantly higher optical density is attained with thick and porous

nanostructured WO_3 layers compared to above described thin films (Fig. 6). Direct band gap values determined from Tauc plots shown in the inset in Fig. 20 ranged between 2.7 and 2.8 eV.
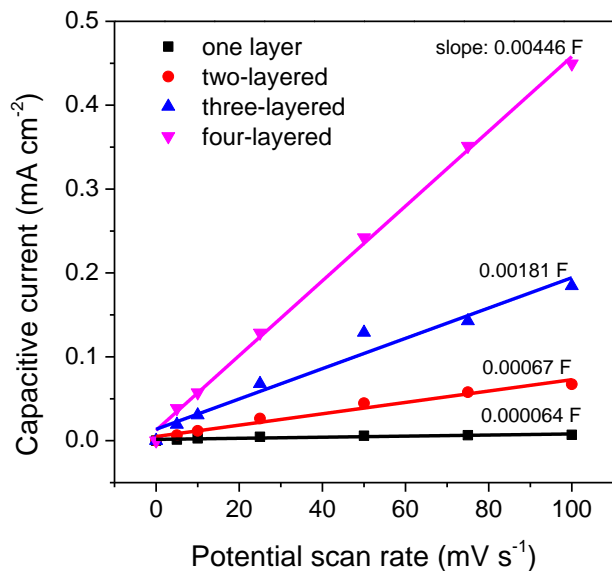
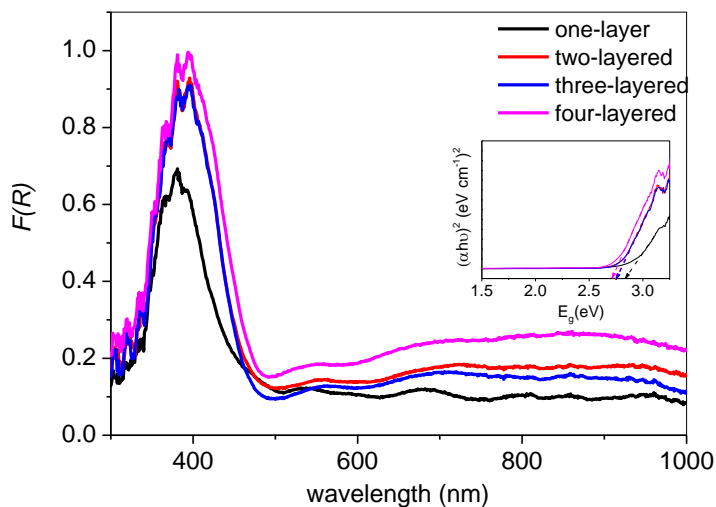Figure 19. Evaluation of double layer capacitance of 1-, 2-, 3- , and 4-layered WO_3 films

Figure 20. Diffuse reflectance spectra of 1-, 2-, 3- and 4-layered WO_3 films

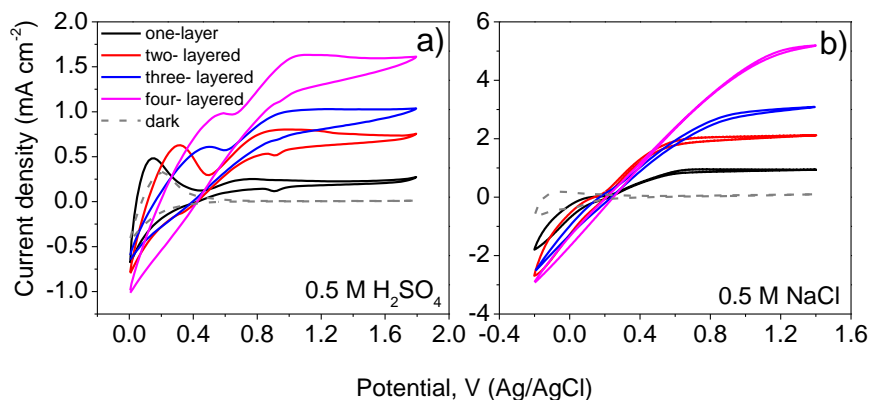### 4.2.2. Photoelectrochemical performance of WO_3 coatings in 0.5 M H_2SO_4 and 0.5 M NaCl electrolytes

Figure 21. Cyclic voltammograms of 1-, 2-, 3- and 4-layered WO_3 in a) 0.5 M H_2SO_4 and b) 0.5 M NaCl; 50 mVs^{-1} illumination intensity ~100 mW cm^{-2}; curves in dark are those of 1-layered samples.

The cyclic voltammograms of 1 to 4-layered WO_3 films recorded in 0.5 M H_2SO_4 and 0.5 M NaCl solutions in dark and under illumination are shown in Fig. 21. Enhancement in photocurrent density is observed as the thickness of coating increases. It is noteworthy that photocurrents achieved with thick and porous nanostructured WO_3 layers prepared via "tungstic acid route" were 3 to 5 times higher than those obtained in the case of thin plate-shaped WO_3 films described above (Figs. 7, 10). Slight distortion of CV shape within oxide reduction range below 0.5 V or 0.3 V in 0.5 M H_2SO_4 or 0.5 M NaCl electrolytes, respectively, can be attributed to increasing resistance of the films with increasing layer thickness.

The plots of applied bias photon-to-current efficiency evaluated from photocurrent-potential characteristics in 0.5 M H_2SO_4 and 0.5 M NaCl using eq. (5) are shown in Fig. 22. The highest ABPE values obtained in the case of 4-layered coating were 3.6% and 1% in 0.5 M H_2SO_4 and 0.5 M NaCl, respectively. It is important to note, that these values of efficiency are by an order of magnitude larger compared to those of thin WO_3 fims prepared via „peroxotungstic acid route") (Fig. 12.). Moreover, the obtained ABPEs are among the largest, reported in literature so far [155]. Significantly better performance of thick „tungstic acid route" films should be attributed to higher optical density resulting in more efficient light absorption (Fig. 20) and porous nanostructure with highly developed surface (Fig. 17), which provides more favourable conditions for photo-induced holes to reach electrode/electrolyte interface.
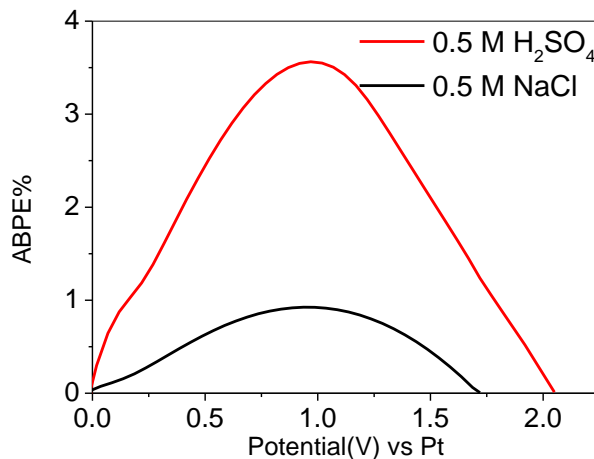
Figure 22. ABPE plots of 4-layered WO_3 coatings in 0.5 M H_2SO_4 and 0.5 M NaCl; 50 mV s^{-1}, intensity of illumination 100 mW cm^{-2}

In view of the fact that thicker coatings demonstrated superior PEC performance, further experiments for evaluation of Faradaic efficiency of light-induced generation of reactive chlorine and sulphate species as well as assesment of coating stability during photoelectrolysis were performed with 3- and 4-layered WO_3 films.
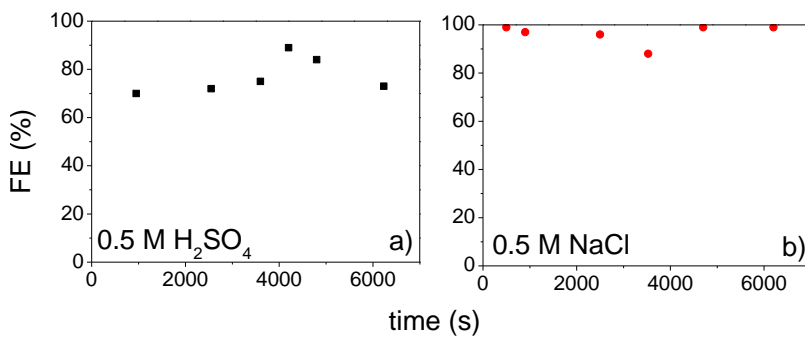
Figure 23. Variation of Faradaic efficiency of photoelectrochemical generation of (a) $S_2O_8^{2-}$ and (b) reactive chlorine species ($ClO^- + ClO_2^-$) on 3- and 4-layered WO_3 coatings during photoelectrolysis in solutions of 0.5 M H_2SO_4 and 0.5 M NaCl, respectively; intensity of illumination 100 mW cm^{-2}

FEs varied between 70 and 90% for $S_2O_8^{2-}$ (Fig. 23a) and between 85 and 100% for RCS (Fig. 23b). It is notworthy that Faradic efficiency of PEC generation of persulfate in the case of thick and porous WO_3 films was higher and more stable in time compared to results of „peroxotungtic acid route" coatings (Fig. 11). FE of RCS formation (Fig. 23b) was rather similar to that of thin films and stayed close to 100% even after longer periods of photoelectrolysis.
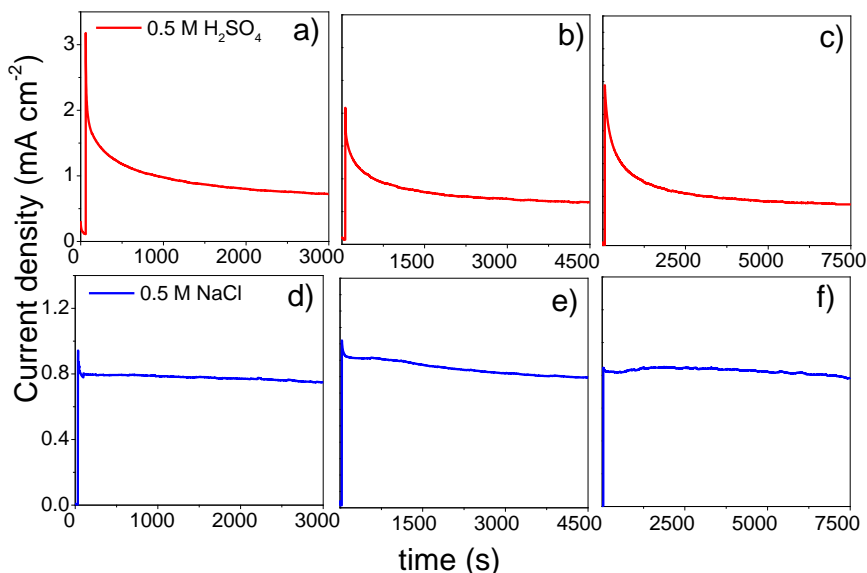
Figure 24.Chronoamperograms of 4-layered WO_3 films recorded during three consecutive photoelectrolysis experiments with increasing duration in 0.5 M H_2SO_4 at cell voltage of 1.8 V (a-c) and 0.5 M NaCl at cell voltage of 1.6 V (d-f), intensity of illumination ~ 100 mW cm^{-2}.

Photocurrent profiles of 4-layered WO_3 films recorded during prolonged photoelectroysis in 0.5 M H_2SO_4 and 0.5 M NaCl electrolytes are shown in Fig. 24. The variation of j_{ph} was similar to that of "peroxotungstic acid route"-derived WO_3 coatings shown in Fig. 13: photocurrent decay in sulfuric acid solution was more pronounced compared to neutral chloride medium, however, differently from previous results, the values of stationary photocurrent at the end of each experiment shown in Figs. 24 a-c, were decreasing significantly less than those of thin tungsten (VI) oxide films (Fig. 13 a-e). This, together with stability of FEs of PEC persulfate formation (Fig. 23) as well as high ABPEs (Fig. 22) suggest that efficient scavenging of photo-induced holes by SO_4^{2-} ions prevented hole-induced formation of peroxo-species and degradation/passivation of WO_3 coatings.

4.3. Applicability of PEC systems with WO_3 photoelectrode

4.3.1. Antimicrobial effect of RCS generated with WO_3 photoanode
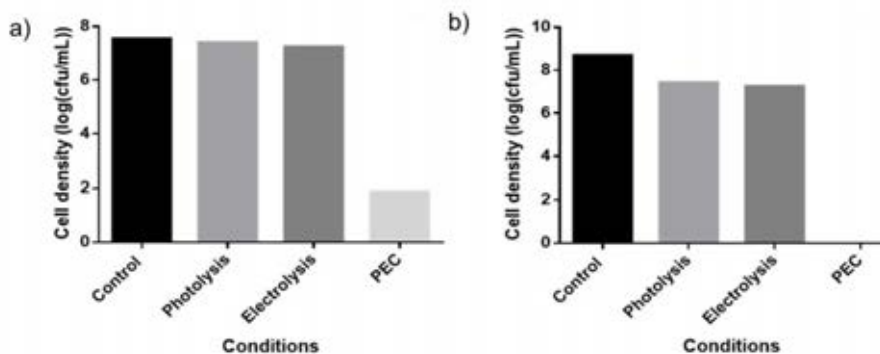
Figure 25. Comparison of disinfection efficiencies under photolytic (100 mW cm^{-2}, 0 V), electrolytic (0 mW cm^{-2}, 1.6 V) and photoelectrochemical (100 mW cm^{-2}, 1.6 V) conditions in the case of *Bacillus sp* (a) and *E.coli* C41(DE3) (b) suspensions in 0.5 M NaCl

Effect of PEC chlorination with polyethylene glycol-modified WO_3 photoanodes formed via sol-gel route decribed in [133] was successfully demonstrated in suspensions of Gram-positive Bacillus sp. and Gram-negative E.coli bacteria strains in 0.5 M NaCl. The results of photolytic, electrolytic and PEC disinfection are compared in Fig.25. Photoelectrochemically produced RCS displayed strong inhibitory effect on the growth of *Bacillus sp* and *E.coli*, whereas rather low disinfection efficiencies were obtained under purely electrolytic and purely photolytic conditions. Charge of approximately 5 C was passed through the photoelectrochemical cell during experiments. Under the conditions of experiment described in [133], such amount of charge would produce ~0.005% solution of sodium hypochlorite. Usually concentration of 0.5% is considered to be sufficient for the purpose of water disinfection [156]. Our results show that in the case of Gram-negative *E.coli* C41(DE3) species (Fig. 25b) almost hundredfold smaller amount of hypochlorite was sufficient to achieve complete disinfection. This could be related with photoelectrochemical generation of chlorine radicals ($Cl\cdot$, $Cl_2^{-}\cdot$), which have significantly stronger bacteria-killing power than ClO^-.

4.3.2. Antimicrobial effect of persulfate species generated with WO$_3$ photoanode
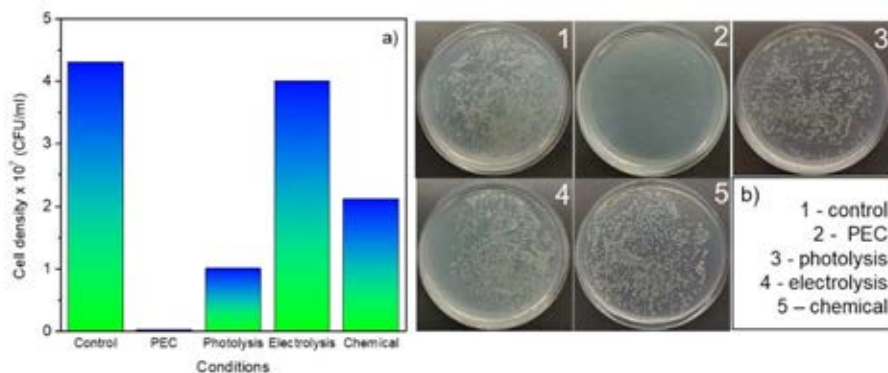
Figure 26. a) Comparison of disinfection efficiencies under photoelectrochemical (100 mW cm^{-2}, 1.6 V), photolytic (100 mW cm^{-2}, 0 V), electrolytic (0 mW cm^{-2}, 1.6 V) and chemical oxidation conditions in the case of Bacillus spp suspensions in 0.1 M Na$_2$SO$_4$; b) optical microscope images of microbial CFUs before and after indicated treatments at 10^{-3} dilution

Effect of photo-assisted generation of persulfate species on WO$_3$ photoelectrode formed via "peroxoungstic acid route" with IsoPrOH as a reductant was successfully demonstrated in suspensions of Gram-positive Bacillus sp. strains in in 0.1 M Na$_2$SO$_4$. The results of photoelectrochemical, photolytic, electrolytic, and chemical impact on the viability of microorganisms are compared in Fig. 26. Most significant decrease in cell density was observed in the case of PEC treatment. Photolytic treatment was more effective than the chemical one. It was reported in [157] that persulfate alone had almost no effect on *Bacillus subtilis* spores, but in combination with UV irradiation better results were achieved. The effect of UV illumination is most likely related with photolytic decomposition of persulfate leading to the formation of radical species, which have high bacteria-killing power [158]. Sulfate radical, $SO_4^{-}\cdot$, is known to be capable of quickly decomposing most of the organic pollutants and biological toxins in water [159]. In the system investigated herein, higher disinfection efficiencies obtained in the case of light-assisted treatments should also be attributed to the formation of highly active radical species as a result of interaction of photogenerated WO$_3$ holes with water molecules and sulfate ions (Eqs. (14, 17)). Most importantly, inactivation of bacteria in these experiments was achieved using visible light. These findings suggest that WO$_3$ photoanodes are promising candidates to be used in green energy systems for water disinfection.

CONCLUSIONS

1. Faradaic efficiency of photoelectrochemical formation of $S_2O_8^{2-}$ and RCS (ClO^- + ClO_2^-) in the case of 0.5 – 1 µm thick WO_3 films composed plate-shaped particles („peroxotungstic acid" route) in 0.5 M H_2SO_4 and 0.5 M NaCl electrolytes was 35 – 80 % and 50 – 99 %, whereas ABPE was 0.27% and 0.08%, respectively.
   Faradaic efficiency of photoelectrochemical formation of $S_2O_8^{2-}$ and RCS in the case of 5 – 10 µm thick, highly porous, nanostructured WO_3 films („tungstic acid" route) in 0.5 M H_2SO_4 and 0.5 M NaCl electrolytes was 70 – 90 % and 85 – 100 %, whereas ABPE was 3.4% and 1.0%, respectively.
   Superior performance achieved in the latter case was attributed to more efficient light absorption by thick oxide layers as well as more effective hole scavenging, because fine nanostructure of the coating provided shorter distance for photogenerated holes to reach electrode/electrolyte interface.

2. It was demonstrated that chloride ions tend to adsorb specifically on the surface of WO_3, what provides them with a kinetic advantage over other solution species in the process of hole scavenging and leads to high Faradaic efficiencies (up to 100%) of photoelectrochemical RCS formation.

3. Photoelectrochemical behavior of WO_3 photoelectrodes in H_2SO_4 and NaCl electrolytes was analysed on the basis of novel approach in which PEC processes are treated as electrode potential assisted photochemical reactions involving hole-mediated formation of radical intermediates (OH•, Cl•, Cl_2^-•, SO_4^-•). It is shown that in H_2SO_4 solution, photoanodic formation of SO_4^-• is thermodynamically favoured over oxidation of water molecules to OH•. In neutral NaCl thermodynamic likelihood of OH• formation is higher compared to Cl•, however, photoanodic oxidation of chloride anions prevails because of their specific adsorption on WO_3 surface.

4. The sequence of reactions: $Cl^- \xrightarrow{h^+} Cl^• \xrightarrow{Cl^-} Cl_2^{•-} \xrightarrow{e^-} 2Cl^-$ was suggested as a possible surface-charge recombination mechanism occurring on the surface of WO_3 photoelectrodes in chloride solutions.

5. Formation of photoelectrochemically inactive peroxotungstate compounds, induced by oxidative cleavage of W–O–W bonds either by photogenerated holes or SO_4^-•/OH• radicals was suggested as the possible cause of deterioration of WO_3 PEC performance, which was more significant in H_2SO_4

compared to NaCl electrolyte. Strong adsorption of chloride ions as well as the products of their photoanodic oxidation together with efficient hole scavenging was suggested to prevent formation of peroxo species, thus contributing to higher stability of WO_3 photoelectrodes in neutral NaCl solutions.

6. Efficient deactivation of Gram-positive and Gram-negative bacteria species suspended in a neutral chloride and sulfate medium was demonstrated in a photoelectrochemical cell with tungsten (VI) oxide photoanodes under visible light illumination. High bacteria-killing power of the investigated systems was attributed to generation of highly reactive radical species, which form as a result of interaction between photogenerated holes and solution species. The results of investigations can be helpful in engineering semiconductor/electrolyte interfaces for advanced oxidation processes and find applications in the area of water disinfection.

AUTHOR CONTRIBUTION

The author of this thesis is responsible for the synthesis, (photo)electrochemical characterizations, analysis and visualization of data, preparation of publications.

LIST OF REFERENCES

[1]   N. S. Lewis, D. G. Nocera, "Powering the planet: Chemical challenges in solar energy utilization". *Proceedings of the National Academy of Sciences*, vol.103*, no.43, 15729-15735, 2006

[2]   P. D. Nguyen, T. M. Duong, and P. D. Tran, "Current progress and challenges in engineering viable artificial leaf for solar water splitting," *J. Sci. Adv. Mater. Devices*, vol. 2, no. 4, pp. 399–417, 2017.

[3]   W. Yang, R. R. Prabhakar, J. Tan, S. D. Tilley, and J. Moon, "Strategies for enhancing the photocurrent, photovoltage, and stability of photoelectrodes for photoelectrochemical water splitting," *Chem. Soc. Rev.*, vol. 48, no. 19, pp. 4979–5015, 2019.

[4]   D. Abbott, "Keeping the energy debate clean: How do we supply the world's energy needs?," *Proc. IEEE*, vol. 98, no. 1, pp. 42–66, 2010.

[5]   R. Kothari, D. Buddhi, and R. L. Sawhney, "Comparison of environmental and economic aspects of various hydrogen production methods," *Renew. Sustain. Energy Rev.*, vol. 12, no. 2, pp. 553–563, 2008.

[6]   P. Sinha and A. Pandey, "An evaluative report and challenges for fermentative biohydrogen production," *Int. J. Hydrogen Energy*, vol. 36, no. 13, pp. 7460–7478, 2011.

[7]   J. Luo, J.H. Im, M.T. Mayer, M. Schreier, M.K. Nazeeruddin, N.G. Park, S.D. Tilley, H.J. Fan, and M. Grätzel, "Water photolysis at 12.3% efficiency via perovskite photovoltaics and Earth-abundant catalysts," *Science (80-.).*, vol. 345, no. 6204, pp. 1593–1596, 2014.

[8]   C. R. Cox, J. Z. Lee, D. G. Nocera, and T. Buonassisi, "Ten-percent solar-to-fuel conversion with nonprecious materials," *Proc. Natl. Acad. Sci. U. S. A.*, vol. 111, no. 39, pp. 14057–14061, 2014.

[9]   T. Bak, J. Nowotny, M. Rekas, and C. C. Sorrell, "Photo-electrochemical hydrogen generation from water using solar energy. Materials-related aspects," *International journal of hydrogen energy* ., vol. 27, no. 10, pp. 991-1022. 2002.

[10]   J. K. Kim, K. Shin, S. M. Cho, T. W. Lee, and J. H. Park, "Synthesis of transparent mesoporous tungsten trioxide films with enhanced photoelectrochemical response: Application to unassisted solar water splitting," *Energy Environ. Sci.*, vol. 4, no. 4, pp. 1465–1470, 2011.

[11]   C. Ding *et al.*, "Solar-to-hydrogen efficiency exceeding 2.5% achieved for overall water splitting with an all earth-abundant dual-photoelectrode," *Phys. Chem. Chem. Phys.*, vol. 16, no. 29, pp. 15608–15614, 2014.

[12]   K. Sayama, "Production of high-value-added chemicals on oxide semiconductor photoanodes under visible light for solar chemical-conversion processes," *ACS Energy Lett.*, vol. 3, no. 5, pp. 1093–1101, 2018.

[13]   K. Fuku, N. Wang, Y. Miseki, T. Funaki, and K. Sayama,

"Photoelectrochemical Reaction for the Efficient Production of Hydrogen and High-Value-Added Oxidation Reagents," *ChemSusChem*, vol. 8, no. 9, pp. 1593–1600, 2015.

[14] T. Nakajima *et al.*, "Diffusion controlled porous WO_3 thin film photoanodes for efficient solar-driven photoelectrochemical permanganic acid production," *Sustain. Energy Fuels*, vol. 3, no. 9, pp. 2380–2390, 2019.

[15] S. Iguchi, Y. Miseki, and K. Sayama, "Sustainable Energy & Fuels photoelectrochemical solar energy conversion," pp. 155–162, 2018.

[16] D. L. Caldwell, "Production of Chlorine," *Compr. Treatise Electrochem.*, no. 3, pp. 105–166, 1981.

[17] R. K. B. Karlsson and A. Cornell, "Selectivity between Oxygen and Chlorine Evolution in the Chlor-Alkali and Chlorate Processes," *Chem. Rev.*, vol. 116, no. 5, pp. 2982–3028, 2016.

[18] C. R. Lhermitte and K. Sivula, "Alternative Oxidation Reactions for Solar-Driven Fuel Production," *ACS Catal.*, vol. 9, no. 3, pp. 2007–2017, 2019.

[19] E. Fabbri, A. Habereder, K. Waltar, R. Kötz, and T. J. Schmidt, "Developments and perspectives of oxide-based catalysts for the oxygen evolution reaction," *Catal. Sci. Technol.*, vol. 4, no. 11, pp. 3800–3821, 2014.

[20] D. Desai *et al.*, "Electrochemical Desalination of Seawater and Hypersaline Brines with Coupled Electricity Storage," *ACS Energy Lett.*, vol. 3, no. 2, pp. 375–379, 2018.

[21] Y. Surendranath, M. Dincă, and D. G. Nocera, "Electrolyte-dependent electrosynthesis and activity of cobalt-based water oxidation catalysts," *J. Am. Chem. Soc.*, vol. 131, no. 7, pp. 2615–2620, 2009.

[22] M. Jadwiszczak, K. Jakubow-Piotrowska, P. Kedzierzawski, K. Bienkowski, and J. Augustynski, "Highly Efficient Sunlight-Driven Seawater Splitting in a Photoelectrochemical Cell with Chlorine Evolved at Nanostructured WO_3 Photoanode and Hydrogen Stored as Hydride within Metallic Cathode," *Adv. Energy Mater.*, vol. 10, no. 3, pp. 1–8, 2020.

[23] M. S. Koo, X. Chen, K. Cho, T. An, and W. Choi, "In Situ Photoelectrochemical Chloride Activation Using a WO_3 Electrode for Oxidative Treatment with Simultaneous H_2 Evolution under Visible Light," *Environ. Sci. Technol.*, vol. 53, no. 16, pp. 9926–9936, 2019.

[24] C. Jiang, S. J. A. Moniz, A. Wang, T. Zhang, and J. Tang, "Photoelectrochemical devices for solar water splitting-materials and challenges," *Chem. Soc. Rev.*, vol. 46, no. 15, pp. 4645–4660, 2017.

[25] C. Liu, Y. Yang, J. Li, S. Chen, W. Li, and X. Tang, "An in situ transformation approach for fabrication of $BiVO_4/WO_3$ heterojunction photoanode with high photoelectrochemical activity," *Chem. Eng. J.*, vol. 326, pp. 603–611, 2017.

[26] J. P. Song, P. F. Yin, J. Mao, S. Z. Qiao, and X. W. Du, "Catalytically

active and chemically inert $CdIn_2S_4$ coating on a CdS photoanode for efficient and stable water splitting," *Nanoscale*, vol. 9, no. 19, pp. 6296–6301, 2017.

[27]   J. Su, T. Minegishi,Y. Kageshima, H. Kobayashi,T. Hisatomi, T. Higashi, M. Katayama, and K. Domen,"CdTe-Based Photoanode for Oxygen Evolution from Water under Simulated Sunlight," *J. Phys. Chem. Lett.*, vol. 8, no. 23, pp. 5712–5717, 2017.

[28]   S. Chen and L. W. Wang, "Thermodynamic oxidation and reduction potentials of photocatalytic semiconductors in aqueous solution," *Chem. Mater.*, vol. 24, no. 18, pp. 3659–3666, 2012.

[29]   A. Fujishima and K. Honda, "Electrochemical Photolysis of Water at a Semiconductor Electrode," *Nature*, vol. 238, no. 5358, pp. 37–38, 1972.

[30]   A. Eftekhari, V. J. Babu, and S. Ramakrishna, "Photoelectrode nanomaterials for photoelectrochemical water splitting," *Int. J. Hydrogen Energy*, vol. 42, no. 16, pp. 11078–11109, 2017.

[31]   A. Fujishima, T. Inoue, and K. Honda, "Competitive P hotoelect rochemical Oxidation of Reducing Agents at the TiO_2 Photoanode," 1979.

[32]   Y. Gai, J. Li, S. S. Li, J. B. Xia, and S. H. Wei, "Design of narrow-gap TiO_2: A passivated codoping approach for enhanced photoelectrochemical activity," *Phys. Rev. Lett.*, vol. 102, no. 3, pp. 23–26, 2009.

[33]   P. Lianos, "Production of electricity and hydrogen by photocatalytic degradation of organic wastes in a photoelectrochemical cell. The concept of the Photofuelcell: A review of a re-emerging research field," *J. Hazard. Mater.*, vol. 185, no. 2–3, pp. 575–590, 2011.

[34]   Y. Liu, F. Le Formal, F. Boudoire, and N. Guijarro, "Hematite Photoanodes for Solar Water Splitting: A Detailed Spectroelectrochemical Analysis on the pH-Dependent Performance," *ACS Appl. Energy Mater.*, vol. 2, no. 9, pp. 6825–6833, 2019.

[35]   X. Liang, J. Qian, Y. Liu, Z. Zhang, and D. Gao, "Efficient electrocatalyst of α-Fe_2O_3 nanorings for oxygen evolution reaction in acidic conditions," *RSC Adv.*, vol. 10, no. 49, pp. 29077–29081, 2020.

[36]   S. Gim, J. Bisquert, F. B. Principles, and A. Devices, "Photoelectrochemical Solar Fuel Production." *Photoelectrochem. Sol. Fuel Prod* , pp. 189-194 ,2016.

[37]   M. Dare-Edwards, J. Goodenough, A. Hamnett, and P. Trevelick, "Electrochemistry and Photoelectrochemistry of," *J. Chem. SOC., Faraday Trans. I*, vol. 79, no. 1, pp. 2027–2041, 1983.

[38]   K. Sivula, F. Le Formal, and M. Grätzel, "Solar water splitting: Progress using hematite (α-Fe_2O_3) photoelectrodes," *ChemSusChem*, vol. 4, no. 4, pp. 432–449, 2011.

[39]   A. I. Kokorin, "Photooxidation of Water at Hematite Electrodes," *Chem. Phys. Nanostructured Semicond.*, pp. 99–126, 2020.

[40] B.S. Wang, R.Y. Li, Z.Y. Zhang, X.L. Wu, G.A Cheng, and R.T. Zheng, "An overlapping ZnO nanowire photoanode for photoelectrochemical water splitting," *Catal. Today*, vol. 321, pp. 100–106, 2019.

[41] X. Sheng, T. Xu, and X. Feng, "Rational Design of Photoelectrodes with Rapid Charge Transport for Photoelectrochemical Applications," *Adv. Mater.*, vol. 31, no. 11, pp. 1–29, 2019.

[42] N. Jayababu and D. Kim, "ZnO nanorods@conductive carbon black nanocomposite based flexible integrated system for energy conversion and storage through triboelectric nanogenerator and supercapacitor," *Nano Energy*, vol. 82, pp. 105726, 2021.

[43] C. F. Liu, Y. J. Lu, and C. C. Hu, "Effects of Anions and pH on the Stability of ZnO Nanorods for Photoelectrochemical Water Splitting," *ACS Omega*, vol. 3, no. 3, pp. 3429–3439, 2018.

[44] A. Kudo, K. Omori, and H. Kato, "A novel aqueous process for preparation of crystal form-controlled and highly crystalline $BiVO_4$ powder from layered vanadates at room temperature and its photocatalytic and photophysical properties," *J. Am. Chem. Soc.*, vol. 121, no. 49, pp. 11459–11467, 1999.

[45] Z. F. Huang, L. Pan, J. J. Zou, X. Zhang, and L. Wang, "Nanostructured bismuth vanadate-based materials for solar-energy-driven water oxidation: A review on recent progress," *Nanoscale*, vol. 6, no. 23, pp. 14044–14063, 2014.

[46] J. Song *et al.*, "Template-engineered epitaxial BiVO4 photoanodes for efficient solar water splitting," *J. Mater. Chem. A*, vol. 5, no. 35, pp. 18831–18838, 2017.

[47] X. Li *et al.*, "The ClO· generation and chlorate suppression in photoelectrochemical reactive chlorine species systems on $BiVO_4$ photoanodes," *Appl. Catal. B Environ.*, vol. 296, pp. 120387, 2021.

[48] Z. Chi, J. Zhao, Y. Zhang, H. Yu, and H. Yu, "Coral-like WO_3/$BiVO_4$ photoanode constructed via morphology and facet engineering for antibiotic wastewater detoxification and hydrogen recovery," *Chem. Eng. J.*, vol. 428, pp. 131817, 2022.

[49] S. S. Kalanur, Y. J. Hwang, S. Y. Chae, and O. S. Joo, "Facile growth of aligned WO3 nanorods on FTO substrate for enhanced photoanodic water oxidation activity," *J. Mater. Chem. A*, vol. 1, no. 10, pp. 3479–3488, 2013.

[50] Q. Mi, A. Zhanaidarova, B. S. Brunschwig, H. B. Gray, and N. S. Lewis, "A quantitative assessment of the competition between water and anion oxidation at WO_3 photoanodes in acidic aqueous electrolytes," *Energy Environ. Sci.*, vol. 5, no. 2, pp. 5694–5700, 2012.

[51] A. Jelinska *et al.*, "Enhanced Photocatalytic Water Splitting on Very Thin WO3 Films Activated by High-Temperature Annealing," *ACS Catal.*, vol. 8, no. 11, pp. 10573–10580, Nov. 2018.

[52] Q. Zeng, J. Li, J. Bai, X. Li, L. Xia, and B. Zhou, "Preparation of

vertically aligned WO₃ nanoplate array films based on peroxotungstate reduction reaction and their excellent photoelectrocatalytic performance," *Appl. Catal. B Environ.*, vol. 202, pp. 388–396, 2017.

[53] J. Zhang, X. Chang, C. Li, A. Li, S. Liu, T. Wang, and J. Gong, "WO₃ photoanodes with controllable bulk and surface oxygen vacancies for photoelectrochemical water oxidation," *J. Mater. Chem. A*, vol. 6, no. 8, pp. 3350–3354, 2018.

[54] J. Zhang, I. Salles, S. Pering, P. J. Cameron, D. Mattia, and S. Eslava, "Nanostructured WO₃ photoanodes for efficient water splitting: Via anodisation in citric acid," *RSC Adv.*, vol. 7, no. 56, pp. 35221–35227, 2017.

[55] J. Kn ppel, A. Kormányos, B. Mayerh fer, A. Hofer, M. Bierling, J. Bachmann, S. Thiele, and S. Cherevko, " Photocorrosion of WO₃ Photoanodes in Different Electrolytes ," *ACS Phys. Chem. Au*, vol. 1, no. 1, pp. 6–13, 2021.

[56] K. Sivula and R. Van De Krol, "Semiconducting materials for photoelectrochemical energy conversion," *Nat. Rev. Mater.*, vol. 1, no. 2, 2016.

[57] F. Wang, C. DiValentin, and G. Pacchioni, "Rational Band Gap Engineering of WO 3 Photocatalyst for Visible light Water Splitting," *ChemCatChem*, vol. 4, no. 4, pp. 476–478, 2012.

[58] L. Sun, Y. Wang, F. Raziq, Y. Qu, L. Bai, and L. Jing, "Enhanced photoelectrochemical activities for water oxidation and phenol degradation on WO₃ nanoplates by transferring electrons and trapping holes," *Sci. Rep.*, vol. 7, no. 1, pp. 1–9, 2017.

[59] K. Sayama, H. Hayashi, T. Arai, M. Yanagida, T. Gunji, and H. Sugihara, "Highly active WO₃ semiconductor photocatalyst prepared from amorphous peroxo-tungstic acid for the degradation of various organic compounds," *Appl. Catal. B Environ.*, vol. 94, no. 1–2, pp. 150–157, 2010.

[60] F. Amano, M. Tian, G. Wu, B. Ohtani, and A. Chen, "Facile preparation of platelike tungsten oxide thin film electrodes with high photoelectrode activity," *ACS Appl. Mater. Interfaces*, vol. 3, no. 10, pp. 4047–4052, 2011.

[61] K. Jakubow-Piotrowska, D. Kurzydlowski, P. Wrobel, and J. Augustynski, "Photoelectrochemical Behavior of WO₃ in an Aqueous Methanesulfonic Acid Electrolyte," *ACS Phys. Chem. Au*, 2022.

[62] J. C. Hill and K. S. Choi, "Effect of electrolytes on the selectivity and stability of n-type WO₃ photoelectrodes for use in solar water oxidation," *J. Phys. Chem. C*, vol. 116, no. 14, pp. 7612–7620, 2012.

[63] G. Liu, L. Zhu, Y. Yu, M. Qiu, H. Gao, and D. Chen, "WO₃ nanoplates for sensitive and selective detections of both acetone and NH₃ gases at different operating temperatures," *J. Alloys Compd.*, vol. 858, p. 157638, 2021.

[64] S. Wang, H. Xu, J. Zhao, and Y. Li, "Two-dimensional WO₃

nanosheets for high-performance electrochromic supercapacitors," *Inorg. Chem. Front.*, vol. 9, no. 3, pp. 514–523, 2022.

[65]   G. Xi, J. Ye, Q. Ma, N. Su, H. Bai, and C. Wang, "In situ growth of metal particles on 3D urchin-like WO_3 nanostructures," *J. Am. Chem. Soc.*, vol. 134, no. 15, pp. 6508–6511, 2012.

[66]   W. Li, P. Da, Y. Zhang, Y. Wang, X. Lin, and X. Gong, " WO_3 Nano fl akes for Enhanced Photoelectrochemical Conversion," *ACS Nano*, vol. 8, no. 11, pp. 11770–11777, 2014.

[67]   J.R. Navarro, A. Mayence, J. Andrade, F. Lerouge, F. Chaput, P. Oleynikov, L. Bergstrom, S. Parola, and A. Pawlicka, "WO_3 nanorods created by self-assembly of highly crystalline nanowires under hydrothermal conditions," *Langmuir*, vol. 30, no. 34, pp. 10487–10492, 2014.

[68]   X. C. Song, Y. F. Zheng, E. Yang, and Y. Wang, "Large-scale hydrothermal synthesis of WO_3 nanowires in the presence of K_2SO_4," *Mater. Lett.*, vol. 61, no. 18, pp. 3904–3908, 2007.

[69]   Q. Zeng, J. Li, J. Bai, X. Li, L. Xia, and B. Zhou, "Preparation of vertically aligned WO_3 nanoplate array films based on peroxotungstate reduction reaction and their excellent photoelectrocatalytic performance," *Appl. Catal. B Environ.*, vol. 202, pp. 388–396, 2017.

[70]   M. Wang, Y. Wang, X. Li, C. Ge, S. Hussain, G. Liu, and G. Qiao, "WO_3 porous nanosheet arrays with enhanced low temperature NO_2 gas sensing performance," *Sensors Actuators, B Chem.*, vol. 316, no. 2, pp. 128050, 2020.

[71]   S. Cao, C. Zhao, T. Han, and L. Peng, "Hydrothermal synthesis, characterization and gas sensing properties of the WO_3 nanofibers," *Mater. Lett.*, vol. 169, pp. 17–20, 2016.

[72]   Y. O. Kim, S. H. Yu, K. S. Ahn, S. K. Lee, and S. H. Kang, "Enhancing the photoresponse of electrodeposited WO_3 film: Structure and thickness effect," *J. Electroanal. Chem.*, vol. 752, pp. 25–32, 2015.

[73]   A. Tacca, L. Meda, G. Marra, A. Savoini, S. Caramori, V. Cristino, C.A. Bignozzi, V.G. Pedro, P.P. Boix, S. Gimenez, and J. Bisquert, "Photoanodes based on nanostructured WO_3 for water splitting," *ChemPhysChem*, vol. 13, no. 12, pp. 3025–3034, 2012.

[74]   J. Ma, J. Zhang, S. Wang, T. Wang, J. Lian, X. Duan, and W. Zheng, W. "Topochemical preparation of WO_3 nanoplates through precursor H_2WO_4 and their gas-sensing performances," *The Journal of Physical Chemistry C*, vol. 115, no. 37, 18157-18163, 2011.

[75]   M. Epifani, T. Andreu, J. Arbiol, R. Díaz, P. Siciliano, and J. R. Morante, "Chloro-alkoxide route to transition metal oxides. Synthesis of WO_3 thin films and powders from a tungsten chloro-methoxide," *Chem. Mater.*, vol. 21, no. 21, pp. 5215–5221, 2009.

[76]   J. Shi, Z. Cheng, L. Gao, Y. Zhang, J. Xu, and H. Zhao, "Facile synthesis of reduced graphene oxide/hexagonal WO_3 nanosheets composites with enhanced H_2S sensing properties," *Sensors Actuators,*

B Chem., vol. 230, pp. 736–745, 2016.

[77] H. Ahmadian, F. S. Tehrani, and M. Aliannezhadi, "Hydrothermal synthesis and characterization of WO$_3$ nanostructures: Effects of capping agent and pH," *Mater. Res. Express*, vol. 6, no. 10, 2019.

[78] W. L. Kwong, N. Savvides, and C. C. Sorrell, "Electrodeposited nanostructured WO$_3$ thin films for photoelectrochemical applications," *Electrochim. Acta*, vol. 75, pp. 371–380, 2012.

[79] L. Liu, M., Layani, S., Yellinek, A. Kamyshny, H. Ling, P.S. Lee, S. Magdassi, and D. Mandler, "Nano to nano" electrodeposition of WO$_3$ crystalline nanoparticles for electrochromic coatings, *J. Mater. Chem. A*, vol. 2, no. 38, pp. 16224–16229, 2014.

[80] T. Pauporté, "A Simplified Method for WO$_3$ Electrodeposition," *J. Electrochem. Soc.*, vol. 149, no. 11, p. C539, 2002.

[81] A. E. Danks, S. R. Hall, and Z. Schnepp, "The evolution of 'sol-gel' chemistry as a technique for materials synthesis," *Mater. Horizons*, vol. 3, no. 2, pp. 91–112, 2016.

[82] P. K. Biswas, N. C. Pramanik, M. K. Mahapatra, D. Ganguli, and J. Livage, "Optical and electrochromic properties of sol-gel WO3 films on conducting glass," *Mater. Lett.*, vol. 57, no. 28, pp. 4429–4432, 2003.

[83] P. Judeinstein and J. Livage, "Synthesis of WO$_3$ Thin Films," *J. Mater. Chem.*, vol. 1, no. 4, pp. 621–627, 1991.

[84] H. Okamoto and A. Ishikawa, "Tungsten metal film formed by spin-coating amorphous peroxopolytungstic acid," *Appl. Phys. Lett.*, vol. 55, no. 18, pp. 1923–1925, 1989.

[85] L.M. Bertus, C. Faure, A. Danine, C. Labrugère, G. Campet, A. Rougier, and A. Duta, "Synthesis and characterization of WO$_3$ thin films by surfactant assisted spray pyrolysis for electrochromic applications," *Mater. Chem. Phys.*, vol. 140, no. 1, pp. 49–59, 2013.

[86] C. Santato, M. Odziemkowski, M. Ulmann, and J. Augustynski, "Crystallographically oriented mesoporous WO$_3$ films: Synthesis, characterization, and applications," *J. Am. Chem. Soc.*, vol. 123, no. 43, pp. 10639–10649, 2001.

[87] Z. Jiao, J. Wang, L. Ke, X. W. Sun, and H. V. Demir, "Morphology-tailored synthesis of tungsten trioxide (hydrate) thin films and their photocatalytic properties," *ACS Appl. Mater. Interfaces*, vol. 3, no. 2, pp. 229–236, 2011.

[88] C. Ng, Y. H. Ng, A. Iwase, and R. Amal, "Influence of annealing temperature of WO$_3$ in photoelectrochemical conversion and energy storage for water splitting," *ACS Appl. Mater. Interfaces*, vol. 5, no. 11, pp. 5269–5275, 2013.

[89] C.D. Lokhande, "Chemical deposition of metal chalcogenide thin films", *Materials Chemistry and Physics*, vol.27, no.1, pp. 1-43, 1991.

[90] M. Z. Najdoski and T. Todorovski, "A simple method for chemical bath deposition of electrochromic tungsten oxide films," *Mater. Chem.*

Phys., vol. 104, no. 2–3, pp. 483–487, 2007.

[91] T. Özdal and H. Kavak, "Determination of crystallization threshold temperature for sol-gel spin coated Cu_2ZnSnS_4 thin films," *Ceram. Int.*, vol. 44, no. 15, pp. 18928–18934, 2018.

[92] S. K. Sen, T. C. Paul, S. Dutta, M. N. Hossain, and M. N. H. Mia, "XRD peak profile and optical properties analysis of Ag-doped h-MoO3 nanorods synthesized via hydrothermal method," *J. Mater. Sci. Mater. Electron.*, vol. 31, no. 2, pp. 1768–1786, 2020.

[93] Z. Zhou, Z. Wu, Q. Xu, and G. Zhao, "A solar-charged photoelectrochemical wastewater fuel cell for efficient and sustainable hydrogen production," *J. Mater. Chem. A*, vol. 5, no. 48, pp. 25450–25459, 2017.

[94] H. Ali, N. Ismail, A. Hegazy, and M. Mekewi, "A novel photoelectrode from TiO_2-WO_3 nanoarrays grown on FTO for solar water splitting," *Electrochim. Acta*, vol. 150, pp. 314–319, 2014.

[95] V. B. Patil, P. V Adhyapak, S. S. Suryavanshi, and I. S. Mulla, "Oxalic acid induced hydrothermal synthesis of single crystalline tungsten oxide nanorods," *J. Alloys Compd.*, vol. 590, pp. 283–288, 2014.

[96] Y. Xiong, Z. Zhu, T. Guo, H. Li, and Q. Xue, "Synthesis of nanowire bundle-like WO3-W18O49 heterostructures for highly sensitive NH_3 sensor application," *J. Hazard. Mater.*, vol. 353, pp. 290–299, 2018.

[97] Y. T. Moon, H. K. Park, D. K. Kim, and C. H. Kim, "Preparation of Monodisperse and Spherical Zirconia Powders by Heating of Alcohol_Aqueous Salt Solutions," *J. Am. Chem. Soc.*, vol. 78, pp. 2690–94, 1995.

[98] K. H. Kim, Y. B. Lee, E. Y. Choi, H. C. Park, and S. S. Park, "Synthesis of nickel powders from various aqueous media through chemical reduction method," *Mater. Chem. Phys.*, vol. 86, no. 2–3, pp. 420–424, 2004.

[99] D. Wang, J. Sun, X. Cao, Y. Zhu, Q. Wang, G. Wang, Y. Han, G. Lu, G. Pang, and S. Feng, "High-performance gas sensing achieved by mesoporous tungsten oxide mesocrystals with increased oxygen vacancies," *J. Mater. Chem.*, vol. 1, pp. 8653–8657, 2013.

[100] M. Mohsen-Nia, H. Amiri, and B. Jazi, "Dielectric constants of water, methanol, ethanol, butanol and acetone: Measurement and computational study," *J. Solution Chem.*, vol. 39, no. 5, pp. 701–708, 2010.

[101] C. G. Malmberg and A. A. Maryott, "Dielectric constant of water from 0 to 100 C," *J. Res. Natl. Bur. Stand. (1934).*, vol. 56, no. 1, p. 1, 1956.

[102] R.M. Shirke, A. Chaudhari, N.M. More, and P.B. Patil, "Temperature dependent dielectric relaxation study of ethyl acetate—Alcohol mixtures using time domain technique", *Journal of molecular liquids*, vol.94, no.1, pp.27-36., 2001

[103] B. Lone and V. Madhurima, "Dielectric and conformal studies of 1-propanol and 1-butanol in methanol," *J. Mol. Model.*, vol. 17, no. 4,

pp. 709–719, 2011.

[104] R. D. Bezman, E. F. Casassa, and R. L. Kay, "The temperature dependence of the dielectric constants of alkanols," *J. Mol. Liq.*, vol. 73–74, pp. 397–402, 1997.

[105] P. Wang and A. Anderko, "Computation of dielectric constants of solvent mixtures and electrolyte solutions," *Fluid Phase Equilib.*, vol. 186, no. 1–2, pp. 103–122, 2001.

[106] J. M. Chem, Y. P. Xie, G. Liu, L. Yin, and H. Cheng, "Crystal facet-dependent photocatalytic oxidation and reduction reactivity of monoclinic WO 3 for solar energy conversion," *J. Mater. Chem.*, vol. 22, pp. 6746–6751, 2012.

[107] D. Sánchez-Martínez, A. Martínez-De La Cruz, and E. López-Cuéllar, "Synthesis of WO3 nanoparticles by citric acid-assisted precipitation and evaluation of their photocatalytic properties," *Mater. Res. Bull.*, vol. 48, no. 2, pp. 691–697, 2013.

[108] M. Farhadian, P. Sangpout, and G. Hosseinzadeh, "Morphology dependent photocatalytic activity of WO$_3$ nanostructures," *J. Energy Chem.*, vol. 24, no. 2, pp. 171–177, 2015.

[109] A. Subrahmanyam and A. Karuppasamy, "Optical and electrochromic properties of oxygen sputtered tungsten oxide (WO$_3$) thin films," *Sol. Energy Mater. Sol. Cells*, vol. 91, no. 4, pp. 266–274, 2007.

[110] A. I. Inamdar *et al.*, "Effects of oxygen stoichiometry on electrochromic properties in amorphous tungsten oxide films," *Thin Solid Films*, vol. 520, no. 16, pp. 5367–5371, 2012.

[111] M. Petruleviciene, M. Parvin, I. Savickaja, G. Gece, A. Naujokaitis, V. Pakstas, J. Pilipavicius, A. Gegeckas, G. Gaigalas, and J. Juodkazyte, "WO$_3$ coatings for photoelectrochemical synthesis of persulfate: efficiency, stability and applicability. *Journal of Solid State Electrochemistry*, vol. 26, no. 4, pp.1021-1035,2022..

[112] C. Ng, A. Iwase, and R. Amal, "Influence of Annealing Temperature of WO$_3$ in Photoelectrochemical Conversion and Energy Storage for Water Splitting," *ACS Appl. Mater. Interfaces*, vol. 5, pp. 5269–5275, 2013.

[113] A. S. Hammad, H. M. El-Bery, A. H. EL-Shazly, and M. F. Elkady, "Effect of WO$_3$ morphological structure on its photoelectrochemical properties," *Int. J. Electrochem. Sci.*, vol. 13, no. 1, pp. 362–372, 2018.

[114] K. Song, Z. Ma, W. Yang, H. Hou, and F. Gao, "Electrospinning WO$_3$ nanofibers with tunable Fe-doping levels towards efficient photoelectrochemical water splitting," *J. Mater. Sci. Mater. Electron.*, vol. 29, no. 10, pp. 8338–8346, 2018.

[115] K. H. Ng, L. J. Minggu, and M. B. Kassim, "Gallium-doped tungsten trioxide thin film photoelectrodes for photoelectrochemical water splitting," *Int. J. Hydrogen Energy*, vol. 38, no. 22, pp. 9585–9591, 2013.

[116] G. Wang, Y. Ling, H. Wang, X. Yang, C. Wang, J.Z. Zhang, and Y.

Li, "Hydrogen-treated WO$_3$ nanoflakes show enhanced photostability," *Energy Environ. Sci.*, vol. 5, no. 3, pp. 6180–6187, 2012.

[117] B. Theories and S. Electrochemistry, "Basic Theories of Semiconductor Electrochemistry," *Electrochem. Silicon Its Oxide*, pp. 1–43, 2005.

[118] R. De Gryse, W. P. Gomes, F. Cardon, and J. Vennik, "On the Interpretation of Mott-Schottky Plots Determined at Semiconductor/Electrolyte Systems," *J. Electrochem. Soc.*, vol. 122, no. 5, pp. 711–712, 1975.

[119] S. Corby, L. Francàs, A. Kafizas, and J. R. Durrant, "Determining the role of oxygen vacancies in the photoelectrocatalytic performance of WO$_3$ for water oxidation," *Chem. Sci.*, vol. 11, no. 11, pp. 2907–2914, 2020.

[120] J. Wang, P. S. Lee, and J. Ma, "Synthesis, growth mechanism and room-temperature blue luminescence emission of uniform WO$_3$ nanosheets with W as starting material," *J. Cryst. Growth*, vol. 311, no. 2, pp. 316–319, 2009.

[121] J. Sungpanich, T. Thongtem, and S. Thongtem, "Large-scale synthesis of WO 3 nanoplates by a microwave-hydrothermal method," *Ceram. Int.*, vol. 38, no. 2, pp. 1051–1055, 2012.

[122] S. Mohammed Harshulkhan, K. Janaki, G. Velraj, R. Sakthi Ganapathy, and S. Krishnaraj, "Structural and optical properties of Ag doped tungsten oxide (WO$_3$) by microwave-assisted chemical route," *J. Mater. Sci. Mater. Electron.*, vol. 27, no. 4, pp. 3158–3163, 2016.

[123] C. Yang, Q. Zhu, S. Zhang, Z. Zou, K. Tian, and C. Xie, "A comparative study of microstructures on the photoelectric properties of tungsten trioxide films with plate-like arrays," *Appl. Surf. Sci.*, vol. 297, pp. 116–124, 2014.

[124] C. Yang, Q. Zhu, T. Lei, H. Li, and C. Xie, "The coupled effect of oxygen vacancies and Pt on the photoelectric response of tungsten trioxide films," *J. Mater. Chem. C*, vol. 2, no. 44, pp. 9467–9477, 2014.

[125] K. Kriti, P. Kaur, S. Kaur, D. Arora, K. Asokan, and D. P. Singh, "Influence of defect structure on colour tunability and magneto optical behaviour of WO$_3$ nanoforms," *RSC Adv.*, vol. 9, no. 36, pp. 20536–20548, 2019.

[126] M. Petruleviciene, J. Juodkazyte, M. Parvin, A. Tereshchenko, S. Ramanavicius, R. Karpicz, R., U. Samukaite-Bubniene, and A. Ramanavicius, "Tuning the Photo-Luminescence Properties of WO$_3$ Layers by the Adjustment of Layer," *Materials (Basel).*, vol. 12, no. 13, pp. 2814, 2020.

[127] M. Pourbaix, "Atlas of Electrochemical Equilibria in-Aqueous Solutions." *NACE* , vol. 307, 1974.

[128] F. Dionigi, T. Reier, Z. Pawolek, M. Gliech, and P. Strasser, "Design

Criteria, Operating Conditions, and Nickel-Iron Hydroxide Catalyst Materials for Selective Seawater Electrolysis," *ChemSusChem*, vol. 9, no. 9, pp. 962–972, 2016.

[129] S. S. Kalanur, L. T. Duy, and H. Seo, "Recent Progress in Photoelectrochemical Water Splitting Activity of WO_3 Photoanode*s″*, *Topics in Catalysis*, vol. 61, no. 9, pp 1043-1076, 2018.

[130] J. A. Seabold and K. S. Choi, "Effect of a cobalt-based oxygen evolution catalyst on the stability and the selectivity of photo-oxidation reactions of a WO_3 photoanode," *Chem. Mater.*, vol. 23, no. 5, pp. 1105–1112, 2011.

[131] P. Singh, R. Singh, R. Gale, K. Rajeshwar, and J. DuBow, "Surface charge and specific ion adsorption effects in photoelectrochemical devices," *J. Appl. Phys.*, vol. 51, no. 12, pp. 6286–6291, 1980.

[132] J. Moser and M. Grätzel, "Photoelectrochemistry with Colloidal Semiconductors; Laser Studies of Halide Oxidation in Colloidal Dispersions of TiO_2 and α-Fe_2O_3," *Helv. Chim. Acta*, vol. 65, no. 5, pp. 1436–1444, 1982.

[133] J. Juodkazytė, M. Petrulevičienė, M. Parvin, B. Šebeka, I. Savickaja, ,V. Pakštas, A. Naujokaitis, J. Virkutis, and A. Gegeckas, "Activity of sol-gel derived nanocrystalline WO_3 films in photoelectrochemical generation of reactive chlorine species," *J. Electroanal. Chem.*, vol. 871, 2020.

[134] C. Ros, T. Andreu, and J. R. Morante, "Photoelectrochemical water splitting: a road from stable metal oxides to protected thin film solar cells," *J. Mater. Chem. A*, vol. 8, no. 21, pp. 10625–10669, 2020.

[135] M. Desseigne, N. Dirany, V. Chevallier, and M. Arab, "Shape dependence of photosensitive properties of WO_3 oxide for photocatalysis under solar light irradiation," *Appl. Surf. Sci.*, vol. 483, pp. 313–323, 2019.

[136] A. D. Proctor and B. M. Bartlett, "Hydroxyl radical suppression during photoelectrocatalytic water oxidation on WO_3|FeOOH," *Journal of Physical Chemistry C*, vol. 124, no. 33. pp. 17957–17963, 2020.

[137] V. Cristino *et al.*, "Some aspects of the charge transfer dynamics in nanostructured WO_3 films," *J. Mater. Chem. A*, vol. 4, no. 8, pp. 2995–3006, 2016.

[138] Y. Ji, J. Bai, J. Li, T. Luo, L. Qiao, Q. Zeng, and B. Zhou, "Highly selective transformation of ammonia nitrogen to N_2 based on a novel solar-driven photoelectrocatalytic-chlorine radical reactions system," *Water Res.*, vol. 125, no. 800, pp. 512–519, 2017.

[139] Y.Zhang, J. Li, J. Bai, X. Li, X., Z. Shen, L. Xia, S. Chen, Q. Xu, and B. Zhou, "Total organic carbon and total nitrogen removal and simultaneous electricity generation for nitrogen-containing wastewater based on the catalytic reactions of hydroxyl and chlorine radicals", *Applied Catalysis B: Environmental*, vol.238, pp.168-176, 2018.

[140] J. Juodkazytė, M. Petrulevičienė, M. Parvin, B. Šebeka, I. Savickaja, ,V. Pakštas, A. Naujokaitis, J. Virkutis, and A. Gegeckas, "Activity of sol-gel derived nanocrystalline WO_3 films in photoelectrochemical generation of reactive chlorine species," *J. Electroanal. Chem.*, vol. 871, 2020.

[141] M. S. Koo, X. Chen, K. Cho, T. An, and W. Choi, "In Situ Photoelectrochemical Chloride Activation Using a WO_3 Electrode for Oxidative Treatment with Simultaneous H_2 Evolution under Visible Light," *Environ. Sci. Technol.*, vol. 53, no. 16, pp. 9926–9936, 2019.

[142] J. Zheng, J. Li, J. Bai, X. Tan, Q. Zeng, L. Li, and B. Zhou, "Efficient degradation of refractory organics using sulfate radicals generated directly from WO_3 photoelectrode and the catalytic reaction of sulfate," *Catalysts*, vol. 7, no. 11, 2017.

[143] D. A. Armstrong *et al.*, "Standard electrode potentials involving radicals in aqueous solution: Inorganic radicals (IUPAC Technical Report)," *Pure Appl. Chem.*, vol. 87, no. 11–12, pp. 1139–1150, 2015.

[144] M. Jia, C. Zhang, and J. Cheng, "Origin of Asymmetric Electric Double Layers at Electrified Oxide/Electrolyte Interfaces," *J. Phys. Chem. Lett.*, vol. 12, no. 19, pp. 4616–4622, 2021.

[145] T. Sata, " Ion exchange membranes: preparation, characterization, modification and application", Royal Society of chemistry ,2007.

[146] M. Krivec, R. Dillert, D. W. Bahnemann, A. Mehle, J. Štrancar, and G. Dražić, "The nature of chlorine-inhibition of photocatalytic degradation of dichloroacetic acid in a TiO_2-based microreactor," *Phys. Chem. Chem. Phys.*, vol. 16, no. 28, pp. 14867–14873, 2014.

[147] Y. Lei, X. Lei, P. Westerhoff, X. Zhang, and X Yang," Reactivity of chlorine radicals ($Cl^{\bullet}$ and $Cl_2^{\bullet-}$) with dissolved organic matter and the formation of chlorinated byproducts. *Environmental Science & Technology*, vol. 55, no. 1, pp.689-699,2020

[148] K. Zhang and K. M. Parker, "Halogen Radical Oxidants in Natural and Engineered Aquatic Systems," *Environ. Sci. Technol.*, vol. 52, no. 17, pp. 9579–9594, 2018.

[149] R. Br ninghoff, A.K. Van Duijne, L. Braakhuis, P. Saha, A.W. Jeremiasse, B. Mei, and G. Mul, "Comparative Analysis of Photocatalytic and Electrochemical Degradation of 4-Ethylphenol in Saline Conditions," *Environmental Science and Technology*, vol. 53, no. 15. pp. 8725–8735, 2019.

[150] J. Kn ppel, A. Kormányos, B. Mayerh fer, A. Hofer, M. Bierling, J. Bachmann, S. Thiele, and S. Cherevko, S., "Photocorrosion of WO_3 photoanodes in different electrolytes. *ACS Physical Chemistry Au*, vol.1 , no.1, pp.6-13, 2021

[151] J. Knöppel, S. Zhang, F. D. Speck, K. J. J. Mayrhofer, C. Scheu, and S. Cherevko, "Time-resolved analysis of dissolution phenomena in photoelectrochemistry – A case study of WO_3 photocorrosion," *Electrochem. commun.*, vol. 96, pp. 53–56, 2018.

[152] H. V. Le, P. T. Pham, L. T. Le, A. D. Nguyen, N. Q. Tran, and P. D. Tran, "Fabrication of tungsten oxide photoanode by doctor blade technique and investigation on its photocatalytic operation mechanism," *Int. J. Hydrogen Energy*, vol. 46, no. 44, pp. 22852–22863, 2021.

[153] A. G. Breuhaus-Alvarez, Q. Cheek, J. J. Cooper, S. Maldonado, and B. M. Bartlett, "Chloride Oxidation as an Alternative to the Oxygen-Evolution Reaction on H_xWO_3 Photoelectrodes," *J. Phys. Chem. C*, vol. 125, no. 16, pp. 8543–8550, 2021.

[154] S. Trasatti and O. A. Petrii, "International Union of Pure and Applied Chemistry Physical Chemistry Division Commission on Electrochemistry: Real Surface Area Measurements in Electrochemistry," *Pure Appl. Chem.*, vol. 63, no. 5, pp. 711–734, 1991.

[155] T. Nakajima, A. Hagino, T. Nakamura, T. Tsuchiya, and K. Sayama, "WO_3 nanosponge photoanodes with high applied bias photon-to-current efficiency for solar hydrogen and peroxydisulfate production," *J. Mater. Chem. A*, vol. 4, no. 45, pp. 17809–17818, 2016.

[156] S. A. Farook, V. Shah, D. Lenouvel, O. Sheikh, Z. Sadiq, and L. Cascarini, "Guidelines for management of sodium hypochlorite extrusion injuries," *Br. Dent. J.*, vol. 217, no. 12, pp. 679–684, 2014.

[157] M. Petruleviciene, M. Parvin, I. Savickaja, G. Gece, A. Naujokaitis, V. Pakstas, J. Pilipavicius, A. Gegeckas, G. Gaigalas, and J. Juodkazyte, , "WO_3 coatings for photoelectrochemical synthesis of persulfate: efficiency, stability and applicability," *J. Solid State Electrochem.*, vol. 26, no. 4, pp. 1021–1035, 2022.

[158] J. Moreno-Andrés, R. Rios Quintero, A. Acevedo-Merino, and E. Nebot, "Disinfection performance using a UV/persulfate system: Effects derived from different aqueous matrices," *Photochem. Photobiol. Sci.*, vol. 18, no. 4, pp. 878–883, 2019.

[159] Z. Sabeti, M. Alimohammadi, S. Yousefzadeh, H. Aslani, M. Ghani, and R. Nabizadeh, "Application of response surface methodology for modeling and optimization of Bacillus subtilis spores inactivation by the UV/persulfate process," *Water Sci. Technol. Water Supply*, vol. 17, no. 2, pp. 342–351, 2017.

CURRICULUM VITAE

Name: Maliha Parvin
Nationality: Bangladeshi
Date of birth: 08.11.1985
Marital status: Married

Scholastic Records

2018- present: Ph.D. Researcher
                   Department of Chemical Engineering and Technology
                   State Research Center for Physical Sciences and
                   Technology, Vilnius, Lithuania

2012 – 2015:   Master of Science (M.Sc.) in Chemistry
                   UAE University, UAE
                   GPA 3.73 out of 4

2011 – 2012:   Master of Science (M.Sc.) in Chemistry
                   National University of Singapore
                    (Discontinued)

2004 – 2010:   Bachelor of Science (B.Sc. Honors), Chemistry
                    National University, Gazipur, Bangladesh

2001-2003:   Higher Secondary Certificate
                    Ideal school & college, Motijheel, Dhaka-1000

1999-2001:   Secondary School Certificate
                    Ideal school & college, Motijheel, Dhaka-1000

Major Areas Studied in M.Sc.

1.   Chemical Instrumentation (Analytical Chemistry)
2.   Electroanalytical Techniques
3.   Separation and Chromatographic Technique
4.   Spectro. Methods of Structure
5.   Advanced Organic Chemistry

Major Areas Studied in Ph.D.
1.   Electrochemical Methods of Analysis

2. Sol-gel chemistry of transition metal oxides
3. Electrochemical Kinetics

<u>Work Experience :</u>

- Junior researcher at Center for Physical Sciences and Technology (FTMC) in M-era.Net project (Multiscale computer modelling, synthesis and rational design of photo(electro)catalysts for efficient visible-light-driven seawater splitting (CatWatSplitt) (Reference Number: project8168)), 01 May 2021 – 30 April 2022
- Ph.D. researcher at Center for Physical Sciences and Technology (FTMC), October 2018 – Present, Vilnius, Lithuania
- Chemistry Teacher(Senior Section), CIDER International School, May 2017 – 30 September 2018
- Research Assistant, UAE University, January 2015 - May 2015

SANTRAUKA

ĮVADAS

Siekdama mažinti oro taršą bei užkirsti kelią klimato atšilimui Europos Komisija paskelbė "Žaliąjį kursą", t.y. veiksmų planą, kurio vienas pagrindinių tikslų - iki 2050 m visiškai sustabyti šiltnamio efektą sukeliančių dujų išmetimą į atmosferą. Chemijos pramonė yra vienas taršiausių bei ištekliams ir energijai imlių sektorių. Todėl siekiama kurti naujas, aplinkai draugiškas ir ekonomiškai efektyvias sintezės technologijas, kuriose būtų naudojami atsinaujinantys energijos šaltiniai. Pastaruoju metu vis daugiau dėmesio sulaukia dribtine fotosinteze vadinami fotoelektrocheminiai (FEC) procesai, kuriuose šviesos energija yra paverčiama chemine energija. Vienas plačiausiai tiriamų dirbtinės fotosintezės procesų – FEC vandens skaidymas tvariai vandenilio kaip ateities kuro gamybai. Tačiau neseniai parodyta, kad šis metodas yra tinkamas sintetinti ir kitas vertingas chemines medžiagas, ypač stiprius oksidatorius ($HClO$, H_2O_2, $H_2S_2O_8$ ir kt.), kurie naudojami dezinfekcijai. Pasaulinis dezinfekcinių medžiagų poreikis nuolatos auga, žmonijai siekiant užkirsti kelią užkrečiamoms ligoms. Fotoelektrocheminė stiprių oksidatorių sintezė yra palyginti nauja tyrimų sritis, todėl nauji duomenys apie efektyvias sistemas bei procesų mechanizmus yra būtini jos tolimesniam vystymuisi. Norint pasiekti aukštą energijos konversijos efektyvumą labai svarbu tinkamai parinkti fotoelektrocheminę sistemą, t.y. fotoelektrodą ir elektrolitą. Volframo (VI) oksidas, WO_3, yra perspektyvi fotoanodinė medžiaga, pasižyminti vidutiniu draustinės juostos pločiu (2.6 – 2.8 eV), palyginti nemažu skylių difuzijos nuotoliu (150 - 500 nm) bei aukštu valentinės juostos potencialu (~ 3 V (NHE)), dėl kurio šviesos generuojamos skylės turi didelę oksidacinę galią. Kadangi FEC reakcijos yra daugiapakopiai procesai, apimantys šviesos absorbciją, krūvininkų generaciją, atskyrimą, transportą bei pernašą per elektrodo/elektrolito fazių sąlyčio ribą, svarbų vaidmenį juose vaidina puslaidininkinio fotoelektrodo kristališkumas, struktūra bei morfologija. Taigi, reikalingas kruopštus puslaidininkio/elektrolito sandūros optimizavimas.

Šios daktaro disertacijos tikslas – susintetinti fotoelektrocheminiškai aktyvias skirtingos morfologijos bei storio WO_3 dangas ir ištirti jų savybes fotoelektrocheminėje stiprių oksidatorių sintezėje sulfatiniuose bei chloridiniuose elektrolituose. Tikslui įgyvendinti buvo suformuluoti šie uždaviniai:

1. Ištirti, kaip skirtingi alkoholiai (metanolis, etanolis, izopropanolis ir butanolis), naudojami reduktoriais cheminiame WO_3 dangų nusodinime, o taip pat atkaitinimo temperatūra įtakoja WO_3 kristalizaciją, dangų morfologiją bei FEC aktyvumą;

2. Suformuoti skirtingo storio (nuo ~0.5 iki ~10 µm) labai poringas nanostruktūrizuotas WO_3 dangas bei ištirti jų FEC aktyvumą;

3. Ištirti skirtingo storio ir morfologijos WO_3 dangų energijos konversijos efektyvumą fotoelektrocheminėje aktyvių chloro junginių ($ClO^- + ClO_2^-$) bei persulfato ($S_2O_8^{2-}$) sintezėje;

4. Ištirti konkurenciją tarp fotoanodinių vandens ir anijonų oksidacijos procesų, o taip pat skirtingų WO_3 dangų stabilumą fotoelektrolizės sąlygomis sulfatiniuose ir chloridiniuose elektrolituose;

5. Patikrinti antimikrobinį fotoelektrocheminės stiprų oksidatorių sintezės su WO_3 fotoanodu poveikį.

Daktaro disertaijos naujumas ir originalumas:

- Pirmą kartą kartą nagrinėta WO_3 dangų morfologijos įtaka konkurencijai tarp fotoanodinių vandens bei anijonų oksidacijos procesų, vykstančių sulfatiniuose ir chloridiniuose elektrolituose.

- Pateikta nauja WO_3 fotoelektrocheminės elgsenos interpretacija, pagal kurią galimos fotoanodinės reakcijos H_2SO_4 ir $NaCl$ tirpaluose nagrinėtos kaip elektrodo potencialo įtakojami fotocheminiai procesai, kuriuose kaip tarpiniai junginiai dalyvauja laisvieji radikalai.

- Padaryta prielaida, kad ant WO_3 paviršiaus specifiškai adsorbuoti chlorido jonai bei tarpiniai jų oksidacijos produktai ($Cl\bullet$, $Cl_2^-\bullet$) gali sumažinti fotosrovės pradžios potencialą, veikti kaip krūvininkų gaudyklės bei apsaugoti WO_3 paviršių nuo žalingo perokso junginių susidarymo.

METODIKA

Šiame darbe fotoelektrochemiškai aktyvūs volframo (VI) oksido sluoksniai ant elektrai laidaus stiklo (FTO) pagrindo buvo formuojami, panaudojant dvi cheminio nusodinimo metodikas, kurios skyrėsi WO_3 pirmtaku ir toliau yra vadinamos "perokso volframo rūgšties" (PVR) bei "volframo rūgšties" (VR) metodais. PVR sintezėje WO_3 dangų morfologinės bei struktūrinės savybės buvo modifikuojamos reduktoriais naudojant skirtingus alkoholius (MeOH, EtOH, IsoPrOH, BuOH) bei keičiant dangų atkaitinimo temperatūrą (400 °C arba 500 °C). VR metodo atveju WO_3 dangų

storis buvo keičiamas naudojant skirtingą nusodinimo ciklų skaičių (nuo 1 iki 4).

WO$_3$ dangų paviršiaus morfologija bei struktūra buvo charakterizuojamos skenuojančios elektroninės mikroskopijos bei rentgeno spindulių difrakcijos metodais. Volframo oksido fazės formavimasis bei fazinė sudėtis tirta termogravimetrinės analizės ir infraraudonųjų spindulių spektroskopijos (FTIR) metodais. Optinės sluoksnių savybės charakterizuotos fotoliuminescencijos bei atspindžio spektroskopijos metodais. WO$_3$ dangų FEC elgsena buvo tiriama ciklinės voltamperometrijos, chronoamperometrijos, elektrocheminės impedanso spektroskopijos metodais 0.5 M H$_2$SO$_4$, 0.5 M NaCl bei mišriame (0.5 M H$_2$SO$_4$ + 0.5 M NaCl) elektrolituose. Fotoelektrocheminio aktyvių chloro junginių (ClO$^-$ + ClO$_2$$^-$) bei persulfato (S$_2O_8$$^{2-}$) susidarymo išeiga pagal srovę 0.5 M NaCl ir 0.5 M H$_2$SO$_4$ tirpaluose po fotoelektrolizės buvo nustatoma, atitinkamai, jodometrinės arba chromatometrinės tirpalų analizės būdu. Baktericidinio fotoelektrolizės poveikio tyrimams buvo naudojamos *Bacillus sp.* ir *E.coli* bakterijų suspensijos 0.5 M NaCl arba 0.1 M Na$_2$SO$_4$ tirpaluose.

REZULTATAI

PVR metodu gautų WO$_3$ dangų savybės ir fotoelektrocheminė elgsena

PVR metodu buvo gauti 0.5 – 1.0 µm storio WO$_3$ sluoksniai, sudaryti iš plokštelių pavidaro dalelių, kurių dydis ir forma skyrėsi, priklausomai nuo to, koks alkholis naudotas sintezejė kaip reduktorius. Stambiausios (700 - 1200 nm) plokštelės susiformavo naudojant izopropillo alkoholį (IsoPrOH_WO$_3$), o smulkiausios (400 - 600 nm) dalelės gautos naudojant metilo alkoholį (MeOH_WO$_3$) (4 pav.)[1]. Dangų atkaitinimo temperatūra taip pat turėjo įtakos sluoksnių morfologijai: EtOH_WO$_3$ bei BuOH_WO$_3$ atveju po atkaitinimo 500°C temperatūroje dangą sudarančios plokštelės buvo akivaizdžiai stambesnės. Skirtingų alkoholių, naudotų sintezejė, įtaka dangų morfologijai buvo paaiškinta skirtinga jų redukcine galia, kuri mažėja, ilgėjant anglies atomų grandinei, bei skirtingu koloidinių dalelių stabilumu reakcijos mišinyje, kuris labai priklauso nuo terpės dielektrinės skvarbos (1 lentelė). Alkoholio su mažesne dielektrine skvarba pridėjimas į vandeninį tirpalą sumažina medžiagos tirpumą dėl solvatacijos energijos sumažėjimo. Be to, energijos

---

[1] Santraukoje pateiktos nuorodos į disertacijos paveikslėlius, lenteles ir lygtis naudojant tą pačią numeraciją.

barjeras, kuris stabdo nuosėdų aglomeraciją ir dalelių augimą yra tiesiai proporcingas terpės dielektrinei skvarbai ir paviršiniam potencialui. Todėl mažesnė aglomeracija ir mažesnės plokštelės susidarė, kai reduktoriais buvo naudojami alkoholiai su didesne dielektrine skvarba. BuOH atveju santykinai mažų plokštelių susidarymą veikiausiai nulėmė žema redukcinė galia ir mažesnis reakcijos greitis.

Rentgeno spindulių difrakcijos tyrimai parodė, kad visais atvejais susiformuoja monoklininė WO_3 fazė su dominuojančiomis (020) ir (200) plokštumomis (5 pav.), dangų draustinės juostos plotis, įvertintas iš atspindžio spektrų, buvo apie 2.7 eV (6 pav.).

Fotoelektrocheminės WO_3 fotoelektrodų elgsenos tyrimai 0.5 M H_2SO_4 tirpale parodė, kad visos dangos buvo fotoelektrochemiškai aktyvios, tačiau atkaitinimas 500 °C temperatūroje akivaizdžiai sumažino WO_3 sluoksnių fotosroves potencialų srityje E > 0.5 V, o taip pat ir nuo apšvietimo nepriklausančias sroves grįžtamos oksido redukcijos (6 lygtis) srityje ties E < 0.5 V (7 pav.). Pasiremiant XRD bei FTIR duomenimis, šie pokyčiai buvo paaiškinti 400 - 500 °C intervale vykstančiais WO_3 kristalinės struktūros pokyčiais, kuomet smulkesniems kristalitams jungiantis į didesnius veikiausiai padaugėja gardelės defektų, kurie neigiamai veikia šviesos generuojamų krūvininkų judėjimą fotosrovės, j_{ph}, potencialų srityje (E > 0.5 V) bei protonų interkaliaciją oksido redukcijos E srityje (E < 0.5 V). Prieita išvados, kad siekiant gauti fotoelektrochemiškai aktyvias WO_3 dangas PVR sintezės metodu, optimali sluoksnių atkaitinimo temperatūra yra 400 °C, todėl ji buvo pasirinkta tolimesniems tyrimams. Fotosrovę 0.5 M H_2SO_4 tirpale gali sąlygoti ant WO_3 paviršiaus vykstančios vandens molekulių arba SO_4^{2-} anijonų oksidacijos reakcijos (7 – 10 lygtys).

WO_3 dangų morfologijos bei struktūros įtaka FEC krūvio pernašos procesams, o taip pat krūvininkų koncentracijai tirta elektrocheminės impedanso spektroskopijos metodu (8 pav.). Didžiausia krūvio pernašos varža (R_{ct}) bei mažiausia krūvininkų koncentracija (N_D), kuri metalų oksiduose siejama su deguonies vakansijomis, nustatyta MeOH_WO_3 atveju, o viena mažiausių R_{ct} ir didžiausia N_D gauta IsoPrOH_WO_3 dangai. Nustatytų parametrų suvestinė pateikta 2 lentelėje. R_{ct} vertės koreliavo su struktūrinės netvarkos laipsniu, o N_D – su vidutiniu kristalitų dydžiu, įvertintais iš XRD duomenų.

Šviesos generuojamų krūvininkų gyvavimo trukmė bei taškinių defektų, kurie gali veikti kaip rekombinacijos centrai, kiekis WO_3 bandinių paviršiuje buvo tiriami fotoliuminescencijos (PL) spektroskopijos pagalba (9 pav.). Spektruose matomos dvi plačios emisijos juostos: mėlynoji ties 435 - 450 nm,

susijusi su radiacine krūvininkų rekombinacija, ir žalioji ties $\lambda > 500$ nm, kurią lemia deguonies vakansijos, lokalizuotos būsenos bei draustinės juostos defektai. Fotoliuminescencijos intensyvumas mažėjo sekoje MeOH_WO$_3$ > BuOH_WO$_3$ > EtOH_WO$_3$ > IsoPrOH_WO$_3$, kuri atitinka dangas sudarančių plokštelių stambėjimo tendenciją. Be to, PL intensyvumo mažėjimas koreliavo su struktūrinės netvarkos mažėjimu, įvertintu XRD metodu. Ilgiausia fotoliuminescencijos gesimo trukmė, kuri yra proporcinga vidutinei krūvininkų gyvavimo trukmei, nustatyta IsoPrOH_WO$_3$ dangos atveju (τ_{ave} = 1.4 ns). Pažymėtina, kad 500 °C temperatūroje kaitintų dangų τ_{ave} siekė 11 ns, tačiau jų FEC aktyvumas buvo mažas veikiausiai dėl krūvininkų pagavimo gaudyklėse.

Fotoelektrocheminis WO$_3$ dangų atsakas 0.5 M NaCl tirpale skyrėsi nuo jų elgsenos 0.5 M H$_2$SO$_4$ tirpale: srovė oksido redukcijos srityje (E < 0.3 V) didėjo proporcingai laikui, kurį elektrodas buvo poliarizuojamas esant apšvietimui fotosrovės E intervale. Nustatyta, kad katodinio piko srovė yra tiesiogiai proporcinga v$^{1/2}$ (v - potencialo skleidimo greitis) (10 pav.), kas būdinga difuzijos kontroliuojamiems procesams. Šie dėsningumai rodo, kad katodinę srovę sąlygoja fotoanodinės reakcijos produktų, patekusių į tirpalą, o ne adsorbuotų ant elektrodo paviršiaus, redukcija. Fotosrovę 0.5 M NaCl tirpale gali sąlygoti ant WO$_3$ paviršiaus vykstanti vandens molekulių arba Cl$^-$ anijonų oksidacija (11, 12 lygtys).

FEC reakcijų metu susidarančių produktų analizė parodė, kad 0.5 M H$_2$SO$_4$ tirpale S$_2$O$_8$$^{2-}$ išeiga pagal fotosrovę svyruoja tarp 35 ir 80 %, o 0.5 M NaCl tirpale aktyvių chloro junginių (ClO$^-$ + ClO$_2$$^-$) susidarymo išeiga yra gerokai didesnė, artima 100 % (11 pav.). Pastarasis faktas leidžia daryti išvadą, kad aukščiau aptarta katodinė srovė, stebima NaCl tirpale ties E < 0.3 V, veikiausiai yra susijusi su aktyvių chloro junginių redukcija. Fotosrovės dalis, nepanaudota S$_2$O$_8$$^{2-}$ ar (ClO$^-$ + ClO$_2$$^-$) susidarymui, priskirta H$_2$O molekulių oksidacijai iki O$_2$ arba H$_2$O$_2$ (7 - 9 lygtys). Šie rezultatai rodo, kad fotoanodiniai vandens ir anijonų oksidacijos procesai yra konkuruojantys, tačiau 0.5 M NaCl tirpale vyrauja anijonų oksidacija.

Šviesos energijos konversijos į elektros energiją efektyvumo (ABPE) vertės 0.5 M H$_2$SO$_4$ tirpale neviršijo 0.27%, o 0.5 M NaCl tirpale – 0.08% (12 pav.)
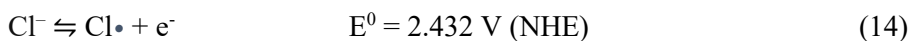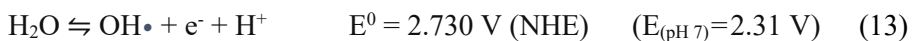
Tiriant WO$_3$ dangų stabilumą fotoelektrolizės sąlygomis pastebėta, kad visais atvejais 0.5 M NaCl tirpale fotosrovė buvo gerokai stabilesnė nei 0.5 M H$_2$SO$_4$ tirpale (13 pav.). Literatūroje j$_{ph}$ mažėjimas siejamas su perokso junginių susidarymu ir kaupimusi ant WO$_3$ paviršiaus fotoanodinės vandens

oksidacijos metu. Padaryta prielaida, kad chlorido jonai apsaugo fotoelektrodo paviršių nuo perokso junginių susidarymo.

Tolimesni tyrimai buvo skirti suprasti Cl⁻ jonų įtaką fotoelektrocheminei skirtingos morfologijos WO₃ dangų elgsenai. 14 pav. palyginta fotoelektrodų elgsena potenciostatinėmis sąlygomis 0.5 M H₂SO₄ ir 0.5 M NaCl tirpaluose esant periodiniam apšvietimui. Eksperimentui abiejuose tirpaluose buvo naudojamas tas pats bandinys, siekiant užtikrinti, kad dangos morfologija, defektų bei krūvininkų koncentracijos būtų identiškos ir fotosrovę iš esmės lemtų krūvininkų sąveikos su tirpalo komponentėmis efektyvumas. Pastebėta, kad fotosrovės 0.5 M NaCl tirpale buvo didesnės ar panašios kaip 0.5 M H₂SO₄ tirpale visais atvejais, išskyrus IsoPrOH_WO₃, kurio FEC aktyvumas sulfatinėje terpėje buvo gerokai didesnis nei chloridinėje. Šie duomenys rodo, kad WO₃ bandinių FEC aktyvumui tirtuose elektrolituose įtakos turi sluoksnio morfologija: iš smulkiausių plokštelių sudarytas MeOH_WO₃ pasižymėjo gerokai didesniu aktyvumu 0.5 M NaCl tirpale, o iš stambiausių plokštelių sudarytas IsoPrOH_WO₃ - 0.5 M H₂SO₄ tirpale.
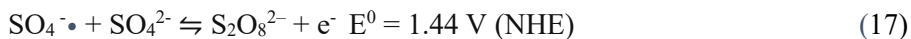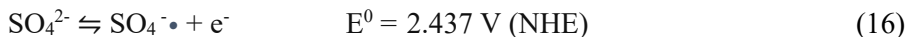
Konkurencija tarp fotoanodinių procesų buvo tiriama, lyginant skirtingos morfologijos WO₃ dangų atsaką 0.5 M H₂SO₄ tirpaluose be ir su chlorido jonais (15 pav.). Pastebėta, kad pridėjus Cl⁻, fotosrovė atsiranda esant mažesnėms E vertėms. Šis reiškinys paaiškintas specifine Cl⁻ adsorbcija, kuri padidina elektrinio lauko stiprumą puslaidininkio erdvinio krūvio sluoksnyje, kas sumažina elektronų ir skylių rekombinaciją ir depoliarizuoja j_{ph} pradžios potencialą. Be to, Cl⁻ pridėjimas sumažino fotosroves visais atvejais, išskyrus MeOH_WO₃. IsoPrOH_WO₃ bandinio atveju sumažėjimas buvo pats didžiausias. Gauti rezultatai rodo, kad chloridų pridėjimas sumažina skylių pernašos efektyvumą, o šio reiškinio mąstas koreliuoja su WO₃ dangų morfologiniais ypatumais.

Siekiant suprasti stebimus dėsningumus buvo nagrinėjamos fotoanodinės reakcijos, kurios yra galimos mišriuose elektrolituose. Yra žinoma, kad WO₃ valentinės juostos potencialas yra ~3 V (NHE), o tai reiškia, kad šviesos generuojamos skylės turi pakankamai aukštą energiją, kad oksidacijos reakcijose kaip tarpiniai junginiai susidarytų laisvieji radikalai. Mokslinėje literatūroje gausu šią prielaidą patvirtinančių įrodymų apie OH•, Cl• bei SO₄⁻• susidarymą ant WO₃ fotoelektrodų vykstančių procesų metu. Šių reakcijų standartiniai potencialai, E^0, palyginti žemiau:

$$H_2O \leftrightarrows OH\bullet + e^- + H^+ \qquad E^0 = 2.730 \text{ V (NHE)} \qquad (E_{(pH\ 7)} = 2.31 \text{ V}) \qquad (13)$$

$$Cl^- \leftrightarrows Cl\bullet + e^- \qquad E^0 = 2.432 \text{ V (NHE)} \qquad (14)$$

$Cl^- + H_2O \leftrightharpoons ClOH^- \bullet + e^- + H^+$

$$E^0 = 2.740 \text{ V (NHE)} \quad (E_{(pH\ 7)} = 2.32 \text{ V}) \quad (15)$$

$SO_4{}^{2-} \leftrightharpoons SO_4{}^- \bullet + e^- \quad\quad E^0 = 2.437 \text{ V (NHE)} \quad\quad\quad\quad (16)$

$SO_4{}^- \bullet + SO_4{}^{2-} \leftrightharpoons S_2O_8{}^{2-} + e^- \quad E^0 = 1.44 \text{ V (NHE)} \quad\quad (17)$

Toks elektrocheminių potencialų išsidėstymas rodo, kad rūgščioje terpėje Cl• ir SO$_4{}^-$• susidarymas termodinamiškai yra labiau tikėtinas procesas nei OH• ar ClOH·• formavimasis, tačiau neutralioje terpėje pastarieji procesai būtų labiau tikėtini. Be to, (14) ir (16) reakcijų tikimybė yra praktiškai tokia pati, todėl konkurenciją tarp šių procesų turėtų lemti kinetiniai faktoriai. Kadangi fotoanodinės reakcijos vyksta fotoelektrodo/elektrolito fazių sąlyčio riboje, tirpalo komponenčių adsorbcija ant elektrodo paviršiaus turi stipriai įtakoti vykstančius procesus. Aukščiau aptartas fotosrovės atsiradimo potencialo pasislinkimas mažesnių E verčių link pridėjus NaCl į 0.5 M H$_2$SO$_4$ (15 pav.) rodo, kad pirmiausia oksiduojami tie anijonai, kurie yra adsorbuoti ant elektrodo paviršiaus, t.y. Cl$^-$. Specifinė Cl$^-$ adsorbcija paaiškina ir aukštas aktyvių chloro junginių išeigos pagal fotosrovę vertes (11 pav.), nors H$_2$O oksidacijos tikimybė neutraliame tirpale turėtų būti didesnė (13 ir 14 lygtys).

Nagrinėjant WO$_3$ morfologijos įtaką konkurencijai tarp fotoanodinių reakcijų buvo atsižvelgta į tai, kad tiriami procesai vyksta ant šiurkščių įelektrintų paviršių, kur elektrinio lauko pasiskirstymas bei dvigubo elektrinio sluoksnio struktūra ir vandens molekulių bei jonų dinamika yra stipriai įtakojami jonų krūvio bei dydžio. Chronoamperometriniai tyrimai (14 pav.) parodė, kad iš smulkių plokštelių sudarytų MeOH_WO$_3$ ir BuOH_WO$_3$ dangų atveju krūvininkų rekombinacija yra didesnė 0.5 M H$_2$SO$_4$ nei 0.5 M NaCl terpėje, o iš stambių plokštelių sudaryto IsoPrOH_WO$_3$ atveju – priešingai. Tai paaiškinta steriniais efektais: paviršiaus prieinamumas didesniems, hidratuotiems sulfato anijonams IsoPrOH_WO$_3$ dangos atveju turėtų būti geresnis. Šią prielaidą paremia ir stabilios S$_2$O$_8{}^{2-}$ išeigos pagal fotosrovę vertės, gautos naudojant IsoPrOH_WO$_3$ (11 pav.).

Palyginti mažas IsoPrOH_WO$_3$ fotoelektrocheminis aktyvumas chloridinėje terpėje (14 ir 15 pav.) paaiškintas atsižvelgiant į žemiau aptartus procesus. Yra žinoma, kad Cl• radikalai yra linkę greitai sudaryti kompleksus su Cl$^-$ jonais:

$Cl\bullet + Cl^- \rightarrow Cl_2\bullet^- \quad\quad K = (1.4 \pm 0.2) \times 10^5 \text{ M}^{-1} \quad\quad\quad (18)$
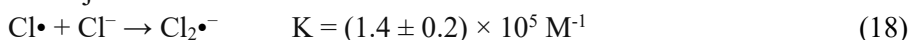
Neigiamą krūvį turintys Cl$_2\cdot{}^-$ radikalai turėtų būti elektrostatiškai pritraukiami prie teigiamai poliarizuoto WO$_3$ paviršiaus, tokiu būdu blokuodami priėjimą H$_2$O molekulėms ar kitiems jonams. Be to, adsorbuoti Cl$_2\bullet^-$ gali veikti kaip

rekombinacijos centrai reaguodami su fotoelektronais, vėl susidarant chlorido jonams:

$$Cl_2 \bullet^- + e^- \rightarrow 2Cl^- \qquad E^0 = 2.126V \text{ (NHE)} \qquad (19)$$
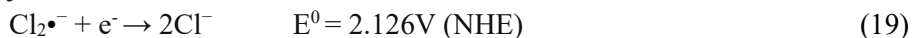
Reakcijų (14), (18) ir (19) seka paaiškintos mažos IsoPrOH_WO$_3$ fotosrovės tirpaluose su chloridais (14 ir 15 pav.). Padaryta prielaida, kad specifinė Cl$^-$ bei Cl$_2 \bullet^-$ adsorbcija užkerta kelią perokso junginių susidarymui ir užtikrina WO$_3$ fotoanodų stabilumą neutralioje terpėje. Smulkesnių plokštelių morfologijos atveju (MeOH_WO$_3$, BuOH_WO$_3$), sąlygos tarpinių chloro junginių adsorbcijai veikiausiai yra mažiau palankios dėl stipresnių stūmos jėgų tarp neigiamą krūvį turinčių dalelių, todėl (19) reakcijos indėlis turėtų būti mažesnis.

Gana žymus WO$_3$ sluoksnių FEC aktyvumo mažėjimas fotoelektrolizės 0.5 M H$_2$SO$_4$ tirpale metu paaiškintas fotoelektrochemiškai neaktyvių bei didesnio tirpumo paviršinių peroksovolframatų susidarymu, kuris vyksta dėl WO$_3$ sąveikos tiek su SO$_4^-\bullet$ ar OH$\bullet$ radikalais, tiek su pačiomis šviesos generuojamomis skylėmis (16 pav.), jeigu jos nėra efektyviai surišamos fotoanodinėse reakcijose su tirpalo komponentėmis.

VR metodu gautų WO$_3$ dangų savybės ir fotoelektrocheminė elgsena

SEM tyrimai parodė, kad „volframo rūgšties" metodu gautos WO$_3$ dangos yra sudarytos iš chaotiškai orientuotų 10 - 20 nm dydžio nanolakštelių, susijungusių į labai poringus sferinius mikrodarinius (17 pav.). Nusodinimų ciklų skaičiui augant nuo 1 iki 4, oksido sluoksnio (sl.) storis padidėjo nuo ~ 0.4 iki 5-10 μm. Rentgenostruktūrinės analizės duomenimis sluoksnius sudarė monoklininė WO$_3$ fazė, o vidutinis kristalitų dydis buvo apie 14 nm, t.y. šiek tiek didesnis nei PVR sintezės būdu gautų dangų (2 lentelė).

Poringų WO$_3$ sluoksnių elektrochemiškai aktyvus paviršiaus plotas buvo įvertintas, matuojant bandinių dvigubo elektros sluoksnio talpas 0.5 M H$_2$SO$_4$ tirpale potencialų srityje tarp 0.5 ir 0.7 V, kur, nesant apšvietimo, nevyksta jokie faradėjiniai procesai. Gauti duomenys parodė, kad 4 sl. WO$_3$ dangų elektrochemiškai aktyvus plotas buvo maždaug 70 kartų didesnis nei 1 sl. dangos (19 pav.). Dangų draustinės juostos plotis, įvertintas iš atspindžio spektrų, kito tarp 2.7 ir 2.8 eV (20 pav.), be to, jos gerokai stipriau absorbavo šviesą palyginti su PVR metodu gautomis dangomis (6 pav.).

Fotoelektrocheminės elgsenos tyrimai 0.5 M H$_2$SO$_4$ ir 0.5 M NaCl tirpaluose parodė, kad fotosrovė auga, didėjant WO$_3$ sluoksnių skaičiui (21 pav.). Svarbu pažymėti, kas j$_{ph}$ vertės, gautos su storais ir poringais WO$_3$ sluoksniais buvo 3-5 kartus didesnės nei PVR sintezės būdu gautų plonų WO$_3$

sluoksnių. Maksimalus šviesos į elektros energijos konversijos efektyvumas (ABPE) 4 sl. dangų atveju buvo 3.6% ir 1.0% 0.5 M H_2SO_4 ir 0.5 M NaCl tirpaluose, atitinkamai (22 pav.). Tai yra vienos didžiausių iki šiol nustatytų ABPE verčių WO_3 fotoelektrodams. Geresnius FEC rezultatus, gautus VR sintezės atveju reikėtų sieti su efektyvesne šviesos absorbcija storesniuose WO_3 sluoksniuose bei poringa didelio paviršiaus nanostruktūra, kuri sudaro palankesnes sąlygas šviesos generuojamoms skylėms pasiekti elektrodo/elektrolito fazių sąlyčio ribą.

3 ir 4 sl. WO_3 dangų atveju $S_2O_8^{2-}$ susidarymo išeiga pagal fotosrovę svyravo tarp 70% ir 90%, o aktyvių chloro junginių – tarp 85% ir 100% (23 pav.). Pažymėtina, kad fotosrovės mažėjimas ilgalaikės fotoelektrolizės 0.5 M H_2SO_4 tirpale metu šiuo atveju buvo mažesnis nei PVR būdu gautų dangų (24 pav.). Šis rezultatas kartu su stabilia išeiga pagal fotosrovę bei aukštomis ABPE vertėmis rodo, kad efektyvus skylių surišimas reakcijoje su SO_4^{2-} jonais apsaugo WO_3 paviršių nuo perokso junginių formavimosi bei degradacijos/pasyvacijos procesų.

Dezinfekcinis fotoelektrolizės su WO_3 bandiniais poveikis buvo patikrintas gramteigiamų ir gramneigiamų bakterijų (*Bacillus sp* ir *E.coli*) suspensijose 0.5 M NaCl ir 0.1 M Na_2SO_4 tirpaluose. Palyginimui atlikti eksperimentai, kur bakterijų suspensijos buvo veikiamos vien tik šviesa (fotolizė) arba vien tik elektrolize be apšvietimo. Sulfatinės terpės atveju buvo patikrintas ir cheminis $S_2O_8^{2-}$ poveikis, kuomet reagento buvo pridėta apytiksliai tiek, kiek susidaro fotoelektrolizės metu. Visais atvejais efektyviausias antimikrobinis veikimas pasireiškė fotoelektrocheminėmis sąlygomis (25, 26 pav.), kas rodo tokių sistemų perspektyvumą vandens dezinfekcijos srityje.

IŠVADOS

1. Nustatyta, kad 0.5 – 1 μm storio bei plokštelių morfologijos WO_3 dangų atveju (PVR sintezė) fotoelektrocheminio $S_2O_8^{2-}$ bei aktyvių chloro junginių (ClO^- + ClO_2^-) susidarymo 0.5 M H_2SO_4 ir 0.5 M NaCl tirpaluose išeigos pagal fotosrovę yra 35 – 80 % ir 50 – 99 %, o šviesos energijos konversijos į elektros energiją efektyvumas (ABPE) siekia 0.27% ir 0.08%, atitinkamai.
Nustatyta, kad 5 – 10 μm storio, poringų nanostruktūrizuotų WO_3 dangų atveju (VR sintezė) fotoelektrocheminio $S_2O_8^{2-}$ bei aktyvių chloro junginių susidarymo 0.5 M H_2SO_4 ir 0.5 M NaCl tirpaluose išeigos pagal fotosrovę yra 70 – 90 % ir 85 – 100 %, o šviesos energijos konversijos į elektros energiją efektyvumas siekia 3.4% ir 1.0%, atitinkamai.

Tokį rezultatą lemia stipresnė šviesos absorbcija didesnio storio poringuose WO$_3$ sluoksniuose, o taip pat efektyvesnis skylių surišimas, kurį sąlygoja poringa nanostruktūra, užtikrinanti trumpesnį atstumą šviesos generuojamoms skylėms iki elektrodo/elektrolito sandūros.

2. Parodyta, kad specifinė chlorido jonų adsorbcija ant WO$_3$ paviršiaus suteikia jiems kinetinį pranašumą fotoanodinėse reakcijose prieš kitas tirpalo komponentes bei lemia aukštą - iki 100 % aktyvių chloro junginių (ClO$^-$ + ClO$_2^-$) susidarymo išeigą pagal fotosrovę.

3. Pateikta nauja fotoelektrocheminės WO$_3$ elgsenos H$_2$SO$_4$ ir NaCl elektrolituose interpretacija, pagal kurią FEC reakcijos nagrinėjamos kaip elektrodo potencialo įtakojami fotocheminiai procesai, kuriuose kaip tarpiniai junginiai dalyvauja laisvieji radikalai (OH•, Cl•, Cl$_2^{•-}$, SO$_4^-$•). Parodyta, kad H$_2$SO$_4$ tirpale fotoanodinis SO$_4^-$• susidarymas yra labiau termodinamiškai tikėtinas nei vandens molekulių oksidacija iki OH•. Neutraliame NaCl elektrolite termodinaminė OH• susidarymo tikimybė yra didesnė nei Cl•, tačiau dėl specifinės chlorido jonų adsorbcijos ant WO$_3$ paviršiaus vyraujantis procesas yra fotoanodinė Cl$^-$ oksidacija.

4. Reakcijų seka: $Cl^- \xrightarrow{h^+} Cl^• \xrightarrow{Cl^-} Cl_2^{•-} \xrightarrow{e^-} 2Cl^-$ pasiūlyta kaip galimas paviršinės krūvininkų rekombinacijos, vykstančios ant WO$_3$ fotoelektrodų paviršiaus chloridų tirpaluose, mechanizmas.

5. Nustatyta, kad WO$_3$ fotoelektrocheminio aktyvumo mažėjimas fotoelektrolizės metu yra žymesnis 0.5 M H$_2$SO$_4$ tirpale nei 0.5 M NaCl. Padaryta prielaida, kad tai gali būti sąlygojama fotoelektrochemiškai neaktyvių paviršinių peroksovolframatų susidarymu, kuomet W-O-W jungtys yra pažeidžiamos dėl sąveikos su šviesos generuojamomis skylėmis ar SO$_4^-$•/OH• radikalais. Stipri chlorido jonų, o tai pat ir jų fotoanodinės oksidacijos produktų (Cl•, Cl$_2^{•-}$) adsorbcija bei efektyvus skylių surišimas apsaugo WO$_3$ paviršių nuo perokso junginių susidarymo bei užtikrina didesnį fotoelektrodų stabilumą neutraliuose NaCl tirpaluose.

6. Pademonstruotas efektyvus antibakterinis fotoelektrolizės su WO$_3$ fotoanodais poveikis gramteigiamų ir gramneigiamų bakterijų suspensijose neutraliuose chloridiniuose bei sulfatiniuose tirpaluose. Padaryta prielaida, kad stiprų dezinfekcinį veikimą lemia aktyvūs laisvieji radikalai, susidarantys

sąveikaujant šviesos generuojamoms skylėms su tirpalo komponentėmis. Šių tyrimų rezultatai gali būti naudingi, kuriant fotoelektrochemines sistemas pažangiems oksidacijos procesams bei būti pritaikyti vandens dezinfekcijos srityje.

ACKNOWLEDGEMENT

LIST OF PUBLICATIONS AND CONFERENCES

Publications

1. Juodkazytė, J., Petrulevičienė, M., Parvin, M., Šebeka, B., Savickaja, I., Pakštas, V., & Gegeckas, A. "Activity of sol-gel derived nanocrystalline WO3 films in photoelectrochemical generation of reactive chlorine species." Journal of Electroanalytical Chemistry 871 (2020) 114277. DOI:10.1016/j.jelechem.2020.114277.

2. Petruleviciene, M., Juodkazyte, J., Parvin, M., Tereshchenko, A., Ramanavicius, S., Karpicz, R., & Ramanavicius, A. "Tuning the photo-luminescence properties of WO_3 layers by the adjustment of layer formation conditions." *Materials* 13, no. 12 (2020) 2814. DOI: 10.3390/ma13122814.

3. Parvin, M., M. Petrulevičienė, I. Savickaja, B. Šebeka, R. Karpicz, A. Grigucevičienė, R. Ramanauskas, and J. Juodkazytė. "Influence of morphology on photoanodic behaviour of WO_3 films in chloride and sulphate electrolytes." *Electrochimica Acta* 403 (2022) 139710. DOI: 10.1016/j.electacta.2021.139710.

4. Petruleviciene, M., Parvin, M., Savickaja, I., Gece, G., Naujokaitis, A., Pakstas, V., Pilipavicius, J., Gegeckas, A., Gaigalas, G. and Juodkazyte, J. "WO_3 coatings for photoelectrochemical synthesis of persulfate: efficiency, stability and applicability." Journal of Solid State Electrochemistry 26, no.4 (2022) 1021-1035. DOI: 10.1007/s10008-022-05144-8.

Conferences

1. M. Parvin, M. Petrulevičienė, I. Savickaja, B. Šebeka, A. Naujokaitis, V. Pakštas and J. Juodkazytė; Photoelectrochemical activity of sol-gel derived WO_3 films in artificial photosynthesis. 62nd International Conference for Students of Physics and Natural Sciences Open Readings, March 19-22, 2019, Vilnius, Lithuania.

2. M. Parvin, M. Petrulevičienė, I. Savickaja, B. Šebeka, A. Naujokaitis, V. Pakštas and J. Juodkazytė; Photoelectrochemical generation of active chlorine species at sol-gel derived nanostructured WO_3 electrode. Lithuania-Poland Workshop on Physics and Technology, September 26-27, 2019, Vilnius, Lithuania.

3. M. Parvin, M. Petrulevičienė, I. Savickaja, B. Šebeka, A. Naujokaitis, V. Pakštas and J. Juodkazytė; Effect of reductant on photoelectrochemical activity of sol-gel derived nanostructured WO_3 films. 9th Conference of Doctoral Students and Young Researchers FizTech 2019, October 23 – 24, 2019, Vilnius, Lithuania.

4. M. Parvin, M. Petrulevičienė, I. Savickaja, B. Šebeka, A. Naujokaitis, V. Pakštas and J. Juodkazytė. Production of Active Chlorine Species via Photoelectrochemical Solar Energy Conversion Using Sol-Gel Prepared Nanostructured WO_3 Photoanode. Advanced materials and technologies 2020, 22nd International Conference-School, August 24–28, 2020, Palanga, Lithuania.

5. M. Parvin, M. Petrulevičienė, I. Savickaja, B. Šebeka, A. Naujokaitis, V. Pakštas and J. Juodkazytė; "Tuning of photoelectrochemical activity of nanostructured WO_3 films through modification of sol-gel synthesis procedure" International Society of Electrochemistry 71st ISE Belgrade Online Meeting, August 30 - September 4, 2020 Belgrade, Serbia.

6. M. Parvin, M. Petrulevičienė, I. Savickaja, B. Šebeka, A. Naujokaitis, V. Pakštas and J. Juodkazytė. Optimization of sol-gel synthesis of WO_3 films towards efficient photoelectrochemical performance. 10th Conference of Doctoral Students and Young Researchers FizTech 2020, October 22 –23, 2020, Vilnius, Lithuania.

7. M. Parvin, M. Petrulevičienė, I. Savickaja, B. Šebeka, A. Naujokaitis, V. Pakštas, A. Gegeckas, J. Virkutis, J. Juodkazytė. Bacterial inactivation using WO_3 photoanode for production of reactive chlorine species in situ" "NANOSTRUCTURED BIOCERAMIC MATERIALS 2020", Vilnius University, December 1 – 3, 2020, Vilnius, Lithuania.

8. M. Parvin, M. Petrulevičienė, I. Savickaja, B. Šebeka, A. Naujokaitis, V. Pakštas, R. Karpicz, J. Juodkazytė; Investigation of Competition Between Photo-Oxidation of Water and Anions on WO_3 Photoanode in Chloride and Sulfate Electrolytes. Advanced Materials and Technologies, 23rd International Conference - School, August 23-27, 2021, Palanga, Lithuania.

9. M. Parvin, M. Petrulevičienė, I. Savickaja, B. Šebeka, A. Naujokaitis, V. Pakštas, R. Karpicz, J. Juodkazytė; Investigation of Charge Transfer Kinetics of Sol-Gel Prepared WO_3 Photoanode in Different Electrolytes. 72nd Annual Metting of the International Society of Electrochemistry, August 29 - September 3, 2021, Jeju Island, Korea.

10. M. Parvin, M. Petrulevičienė, I. Savickaja, J. Juodkazytė; Synthesis of Highly porous photoactive WO_3 for generation of ClO-. Chemistry and Chemical Technology 2021, September 24, 2021, Vilnius, Lithuania.

11. M. Parvin, M. Petrulevičienė, I. Savickaja, J. Juodkazytė; Generation of reactive chlorine species on highly porous thick WO_3 photoanode.11th Conference of Doctoral Students and Young Researchers FizTech 2021, October 20 – 21, 2021, Vilnius, Lithuania.

12. M. Parvin, M. Petrulevičienė, I. Savickaja, A. Naujokaitis, V. Pakštas and J. Juodkazytė; WO_3 photoanode for advanced oxidation processes.65th international conference for students of Physics and Natural sciences Open Reading, March 15-18, 2022, Vilnius, Lithuania

COPIES OF PUBLICATIONS

1ˢᵗ publication

Activity of sol-gel derived nanocrystalline WO$_3$ films in photoelectrochemical generation of reactive chlorine species

Juodkazytė, J., Petrulevičienė, M., **Parvin, M.**, Šebeka, B., Savickaja, I., Pakštas, V., Naujokaitis, A., Virkutis, J. and Gegeckas, A.,

Activity of sol-gel derived nanocrystalline WO₃ films in photoelectrochemical generation of reactive chlorine species

Jurga Juodkazyt [a,], Milda Petrulevi ien [a], Maliha Parvin [a], Benjaminas Šebeka [a], Irena Savickaja [a], Vidas Pakštas [a], Arnas Naujokaitis [a], Jonas Virkutis [b], Audrius Gegeckas [b]

[a] Center for Physical Sciences and Technology, Saul tekio av. 3, LT-10257 Vilnius, Lithuania
[b] Life Sciences Center, Vilnius University, Saul tekio av. 7, LT-10257 Vilnius, Lithuania

ARTICLE INFO

ABSTRACT

Conventional chlor-alkali method used for production of chlorine gas and chlorine-based disinfectants is among the most energy-intensive processes in chemical industry, therefore, more sustainable alternatives with lower carbon footprint are sought. Photoelectrochemical (PEC) generation of reactive chlorine species (Cl_2, $HClO$, ClO^-) is a promising technology in the area of water disinfection and purification, as it combines the advantages of (i) using the renewable solar energy; (ii) possibility to produce disinfectants on-site and on-demand and (iii) eliminates the need for sophisticated infrastructure for storage and handling of chlorine species.
In the present study nanocrystalline tungsten (VI) oxide layers were formed on conducting glass substrate using simple sol-gel synthesis technique and polyethylene glycol as a structure-directing agent. It is shown that addition of PEG in moderate amounts favours formation of the structure of interconnected nanocrystalline particles, which ensures effective separation and transport of photogenerated charge carriers and, therefore, is crucial for the photoelectrochemical activity of the films. This is corroborated by the analysis of SEM and XRD data, revealing the influence of polyethylene glycol from the initial stages of WO₃ phase crystallization. Faradaic efficiency of photoelectrochemical hypochlorite formation is shown to be about 30%, and antimicrobial effect of PEC chlorination with WO₃ photoanodes is demonstrated on Gram-positive *Bacillus* sp. and Gram-negative *E.coli* C41(DE3) bacteria.

1. Introduction

The global demand for chlorine-based disinfectants is increasing continually due to growing efforts to prevent the spread of infectious diseases. In Japan alone more than 900 thousands tons of sodium hypochlorite are produced annually and this is about 1/20 of the total consumption of this chemical in the world [1]. The main area of application of hypochlorites is industrial water disinfection and sanitization. Traditionally, sodium hyplochlorite is produced by passing of electrolytically formed chlorine gas into NaOH solution. In addition to hazards related with Cl_2 handling and storage, the production of Cl_2 is the second highest energy-consuming technology among the electrolytic processes after aluminum manufacturing [2], thus the CO_2 emission factor related with production of these chemicals by conventional chlor-alkali process is very high. It has been demonstrated recently that many valuable chemicals, especially oxidants such as $HClO$, H_2O_2, $H_2S_2O_8$, etc., can be produced photo-electrochemically using solar energy and light-sensitive semiconductor photoelectrodes [3,4]. Such processes can be attributed to the category of artificial photosynthesis, as they convert the energy of light into the

chemical energy. Photoelectrochemical (PEC) generation of reactive chlorine-species (RCS), i.e. Cl_2, $HClO$, ClO, is a process of high practical interest, because it offers the possibility to generate the disinfectant chemicals on-demand and on-site. To make the process even more sustainable, it would be beneficial to exploit seawater as natural electrolyte and the Earth's most abundant natural resource. Thus it is important to find photoelectrochemical system which would ensure efficient generation of RCS from chloride solutions. In this regard WO₃ photoanodes are of particular interest as it is well-known that the product of photoanodic reaction depends largely on the composition of the electrolyte used [5–8]. Moreover, tungsten trioxide is attractive material due to its relatively low cost and ability to absorb visible light (band gap of 2.5–2.8 eV [9]) contrary to TiO₂, which has also been explored for PEC degradation of pollutants [10]. Majority of the studies reported in scientific literature so far were devoted to investigations of water splitting activity of tungsten (VI) oxide photoanodes and have been reviewed recently in [9]. There are not many papers addressing the performance of WO₃ photoanodes in chloride-containing solutions and most of them were published quite recently [11–18]. It has been shown that in the presence of chlorides, photoanodic

Corresponding author.
E-mail address: jurga.juodkazyte@ftmc.lt. (J. Juodkazyt).

oxidation of Cl^- anions prevails over the oxidation of water molecules and competition between these processes is strongly influenced by electrolyte composition and pH [6,11,12]. In their recent series of papers Zhou with co-authors [15–17,19] have demonstrated how efficiently the property of WO_3 films to form RCS can be applied in solar-driven wastewater treatment. Choi et al. [20] revealed that the efficiency of photoelectrochemical chlorination in degradation of organic compounds is much higher compared to purely photochemical (no electrolysis) or electrochemical (no illumination) chlorination processes. It was also shown that the crucial role in these reactions is played by chlorine radicals ($Cl^\bullet$, Cl_2^-) which form on the surface of WO_3 photoanode as a result of interaction between photogenerated holes and Cl^- ions. Coupled with production of H_2 on cathode, as reported recently in [11], PEC chlorination could offer a sustainable method for water disinfection or wastewater purification. Thus, it is obvious that this area of research is gaining momentum and new data on efficient photoelectrochemical systems as well as proper understanding of the mechanism of the processes involved are of particular interest.

In this study photoelectrochemically active WO_3 films were synthesized using simple sol-gel technique and polyethylene glycol (PEG) as an additive. The photoelectrochemical performance of tungsten (VI) oxide films was investigated in acid and neutral solutions in the absence and presence of chloride. Faradaic efficiency of photoelectrochemical hypochlorite generation was evaluated. Antimicrobial effect of PEC chlorination with WO_3 photoanodes was tested in the suspensions of Gram-positive *Bacillus* sp. and Gram-negative *E.coli* C41(DE3) bacteria.

2. Experimental

2.1. Formation of tungsten oxide layers

WO_3 thin films on fluorinedoped tin oxide (FTO) - coated glass substrate were prepared using aqueous sol-gel synthesis method and drop casting technique. Synthesis scheme is presented in Fig. 1. In the sol-gel process, 3 g of sodium tungstate ($Na_2WO_4 \cdot 2H_2O$) (Carl Roth) were dissolved in 100 cm^3 of deionized water and 2.5 cm^3 of concentrated HNO_3 was added by small portions under continuous stirring to reach pH < 1. The solution was stirred for 4 h at 50 °C. Next, solution was filtered and washed few times until pH of filtrate was about 5. Pale yellow tungstic acid precipitates formed. Afterwards the precipitates were dissolved in 60 cm^3 of H_2O_2 and H_2O mixture (volume ratio 1:1) under continuous stirring for 24 h at 50 °C. Then solution was left to evaporate at 80 °C for 12 h and yellow peroxytungstic acid (PTA) powder was obtained. Finally, PTA powder

was dissolved in water and ethanol solution (volume ratio 1:6), what resulted in formation of white-colored sol-gel solution. Polyethylene glycol (PEG)-modified samples were prepared by the same synthesis scheme by means of adding different amounts of PEG 300 (Chempur) to final sol-gel. PEG to PTA mass ratios investigated were 1:5, 1:10 and 1:15. Prepared sol-gel was deposited on FTO (5–7 Ω/sq) coated glass substrates (1 × 2.5 cm^2) by drop casting technique. Prior to drop casting substrates were sequentially washed with acetone, ethanol and deionized water in ultrasonic bath for 15 min per wash [21,22]. After the coating procedure samples were annealed at T_{anneal} = 300 °C, 400 °C or 500 °C for 2 h with heating rate of 5 °C min^{-1}. For the sake of brevity, WO_3 samples formed from PTA sol-gel without PEG or with different PEG to PTA ratios are further labelled as PTA(w/o PEG), PEG:PTA(1:5), PEG:PTA(1:10) and PEG: PTA(1:15), respectively.

2.2. Characterization of oxide layers

2.2.1. Scanning electron microscopy and X-ray diffraction measurements

The surface morphology of tungsten oxide layers was investigated using Helios NanoLab dual beam workstation equipped with X-Max 20 mm^2 energy dispersion spectrometer (Oxford Instruments).

XRD patterns of the films were measured using an X-ray diffractometer SmartLab (Rigaku) equipped with 9 kW rotating Cu anode X-ray tube. Grazing incidence (GIXRD) method was used in 2θ range 20–70°. Angle between parallel beam of X-rays and a specimen surface (ω angle) was adjusted to 0.5°. Phase identification was performed using software package PDXL (Rigaku) and Crystallography Open Database (COD). Evaluation of crystallite size in sol-gel derived WO_3 films was performed using Halder–Wagner method.

2.2.2. Photoelectrochemical measurements

Voltammetric measurements were performed using three-electrode cell and potentiostat/galvanostat AUTOLAB 302. FTO-supported tungsten oxide films were used as working electrodes. Only the samples annealed at T_{anneal} = 500 °C were used in PEC experiments. Silver chloride electrode with saturated KCl solution (Ag/AgCl/sat. KCl) and Pt wire were used as reference and counter electrodes, respectively. The surface of working electrodes was illuminated with high intensity discharge Xe-lamp with 6000 K spectrum and calibrated with a silicon diode to simulate AM 1.5 illumination with power density $P \approx 100$ mW cm^{-2} at the sample surface. The same light source was used in all the experiments described further. Photoelectrochemical behavior of WO_3 films was investigated in acid and neutral sulphate solutions in absence and presence of chloride ions. All solutions used in the experiments were prepared from reagents of analytical
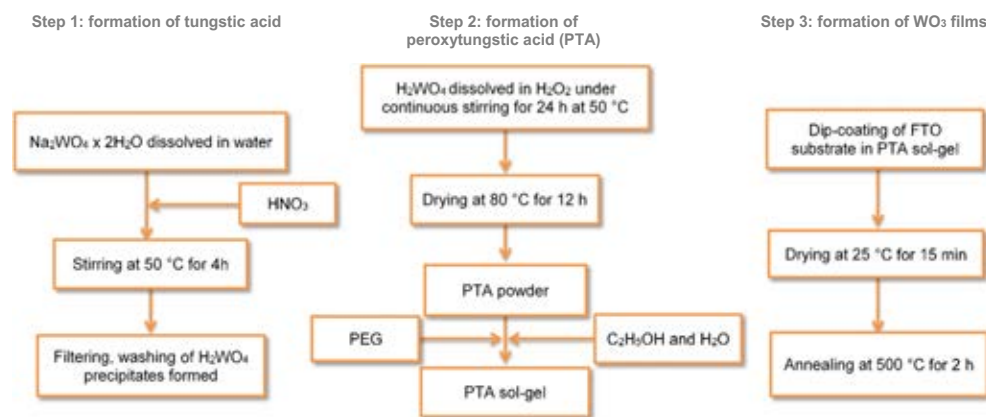

Step 1: formation of tungstic acid   **Step 2: formation of peroxytungstic acid (PTA)**   **Step 3: formation of WO_3 films**

Fig. 1. Schematic representation of sol-gel synthesis route of WO_3 films.

grade and deionized water. Measurements were performed at room temperature. Current density values were calculated based on the geometric area of the working electrode.

2.3. Quantitative determination of amount of hypochlorite formed during photoelectrolysis

To quantitatively evaluate the amount of hypochlorite formed during photoelectrolysis with WO_3 electrodes the experiments were performed in a two-electrode cell with a fritted glass separator between the anode and cathode compartments and the solution of 0.5 M NaCl. PEG:PTA(1:10) samples (T_{anneal} = 500 °C) were used as photoanodes and Pt plate (1×1 cm^2) was used as cathode. Photoelectrolysis was performed for certain periods of time at cell voltage, U_{cell}, of 1.6 V. After that the electrolyte from the anodic compartment of the cell was subjected to iodometric titration to determine the amount, m_{exp} (g), of photoelectrochemically formed ClO^- in the solution. Three assays of anolyte were taken for titration each time and the average m_{exp} was evaluated. Then the values of m_{exp} were compared with the theoretical ones, m_{theor}, calculated according to Faraday law of electrolysis, on the basis of electric charge, Q (C), passed through the cell during photoelectrolysis. The Faradaic efficiency of the photoelectrochemical ClO^- generation was evaluated as ratio m_{exp}/m_{theor}.

2.4. Evaluation of antimicrobial effect of PEC chlorination with WO_3 photoanodes

Bacillus sp. and *E.coli* C41(DE3) were selected as the biological objects to evaluate the antimicrobial effect of photoelectrochemical chlorination with synthesized WO_3 photoelectrodes. Bacterial strains were cultured in Lysogeny broth at 37 °C for 6 h with shaking 180 rpm. The cells were harvested by centrifugation at 3000 rpm for 15 min, washed twice with 0.9% NaCl and then suspended in 50 cm^3 of 0.5 M NaCl. Samples of 10 cm^3 were taken for bacterial disinfection experiments, which were conducted under photoelectrochemical (electrolysis under illumination), electrolytic (electrolysis without illumination) and photolytic (illumination without electrolysis) conditions. The experiments were performed in a two-compartment quartz cell. The compartments were separated with Millipore membrane filter (0.22 μm pore size). Pt plate (1×1 cm^2) served as cathode and WO_3 samples PEG:PTA(1:10), T_{anneal} = 500 °C, were used as photoanodes. The cathodic compartment of the cell was filled with pure 0.5 M NaCl solution, whereas the anodic one was filled with suspension of cells in 0.5 M NaCl. The photoelectrolysis was performed at cell voltage, U_{cell}, of 1.6 V and $P \approx 100$ mW cm^{-2}. The same voltage with no illumination (P = 0 mW cm^{-2}, U_{cell} = 1.6 V) was used in the electrolytic disinfection experiments, whereas in the case of photolytic disinfection just illumination without external bias was applied ($P \approx 100$ mW cm^{-2}, U_{cell} = 0 V). In the photolytic setup both electrodes were kept immersed in the solution to make the conditions of all three experiments as similar as possible.

After each experiment, 1.5 cm^3 aliquots were acquired for the analysis of bacterial survival by doing serial dilutions with sterile physiological solution. From that, 0.1 cm^3 of the diluted sample was spread on plate count agar plates which were incubated at 37 °C for 16 h. The formed colonies were counted before and after the disinfection experiments.

3. Results and discussion

3.1. Influence of synthesis conditions on crystallinity, phase composition and morphology of WO_3 films

Synthesis conditions (additives, annealing temperature, etc.) are known to strongly influence crystallization, defect states (bulk and surface) and band gap of WO_3. Among various crystal structures, the monoclinic structure of tungsten (VI) oxide is highly stable and was found to be more efficient in photoelectrochemical applications. Crystal facet also affects photoelectrochemical activity of tungsten oxide, because overpotential

required for the photooxidation process on the tungsten oxide surface depends on the crystal facet orientation. On the basis of density functional theory calculations it has been shown that (200), (020) and (002) facets of WO_3 require 1.04, 1.10, and 1.05 V overpotential, respectively, for photooxidation of water molecules [23]. Xie et al. [24] and Guo et al. [25] have reported that (002) crystal facet was possibly more favorable in absorption and degradation of pollutants than preferential orientation of (020) planes. In the earlier reports on the use of PEG in the sol-gel synthesis of WO_3 it was shown that this organic surfactant modulates the morphology and structure of tungsten oxide films [11,26–32] and affects electrochromic [26,27,31–33], biosensing [28] and photoelectrochemical properties [29,30,32,34–37] of WO_3. Depending on molecular mass of PEG and synthesis conditions, various nanoarchitectures of WO_3 with different degree of porosity can be obtained. It should be pointed out here that presentation of XRD and SEM results in this section is limited to samples with PEG to PTA ratio 1:10, because this ratio was found to be the most efficient from the photoelectrochemical point of view, as will be shown in Section 3.2.

X-ray diffractograms of tungsten oxide samples PTA(w/o PEG) and PEG:PTA(1:10) annealed at different temperatures are shown in Figs. S1 and S2, respectively. Coatings annealed at 300 °C are amorphous and only small peaks attributed to FTO substrate can be observed (curves 1 in Figs. S1 and S2). Spectra of samples PTA(w/o PEG) (Fig. S1) annealed at 400 °C and 500 °C exhibit clusters of three peaks at 2θ = 23.13°, 23.56°, 24.33° and two peaks at 2θ = 33,29°, 34.07° (marked an with an asterisk), which correspond to the (002), (020) (200) and (022), (202) crystallographic planes of monoclinic tungsten oxide, respectively, in accordance with PDF no. 96–210-6383 of the Crystallography Open Database (COD). Intensity and ratio of peaks changes with increase in T_{anneal}. The dominant crystallographic plane of sample annealed at 500 °C is (200). Peaks of lower intensity at 2θ = 28.40°, 28.69°, 35.61°,41.67°, 44.28°, 45.74°, 47.24°, 48.35°, 49.89°, 50.62°, 53.63°, 54.25°, 54.88°, 55.86° correspond to monoclinic tungsten oxide. Additional phases of $W_{17}O_{47}$ (marked with diamond) and tin oxide (marked with circle), represented by very low intensity peaks, were also identified.

XRD spectra of WO_3 samples PEG:PTA(1:10) (Fig. S2) annealed at the same temperatures are analogous to those described above, but it is noteworthy, that the crystallinity of the coating annealed at 400 °C was higher in the absence of PEG, which means that this additive retards the crystallization of tungsten oxide films as will be discussed further.

In Fig. 2 XRD spectra of samples PTA(w/o PEG) and PEG:PTA(1:10) with T_{anneal} = 500 °C are compared. One can see that essentially the spectra are similar, just the intensity ratio of three main peaks at 2θ = 23.13°, 23.56°, 24.33° corresponding to (002), (020) and (200) crystallographic

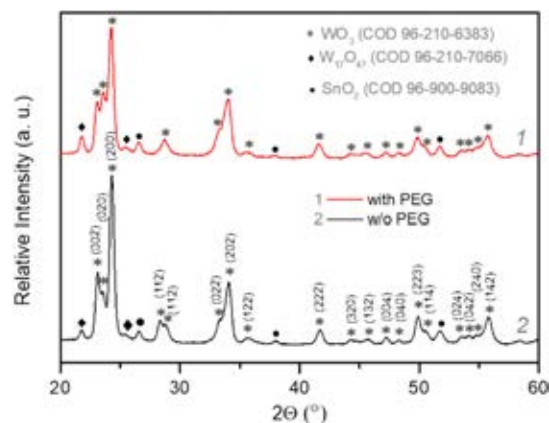**Fig. 2.** XRD patterns of FTO/WO_3 samples PEG:PTA(1:10) (*1*) and PTA(w/o PEG) (*2*), T_{anneal} = 500 °C.

facets differs. In both samples the dominant crystallographic facet is (200), however intensity of (002) and (020) facets differs.

Surface morphology of tungsten oxide coatings was investigated using scanning electron microscopy (SEM). In Fig. 3 SEM images of the samples PTA(w/o PEG) (a, b, c) and PEG:PTA(1:10) (d, e, f) annealed at 300 °C (a, d), 400 °C (b, e) and 500 °C (c, f) are presented. In the coating PTA(w/o PEG), T_{anneal} = 300 °C, (Fig. 3a) agglomerates of flakes of approximately 400 nm size are observed. Sample PTA(w/o PEG) with T_{anneal} = 400 °C (Fig. 3b), has higher crystallinity (Fig. S1) and particles of different size (50–400 nm) can be seen in the image. Surface is rough, uneven, with pores and cracks of various size, which are highly undesirable from the view point of diffusion of photogenerated charge carriers. Annealing at 500 °C (Fig. 3c) leads to higher degree of crystallization and merging of nanoparticles to form 400 nm-sized plates with less pores in the structure. It is obvious that coating is uneven and there are no clear boundaries between nanoplates and nanosheets. Mixture of differently shaped nanoplates and nanosheets is observed without certain growth direction.

Effect of T_{anneal} on the morphology of samples PEG:PTA(1:10) is revealed in Figs.3d–f. Agglomerates of nanoparticles can be seen in the image of WO$_3$ film annealed at 300 °C (Fig. 3d). As T_{anneal} increases, formation, growth and expansion of nanosheets takes place as can be seen from Fig. 3e. Coating is uneven, rough with small cracks between nanosheets. PEG:PTA(1:10) film annealed at 500 °C looks different: formation of submicrometer-sized sheets can be seen with less amount of cracks and high degree of crystallinity, as can be judged from XRD results (Fig. S2).

The main difference between the surface morphology of WO$_3$ films synthesized with and without PEG is the presence of fine-grained subnanostructure, which is seen in the SEM images of the samples PEG:PTA(1:10) (Fig. 3d–f). These nano-grains are especially clearly visible in the WO$_3$ films annealed at 300 °C (Fig. 3d). With increase in T_{anneal}, this subnanostructure becomes less pronounced because of coalescence of nanoparticles and formation of larger microstructural units.

These observations are consistent with the results of crystallite size evaluation from XRD spectra of WO$_3$ coatings. The summary of results is presented in Table. 1. The largest, more than tenfold difference (8.7 nm vs 0.69 nm) between the crystallite size is found in the coatings annealed at 300 °C, implying that PEG limits the growth crystallites from the initial stages of tungsten (VI) oxide crystallization. Increase in T_{anneal} from 300 °C to 400 °C marks very significant change in crystallite size: in the case of PTA(w/o PEG) films the crystallite size increases almost twice (from

Table 1
Effect of PEG and annealing temperature on crystallite size of sol-gel derived WO$_3$ films.

T_{anneal}	Crystallite size, nm	
	PTA(w/o PEG)	PEG:PTA(1:10)
300 °C	8.7 ± 0.17	0.69 ± 0.016
400 °C	16.8 ± 0.24	13.6 ± 0.3
500 °C	17.5 ± 0.21	14.5 ± 0.13

8.7 nm to 16.8 nm), while in the PEG:PTA(1:10) films this increase is twentyfold (from 0.69 nm to 13.6 nm). This means that in the range between 300 °C and 400 °C the process of crystallization in PEG-doped WO$_3$ proceeds significantly faster. Most likely, this is related with elimination of organic content. Further growth of crystallites in the temperature range between 400 °C and 500 °C is negligible, though certain rearrangement in crystalline structure, especially in PEG-doped tungsten (VI) oxide films, is evident (cf. spectra 2 and 3 in Figs.S1, S2). After annealing at 500 °C the size of crystallites in PEG-doped WO$_3$ remains smaller and is about 80% of crystallite dimensions found in PEG-free films. As will be shown further, these differences in crystallization process were found to have crucial effect on the photoelectrochemical activity of sol-gel derived WO$_3$ films. Since complete crystallization of PEG-doped WO$_3$ samples was achieved after annealing at 500 °C, only the films annealed at this temperature were subjected to further PEC investigations.

3.2. Photoelectrochemical performance of WO$_3$ films

Photoelectrochemical performance of WO$_3$ samples synthesized without and with different amounts of PEG was tested in acid and neutral sulphate solutions in the absence and presence of chloride ions. Fig. 4 illustrates voltammetric behavior of the samples PTA(w/o PEG), PEG:PTA (1:5), PEG:PTA(1:10) and PEG:PTA(1:15) in dark. One can see that all tested specimens demonstrate typical response of tungsten (VI) oxide electrodes with symmetric cathodic and anodic peaks at $E < 0.4$ V, which reflect reversible processes of WO$_3$ reduction to lower oxides and their subsequent oxidation back to WO$_3$ [38]. Scanning of the electrode potential to more negative E values could lead to reduction of oxide layer to metallic tungsten. Another distinct feature observed in all cyclic voltammograms (CVs) in Fig. 4 is the increase of anodic current at $E > 1.6$ V or $E > 1.2$ V
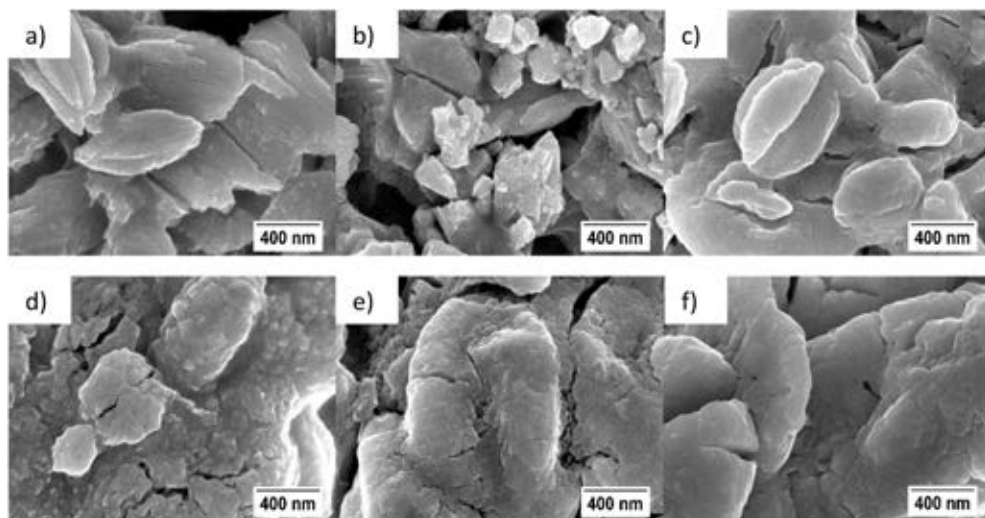

Fig. 3. Top-view SEM images of WO$_3$ thin films PTA(w/o PEG) (a, b, c) and PEG:PTA(1:10) (d, e, f) annealed at 300 °C (a, d), 400 °C (b, e) and 500 °C (c, f).
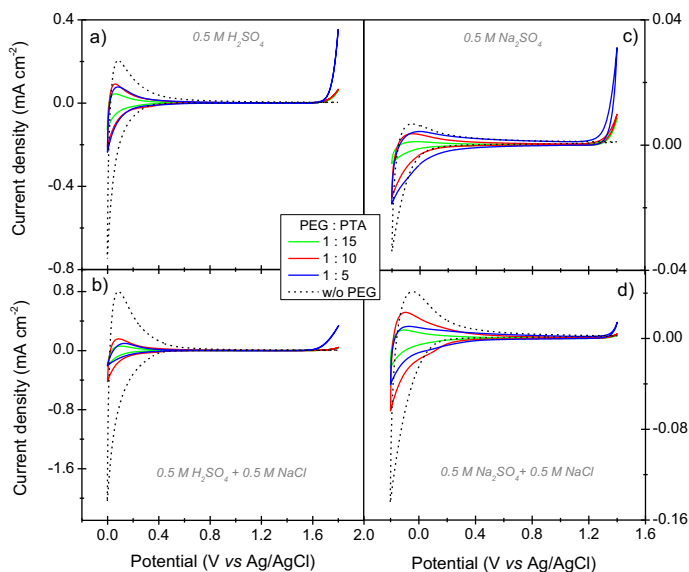
Fig. 4. Cyclic voltammograms of FTO/WO$_3$ samples PTA(w/o PEG), PEG:PTA(1:5), PEG:PTA(1:10) and PEG:PTA(1:15), T_{anneal} = 500 °C, recorded in the solutions of 0.5 M H$_2$SO$_4$ (a), 0.5 M H$_2$SO$_4$ + 0.5 M NaCl (b), 0.5 M Na$_2$SO$_4$ (c) and 0.5 M Na$_2$SO$_4$ + 0.5 M NaCl (d) in dark; potential scan rate 50 mV s^{-1}.

in acidic and neutral medium, respectively. The fact that the onset of this process is observed at the same potential values irrespective of the presence/absence of chloride (compare Fig. 4 a with b and c with d) as well as the shift of this reaction towards more negative potentials with increasing solution pH (Fig. 4 a, b vs c, d) suggest that it should be attributed to the beginning of oxygen evolution reaction (OER), because the potential of chlorine evolution reaction (ClER) is pH-independent ($E^0_{Cl_2/2Cl^-}$ = 1.16 V (vs. Ag/AgCl)).

WO$_3$ sample PTA(w/o PEG) shows the highest currents in the oxide reduction/formation region ($E < 0.4$ V) in all the solutions investigated. Comparison of voltammetric behavior of WO$_3$ electrodes prepared with different amounts of PEG reveals that the lowest currents are observed in the case of PEG:PTA(1:15), where the amount of PEG is the smallest. These differences should most likely be attributed to differences in electrochemically active surface area. The responses of samples PEG:PTA(1:10) and PEG:PTA (1:5) are quite similar especially in the absence of chloride (Fig. 4 a and c).
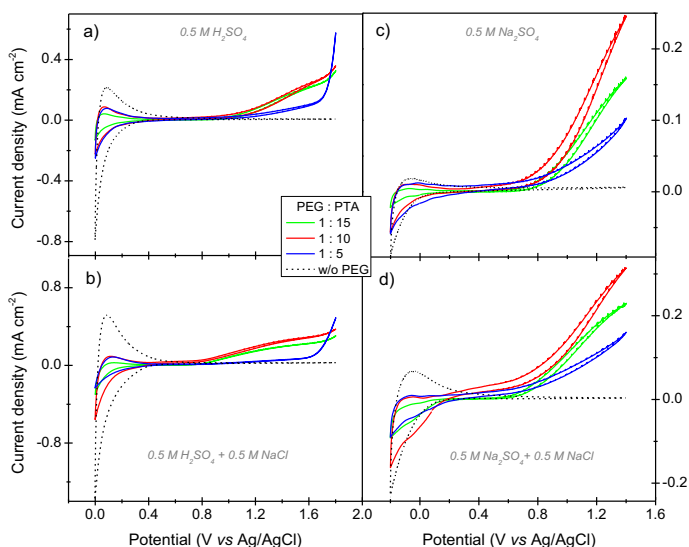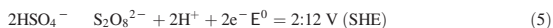

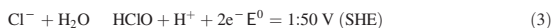**Fig. 5.** Cyclic voltammograms of FTO/WO$_3$ samples PTA(w/o PEG), PEG:PTA(1:5), PEG:PTA(1:10), PEG:PTA(1:15), T = 500 °C, recorded in the solutions of 0.5 M H$_2$SO$_4$ (a), 0.5 M H$_2$SO$_4$ + 0.5 M NaCl (b), 0.5 M Na$_2$SO$_4$ (c) and 0.5 M Na$_2$SO$_4$ + 0.5 M NaCl (d) under illumination ($P \approx 100$ mW cm^{-2}); potential scan rate 50 mV s^{-1}.

Though in the presence of chloride sample PEG:PTA(1:10) outperforms PEG:PTA(1:5) in the range of oxide reduction/formation region ($E < 0.4$ V, Fig. 4 b and d), the sample PEG:PTA(1:5) exhibits the highest activity towards OER in all the solutions studied. It is also evident that the highest potential for the onset of oxygen evolution reaction is required in the case of WO$_3$ coating synthesized without addition of polyethylene glycol, because on the surface of PTA(w/o PEG) OER does not even start in the E range investigated. This might be attributed to different proportions of (200), (020) and (002) facets exposed to solution as discussed above.

Cyclic voltammograms of the samples PTA(w/o PEG), PEG:PTA(1:5), PEG:PTA(1:10) and PEG:PTA(1:15) recorded in the same solutions under illumination are compared in Fig. 5. All electrodes prepared using PEG as an additive were photoelectrochemically active as reflected by the increase of photoanodic current at $E > 0.8$ V, contrary to the specimen PTA(w/o PEG). The photoelectrochemical activity of the latter electrode was negligible irrespective of solution pH and absence/presence of chloride. The sample PEG:PTA(1:5), in which the amount of PEG was the largest, exhibited the lowest photocurrents in all the solutions tested, implying that excess of this additive is deleterious for photoelectrochemical performance of WO$_3$ films. It is noteworthy that steep increase in anodic current seen in Fig. 5 a and b at $E > 1.6$ V was also observed under dark conditions and is not related with photoelectrochemical activity of the samples. Comparison of the photocurrents of the other two electrodes shows that the PEG:PTA(1:10) with intermediate amount of PEG outperforms the sample PEG:PTA(1:15) with the lowest PEG content, in all the solutions except for 0.5 M H$_2$SO$_4$, where the response of both electrodes at $E > 0.8$ V is almost identical. For greater clarity, CVs of the most active sample PEG:PTA(1:10) recorded in dark and under illumination in all the solutions investigated are shown in Fig. S3. Another important observation is that, contrary to the results obtained under dark conditions, addition of chloride clearly effects the photoelectrochemical response of WO$_3$ films by shifting the onset of photocurrent towards more negative E values. This can be explicitly seen in Fig. 6, where the voltammograms of the sample PEG:PTA(1:10) recorded under illumination in acidic (Fig. 6a) and neutral medium (Fig. 6b) in the absence and presence of chloride are compared. The fact that onset of photocurrent shifts to lower E values means that presence of chlorides gives rise to photoinduced oxidation reaction, which is more facile than the one taking place in chloride-free sulphate solutions. In accordance with the above discussed literature data, this can be the photoelectrochemical oxidation of Cl$^-$ ions to reactive chlorine species (Cl$_2$, HClO, ClO$^-$). Considering the below listed values of standard redox potentials of the solution species, which can be oxidized by holes photogenerated in tungsten (VI) oxide, Cl$^-$ ions have the

second lowest E^0 after oxidation of H$_2$O to O$_2$ [38]:

$$2H_2O \quad O_2 + 4H^+ + 4e^- \ E^0 = 1{:}23 \ V \ (SHE) \tag{1}$$

$$2Cl^- \quad Cl_2 + 2e^- \ E^0 = 1{:}39 \ V \ (SHE) \tag{2}$$

$$Cl^- + H_2O \quad HClO + H^+ + 2e^- \ E^0 = 1{:}50 \ V \ (SHE) \tag{3}$$

$$2H_2O \quad H_2O_2 + 2H^+ + 2e^- \ E^0 = 1{:}77 \ V \ (SHE) \tag{4}$$

$$2HSO_4^- \quad S_2O_8^{2-} + 2H^+ + 2e^- \ E^0 = 2{:}12 \ V \ (SHE) \tag{5}$$

It is well known that due to complexity of the mechanism related with the transfer of 4 electrons, the oxidation of water to molecular oxygen (Eq. (1)) proceeds at an overpotential, which in the case of the best known OER electrocatalyst, IrO$_x$, is >0.3 V [39]. Thus oxidation of Cl$^-$ ions turns to be favoured kinetically over OER, especially in acidic medium [40]. Therefore it is reasonable to assume that photoanodic process observed in chloride containing solutions is related with oxidation of chloride ions by photogenerated holes. Eq. (3) represents direct electrochemical oxidation of Cl$^-$ ions to hypochlorous acid, however formation of HClO is more likely to proceed via chemical disproportionation reaction of electrochemically produced chlorine gas (Eq. (1)) in water [41]:

$$Cl_2 + H_2O \quad HClO + H^+ + Cl^- \tag{6}$$

The distribution of RCS formed in the photoanodic reaction depends on solution pH [38]. In acidic medium the main product is Cl$_2$ (Eq. (2)), which can escape from the solution, whereas in neutral medium formation of HClO/ClO$^-$ prevails. Hypochlorite ions accumulate in solution in the vicinity of photoelectrode surface and can be reduced during negative-going scan. The increase in cathodic current at $E < 0.2$ V in the CV of sample PEG:PTA(1:10) recorded in the solution of 0.5 M Na$_2$SO$_4$ + 0.5 M NaCl under illumination (Fig. 6b) should most likely be attributed to the reduction of photoelectrochemically generated RCS. Results of quantitative determination of the amount of photoelectrochemically formed hypochlorite are presented in the next section.

Thus it is evident that addition of polyethylene glycol in the sol-gel synthesis of WO$_3$ films described herein had critical effect on the photoelectrochemical activity of the deposits. Most likely, PEG acted as a structure-directing agent, which adsorbed on the surface of tungsten oxide colloids and restricted the growth of WO$_3$ crystallites to a particular direction, facilitating the formation of a structure of interconnected
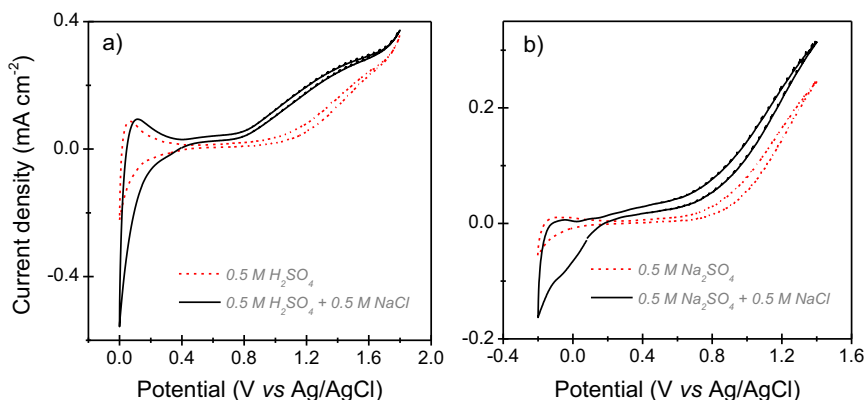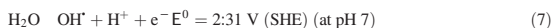

Fig. 6. Cyclic voltammograms of FTO/WO$_3$ sample PEG:PTA(1:10), $T_{anneal} = 500$ °C, in the solutions of a) 0.5 M H$_2$SO$_4$ w/o and with 0.5 M NaCl; b) 0.5 M Na$_2$SO$_4$ w/o and with 0.5 M NaCl under illumination ($P \approx 100$ mW cm^{-2}); potential scan rate 50 mV s^{-1}.

nanoparticles (see Fig. 3d). Increase in annealing temperature improves the crystallinity and contact between the nanoparticles (Fig. 3e), which, in turn, results in longer lifetimes of photogenerated charge carriers and easier hole diffusion. Under conditions investigated, the sample PEG:PTA(1:10), prepared with intermediate amount of polyethylene glycol, demonstrated the highest photoelectrochemical activity, which was especially enhanced in the presence of chlorides (Fig. 6). Most likely, lower concentration of PEG (1:15) was too small to influence the WO_3 crystallization process significantly, whereas the higher one (1:5) was detrimental for the formation of optimal structure of interconnected nanoparticles. These results are consistent with literature data showing that addition of PEG as a surfactant in sol-gel synthesis of tungsten (VI) oxide is beneficial for the formation of the nanocrystalline structure which is of essential importance for the photoelectrochemical performance of the films [11,34–37,42].

3.3. Evaluation of current efficiency of photoelectrochemical hypochlorite formation

In order to quantify the efficiency of photoelectrochemical generation of RCS, photoelectrolysis was performed with samples PEG:PTA(1:10) (T_{anneal} = 500 °C) in a two-electrode setup and solution of 0.5 M NaCl as described in the Experimental Section 2.3. Sulphate-free solution of NaCl was used in these measurements in order to avoid possible photoanodic oxidation of SO_4^{2-} to $S_2O_8^{2-}$ on the surface of WO_3 electrode [3], what could interfere with the determination of hypochlorite. At cell voltage of 1.6 V the dark current was negligible ($<10~\mu A$), as can be seen from the comparison of chronoamperograms in dark and under illumination (Fig. 7a). Therefore, under conditions of our study any possible contributions from other electrochemical reactions were eliminated, which means that current flowing through the cell under illumination can be entirely attributed to the light-induced oxidation of solution species. One can see from Fig. 7a that photocurrent was rather stable, retaining about 90% of its initial magnitude after 3 h long experiment. The amount of hypochlorite, m_{exp}, formed during photoelectrolysis in the anodic compartment of the cell was determined iodometrically. The charge dependence of m_{exp} is shown in Fig. 7b. Average Faradaic efficiency of the process was 30%. It should be noted, however, that under conditions of the experiment certain amount of ClO^- diffused to cathodic compartment of the cell. Up to 5% of the ClO^- amount determined in the anolyte was found in the assays of catholyte taken after longer periods of photoelectrolysis (>4 h). In view of the fact that hypochlorite can be reduced electrochemically on Pt cathode, exact amount of it cannot be determined and the results in Fig. 7b were not corrected. The current efficiency of photoelectrochemical ClO^- generation is almost twice as low as the one reported recently in [11], where ~3 μm thick highly porous WO_3 layers were shown to produce chlorine with average 70% Faradaic

efficiency in the solution of 0.5 M NaCl with pH adjusted to 2. Less efficient production of hypochlorite in our case can be attributed to thinner and less porous WO_3 layers formed under conditions of this study. The rest of charge passing through the cell during photoelectrolysis is, most likely, consumed in oxidation of water molecules. The competition between the processes of water and chloride oxidation could be understood considering the radical-mediated mechanism of photoanodic reactions. In accordance with literature, the potential of valence band edge of WO_3 is 2.8–2.9 V (SHE) [43,44], whereas the standard potentials of OH• and Cl• radicals formation are as follows [45]:

$$H_2O \rightarrow OH^\bullet + H^+ + e^- \quad E^0 = 2.31~V~(SHE)~(at~pH~7) \tag{7}$$

$$Cl^- \rightarrow Cl^\bullet + e^- \quad E^0 = 2.43~V~(SHE) \tag{8}$$

Consequently, photogenerated holes in the valence band of WO_3 have enough energy to drive both of the reactions above. Formation of hydroxyl radicals as primary water oxidation intermediates in PEC process was demonstrated in [44], and the vital role played by chlorine radicals in PEC degradation of organic compounds in chloride-containing solutions was reported in [20]. Since the standard potentials of reactions (7) and (8) are very close, the thermodynamic probability of their occurrence is similar. This could explain the concomitance of these processes in the investigated system. Interplay between the two reactions can be influenced by the ratio of dominant crystallographic planes exposed to solution, as discussed above, as well as morphology of the oxide layer. Porous structure seems to favor oxidation of chloride over water molecules as demonstrated in [6,7,11].

3.4. Antimicrobial effect of photoelectrochemical chlorination with WO_3 photoanode

Further the effect of photoelectrochemical chlorination with WO_3 photoanodes (PEG:PTA(1:10), T_{anneal} = 500 °C) was tested in suspensions of Gram-positive *Bacillus* sp. and Gram-negative *E.coli* bacteria strains in 0.5 M NaCl. The same cell voltage and illumination conditions as described in previous section were applied. It is noteworthy, however, that suspensions of bacteria species were slightly turbid, therefore actual illumination intensity at WO_3 surface, most likely, was less than in pure 0.5 M NaCl. The total charge passed through the cell in PEC experiments was 4.8C and 5.1C for the suspensions of *Bacillus sp* and *E.coli* bacteria, respectively.

The results of photolytic, electrolytic and photoelectrochemical disinfection are compared in Fig. 8. As one can see from Fig. 8a, reactive chlorine species formed during photoelectrolysis displayed strong inhibitory effect on the growth of *Bacillus sp* by 5.72 log reduction. The electrolysis in dark
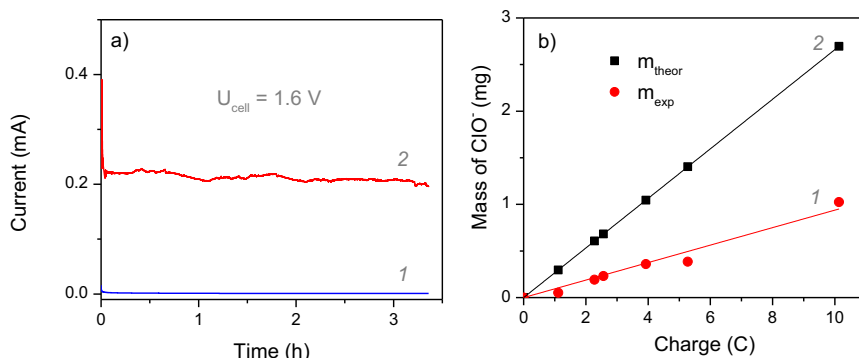

Fig. 7. a) Variation of current with time during electrolysis with WO_3 sample PEG:PTA(1:10), T_{anneal} = 500 °C, in 0.5 M NaCl at cell voltage of 1.6 V in dark (*1*) and under illumination, $P \approx 100$ mW cm^{-2} (*2*); b) dependence between charge passed during photoelectrolysis and amount of ClO^- found in the electrolyte by means of iodometric titration (*1*) and theoretical amount calculated on the basis of Faraday law (*2*).
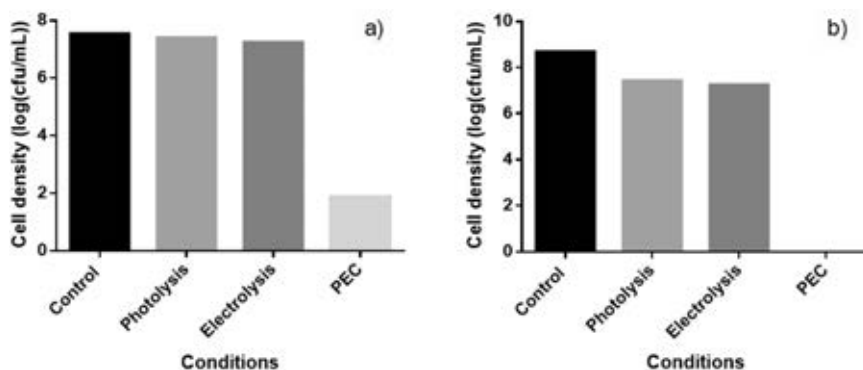
Fig. 8. Comparison of disinfection efficiencies under photolytic ($P \approx 100$ mW cm^{-2}, $U_{cell} = 0$ V), electrolytic ($P = 0$ mW cm^{-2}, $U_{cell} = 1.6$ V) and photoelectrochemical ($P \approx 100$ mW cm^{-2}, $U_{cell} = 1.6$ V) conditions in the case of *Bacillus sp* (a) and *E.coli* C41(DE3) (b) suspensions in 0.5 M NaCl.

and photolysis under zero bias conditions showed no considerable effect on cell density. Fig. 8b shows that complete disinfection of *E.coli* C41(DE3) was achieved in PEC system, whereas lower disinfection efficiencies were obtained under purely electrolytic and purely photolytic conditions, i.e. 1.4 log reduction compared to control sample. As indicated above, the Q of approximately 5C was passed through the photoelectrochemical cell during experiments. In accordance with Fig. 7b, such amount of charge would yield about 0.5 mg of ClO$^-$. In a volume of ~10 cm^3, which was used in our experimental setup, this would correspond to 0.005% concentration of sodium hypochlorite. Usually concentration of 0.5% is considered to be sufficient for the purpose of water disinfection [46]. Our results show that in the case of Gram-negative *E.coli* C41(DE3) species (Fig. 8b) almost hundredfold smaller amount of hypochlorite was sufficient to achieve complete disinfection. This could be related with photoelectrochemical generation of chlorine radicals (Cl$^\cdot$, Cl$_2^\cdot$), which have significantly stronger bacteria-killing power than ClO$^-$.

In summary, the antimicrobial effect of photoelectrochemical chlorination with sol-gel derived PEG-doped WO$_3$ photoanodes was successfully demonstrated in suspensions of Gram-positive *Bacillus* sp. and Gram-negative *E.coli* bacteria strains in 0.5 M NaCl.

4. Conclusions

Semiconducting tungsten (VI) oxide films were formed on conducting glass substrate using sol-gel synthesis technique and polyethylene glycol, PEG 300, as an additive. Effect of PEG on photoelectrochemical performance of WO$_3$ through modulation of the material structure from the initial stages of oxide phase crystallization was demonstrated. Analysis of XRD and SEM data for WO$_3$ films annealed at 300 °C, 400 °C and 500 °C revealed that polyethylene glycol serves as an effective structure-directing agent, which favours formation of WO$_3$ nanostructure comprising good crystallinity, optimal particle size and good connectivity between the particles. These factors are critical for effective separation, longer lifetime and transport of photogenerated charge carriers, and, therefore, account for significantly higher photoelectrochemical activity of PEG-modified WO$_3$ films.

Investigations of the photoelectrochemical response of the films in acid and neutral medium in the absence and presence of chlorides revealed PEG-modified WO$_3$ films are active in PEC generation of reactive chlorine species. It is shown that Faradaic efficiency of hypochlorite formation in neutral chloride medium is about 30%. The antimicrobial effect of photoelectrochemical chlorination with sol-gel derived PEG-modified WO$_3$ electrode was demonstrated with suspensions of Gram-positive *Bacillus sp* and Gram-negative *E.coli* C41(DE3) bacteria in 0.5 M NaCl. It is suggested that high bacteria-killing power of the investigated system should be attributed to generation of highly reactive chlorine radicals, which form as a result of interaction between holes photogenerated in WO$_3$ and

chloride ions in solution. The reported results show that photoelectrochemical chlorination using sol-gel derived nanocrystalline WO$_3$ photoanodes stands as a promising technology for antimicrobial water treatment.

Declaration of Competing Interest

The authors declare that they have no known competing financial interests or personal relationships that could have appeared to influence the work reported in this paper.

Appendix A. Supplementary data

Supplementary data to this article can be found online at https://doi.org/10.1016/j.jelechem.2020.114277.

References

[1] Hypochlorite Bleaches, Chemical Economics Handbook (CEH) | IHS Markit, https://ihsmarkit.com/products/hypochlorite-chemical-economics-handbook.html 2019. (Accessed 25 November 2019).
[2] D.L. Caldwell, Production of chlorine, Compr. Treatise Electrochem, Springer US, Boston, MA 1981, pp. 105–166, https://doi.org/10.1007/978-1-4684-3785-0_2.
[3] K. Sayama, Production of high-value-added chemicals on oxide semiconductor photoanodes under visible light for solar chemical-conversion processes, ACS Energy Lett. 3 (2018) 1093–1101, https://doi.org/10.1021/acsenergylett.8b00318.
[4] K. Fuku, N. Wang, Y. Miseki, T. Funaki, K. Sayama, Photoelectrochemical reaction for the efficient production of hydrogen and high-value-added oxidation reagents, ChemSusChem. 8 (2015) 1593–1600, https://doi.org/10.1002/cssc.201403463.
[5] J. Desilvestro, M. Grätzel, Photoelectrochemistry of polycrystalline n-wo3: electrochemical characterization and photoassisted oxidation processes, J. Electroanal. Chem. Interfacial Electrochem. 238 (1987) 129–150, https://doi.org/10.1016/0022-0728(87)85170-7.
[6] Q. Mi, A. Zhanaidarova, B.S. Brunschwig, H.B. Gray, N.S. Lewis, A quantitative assessment of the competition between water and anion oxidation at WO$_3$ photoanodes in acidic aqueous electrolytes, Energy Environ. Sci. 5 (2012) 5694, https://doi.org/10.1039/c2ee02929d.
[7] K.-S.C. James, C. Hill, Effect of electrolytes on the selectivity and stability of n-type WO$_3$ photoelectrodes for use in solar water oxidation, J. Phys. Chem. C 116 (2012) 7612–7620.
[8] T. Nakajima, A. Hagino, T. Nakamura, T. Tsuchiya, K. Sayama, WO$_3$ nanosponge photoanodes with high applied bias photon-to-current efficiency for solar hydrogen and peroxydisulfate production, J. Mater. Chem. A 4 (2016) 17809–17818, https://doi.org/10.1039/C6TA07997K.
[9] S.S. Kalanur, L. Thai, D. Hyungtak, Recent Progress in Photoelectrochemical Water Splitting Activity of WO 3 Photoanodes, Springer US, 2018https://doi.org/10.1007/s11244-018-0950-1.
[10] S. Xiao, D. Wan, K. Zhang, H. Qu, J. Peng, Enhanced photoelectrocatalytic degradation of ammonia by in situ photoelectrogenerated active chlorine on TiO2 nanotube electrodes, J. Environ. Sci. 50 (2016) 103–108, https://doi.org/10.1016/J.JES.2016.04.028.
[11] M. Jadwiszczak, K. Jakubow-Piotrowska, P. Kedzierzawski, K. Bienkowski, J. Augustynski, Highly efficient sunlight-driven seawater splitting in a photoelectrochemical cell with chlorine evolved at nanostructured WO$_3$ photoanode

and hydrogen stored as hydride within metallic cathode, Adv. Energy Mater. 10 (2020) 1903213, https://doi.org/10.1002/aenm.201903213.

[12] C.S. Jan Augustynski, Renata Solarska, Hans Hagemann, Nanostructured thin-film tungsten trioxide photoanodes for solar water and sea-water splitting, Proc. Vol. 6340, Sol. Hydrog. Nanotechnol2006 (p. 63400J).

[13] S. Ahmed, I.A.I. Hassan, H. Roy, F. Marken, Photoelectrochemical transients for chlorine/hypochlorite formation at "roll-on" Nano-WO$_3$ film electrodes, J. Phys. Chem. C 117 (2013) 7005–7012, https://doi.org/10.1021/jp400962t.

[14] S. Iguchi, Y. Miseki, K. Sayama, Efficient hypochlorous acid (HClO) production *via* photoelectrochemical solar energy conversion using a BiVO$_4$ -based photoanode, Sustain. Energy Fuels 2 (2018) 155–162, https://doi.org/10.1039/C7SE00453B.

[15] Y. Ji, J. Bai, J. Li, T. Luo, L. Qiao, Q. Zeng, B. Zhou, Highly selective transformation of ammonia nitrogen to N$_2$ based on a novel solar-driven photoelectrocatalytic-chlorine radical reactions system, Water Res. 125 (2017) 512–519, https://doi.org/10.1016/J.WATRES.2017.08.053.

[16] Y. Zhang, J. Li, J. Bai, Z. Shen, L. Li, L. Xia, S. Chen, B. Zhou, Exhaustive conversion of inorganic nitrogen to nitrogen gas based on a photoelectro-chlorine cycle reaction and a highly selective nitrogen gas generation cathode, Environ. Sci. Technol. 52 (2018) 1413–1420, https://doi.org/10.1021/acs.est.7b04626.

[17] Z. Shen, J. Li, Y. Zhang, J. Bai, X. Tan, X. Li, L. Qiao, Q. Xu, B. Zhou, Highly efficient total nitrogen and simultaneous total organic carbon removal for urine based on the photoelectrochemical cycle reaction of chlorine and hydroxyl radicals, Electrochim. Acta 297 (2019) 1–9, https://doi.org/10.1016/J.ELECTACTA.2018.11.087.

[18] M.S. Koo, X. Chen, K. Cho, T. An, W. Choi, In situ photoelectrochemical chloride activation using a WO$_3$ electrode for oxidative treatment with simultaneous H$_2$ evolution under visible light, Environ. Sci. Technol. (2019) https://doi.org/10.1021/acs.est.9b02401 (acs.est.9b02401).

[19] Y. Zhang, J. Li, J. Bai, X. Li, Z. Shen, L. Xia, S. Chen, Q. Xu, B. Zhou, Total organic carbon and total nitrogen removal and simultaneous electricity generation for nitrogen-containing wastewater based on the catalytic reactions of hydroxyl and chlorine radicals, Appl. Catal. B Environ. 238 (2018) 168–176, https://doi.org/10.1016/J.APCATB.2018.07.036.

[20] M.S. Koo, X. Chen, K. Cho, T. An, W. Choi, In situ Photoelectrochemical chloride activation using a WO$_3$ electrode for oxidative treatment with simultaneous H$_2$ evolution under visible light, Environ. Sci. Technol. 53 (2019) 9926–9936, https://doi.org/10.1021/acs.est.9b02401.

[21] J. Zhang, J. Tu, X. Xia, X. Wang, C. Gu, Hydrothermally synthesized WO3 nanowire arrays with highly improved electrochromic performance, J. Mater. Chem. 21 (2011) 5492, https://doi.org/10.1039/c0jm04361c.

[22] W. Li, J. Li, X. Wang, J. Ma, Q. Chen, Photoelectrochemical and physical properties of WO$_3$ films obtained by the polymeric precursor method, Int. J. Hydrog. Energy 35 (2010) 13137–13145, https://doi.org/10.1016/j.ijhydene.2010.09.011.

[23] Á. Valdés, G.-J. Kroes, First principles study of the photo-oxidation of water on tungsten trioxide (WO3), J. Chem. Phys. 130 (2009) 114701, https://doi.org/10.1063/1.3088845.

[24] J.M. Chem, Y.P. Xie, G. Liu, L. Yin, H. Cheng, Crystal Facet-Dependent Photocatalytic Oxidation and Reduction Reactivity of Monoclinic WO$_3$ for Solar Energy Conversion, 2012 6746–6751, https://doi.org/10.1039/c2jm16178h.

[25] Y. Guo, X.I.E. Quan, N.A. Lu, High Photocatalytic Capability of Self-Assembled Nanoporous WO 3 with Preferential Orientation of, vol. 41, 2007 4422–4427, https://doi.org/10.1021/es062546c.

[26] N. Wang, D. Wang, M. Li, J. Shi, C. Li, Photoelectrochemical water oxidation on photoanodes fabricated with hexagonal nanoflower and nanoblock WO3, Nanoscale 6 (2014) 2061, https://doi.org/10.1039/c3nr05601e.

[27] W. Chen, H. Shen, X. Zhu, H. Yao, W. Wang, Preparation and photochromic properties of PEG-400 assisted WO$_3$–TiO$_2$–ZnO composite films, Ceram. Int. 41 (2015) 14008–14012, https://doi.org/10.1016/J.CERAMINT.2015.07.013.

[28] V. Hariharan, S. Radhakrishnan, M. Parthibavarman, R. Dhilipkumar, C. Sekar, Synthesis of polyethylene glycol (PEG) assisted tungsten oxide (WO$_3$) nanoparticles for l-dopa bio-sensing applications, Talanta 85 (2011) 2166–2174, https://doi.org/10.1016/j.talanta.2011.07.063.

[29] Clara Santato, Martine Ulmann, J. Augustynski, Photoelectrochemical properties of nanostructured tungsten trioxide films, J. Phys. Chem. B (2001)https://doi.org/10.1021/JP002232Q.

[30] Clara Santato, Marek Odziemkowski, A. Martine Ulmann, J. Augustynski, Crystallographically oriented mesoporous WO3 films: synthesis, characterization, and applications, J. Am. Chem. Soc. (2001) https://doi.org/10.1021/JA011315X.

[31] W.-T. Wu, W.-P. Liao, L.-Y. Chen, J.-S. Chen, J.-J. Wu, Outperformed electrochromic behavior of poly(ethylene glycol)-template nanostructured tungsten oxide films with enhanced charge transfer/transport characteristics, Phys. Chem. Chem. Phys. 11 (2009) 9751, https://doi.org/10.1039/b912202h.

[32] N. Naseri, S. Yousefzadeh, E. Daryaei, A.Z. Moshfegh, Photoresponse and H$_2$ production of topographically controlled PEG assisted sol–gel WO$_3$ nanocrystalline thin films, Int. J. Hydrog. Energy 36 (2011) 13461–13472, https://doi.org/10.1016/J.IJHYDENE.2011.07.129.

[33] A. Tasaso, P. Ngaotrakanwiwat, Synthesis of nano-WO3 particles with polyethylene glycol for chromic film, Energy Procedia 79 (2015) 704–709, https://doi.org/10.1016/J.EGYPRO.2015.11.546.

[34] J.K. Kim, K. Shin, S.M. Cho, T.-W. Lee, J.H. Park, Synthesis of transparent mesoporous tungsten trioxide films with enhanced photoelectrochemical response: application to unassisted solar water splitting, Energy Environ. Sci. 4 (2011) 1465, https://doi.org/10.1039/c0ee00469c.

[35] B.D. Alexander, P.J. Kulesza, I. Rutkowska, R. Solarska, J. Augustynski, Metal oxide photoanodes for solar hydrogen production, J. Mater. Chem. 18 (2008) 2298, https://doi.org/10.1039/b718644d.

[36] C. Santato, M. Ulmann, J. Augustynski, Enhanced visible light conversion efficiency using nanocrystalline WO3 films, Adv. Mater. 13 (2001) 511–514, https://doi.org/10.1002/1521-4095(200104)13:7<511::AID-ADMA511>3.0.CO;2-W.

[37] L. Meda, G. Tozzola, A. Tacca, G. Marra, S. Caramori, V. Cristino, C. Alberto Bignozzi, Photo-electrochemical properties of nanostructured WO3 prepared with different organic dispersing agents, Sol. Energy Mater. Sol. Cells 94 (2010) 788–796, https://doi.org/10.1016/j.solmat.2009.12.025.

[38] M. Pourbaix, Atlas d'equilibres electrochimiques, Gauthier-Villars & Cie, Paris, 1963.

[39] C.C.L. McCrory, S. Jung, J.C. Peters, T.F. Jaramillo, Benchmarking heterogeneous Electrocatalysts for the oxygen evolution reaction, J. Am. Chem. Soc. 135 (2013) 16977–16987, https://doi.org/10.1021/ja407115p.

[40] F. Dionigi, T. Reier, Z. Pawolek, M. Gliech, P. Strasser, Design criteria, operating conditions, and nickel-iron hydroxide catalyst materials for selective seawater electrolysis, ChemSusChem 9 (2016) 962–972, https://doi.org/10.1002/cssc.201501581.

[41] I. Sirés, E. Brillas, M.A. Oturan, M.A. Rodrigo, M. Panizza, Electrochemical advanced oxidation processes: today and tomorrow. A review, Environ. Sci. Pollut. Res. 21 (2014) 8336–8367, https://doi.org/10.1007/s11356-014-2783-1.

[42] L. Ghasemi, H. Jafari, L. Ghasemi, H. Jafari, Morphological characterization of tungsten trioxide nanopowders synthesized by sol-gel modified Pechini's method, Mater. Res. 20 (2017) 1713–1721, https://doi.org/10.1590/1980-5373-mr-2017-0467.

[43] L. Weinhardt, M. Blum, M. Bär, C. Heske, B. Cole, B. Marsen, E.L. Miller, Electronic surface level positions of WO3 thin films for photoelectrochemical hydrogen production, J. Phys. Chem. C 112 (2008) 3078–3082, https://doi.org/10.1021/jp7100286.

[44] V. Cristino, S. Marinello, A. Molinari, S. Caramori, S. Carli, R. Boaretto, R. Argazzi, L. Meda, C.A. Bignozzi, Some aspects of the charge transfer dynamics in nanostructured WO3 films, J. Mater. Chem. A 4 (2016) 2995–3006, https://doi.org/10.1039/c5ta06887h.

[45] D.A. Armstrong, R.E. Huie, S. Lymar, W.H. Koppenol, G. Merényi, P. Neta, D.M. Stanbury, S. Steenken, P. Wardman, Standard electrode potentials involving radicals in aqueous solution: inorganic radicals, Bioinorg. React. Mech. 9 (2013) 59–61, https://doi.org/10.1515/irm-2013-0005.

[46] S.A. Farook, V. Shah, D. Lenouvel, O. Sheikh, Z. Sadiq, L. Cascarini, Guidelines for management of sodium hypochlorite extrusion injuries, Br. Dent. J. 217 (2014) 679–684, https://doi.org/10.1038/sj.bdj.2014.1099.

2$^{\text{nd}}$ publication

Tuning the photo-luminescence properties of WO$_3$ layers by the adjustment of layer formation conditions

Petruleviciene, M., Juodkazyte, J., **Parvin, M.,** Tereshchenko, A., Ramanavicius, S., Karpicz, R., Samukaite-Bubniene, U. and Ramanavicius, A.,

Article

Tuning the Photo-Luminescence Properties of WO₃ Layers by the Adjustment of Layer Formation Conditions

Milda Petruleviciene [1], Jurga Juodkazyte [1] , Maliha Parvin [1] , Alla Tereshchenko [2,3] , Simonas Ramanavicius [1], Renata Karpicz [1] , Urte Samukaite-Bubniene [2] and Arunas Ramanavicius [1,2,*]

1   Center for Physical Sciences and Technology, Sauletekio av. 3, LT-10257 Vilnius, Lithuania; milda.petruleviciene@ftmc.lt (M.P.); jurga.juodkazyte@ftmc.lt (J.J.); maliha.parvin@ftmc.lt (M.P.); simonas.ramanavicius@ftmc.lt (S.R.); renata.karpicz@ftmc.lt (R.K.)
2   Department of Physical Chemistry, Institute of Chemistry, Faculty of Chemistry and Geosciences, Vilnius University, Naugarduko 24, LT-03225 Vilnius, Lithuania; alla_teresc@onu.edu.ua (A.T.); urte.samukaite-bubniene@chf.vu.lt (U.S.-B.)
3   Department of Experimental Physics, Faculty of Mathematics, Physics and Information Technologies, Odesa National I.I. Mechnikov University, Pastera 42, 65023 Odesa, Ukraine
*   Correspondence: arunas.ramanavicius@chf.vu.lt
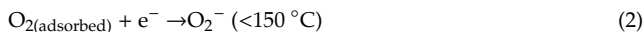
check for updates

Abstract: In this research we have applied sol-gel synthesis for the deposition of tungsten (VI) oxide (WO₃) layers using two different reductants (ethanol and propanol) and applying different dipping times. WO₃ samples were characterized by X-ray diffraction (XRD), scanning electron microscopy (SEM), Fourier Transform Infrared spectroscopy (FTIR), photoluminescence (PL) and time-resolved photoluminescence decay methods. Photoelectrochemical (PEC) behaviour of synthesized coatings was investigated using cyclic voltammetry in the dark and under illumination. Formation of different structures in differently prepared samples was revealed and significant differences in the PL spectra and PEC performance of the samples were observed. The results showed that reductant used in the synthesis and dipping time strongly influenced photo-electrochemical properties of the coatings. Correlation between the morphology, PL and PEC behaviour has been explained.

---

1. Introduction

The demand for sensors with advanced analytical characteristics is constantly increasing [1]. Various metal oxides (TiO₂, ZnO, SnO₂, WO₃, etc.) are widely used for numerous technological purposes including application in analytical signal transduction systems [2,3]. Nanostructured metal oxides are especially attractive in sensors due to their electrochemical properties and their large chemically active surface. Among other oxide materials, tungsten (VI) oxide (WO₃) is very promising n-type semiconductor. Due to relevant physical, photoelectrochemical and catalytic properties, WO₃ is used in lithium-ion batteries [4], electrochromic windows [5], solar energy conversion systems [6–11], volatile organic compounds (VOCs) and gas sensors [12]. The sensors based on WO₃ still suffer from high operating temperature, low sensitivity or high limit of detection (LOD). The improvement of sensitivity and LOD is especially significant for medical purposes, where sensitive and accurate detection is necessary. Therefore, it is very important to find out how different crystallinity and morphology of coatings influence WO₃ activity. The mechanism of gas sensing is a complex process.

It involves adsorption/(catalytic action)/desorption steps, which in air atmosphere are significantly affected by oxygen molecules that are chemisorbed and/or physically-adsorbed on the WO_3 surface. Depending on the operating temperature, the negatively charged (O^-, O_2^- and O^{2-}) oxygen species on the surface of WO_3 can be formed. Formation of these species can be presented by following Equations [13–15]:

$$O_{2(gaseous)} \rightarrow O_{2(adsorbed)} \tag{1}$$

$$O_{2(adsorbed)} + e^- \rightarrow O_2^- \ (<150\ ^\circ C) \tag{2}$$

$$O_2^- + e^- \rightarrow 2O^- (150\text{–}400\ ^\circ C) \tag{3}$$

$$O^- + e^- \rightarrow O^{2-} (>400\ ^\circ C) \tag{4}$$

When analyte gas molecules are adsorbed on tungsten oxide, the electrons are either accepted from the surface (oxidizing gas) or donated to the tungsten oxide surface (reductive gas), which leads to an increase or decrease of WO_3 resistance, respectively. In most cases, the highest catalytic activity of WO_3-based structures is observed at high temperatures. Working at a high temperature requires more sophisticated and expensive sensor construction and additional equipment for regulation of temperature in order to get a stable sensor response, which eventually leads to high power consumption. Therefore, in recent years, low-temperature gas sensors based on light-activated metal oxide semiconductors have attracted a lot of attention [16–23]. It was suggested that light affects gas sensor performance in the following ways: (1) light influences dissociation of oxygen species and, consequently, the adsorption of VOC-based analyte molecules; (2) light increases density of free electron–hole pairs and facilitates carrier generation, thus enabling the sensor to work at room temperature with high sensitivity and selectivity [16,24]. The gas-sensing properties of metal oxide semiconductors are also known to be strongly influenced by illumination conditions [1,25,26] because light modulates the density of charge carriers. Effective generation, separation and transport of light-generated charge carriers and, consequently, the sensing ability of WO_3 are highly dependent on the method of synthesis. Various techniques, including hydrothermal [27,28], reactive sputtering [27], spray pyrolysis [29], sol-gel [30,31] and electrodeposition [32,33] are used for the formation of tungsten (VI) oxide layers. Among them, the sol-gel method is very popular because it is easily controllable, does not require any sophisticated procedures or specialized tools and allows adjustment of the most optimal parameters in a simple way [31,34–36]. Proper understanding of how some factors influence the properties of semiconductor oxide films is essential for tailoring sensors' response to light as well as their sensing performance.

The aim of this research was to form WO_3 layers under different conditions using sol-gel synthesis method and to determine their photo-induced redox properties at room temperature. Crystalline structure, composition, and morphology of WO_3 coatings were characterized using X-ray diffraction (XRD), scanning electron microscopy (SEM) and Fourier Transform Infrared spectroscopy (FTIR). Photoelectrochemical activity of the coatings was evaluated by cyclic voltammetry, and correlation of the data with the results of time-resolved photoluminescence decay measurements was analysed.

2. Experimental

2.1. Chemicals

All chemicals were of 'Analytical grade' and were used as received from suppliers, without any further purification.

Sodium tungstate was purchased from Carl Roth (Karlsruhe, Germany), ammonium oxalate from Chempur (Piekary Śląskie, Poland), hydrochloric acid from Chempur (Piekary Śląskie, Poland), hydrogen peroxide from Chempur (Piekary Śląskie, Poland), ethanol from Reachem (Bratislava, Slovakia), propanol from Reachem (Bratislava, Slovakia), sulfuric acid from Reachem (Bratislava, Slovakia).

2.2. Formation of Photoelectrochemically Active Tungsten Oxide Layers on the FTO and Glass Substrate

WO$_3$ thin films on FTO and glass substrate were prepared by sol-gel method in aqueous solution. Firstly, FTO substrates were cut into 1 mm × 2 mm slides and washed under ultrasonication with acetone, ethanol and finally deionized water for 15 min per wash. During the synthesis, a sodium tungstate dihydrate (Na$_2$WO$_4$ × 2H$_2$O) (from Carl Roth) was used as a precursor and ammonium oxalate ((NH$_4$)C$_2$O$_4$; AO) (from Chempur) was used as capping agent. They were dissolved in distilled water and then HCl (from Chempur) was added under continuous stirring for 10 min at 40 °C. Afterwards the hydrogen peroxide (H$_2$O$_2$) (from Chempur) was added to the above-mentioned solution under continuous stirring for 10 min at 40 °C to obtain peroxotungsten acid (PTA). Further, ethanol (EtOH) (from Reachem) was added as a reductant to the prepared PTA mixture (PTA + EtOH), which was used for the formation of WO$_3$ coating. After 10 min, cleaned FTO substrates were dipped in a 'face-down position' into the prepared mixture and incubated for 140 min and 180 min. Synthesis was carried out at 85 °C constant temperature in a water bath. After the formation of WO$_3$ coating, the slides were rinsed in distilled water for 1 min and then they were dried in the drying oven at 40 °C for 10 h. The same procedures were followed for preparing of PTA and propanol (PrOH) (from Reachem) sol-gels, just instead of ethanol a propanol was added to PTA solution. Finally, samples were annealed at 500 °C for 2 h in ambient atmosphere; heating rate was 1 °C min^{-1} and starting temperature was 20 °C.

2.3. Characterization of Oxide Layers

2.3.1. X-ray Diffraction, Scanning Electron Microscopy

XRD patterns of the films on FTO substrate were obtained using an X-ray diffractometer SmartLab (Rigaku, Oxford, UK) equipped with 9 kW rotating Cu anode X-ray tube. Grazing incidence (GIXRD) method was used in 2θ range at 20–80 °C. An angle between a parallel beam of X-rays and a specimen surface (ω angle) was adjusted to 0.5°. Match software and Crystallography Open Database (COD) was used for phase identification. The average crystallite size D, of each sample was calculated using the Scherrer equation [37,38].

The surface morphology of the tungsten oxide layers on FTO substrate was investigated using Helios NanoLab dual beam workstation equipped with X-Max 20 mm^2 energy dispersion spectrometer (Oxford Instruments, Oxford, UK).

The phase composition was investigated by Fourier Transform Infrared spectroscopy using a PerkinElmer spectrophotometer, with a resolution of 4 cm^{-1} over a wavenumber range of 450–4000 cm^{-1}.

2.3.2. Electrochemical Measurements

Voltammetric measurements were performed using three-electrode cell and potentiostat/galvanostat AUTOLAB 302 from Ecochemie (Utrecht, The Netherlands). Tungsten (VI) oxide films deposited on flouride-doped tin oxide (FTO) substrates were used as working electrodes. Silver chloride electrode with saturated KCl solution (Ag/AgCl/sat. KCl) and Pt wire were used as reference and counter electrodes, respectively. The surface of working electrodes was illuminated with high intensity discharge Xe-lamp with 6000 K spectrum and calibrated with a silicon diode to simulate AM 1.5 illumination (~100 mW cm^{-2}) at the sample surface. Experiments were performed in the solution of 0.5 M H$_2$SO$_4$. Current density values were calculated based on geometric area of the working electrode.

2.3.3. Time-Resolved Photoluminescence Decay Based Evaluation of WO$_3$-Based Coatings

Optical characterization was performed by the evaluation of photoluminescence signal from the samples using a time-correlated single photon counting Edinburgh-F900 spectrophotometer (Edinburg Instruments Ltd., Livingston, UK). The photoluminescence spectra of WO$_3$ coatings were excited by solid-state laser with an excitation wavelength of 375 nm (the average pulse power was about 0.15 mW/mm^2, the pulse duration 76 ps) and measured in the range of 400 to 700 nm.

All photoluminescence spectra were corrected for the instrument sensitivity. The photoluminescence decay kinetics was measured with the same Edinburgh-F900 spectrophotometer. The pulse repetition rate was 1 MHz and the time resolution of the setup was about 100 ps taking into account temporal deconvolution procedure.

The position and intensity of the photoluminescence maximum was determined as the corresponding characteristics of Gauss function using the Origin program.

3. Results and Discussion

3.1. XRD, SEM and FTIR Analysis of WO₃ Coatings

The crystalline structure and surface morphology of tungsten (VI) oxide coatings were characterized by XRD and SEM techniques. In Figure 1, XRD patterns of samples prepared from PTA + PrOH and PTA + EtOH sol-gels and annealed at 500 °C 2 h are shown. It is obvious that different reductants used in the synthesis and different dipping times influence crystalline structure of the coatings. The main crystalline phase of synthesized coatings in all samples is monoclinic tungsten (VI) oxide. Sample prepared from PTA + PrOH sol-gel with 140 min dipping time has the highest crystallinity, because the peaks investigated in the whole range of 2θ values are the most intensive. Clusters of three peaks at 2θ = 23.20°, 23.60°, 24.29° and two peaks at 2θ = 33.42° and 34.12° are attributed to monoclinic tungsten trioxide (marked with asterisk) in accordance with PDF no. 96-210-6383 of the COD. The sample with 180 min dipping time has less intensive peaks, but a cluster of three peaks, which correspond to (002) (020) (200) facets, is well observed. It is noteworthy that the intensity of facet (200) in this sample decreased dramatically. This means that dipping duration influences the formation of the facets in tungsten trioxide crystallite and lattice parameters as well. Diffractograms of the samples prepared from PTA + EtOH sol-gel exhibit the clusters of three and two peaks. The crystallinity of the coating with 180 min dipping time is slightly higher, because peaks are more intensive.

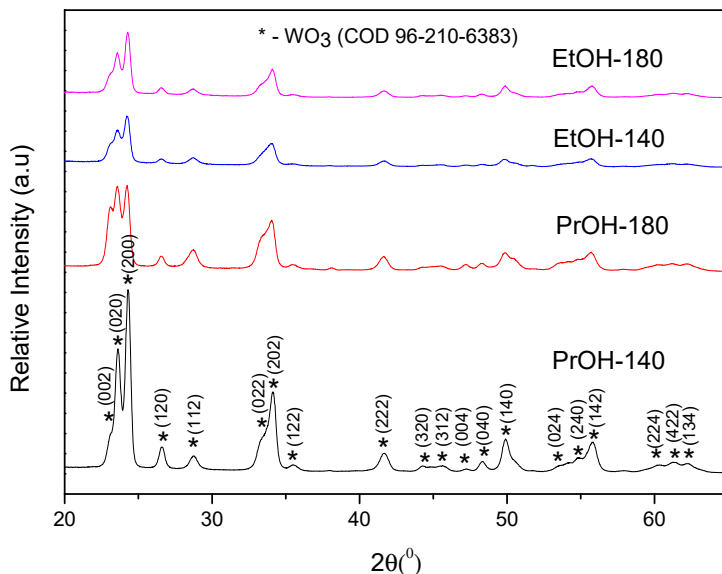
Figure 1. X-ray diffraction (XRD) spectra of WO₃ layers prepared from PTA + EtOH and PTA + PrOH sol-gels using dipping times of 140 min and 180 min; samples wereannealed at 500 °C for 2 h.

The facets are the same as in the case of films formed from PTA + PrOH sol-gel. Facet (200) in all the samples has the highest intensity, suggesting selective orientation of the (200) planes parallel to

the substrate and [200] direction vertical to the substrate. This can be attributed to the fact that this facet is growing parallel to the FTO substrate [39,40]. Among various crystalline structures of WO_3, the monoclinic structure is highly stable and the photoelectrochemical activity of the films is known to depend on the facets exposed to solution phase [41].

The crystallite size is an important parameter that influences the properties of metal oxide nanostructures; therefore, the crystallites size of all samples was evaluated using Scherrer's equation:

$$D = k\lambda/(\beta\cos\theta), \tag{5}$$

where D is the crystallite size, k is a shape factor, λ is the X-ray wavelength (0.15406 nm), β is the full width at half maximum intensity in radians and θ is the Bragg angle. For calculation, the most intensive XRD pattern at 23.20° position was used and results are presented in Table 1. In PrOH-180, EtOH-140 and EtOH-180 coatings 5.58 nm, 5.51 nm and 5.55 nm crystallites were formed, respectively; however, in the coating, PrOH-140 crystallites are approximately 20% bigger and reach 6.57 nm, but in general, the differences in crystallite sizes of the formed samples are insignificant. During the process of synthesis these crystallites combine to form larger particles, i.e., the structural units constituting the coating. Contrary to crystallites, the shape and size of particles was found to differ very significantly depending on synthesis conditions.

Table 1. Crystallite size of PrOH-140, PrOH-180; EtOH-140 and EtOH-180.

Sample	Coating Formation Time (min)	Crystallite Size (nm)
PrOH-140	140	6.57
PrOH-180	180	5.58
EtOH-140	140	5.51
EtOH-180	180	5.55

In Figure 2, the SEM images of tungsten trioxide coatings are presented. Morphology of the coatings formed from PTA + PrOH and PTA + EtOH sol-gels differs significantly. Longer synthesis time influences the growth of the WO_3 H_2O structure as well as the final crystalline tungsten trioxide morphology after annealing [39]. Coatings synthesized from PTA + PrOH sol-gel are composed of very dense layer of 20–100 nm sized particles with randomly distributed 2 μm size agglomerates. With increasing dipping time (180 min), bigger agglomerates are formed (b). Morphology of the samples prepared from PTA + EtOH sol-gel is completely different (c,d). The coatings are dense, composed of randomly oriented submicrometer-sized (200–1000 nm), vertically aligned plates, which are located very close one to each other forming the network with high surface area. Dipping time does not influence the size of the plates significantly, however the presence of very fine-grained areas can be seen on the surface of "180 min" coating. In both samples, small pores between the particles can be observed. All coatings prepared from PTA + EtOH and PTA + PrOH sol-gels are without cracks in the structure, what facilitates the transfer of photogenerated charge carriers. In accordance with literature data, the difference in the morphology of the coatings can be explained considering the colloidal stability of oxide particles in different solvents as well as reducing ability of different alcohols. It has been reported [42] that reducing ability of primary alcohol increases with decreasing carbon chain length. Thus, ethanol is stronger reductant than propanol and the crystallization of $WO_3 \bullet H_2O$ should initiate and proceed faster in EtOH-containing medium. On the other hand, the energy barrier, which inhibits the agglomeration of the particles, is directly proportional to the dielectric constant of the liquid medium and the surface potential [43]. In the case of ethanol, the dielectric constant of solution is relatively high and the energy barrier is high enough. Therefore, the primary oxide particles precipitated from this solution are stable, do not agglomerate and their growth proceeds mainly in two directions, resulting in plate-shaped morphology. When propanol containing solvent is used,

the crystallization and growth of the $WO_3 \bullet H_2O$ phase is slower and the dielectric constant of solution is lower. Consequently, the primary particles are unstable and prone to agglomeration when attraction forces are predominating against repulsion forces. This leads to nanoparticulate morphology with random distribution of micro- and nano-scale agglomerates. SEM observations are in agreement with XRD results, which are quite similar for "EtOH-140" and "EtOH-180" coatings, but differ significantly between "PrOH-140" and "PrOH-180" as well as between "PTA + EtOH" and "PTA + PrOH" sol-gels. Although crystallite sizes in all the synthesized coatings are almost the same (Table 1), the shapes and sizes of particles differ significantly and play a crucial role in determining the photoluminescence properties and photoelectrochemical performance of WO_3 films, as shown below.
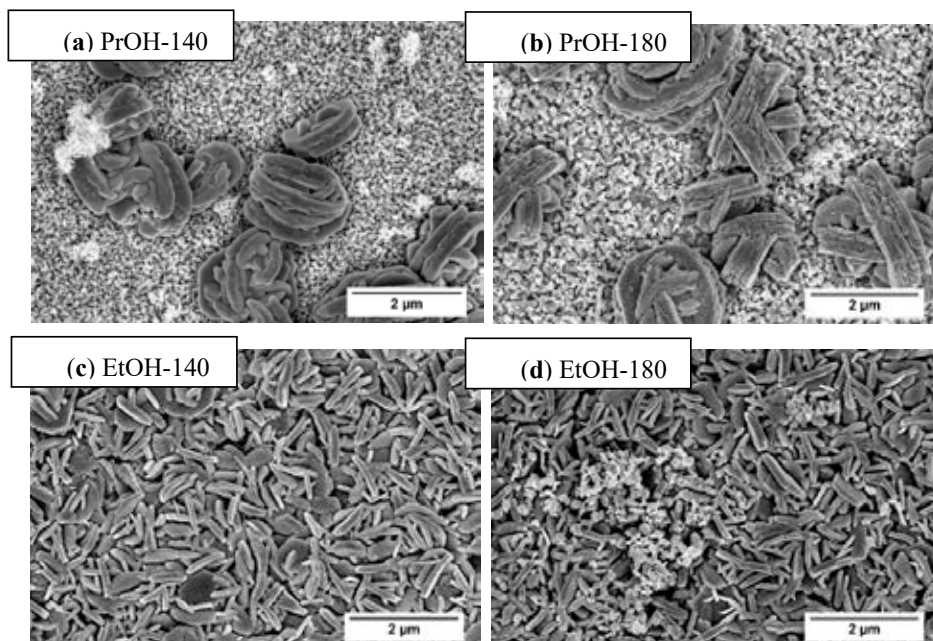

Figure 2. SEM images of WO_3 sample prepared from PTA + PrOH sol-gel dipped for 140 min (**a**); dipped for 180 min (**b**) and PTA + EtOH sol-gel dipped for 140 min (**c**); dipped for 180 min (**d**) and annealed at 500 °C for 2 h. Magnification ×25,000.

Fourier transform infrared (FTIR) spectroscopy confirmed the structural composition and the purity of the formed WO_3. In Figure 3 the broad absorption peaks at <1000 cm^{-1} indicate the presence of pure tungsten oxide. The band at 619 cm^{-1} is attributed to W–O stretching vibration, while bands at 801 and 762 cm^{-1} are attributed to the inter-bridge stretching O-W-O and the corner-sharing mode W-O-W, respectively [44,45]. Tungsten oxide synthesized from PTA + EtOH sol-gel has much sharper peaks due to a more orderly structure with well-expressed W-O stretching vibration. The broad band at 3400 cm^{-1} can be attributed to W-OH stretching vibration, and the peak located at 1625 cm^{-1} corresponds to W-OH bending vibration mode of the adsorbed water molecules [46].
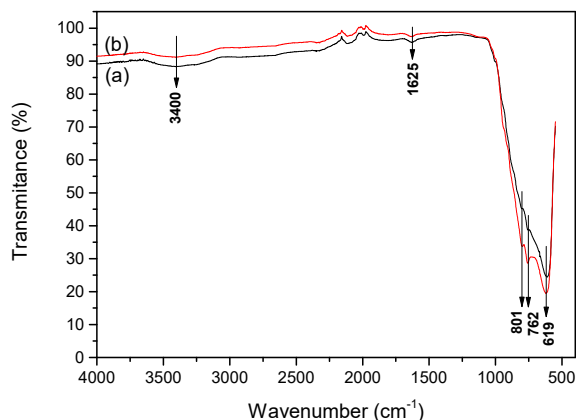
Figure 3. Fourier Transform Infrared (FTIR) spectrum of WO_3 powder prepared from (**a**) PTA + PrOH sol-gel and (**b**) PTA + EtOH sol-gel and annealed at 500 °C.

3.2. Time-Resolved Photoluminescence Decay Based Evaluation of WO_3 Coatings

The normalized photoluminescence spectra of four investigated samples measured at room temperature are presented in Figure 4. It is well known that the PL signals of semiconductors are generated by the recombination of photo-induced charge carriers [47]. The photoluminescence signal is characterized by wide non-symmetric maximum in the range of 400–600 nm, cantered at 426 (2.9 eV), 428 (2.9 eV), 436 (2.85 eV) and 445 (2.8 eV) nm for PrOH-140, PrOH-180, EtOH-140 and EtOH-180 samples, respectively. It is clearly seen that PL maximum shifts to the red spectra region in the case of EtOH-140 and EtOH-180 samples, what can be caused by the differences in particle size and shape compared with PrOH-140 and PrOH-180 samples. Such displacement can be attributed to the fact that different shape of particles can lead to an increase in the concentration of surface defects responsible for PL [48]. It is well known that the size and shape of nanomaterial affect their physicochemical properties [49]. Generally, oxygen vacancies are known to be the most common defects. They usually act as radiative centres in the luminescence processes and can serve as deeply trapped holes in the semiconductors [47]; however, other impurities or defects within WO_3 thin film might also contribute to the emission at 426, 428, 436 and 445 nm [48,50–52] observed in this study.
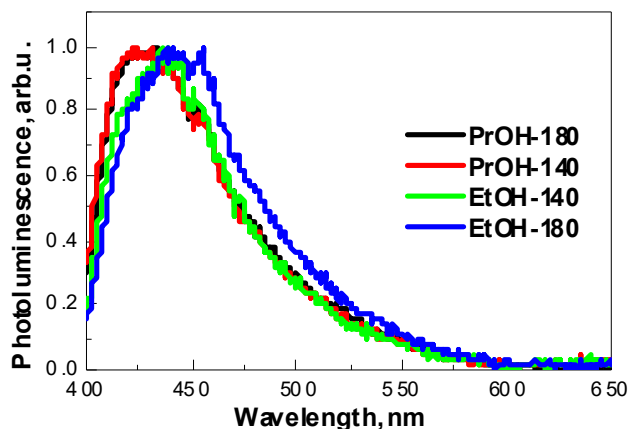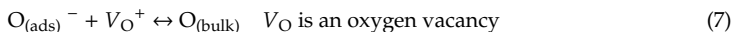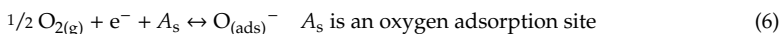

Figure 4. Normalized photoluminescence spectra of samples PrOH-140, PrOH-180, EtOH-140 and EtOH-180 under 375 nm excitation.

It is necessary to mention that blue photoluminescence band in the 400–440 nm region also could be attributed to optical transition in the isolated -OH groups formed at the WO_3 coating surface [53,54]. This correlates well with FTIR results, because W-OH stretching and bending vibrations were observed at 3400 cm^{-1} and 1625 cm^{-1} wavenumbers, respectively. This fact is in good agreement with investigations of several metal oxides, which show the same photoluminescence of -OH-based photoluminescence centres, which are present in oxidized nanocrystalline and porous silicon, hydrated alumina oxide, hydrated lead oxide and zinc oxide [55].

The presence of oxygen in the surrounding atmosphere is also important for the generation of photoluminescence and for the catalytic activity of tungsten oxide layer [56,57] as it can interact with oxygen vacancies as represented by the following equations:

$$1/2\, O_{2(g)} + e^- + A_s \leftrightarrow O_{(ads)}^-\quad A_s \text{ is an oxygen adsorption site} \tag{6}$$

$$O_{(ads)}^- + V_O^+ \leftrightarrow O_{(bulk)}\quad V_O \text{ is an oxygen vacancy} \tag{7}$$

Oxygen adsorption (Equation (6)) and WO_3 oxidation (Equation (7)) are happening consecutively and adsorbed/integrated oxygen (Equations (6) and (7)) leads to the formation of electron depletion layer on the surface of WO_3 film. When adsorbed $O_{(ads)}^-$ oxygen species are removed from the surface reacting with the reducing gases or organic compounds, then the injection of the electrons is narrowing 'the width' of the electron depletion layer, which leads to the decrease in WO_3 layer resistance. Two different charge transfer mechanisms are observed for WO_3 layers: the first is based on n-type conductivity that is typical to stoichiometric WO_3 [58–60] and the other mechanism is based on p-type conductivity that is characteristic for non-stoichiometric tungsten oxide WO_{3-x}. The latter was reported and can be responsible for the low-temperature sensitivity of WO_{3-x}-based layers towards gaseous analytes [61,62].

Time-resolved photoluminescence decay measurements presented in Figure 5 reveal that the average photoluminescence decay time of PrOH-140, PrOH-180, EtOH-140, EtOH-180 samples is 11.2, 11.3, 4.5 and 10.9 ns, respectively (Table 2). It is noteworthy that in the case of sample EtOH-140 the intensity of photoluminescence was the lowest (not shown) and average photoluminescence decay time was the shortest. In addition, it is necessary to mention that, in the case of EtOH-140 sample, no formation of dense nanostructured particles was observed (Figure 2). The reasons for different behaviour of sample EtOH-140 and correlation between PL properties, photoelectrochemical performance and morphological features of WO_3 films formed under different conditions are discussed in the next section.

Table 2. Photoluminescence data of WO_3 samples formed under different conditions.

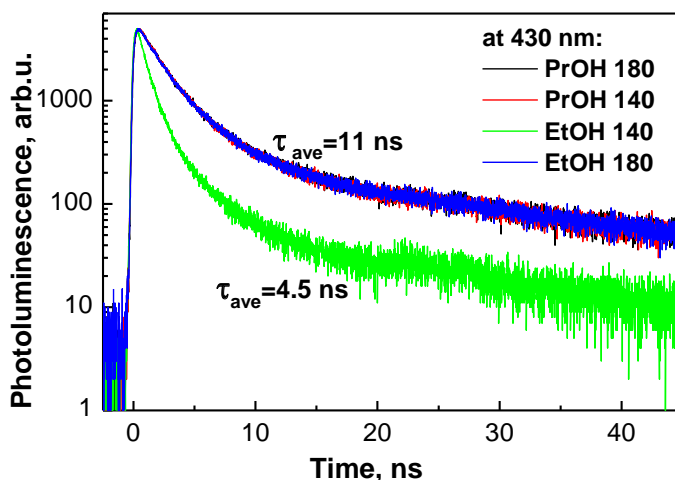| Sample	λ_{em}, nm	τ_1, ns (%)	τ_2, ns (%)	τ_3, ns (%)	τ_{ave}, ns
PrOH-140	426	1.6 (37%)	4.1 (32%)	30 (31%)	11.2
PrOH-180	428	1.6 (37%)	4.4 (32%)	30 (31%)	11.3
EtOH-140	436	0.7 (55%)	2.6 (30%)	22 (15%)	4.5
EtOH-180	443	1.5 (33%)	3.9 (36%)	29 (31%)	10.9

Figure 5. Time resolved photoluminescence decay kinetics of samples PrOH-140, PrOH-180, EtOH-140 and EtOH-180 at 430 nm.

3.3. Photoelectrochemical Evaluation of WO$_3$ Coatings Deposited on FTO-Glass Electrode

Photoelectrochemical behaviour of WO$_3$ films deposited on conducting glass/FTO substrate was investigated in the solution of 0.5 M H$_2$SO$_4$ in dark and under illumination and the results are presented in Figure 6. Cyclic voltammogram (CV) of sample EtOH-140 in the dark (Figure 6a, curve 1) represent a typical response of tungsten (VI) oxide. The increase in cathodic current at E < 0.2 V and the anodic current peak that is observed in the same range of potentials reflects the reversible redox transition between W (VI) and W (V) oxygen species. Under dark conditions, the zone between 0.4 V and 1.8 V is the range of passivity, where no electrochemical processes occur. Under illumination, a remarkable increase of photoanodic current is observed at E > 0.4 V (Figure 6a, curve 2). This is consistent with n-type conductivity of WO$_3$ coatings formed by sol-gel technology. In accordance with references [41,63], the main photoanodic process occurring in sulfuric acid solution is the oxidation of HSO$_4^-$ into S$_2$O$_8^{2}$ by holes photogenerated in tungsten (VI) oxide, because the energy of holes is high enough to drive this redox reaction (E^0(S$_2$O$_8^{2-}$/2HSO$_4^-$) = 2.12 V). The processes of reversible redox transition between W(VI)/W(V) oxygen compounds at E < 0.4 V are not affected by illumination conditions. Comparison of CVs of FTO-supported WO$_3$ films formed under different synthesis conditions is presented in Figure 6b. It should be noted here that in the E range below 0.4 V the curves of all samples practically coincide. This means that electrochemically active surface area of differently formed samples is very similar. In terms of photoelectrochemical activity, the sample EtOH-140 significantly outperforms all the rest WO$_3$ films, as can be seen from the comparison of cyclic voltammograms at E > 0.4 V. These observations imply that the differences in PEC activity of the samples cannot be attributed to mere difference in their surface area. The photoelectrochemical activity of WO$_3$ coatings decreases in the following sequence: EtOH-140 > EtOH-180 > PrOH-140 > PrOH-180. Interestingly, the sample EtOH-140 with the shortest photoluminescence decay time (τ_{ave} = 4.5 ns), i.e., the fastest recombination, exhibits the highest photoelectrochemical activity. Such a discrepancy can be explained by taking into account the morphological features of the samples, as shown in Figure 2. One can see that the sample EtOH-140 is the only one which does not have the very fine-grained nanocrystalline areas discussed above. Most likely, these areas have a very high concentration of grain boundaries, which act as traps for the photogenerated charge carriers. The presence of such traps impedes the radiative recombination of charge carriers, leading to higher values of τ_{ave}. From the viewpoint of PEC performance of the samples, these trap states slow the transport of photogenerated charge carriers towards WO$_3$/solution

interface, resulting in lower photocurrent. Consequently, slower kinetics of recombination due charge carrier trapping correlates with lower photoelectrochemical activity, i.e., the efficiency of charge transfer at the WO_3/solution interface. The effect of particle size and grain morphology on the movement of photogenerated electrons and holes in semiconductors is well-known [64,65]. In the case of tungsten (VI) oxide, it has been reported [40,66] that films composed of irregular disordered perpendicularly oriented crystallites show higher photoelectrochemical performance than films with nanocrystalline particles. Under conditions of applied external bias (Figure 6), the rate of electron-hole recombination is suppressed, and the morphology of vertically aligned submicrometer sized plates results in the highest photocurrent of sample EtOH-140.
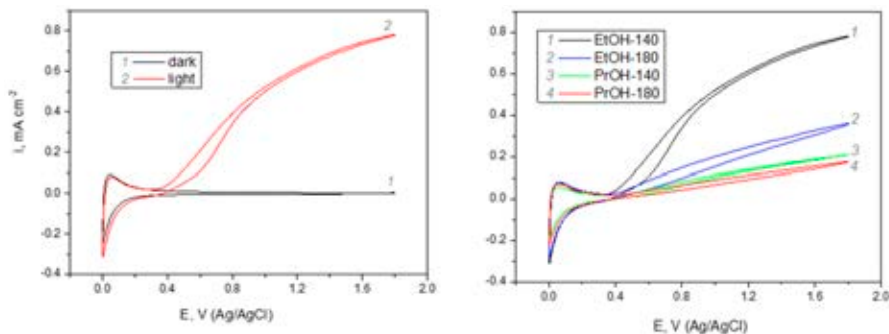

Figure 6. Photoelectrochemical response of FTO/WO_3 samples formed under different synthesis conditions: (**a**) cyclic voltammograms of sample EtOH-140 in dark and under illumination; (**b**) cyclic voltammograms of indicated samples under illumination; solution 0.5 M H_2SO_4, potential scan rate of 50 mV s^{-1}, intensity of illumination~100 mW cm^{-2}.

Here, the presented experimental results reveal that using ethanol as a reductant in the sol-gel synthesis applied in this study and 140 min dipping time in PTA + EtOH-based solution ensures the formation of WO_3 structure, which is optimal for efficient separation and transport of photogenerated charge carriers due to formation of vertically aligned plates. Longer dipping duration or the use of propanol as a reductant favour the formation of a nanocrystalline structure, which is detrimental for fast transport of charge carriers due to presence of numerous grain boundaries which act as traps for photogenerated electrons.

4. Conclusions and Future Trends

Layers of tungsten (VI) oxide were formed on conducting glass substrate by sol-gel synthesis method using two different reducing agents and different durations of coating formation. It was found that using propanol as a reductant leads to formation of dense nanostructured WO_3 films with randomly distributed agglomerates composed of particles of several micrometres size, whereas using ethanol as a reductant favours formation of uniform layers of vertically aligned submicrometer sized plates. Investigations of time-resolved photoluminescence and photoelectrochemical activity of WO_3 films revealed that the latter microstructure is favourable for the efficient transport of photogenerated charge carriers. Vertically aligned plates were found to quench the PL of WO_3 coatings as such morphology is characterized by lower intensity and fast decay (4.5 ns) of photoluminescence compared to the films containing fragments of dense nanostructure. These dense nano-structured areas were suggested to be responsible for rather strong photoluminescence in the range of 400–440 nm and photoluminescence decay times of 11 ns. Moreover, numerous grain boundaries present in the nano-structured fragments of WO_3 coatings contain oxygen vacancies and other defects, which act as traps for the photogenerated charge carriers, slowing down their transport and leading to inferior photo-electrochemical performance. These findings provide guidelines for the synthesis of light-sensitive WO_3 films, which will be assessed for gas sensing properties at room temperature.

References

1. Xu, F.; Ho, H.-P. Light-Activated Metal Oxide Gas Sensors: A Review. *Micromachines* **2017**, *8*, 333. [CrossRef] [PubMed]

2. Tereshchenko, A.; Bechelany, M.; Viter, R.; Khranovskyy, V.; Smyntyna, V.; Starodub, N.; Yakimova, R. Optical biosensors based on ZnO nanostructures: Advantages and perspectives. A review. *Sens. Actuators B Chem.* **2016**, *229*, 664–677. [CrossRef]

3. Tereshchenko, A.; Smyntyna, V.; Ramanavicius, A. Interaction mechanism between TiO_2 nanostructures and bovine leukemia virus proteins in photoluminescence-based immunosensors. *RSC Adv.* **2018**, *8*, 37740–37748. [CrossRef]

4. Zheng, M.; Tang, H.; Hu, Q.; Zheng, S.; Li, L.; Xu, J.; Pang, H. Tungsten-Based Materials for Lithium-Ion Batteries. *Adv. Funct. Mater.* **2018**, *28*, 1707500. [CrossRef]

5. Niklasson, G.A.; Berggren, L.; Larsson, A.-L. Electrochromic tungsten oxide: The role of defects. *Sol. Energy Mater. Sol. Cells* **2004**, *84*, 315–328. [CrossRef]

6. Huang, Z.-F.; Song, J.; Pan, L.; Zhang, X.; Wang, L.; Zou, J.-J. Tungsten Oxides for Photocatalysis, Electrochemistry, and Phototherapy. *Adv. Mater.* **2015**, *27*, 5309–5327. [CrossRef]

7. Nath, N.C.D.; Choi, S.Y.; Jeong, H.W.; Lee, J.-J.; Park, H. Stand-alone photoconversion of carbon dioxide on copper oxide wire arrays powered by tungsten trioxide/dye-sensitized solar cell dual absorbers. *Nano Energy* **2016**, *25*, 51–59. [CrossRef]

8. Zheng, G.; Wang, J.; Liu, H.; Murugadoss, V.; Zu, G.; Che, H.; Lai, C.; Li, H.; Ding, T.; Gao, Q.; et al. Tungsten oxide nanostructures and nanocomposites for photoelectrochemical water splitting. *Nanoscale* **2019**, *11*, 18968–18994. [CrossRef]

9. Sivakarthik, P.; Thangaraj, V.; Parthibavarman, M. A facile and one-pot synthesis of pure and transition metals (M = Co & Ni) doped WO_3 nanoparticles for enhanced photocatalytic performance. *J. Mater. Sci. Mater. Electron.* **2017**, *28*, 5990–5996. [CrossRef]

10. Gao, W.-B.; Ling, Y.; Liu, X.; Sun, J.-L. Simple point contact WO_3 sensor for NO_2 sensing and relevant impedance analysis. *Int. J. Miner. Met. Mater.* **2012**, *19*, 1142–1148. [CrossRef]

11. Juodkazytė, J.; Šebeka, B.; Savickaja, I.; Petrulevičienė, M.; Butkutė, S.; Jasulaitienė, V.; Selskis, A.; Ramanauskas, R. Electrolytic splitting of saline water: Durable nickel oxide anode for selective oxygen evolution. *Int. J. Hydrogen Energy* **2019**, *44*, 5929–5939. [CrossRef]

12. Xu, Y.; Lou, C.; Zheng, L.; Zheng, W.; Liu, X.; Kumar, M.; Zhang, J. Highly sensitive and selective detection of acetone based on platinum sensitized porous tungsten oxide nanospheres. *Sens. Actuators B Chem.* **2020**, *307*, 127616. [CrossRef]

13. Gao, P.; Ji, H.; Zhou, Y.; Li, X. Selective acetone gas sensors using porous WO_3–Cr_2O_3 thin films prepared by sol–gel method. *Thin Solid Films* **2012**, *520*, 3100–3106. [CrossRef]

14. Navarrete, E.; Bittencourt, C.; Umek, P.; Llobet, E. AACVD and gas sensing properties of nickel oxide nanoparticle decorated tungsten oxide nanowires. *J. Mater. Chem. C* **2018**, *6*, 5181–5192. [CrossRef]

15. Urasinska-Wojcik, B.; Vincent, T.A.; Chowdhury, M.F.; Gardner, J.W. Ultrasensitive WO_3 gas sensors for NO_2 detection in air and low oxygen environment. *Sens. Actuators B Chem.* **2017**, *239*, 1051–1059. [CrossRef]

16. Zhang, C.; Boudiba, A.; De Marco, P.; Snyders, R.; Olivier, M.-G.; Debliquy, M. Room temperature responses of visible-light illuminated WO_3 sensors to NO2 in sub-ppm range. *Sens. Actuators B Chem.* **2013**, *181*, 395–401. [CrossRef]

17. Ramanavicius, S.; Tereshchenko, A.; Karpicz, R.; Ratautaite, V.; Bubniene, U.; Maneikis, A.; Jagminas, A.; Ramanavicius, A. TiO₂-x/TiO₂-Structure Based 'Self-Heated' Sensor for the Determination of Some Reducing Gases. *Sensors* **2019**, *20*, 74. [CrossRef]

18. Dilova, T.; Atanasova, G.; Dikovska, A.O.; Nedyalkov, N. The effect of light irradiation on the gas-sensing properties of nanocomposites based on ZnO and Ag nanoparticles. *Appl. Surf. Sci.* **2020**, *505*, 144625. [CrossRef]

19. Chinh, N.D.; Kim, C.; Kim, D. UV-light-activated H₂S gas sensing by a TiO₂ nanoparticulate thin film at room temperature. *J. Alloys Compd.* **2019**, *778*, 247–255. [CrossRef]

20. Trawka, M.P.; Smulko, J.; Hasse, L.Z.; Granqvist, C.-G.; Ionescu, R.; Llobet, E.; Annanouch, F.E.; Kish, L.B. UV-Light Induced Fluctuation Enhanced Sensing by WO₃-based Gas Sensors. *IEEE Sens. J.* **2016**, *16*, 5152–5159. [CrossRef]

21. Trawka, M.; Smulko, J.; Hasse, L.; Granqvist, C.-G.; Annanouch, F.E.; Ionescu, R. Fluctuation enhanced gas sensing with WO₃-based nanoparticle gas sensors modulated by UV light at selected wavelengths. *Sens. Actuators B Chem.* **2016**, *234*, 453–461. [CrossRef]

22. Su, P.-G.; Yu, J.-H.; Pi-Guey, S.; Jia-Hao, Y. Enhanced NO₂ gas-sensing properties of Au-Ag bimetal decorated MWCNTs/WO3 composite sensor under UV-LED irradiation. *Sens. Actuators A Phys.* **2020**, *303*, 111718. [CrossRef]

23. Gonzalez, O.; Welearegay, T.G.; Llobet, E.; Vilanova, X. Pulsed UV Light Activated Gas Sensing in Tungsten Oxide Nanowires. *Procedia Eng.* **2016**, *168*, 351–354. [CrossRef]

24. Saidi, T.; Palmowski, D.; Babicz-Kiewlicz, S.; Welearegay, T.G.; El Bari, N.; Ionescu, R.; Smulko, J.; Bouchikhi, B. Exhaled breath gas sensing using pristine and functionalized WO₃ nanowire sensors enhanced by UV-light irradiation. *Sens. Actuators B Chem.* **2018**, *273*, 1719–1729. [CrossRef]

25. Cho, M.; Park, I. Recent Trends of Light-enhanced Metal Oxide Gas Sensors: Review. *J. Sens. Sci. Technol.* **2016**, *25*, 103–109. [CrossRef]

26. Yao, Y.; Yin, M.; Yan, J.; Yang, N.; Liu, S. Controllable synthesis of Ag-WO₃ core-shell nanospheres for light-enhanced gas sensors. *Sens. Actuators B Chem.* **2017**, *251*, 583–589. [CrossRef]

27. Lemire, C.; Lollman, D.B.; Al Mohammad, A.; Gillet, E.; Aguir, K. Reactive R.F. magnetron sputtering deposition of WO3 thin films. *Sens. Actuators B Chem.* **2002**, *84*, 43–48. [CrossRef]

28. Hu, L.; Hu, P.; Chen, Y.; Lin, Z.; Qiu, C. Synthesis and Gas-Sensing Property of Highly Self-assembled Tungsten Oxide Nanosheets. *Front. Chem.* **2018**, *6*, 4–7. [CrossRef]

29. Nakakura, S.; Arif, A.F.; Rinaldi, F.G.; Hirano, T.; Tanabe, E.; Balgis, R.; Ogi, T. Direct synthesis of highly crystalline single-phase hexagonal tungsten oxide nanorods by spray pyrolysis. *Adv. Powder Technol.* **2019**, *30*, 6–12. [CrossRef]

30. Yamaguchi, Y.; Imamura, S.; Ito, S.; Nishio, K.; Fujimoto, K. Influence of oxygen gas concentration on hydrogen sensing of Pt/WO3 thin film prepared by sol–gel process. *Sens. Actuators B Chem.* **2015**, *216*, 394–401. [CrossRef]

31. Chai, Y.; Ha, F.; Yam, F.; Hassan, Z. Fabrication of Tungsten Oxide Nanostructure by Sol-Gel Method. *Procedia Chem.* **2016**, *19*, 113–118. [CrossRef]

32. Poongodi, S.; Kumar, P.S.; Mangalaraj, D.; Ponpandian, N.; Meena, P.; Masuda, Y.; Lee, C. Electrodeposition of WO₃ nanostructured thin films for electrochromic and H₂S gas sensor applications. *J. Alloys Compd.* **2017**, *719*, 71–81. [CrossRef]

33. Yan, D.; Li, S.; Liu, S.; Tan, M.; Cao, M. Electrodeposited tungsten oxide films onto porous silicon for NO₂ detection at room temperature. *J. Alloys Compd.* **2018**, *735*, 718–727. [CrossRef]

34. Zhou, D.; Che, B.; Kong, J.; Lu, X. A nanocrystalline tungsten oxide electrochromic coating with excellent cycling stability prepared via a complexation-assisted sol–gel method. *J. Mater. Chem. C* **2016**, *4*, 8041–8051. [CrossRef]

35. Au, B.W.-C.; Chan, K.Y.; Knipp, D. Effect of film thickness on electrochromic performance of sol-gel deposited tungsten oxide (WO₃). *Opt. Mater.* **2019**, *94*, 387–392. [CrossRef]

36. Malakauskaite-Petruleviciene, M.; Stankeviciute, Z.; Niaura, G.; Prichodko, A.; Kareiva, A. Synthesis and characterization of sol–gel derived calcium hydroxyapatite thin films spin-coated on silicon substrate. *Ceram. Int.* **2015**, *41*, 7421–7428. [CrossRef]

37. Hariharan, V.; Radhakrishnan, S.; Parthibavarman, M.; Dhilipkumar, R.; Chinnathambi, S. Synthesis of polyethylene glycol (PEG) assisted tungsten oxide (WO₃) nanoparticles for l-dopa bio-sensing applications. *Talanta* **2011**, *85*, 2166–2174. [CrossRef]

38. Ng, K.H.; Minggu, L.J.; Kassim, M.B. Gallium-doped tungsten trioxide thin film photoelectrodes for photoelectrochemical water splitting. *Int. J. Hydrog. Energy* **2013**, *38*, 9585–9591. [CrossRef]

39. Zeng, Q.; Li, J.; Bai, J.; Li, X.; Xia, L.; Zhou, B. Preparation of vertically aligned WO$_3$ nanoplate array films based on peroxotungstate reduction reaction and their excellent photoelectrocatalytic performance. *Appl. Catal. B Environ.* **2017**, *202*, 388–396. [CrossRef]

40. Amano, F.; Li, D.; Ohtani, B. Fabrication and photoelectrochemical property of tungsten(vi) oxide films with a flake-wall structure. *Chem. Commun.* **2010**, *46*, 2769–2771. [CrossRef]

41. Kalanur, S.S.; Duy, L.T.; Seo, H. Recent Progress in Photoelectrochemical Water Splitting Activity of WO$_3$ Photoanodes. *Top. Catal.* **2018**, *61*, 1043–1076. [CrossRef]

42. Xiong, Y.; Zhu, Z.; Guo, T.; Li, H.; Xue, Q. Synthesis of nanowire bundle-like WO$_3$-W$_{18}$O$_{49}$ heterostructures for highly sensitive NH$_3$ sensor application. *J. Hazard. Mater.* **2018**, *353*, 290–299. [CrossRef] [PubMed]

43. Kim, K.H.; Lee, Y.B.; Choi, E.Y.; Park, H.C.; Park, S.S. Synthesis of nickel powders from various aqueous media through chemical reduction method. *Mater. Chem. Phys.* **2004**, *86*, 420–424. [CrossRef]

44. Imran, M.; Rashid, S.S.A.A.H.; Sabri, Y.M.; Motta, N.; Tesfamichael, T.; Sonar, P.M.; Shafiei, M.; Rashi, S.S.A.A.H. Template based sintering of WO$_3$ nanoparticles into porous tungsten oxide nanofibers for acetone sensing applications. *J. Mater. Chem. C* **2019**, *7*, 2961–2970. [CrossRef]

45. Hatel, R.; Baitoul, M. Nanostructured Tungsten Trioxide (WO$_3$): Synthesis, structural and morphological investigations. *J. Phys. Conf. Ser.* **2019**, *1292*, 012014. [CrossRef]

46. Shen, Y.; Wang, W.; Chen, X.; Zhang, B.; Wei, D.; Gao, S.; Cui, B. Nitrogen dioxide sensing using tungsten oxide microspheres with hierarchical nanorod-assembled architectures by a complexing surfactant-mediated hydrothermal route. *J. Mater. Chem. A* **2016**, *4*, 1345–1352. [CrossRef]

47. Zhang, J.; Zhang, W.; Yang, Z.; Yu, Z.; Zhang, X.; Chang, T.C.; Javey, A. Vertically aligned tungsten oxide nanorod film with enhanced performance in photoluminescence humidity sensing. *Sens. Actuators B Chem.* **2014**, *202*, 708–713. [CrossRef]

48. Mendoza-Agüero, N.; Agarwal, V. Optical and structural characterization of tungsten oxide electrodeposited on nanostructured porous silicon: Effect of annealing atmosphere and temperature. *J. Alloys Compd.* **2013**, *581*, 596–601. [CrossRef]

49. Patil, V.; Adhyapak, P.; Suryavanshi, S.; Mulla, I. Oxalic acid induced hydrothermal synthesis of single crystalline tungsten oxide nanorods. *J. Alloys Compd.* **2014**, *590*, 283–288. [CrossRef]

50. Wang, N.; Sun, J.; Cao, X.; Zhu, Y.; Wang, Q.; Wang, G.; Han, Y.; Lu, G.; Pang, G.; Feng, S. High-performance gas sensing achieved by mesoporous tungsten oxide mesocrystals with increased oxygen vacancies. *J. Mater. Chem. A* **2013**, *1*, 8653–8657. [CrossRef]

51. Su, C.-Y.; Lin, H.-C. Direct Route to Tungsten Oxide Nanorod Bundles: Microstructures and Electro-Optical Properties. *J. Phys. Chem. C* **2009**, *113*, 4042–4046. [CrossRef]

52. Feng, M.; Pan, A.L.; Zhang, H.; Li, Z.A.; Liu, F.; Liu, H.; Shi, D.X.; Zou, B.S.; Gao, H.J. Strong photoluminescence of nanostructured crystalline tungsten oxide thin films. *Appl. Phys. Lett.* **2005**, *86*, 141901. [CrossRef]

53. Chernyakova, K.; Karpicz, R.; Zavadski, S.; Poklonskaya, O.; Jagminas, A.; Vrublevsky, I. Structural and fluorescence characterization of anodic alumina/carbon composites formed in tartaric acid solution. *J. Lumin.* **2017**, *182*, 233–239. [CrossRef]

54. Chernyakova, K.; Karpicz, R.; Rutkauskas, D.; Vrublevsky, I.; Hassel, A.W. Structural and Fluorescence Studies of Polycrystalline α-Al2 O3 Obtained From Sulfuric Acid Anodic Alumina. *Phys. Status Solidi (A)* **2018**, *215*, 1700892. [CrossRef]

55. Rückschloss, M.; Wirschem, T.; Tamura, H.; Rühl, G.; Oswald, J.; Veprek, S. Photoluminescence from OH-related radiative centres in silica, metal oxides and oxidized nanocrystalline and porous silicon. *J. Lumin.* **1995**, *63*, 279–287. [CrossRef]

56. Chen, D.; Hou, X.; Li, T.; Yin, L.; Fan, B.; Wang, H.; Li, X.; Xu, H.; Lu, H.; Zhang, R.; et al. Effects of morphologies on acetone-sensing properties of tungsten trioxide nanocrystals. *Sens. Actuators B Chem.* **2011**, *153*, 373–381. [CrossRef]

57. Shi, J.; Hu, G.; Sun, Y.; Geng, M.; Wu, J.; Liu, Y.; Ge, M.; Tao, J.; Cao, M.; Dai, N. WO$_3$ nanocrystals: Synthesis and application in highly sensitive detection of acetone. *Sens. Actuators B Chem.* **2011**, *156*, 820–824. [CrossRef]

58. Horsfall, L.A.; Pugh, D.C.; Blackman, C.; Parkin, I.P. An array of WO3 and CTO heterojunction semiconducting metal oxide gas sensors used as a tool for explosive detection. *J. Mater. Chem. A* **2017**, *5*, 2172–2179. [CrossRef]

59. Vuong, N.M.; Kim, D.; Kim, H. Surface gas sensing kinetics of a WO$_3$ nanowire sensor: Part 2—Reducing gases. *Sens. Actuators B Chem.* **2016**, *224*, 425–433. [CrossRef]
60. Patil, V.B.; Adhyapak, P.V.; Patil, P.S.; Suryavanshi, S.S.; Mulla, I.S. Hydrothermally synthesized tungsten trioxide nanorods as NO$_2$ gas sensors. *Ceram. Int.* **2015**, *41*, 3845–3852. [CrossRef]
61. Ramanavičius, S.; Petrulevičienė, M.; Juodkazytė, J.; Grigucevičienė, A.; Ramanavicius, A. Selectivity of Tungsten Oxide Synthesized by Sol-Gel Method Towards Some Volatile Organic Compounds and Gaseous Materials in a Broad Range of Temperatures. *Materials* **2020**, *13*, 523. [CrossRef] [PubMed]
62. Yao, Y.; Yin, M.; Yan, J.; Liu, S. P-type sub-tungsten-oxide based urchin-like nanostructure for superior room temperature alcohol sensor. *Appl. Surf. Sci.* **2018**, *441*, 277–284. [CrossRef]
63. Sayama, K. Production of High-Value-Added Chemicals on Oxide Semiconductor Photoanodes under Visible Light for Solar Chemical-Conversion Processes. *ACS Energy Lett.* **2018**, *3*, 1093–1101. [CrossRef]
64. Cass, M.J.; Qiu, F.L.; Walker, A.B.; Fisher, A.C.; Peter, L.M. Influence of Grain Morphology on Electron Transport in Dye Sensitized Nanocrystalline Solar Cells. *J. Phys. Chem. B* **2003**, *107*, 113–119. [CrossRef]
65. Amano, F.; Ishinaga, E.; Yamakata, A. Effect of Particle Size on the Photocatalytic Activity of WO$_3$ Particles for Water Oxidation. *J. Phys. Chem. C* **2013**, *117*, 22584–22590. [CrossRef]
66. Thimsen, E.; Rastgar, N.; Biswas, P. Nanostructured TiO$_2$ Films with Controlled Morphology Synthesized in a Single Step Process: Performance of Dye-Sensitized Solar Cells and Photo Watersplitting. *J. Phys. Chem. C* **2008**, *112*, 4134–4140. [CrossRef]

3$^{\text{rd}}$ publication

Influence of morphology on photoanodic behaviour of WO$_3$ films in chloride and sulphate electrolytes

Parvin, M., M. Petrulevičienė, I. Savickaja, B. Šebeka, R. Karpicz, A. Grigucevičienė, R. Ramanauskas, and J. Juodkazytė.,
Electrochimica Acta 403 (2022) 139710

ELSEVIER

Influence of morphology on photoanodic behaviour of WO$_3$ films in chloride and sulphate electrolytes

M. Parvin, M. Petrulevičienė, I. Savickaja, B. Šebeka, R. Karpicz, A. Grigucevičienė, R. Ramanauskas, J. Juodkazytė*

Center for Physical Sciences and Technology, Saulėtekio av. 3, Vilnius LT-10257, Lithuania

ABSTRACT

Photoelectrochemical (PEC) synthesis is gaining an increasing interest amongst the advanced oxidation processes, which can convert solar energy to chemical energy in the form of value-added oxidants suitable for water treatment and disinfection. To ensure the efficient generation of desired product, careful engineering of semiconductor/electrolyte interface is required. In this study the effect of surface morphology on the competition between the photoanodic oxidation of water molecules and anions occurring on the surface of tungsten (VI) oxide electrodes in sulphate and chloride electrolytes is analysed. Four WO$_3$ coatings composed of plate-like particles, similar in shape but of different sizes, were prepared using chemical solution deposition technique and methanol, ethanol, isopropanol or butanol as reductants. Crystalline structure, morphology, surface chemical composition and optical properties of the coatings were characterised applying X-ray diffraction, scanning electron microscopy, X-ray photoelectron spectroscopy and photoluminescence spectroscopy techniques. The photoelectrochemical performance of WO$_3$ layers was studied using the methods of electrochemical impedance spectroscopy, cyclic voltammetry and chronoamperometry. Possible photoanodic processes are analysed on the basis of the proposed potential-assisted photochemical approach, which takes into consideration high oxidizing power of photogenerated holes in WO$_3$ and formation of radicals as intermediates. Significant role of specific adsorption of chloride ions as well as intermediate products of their oxidation (Cl$^·$, Cl$_2^{·-}$) in lowering the photocurrent onset potential, trapping the photogenerated charge carriers as well as protecting WO$_3$ surface from accumulation of hydroxo species is revealed. Influence of morphology on the competition between certain photoanodic reactions occurring at the semiconductor/electrolyte interface in the PEC systems investigated is explained considering the effects of steric hindrance as well as electrostatic interactions between adsorbing/reacting species at rough electrified interfaces.

© 2021 Elsevier Ltd. All rights reserved.

1. Introduction

In an ongoing effort to decrease air pollution and prevent global warming, governments worldwide are struggling to lower the emissions of greenhouse gases. Chemical industry is amongst the most polluting as well as energy- and resource-intensive sectors. Therefore, new, environmentally friendly, sustainable and economically efficient synthesis technologies are sought to replace the conventional ones. Exploitation of renewable energy sources is a prerequisite for the development of new processes. Artificial photosynthesis, which converts energy of light into chemical energy, is a promising technology and has been attracting increasing at-

tention recently. Photoelectrochemical splitting of water for sustainable production of hydrogen is one of the most intensively investigated processes in this area. The benefit of solar water splitting could be increased by coupling generation of H$_2$ on cathode with production of high added-value chemicals, e.g. HClO, H$_2$O$_2$, H$_2$S$_2$O$_8$, etc. on photoanode, as demonstrated recently in [1]. According to a recent review [2], PEC generation of strong oxidants is gaining its place amongst the advanced oxidation processes, which are especially suitable for water disinfection and purification. Deliberate choice of PEC system (photoelectrode + electrolyte) is required in order to achieve high efficiency of the process. Tungsten (VI) oxide as a photoanode material is of special interest here due to its excellent combination of properties as discussed further. Moderate band gap of 2.5 - 2.8 eV makes WO$_3$ visible light responsive, it has good resistance against photocorrosion and chemical stability at pH < 4, high carrier mobility of 10 cm^2 V^{-2} s^{-1}, moderate carrier lifetime of 1 to 9 ns and relatively large hole

diffusion length ranging between 150 and 500 nm [3]. Moreover, the potential of valence band edge in WO_3 is above 3 V (SHE) [4], rendering high oxidizing power to photogenerated holes, which is of great relevance in the processes of organic waste degradation and water disinfection. It is also well known that the product of photoanodic reactions taking place on WO_3 electrodes strongly depends on the composition of electrolyte [1,5–8]. Chloride and sulphate solutions are of particular interest because of the possibility to photoelectrochemically produce active chlorine and sulphate species, which are strong oxidants used for disinfection [2]. In PEC systems anions compete with water molecules at the photoelectrode/electrolyte interface for the active sites to react with photogenerated holes. Interfacial energetics is an important aspect here and it is strongly dependent on the solution composition, presence of specifically adsorbing species, surface roughness as well as concentration of surface states. Therefore, it is very important to identify the factors, which determine the efficiency of the photoanodic reactions and affect the competition between them as well as to understand the mechanism of the processes involved. The influence of morphology of photoactive WO_3 layers on their PEC performance as well as importance of crystal facet engineering are well known and have been addressed in numerous studies and reviews [9–14]. As a rule, the effect of morphology on photoactivity of a material is analysed in terms of overall photocurrent obtained in a certain photoelectrochemical cell, whereas the question of how WO_3 morphology influences the competition between the photoanodic oxidation of water vs anion has not been given due attention so far.

In this study WO_3 layers of different morphology were formed using simple chemical solution deposition technique and their PEC performance in the solutions of H_2SO_4, NaCl and their mixture was investigated in order to understand which factors govern the competition between the photoanodic oxidation of water molecules and Cl^- or SO_4^{2-} ions. Photoelectrochemical behaviour of WO_3 samples was analysed taking into consideration the results of structural and optical characterization of the materials obtained using the methods of X-ray diffraction and photoluminescence spectroscopy. Novel approach invoking potential-assisted photochemical mechanism of photoanodic reactions on WO_3 is applied for the interpretation of the experimental results.

2. Experimental

2.1. Preparation of WO_3 films

All chemicals were of analytical grade and were used as received from suppliers without any further purification. WO_3 thin films on conducting glass (fluoride doped tin oxide - FTO) substrate were prepared using chemical solution deposition method following the slightly modified procedure described in [15]. FTO coated glass substrates (6 - 9 Ω/sq) were cut into fixed 2.5 × 1 cm^2 slides and washed consecutively in acetone (Reachem), isopropanol (Reachem) and deionised water under ultrasonication for 15 min in each solvent. At first, 0.8 mg of $Na_2WO_4 \cdot 2H_2O$ (Carl Roth) and 0.3 mg of $(NH_4)_2C_2O_4$ (Chempur) as capping agent were dissolved in 66 ml of distilled water and 18 ml of HCl (37%) (Chempur) was added into this solution under continuous stirring for 10 min at 50 °C to get tungstic acid (H_2WO_4). Subsequently, 16 ml of H_2O_2 (30%) were added into the suspension to form peroxotungstic acid (PTA) and the solution was stirred for 10 min. Next, 60 ml of reductant (methanol (MeOH), ethanol (EtOH), isopropanol (IsoPrOH) or butanol (BuOH)) were added and after 10 min, 8 pieces of cleaned FTO substrates were dipped into the solution in a FTO side-down position and kept for 180 min under water bath conditions at 85 °C. After that samples were rinsed in distilled water for 1 min and dried in the drying oven at 50 °C for 12 h. Finally, the coat-

ings were annealed at 400 °C for 2 h with heating rate of 1 °C min^{-1} to remove residual carbon and to obtain crystalline WO_3 films. Further in the text WO_3 coatings prepared using different reductants are denoted as MeOH_WO_3, EtOH_WO_3, IsoPrOH_WO_3 and BuOH_WO_3.

2.2. Characterization of oxide layers

2.2.1. X-ray diffraction and scanning electron microscopy measurements

XRD patterns of WO_3 films on FTO substrate were measured using an X-ray diffractometer SmartLab (Rigaku) equipped with 9 kW rotating Cu anode X-ray tube. Grazing incidence (GIXRD) method was used in 2θ range 10–75°. An angle between a parallel beam of X-rays and a specimen surface was adjusted to 0.5 °C. Phase identification was performed using Match software and Crystallography Open Database (COD). The average crystallite size, D, of WO_3 coatings was calculated using the Debye-Scherrer formula [16]:

$$D = \frac{k\,\lambda}{\beta cos\,\theta} \qquad (1)$$

where, k is the Scherrer constant (predictable shape factor of 0.9 was used), λ is the wavelength of the X-ray used (0.15406 nm), θ is the Bragg diffraction angle (in degrees) and β is the full width at half maximum (FWHM) of the diffraction peak (in radians). For calculations all reflections within a 2θ range from 20 to 60° were used.

The average dislocation density (δ) and stacking fault (SF) values were determined using the following equations [17]:

$$\delta = \frac{1}{D^2} \qquad (2)$$

$$SF = \left[\frac{2\pi^2}{45(3tan\theta)^{1/2}} \right]\beta \qquad (3)$$

The surface morphology of the tungsten oxide layers on FTO substrate was investigated using Helios NanoLab dual beam workstation equipped with X-Max 20 mm^2 energy dispersion spectrometer (Oxford Instruments).

Texture of WO_3 coatings deposited on the FTO substrate was analysed by creating 3D surface plots of SEM micrographs using ImageJ software https://imagej.nih.gov/ij/. Dimensions of morphological features of WO_3 films were determined using the same software.

2.2.2. Photoluminescence spectroscopy measurements

To evaluate the optical properties of WO_3 coatings as a function of thin film morphology, photoluminescence (PL) spectroscopy was used. Optical characterization was performed using a time-correlated single photon counting Edinburgh-F900 spectrophotometer (Edinburgh Instruments Ltd., Livingston, UK). The photoluminescence spectra were excited by a solid-state laser with an excitation wavelength of 375 nm (the average pulse power was about 0.15 mW mm^{-2}, the pulse duration was 76 ps) and measured in the range of 400 to 600 nm. All photoluminescence spectra were corrected for the instrument sensitivity.

2.2.3. Photoelectrochemical measurements

Photoelectrochemical measurements (cyclic voltammetry (CV), chronoamperometry (CA) and electrochemical impedance spectroscopy (EIS)) were performed using three-electrode cell and potentiostat/galvanostat AUTOLAB 302 (Ecochemie, Utrecht, The Netherlands). Tungsten (VI) oxide films on FTO substrates were used as working electrodes. Silver/silver chloride electrode with saturated KCl solution (E = 0.197 V (SHE)) and Pt plate (1 × 1 cm^2) were used as reference and counter electrodes, respectively.

All potential values in the text refer to Ag/AgCl scale unless noted otherwise. The surface of working electrodes was illuminated with a high intensity discharge Xe-lamp with 6000 K spectrum and calibrated with a silicon diode to simulate AM 1.5 illumination ($\sim$100 mW cm^{-2}) at the sample surface. The area of WO$_3$ samples exposed to electrolyte was 1 cm^2. Current density values were calculated based on the geometric area of the working electrode.

CA experiments were carried out in 0.5 M H$_2$SO$_4$ and 0.5 M NaCl solutions at a constant applied potential of 0.7 V and 0.4 V, respectively, under chopped illumination. The light on-off condition was controlled manually with a time interval of 100 s.

EIS measurements were conducted under continuous illumination in 0.5 M H$_2$SO$_4$ electrolyte. The spectra were recorded under the open-circuit potential in potentiostatic mode with the AC voltage amplitude of $\pm$ 10 mV. The frequency range from 10^5 to 0.01 Hz was explored. The fitting of EIS data was performed using ZSimpWin software. Mott-Schottky measurements were performed in dark at a fixed frequency of 1000 Hz with an AC voltage amplitude of $\pm$ 10 mV. Donor density, N_D, was evaluated from the slope of $1/C^2$ - E plots according to the equation:

$$\frac{1}{C^2} = \frac{2}{\varepsilon \varepsilon^0 A^2 e N_D}\left(E - E_{FB} - \frac{K_B T}{e}\right) \tag{4}$$

where C is the specific capacitance (F cm^{-2}), ε is the relative permittivity of semiconductor (50 for WO$_3$ [18]) and ε^0 is the permittivity of vacuum (8.854 $\times$ 10^{-14} F cm^{-1}), A is the area of electrode (cm^2), e is the electron charge (1.60$\times$10^{-19}C), N_D is the donor density (cm^{-3}), E is the applied electrode potential, E_{FB} is the flat band potential, K_B is the Boltzman constant and T is the temperature in absolute scale.

To determine the Faradaic efficiency (FE) of photoelectrochemical generation of S$_2$O$_8{}^{2-}$ and active chlorine species (ClO$^-$+ ClO$_2{}^-$), photoelectrolysis experiments were performed in 0.5 M H$_2$SO$_4$ and 0.5 M NaCl solutions, respectively, in a two-electrode cell with Pt cathode. The anodic and cathodic compartments of the cell were separated with a glass frit. Cell voltage of 1.8 V in 0.5 M H$_2$SO$_4$ and 1.6 V in 0.5 M NaCl was applied. Under such conditions the photocurrent was sufficiently high, whereas the dark current was still negligible. Photoelectrolysis with a particular WO$_3$ photoelectrode was performed 5 times with periods of increasing duration: 500 s, 1000 s, 1500 s, 2000 s and 2500 s (the cumulative duration for each sample was 7500 s). After each period, solution from the anodic compartment of the cell was collected and subjected to titrimetric analysis to determine the amount of photoelectrochemically formed S$_2$O$_8{}^{2-}$ or ClO$^-$ + ClO$_2{}^-$ (m_{exp}). For determination of persulfate, dichromatometry was used, whereas the amount of active chlorine species (ACS) was quantified with the help of iodometric titration in slightly alkaline acetate medium (for ClO$^-$) and acidic sulfuric acid medium (for ClO$^-$ + ClO$_2{}^-$). Detailed description of the procedures and calculations involved in this analysis is given in the Supporting Information. The FE (%) of the photoelectrochemical generation of active chlorine and sulfate species was evaluated as the ratio m_{exp}/m_{theor}, where m_{theor} is the theoretical mass calculated according to Faraday's law assuming two electron transfer in Cl$^-$ → ClO$^-$, ClO$^-$ → ClO$_2{}^-$ and 2SO$_4{}^{2-}$ → S$_2$O$_8{}^{2-}$ transitions.

2.2.4. X-ray photoelectron spectroscopy measurements

In order to test the effect of photoelectrolysis on the surface chemical state of WO$_3$, the selected samples were subjected to 1-hour long photoelectrolysis at 1.6 V (vs. Pt) in 0.5 M H$_2$SO$_4$ or at 1.4 V (vs. Pt) in 0.5 M NaCl. After that WO$_3$ photoelectrodes were soaked for 10 min in deionised water and dried in air under ambient conditions. X-ray photoelectron spectra (XPS) of analysed samples were acquired with Kratos Axis Supra XPS spectrometer. The spectra were recorded by using monochromatic Al Kα X-ray source and charge neutraliser to compensate sample charging.

160 eV and 20 eV pass energies were used to acquire survey and region spectra respectively. Binding energy calibration was applied by setting C 1 s binding energy value to 284.8 eV. Region spectra fitting were performed with Kratos Escape software by using Shirley background type and symmetric GL (Gaussian/Lorenzian) lineshape. For fitting W 4f region, 4f 7/2 and 4f 5/2 peak separation and area parameters were constrained to 2.14 eV and 4:3 respectively.

3. Results and discussion

3.1. Morphological and structural properties of WO$_3$ coatings

SEM images of WO$_3$ films deposited on FTO substrate using four different alcohols as reductants are shown in Fig. 1. The coatings are composed of plate-shaped particles of different size and rather random orientation. In terms of morphology, the films can be arranged into the following sequence showing the transition from the finest to the coarsest morphology: MeOH_WO$_3$ < BuOH_WO$_3$ < EtOH_WO$_3$ < IsoPrOH_WO$_3$. The average dimensions (length/thickness) of the platelets determined from the SEM images of WO$_3$ coatings were about 475/65 nm (MeOH_WO$_3$), 1125/225 nm (EtOH_WO$_3$), 1330/250 nm (IsoPrOH_WO$_3$) and 620/100 nm (BuOH_WO$_3$). It is also evident from average surface roughness plots in Fig. 1, that IsoPrOH_WO$_3$ coating is more rough with larger and higher protruding features compared to other films. The differences in morphology indicate that alcohol acts as a structure-directing agent and finely-tuned morphology may be obtained by adjusting the reductant used in the synthesis. A separate study of this research group is devoted to detailed investigation of synthesis-dependent evolution of WO$_3$ structure, therefore only a short explanation is presented herein. It is known that reducing ability of alcohols decreases with increase in carbon chain length [19,20], whereas the stability of WO$_3$ particles strongly depends on the dielectric constant, k, of the reaction mixture [21]. The dielectric constants of water and alcohols used in the synthesis are as follows: H$_2$O - 80.37, MeOH - 32.35, EtOH - 25.0, IsoPrOH - 18.62 and BuOH −17.43 (at 20 °C) [22,23]. Addition of alcohols with lower k to water induces precipitation of dissolved substances due to decrease in solvation energy. Furthermore, the energy barrier which inhibits the agglomeration of precipitating particles, is directly proportional to dielectric constant of the liquid medium and the surface potential. Therefore smaller (less agglomerated) particles are formed in the synthesis with alcohols having higher k. This trend is obvious in the series MeOH_WO$_3$ < EtOH_WO$_3$ < IsoPrOH_WO$_3$ with an exception of BuOH_WO$_3$. Fine-plate morphology of BuOH_WO$_3$ could be attributed to the lowest reducing ability of butanol and more sluggish reaction kinetics. Further we present thorough analysis of phase composition, crystallinity and concentration of defects in the synthesised WO$_3$ layers, because these factors are of great importance in photoelectrochemical studies.

The results of XRD investigations are shown in Fig. 2. All patterns exhibit the clusters of the most prominent peaks at 2θ = 22–25° and 33–34°, which, respectively, correspond to (020), (200), (202) and (022), (202), (212), facets of monoclinic crystalline WO$_3$ phase (COD: 2106382). Diffractogram of the IsoPrOH_WO$_3$ displays the most intense and sharp peaks with lower FWHM, indicating higher crystallinity of this sample compared to the coatings formed with other reductants. The highest FWHM values were obtained for MeOH_WO$_3$ coatings. Fig. 2b illustrates the shift of peak positions of the most prominent peaks within the 2θ range of 22–26°. Peak-broadening and shifting of the reflection peaks (Fig. 2b) can be attributed to decrease in crystallite size, increasing degree of structural disorder (stacking faults, dislocations, grain boundaries) and related lattice strain (microstresses, long range internal stresses)
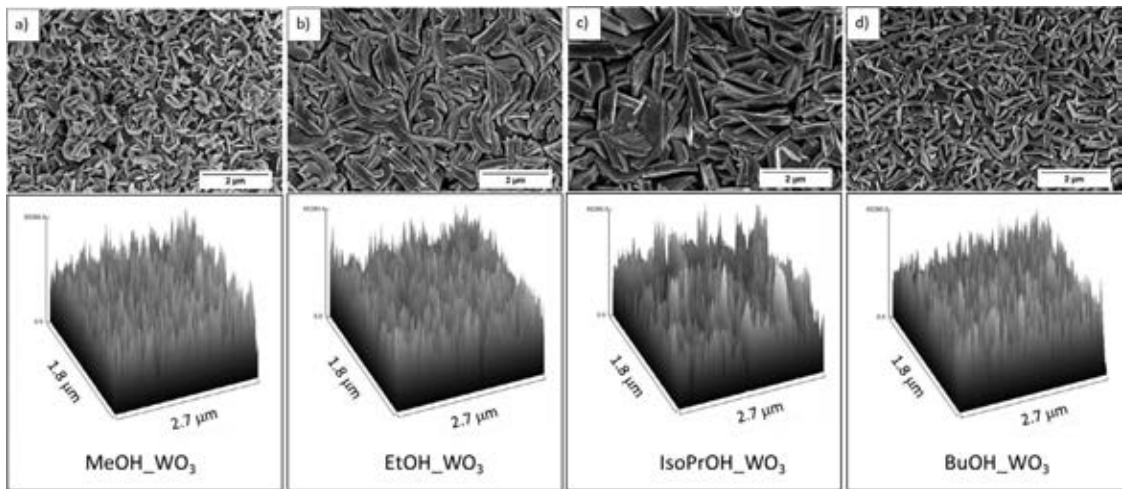
Fig. 1. SEM images (top) and surface roughness plots (bottom) of WO$_3$ films prepared using MeOH (a), EtOH (b), IsoPrOH (c) and BuOH (d) as reductants in synthesis.
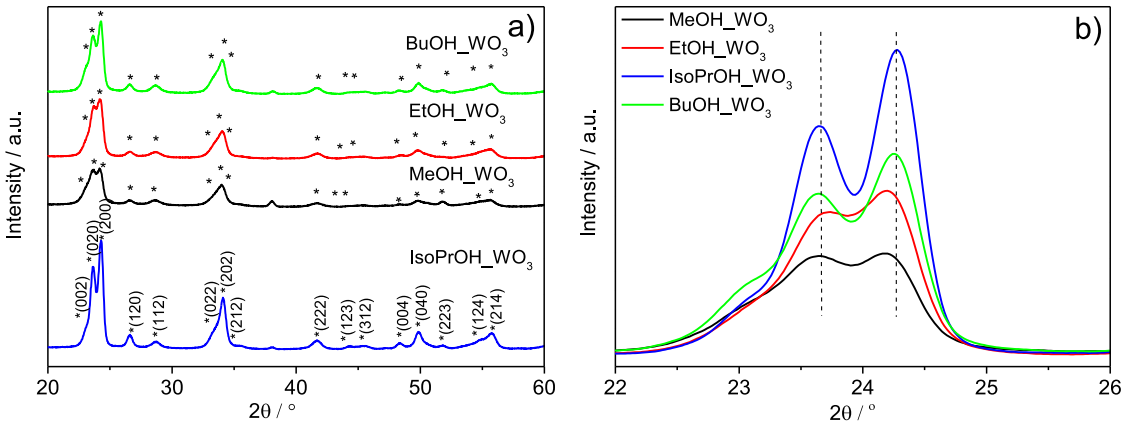

Fig. 2. a) XRD spectra of WO$_3$ films prepared using different reductants; b) comparison of XRD spectra of the same samples within 2θ range 22–26°, showing the shift of peak positions.

Table 1
Summary of results of XRD, EIS and PL analysis of WO$_3$ coatings formed using different reductants.

Sample	Average crystallite size D, nm	Dislocation density $\partial \times 10^{16}$, lines m^{-2}	Stacking fault	Solution resistance R$_s$, Ω cm^2	Constant phase element CPE, Y$_0$, S sec^n	n	Charge transfer resistance R$_{ct}$, Ω cm^2	χ^2	Fitting error Z$_{err}$,%	Donor density N$_D$, cm^{-3}	Carrier lifetime τ_{ave}, ns
MeOH_WO$_3$	8.2 ± 2.8	1.5	0.011	20.14	0.0004356	0.93	3712	2.3×10^{-3}	1.3	1.7×10^{19}	0.83
EtOH_WO$_3$	9.4 ± 3.0	1.1	0.008	36.39	0.0007593	0.92	2004	3.6×10^{-3}	1.7	7.4×10^{19}	0.72
IsoPrOH_WO$_3$	11.3 ± 3.3	0.8	0.006	34.23	0.0006864	0.88	1592	4.9×10^{-3}	2	4.4×10^{20}	1.4
BuOH_WO$_3$	9.5 ± 3.2	1.1	0.008	20.17	0.0007411	0.94	1495	2.1×10^{-3}	1.3	9.2×10^{19}	0.56

[24,25]. The largest crystallites with the least dislocation density and stacking disorder degree were found in IsoPrOH_WO$_3$. In contrast, MeOH_WO$_3$ film had the lowest crystallite size and the highest amount of structural defects (see Table 1).

The above described structural defects, present in the bulk of the synthesised layers, can affect the mobility of photo-generated charge carriers by hindering their transport within the crystal lattice. The influence of these defects on charge transfer resistance of WO$_3$ layers was evaluated by means of electrochemical impedance spectroscopy, whereas the presence of defects on the surface of the coatings was studied using photoluminescence spectroscopy.

3.2. Evaluation of charge transfer resistance, donor density and charge carrier lifetime in WO$_3$ layers

The results of EIS investigations are presented in Fig. 3. Clear semicircle appears for all WO$_3$ coatings. The impedance data were fitted using Randles circuit, which consists of a charge transfer
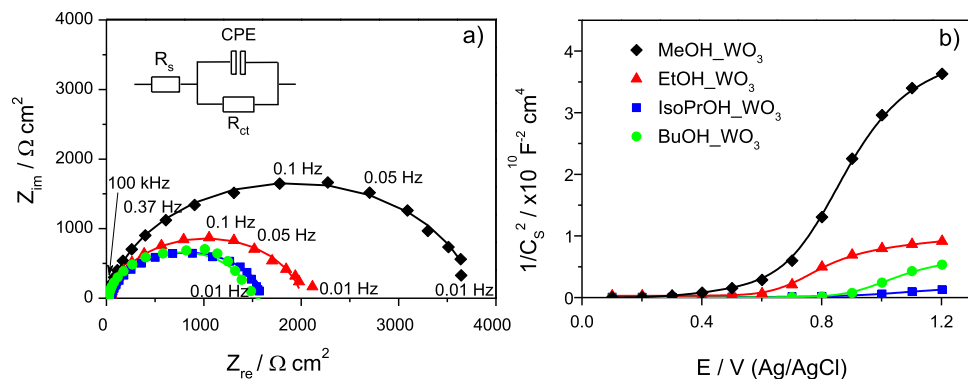
Fig. 3. a) Nyquist plots of WO_3 coatings formed using MeOH, EtOH, IsoPrOH and BuOH as reductants: symbols represent the experimental points and lines represent the fitting data; inset shows the equivalent circuit used for fitting; illumination intensity $\sim$ 100 mW cm^{-2}; b) Mott Schottky plots of the same samples obtained at 1000 Hz in 0.5 M H_2SO_4 solution.
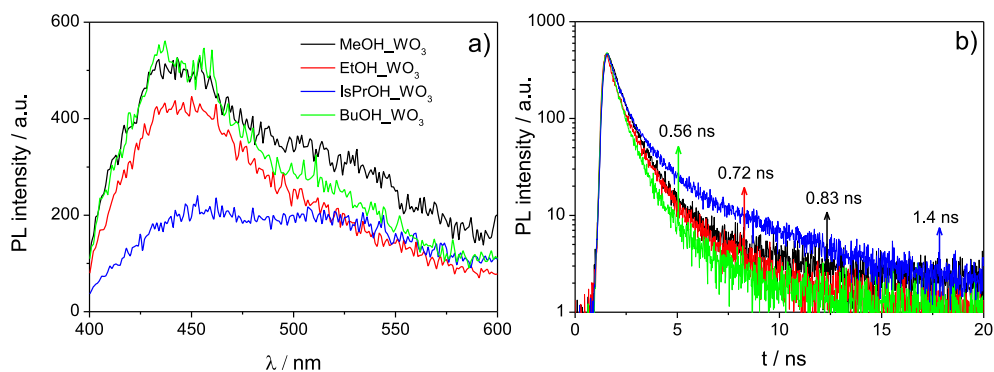

Fig. 4. a) Room-temperature photoluminescence spectra of WO_3 coatings formed using MeOH, EtOH, IsoPrOH and BuOH as reductants; excitation wavelength 375 nm; b) time resolved photoluminescence decay kinetics of the same samples; excitation wavelength 430 nm; values of average decay time are indicated in the figure.

resistance (R_{ct}) that is connected with a constant phase element (CPE) in parallel and solution resistance (R_s) in series (inset in Fig. 3a). The fitted values of these parameters are summarised in Table 1. Smaller arc radius in Nyquist plots (Fig. 3a) is associated with more efficient separation, transport as well as interfacial transfer of photoinduced charge carriers, whereas larger radius suggests a more hindered photoelectrochemical process [13,26]. There is obviously a large gap between R_{ct} of MeOH_WO$_3$ and those of other samples, which can be understood considering the results of morphological and structural observations discussed above: MeOH_WO$_3$ composed of the smallest plates with the smallest crystallite size and having the highest dislocation density as well as stacking fault degree (see Table 1) showed inferior characteristics of charge transport, because high concentration of structural defects provided resistance for migration of charge carriers. Further clues to understanding the EIS results can be obtained from Mott-Schottky plots shown in Fig. 3b. A positive slope expected for n-type semiconductors was observed for all the samples. The donor density, N_D, evaluated from the slope of the plots was 1.7×10^{19}, 7.4×10^{19}, 4.4×10^{20} and 9.2×10^{19} cm^{-3} for MeOH_WO$_3$, EtOH_WO$_3$, IsoPrOH_WO$_3$ and BuOH_WO$_3$ samples, respectively, which is similar to previously reported data for WO$_3$ [27,28]. N_D of MeOH_WO$_3$ was the lowest, which also was a contributing factor to higher R_{ct}, whereas the high donor density and low degree of structural disorder of IsoPrOH_WO$_3$ resulted in

lower charge transfer resistance (Table 1). It is noteworthy that the n-type doping of metal oxides is ascribed mainly to the presence of oxygen vacancies [29]. It can be seen from Table 1 that higher donor density correlated with larger average crystallite size in WO$_3$ films.

Though structural defects in the bulk of oxide layer play an important role in transport of photoinduced charge carriers, the most important processes in PEC systems occur at electrode/electrolyte interface, where the so-called surface states can act as recombination centres for electrons and holes and usually govern the kinetics of interfacial charge transfer. The presence of point defects in the interfacial region of the synthesised WO$_3$ films was probed with the help of photoluminescence spectroscopy. PL spectra in Fig. 4a exhibit two broad bands within the range from 400 to 600 nm. In accordance with literature [30,31], the so-called blue emission band with maximum at 435 - 450 nm is attributed to radiative recombination of photo-induced charge carriers. The green emission band at $\lambda > 500$ nm is due to oxygen vacancies, localised states and defects present within the band gap [32–35]. Considering the whole range of wavelengths shown in Fig. 4a, it can be seen that PL intensity decreases in the sequence MeOH_WO$_3$ > BuOH_WO$_3$ > EtOH_WO$_3$ > IsoPrOH_WO$_3$, which is consistent with transition from the finest to the coarsest morphology of WO$_3$ layers (Fig. 1). Moreover, the decrease in PL intensity correlates with decrease in degree of structural disorder evaluated from XRD investigations
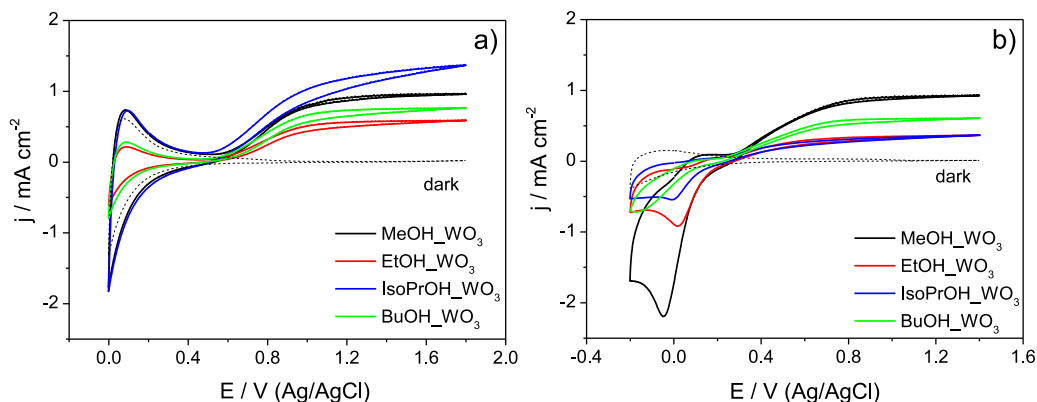
Fig. 5. Cyclic voltammograms of WO$_3$ coatings formed using MeOH, EtOH, IsoPrOH and BuOH as reductants in a) 0.5 M H$_2$SO$_4$ and b) 0.5 M NaCl; the same electrode was used in both solutions; illumination intensity 100 mW cm^{-2}; potential scan rate 50 mV s^{-1}; CVs in dark are those of IsoPrOH_WO$_3$ in both electrolytes.

(Table 1). The lower PL emission intensity implies suppressed recombination rate of photoinduced charge carriers. The significantly lower intensity of blue emission peak (at 450 nm) of IsoPrOH_WO$_3$ compared to other samples suggests that rapid band to band recombination is suppressed due to trapping of charge carriers by oxygen vacancies or some other structural defects of crystal lattice. This is consistent with the highest N_D of IsoPrOH_WO$_3$ as well as the results of time-resolved photoluminescence decay measurements shown in Fig. 4b. It can be seen that the average decay time, which is equivalent to lifetime of charge carriers, τ_{ave}, was significantly longer in the case of IsoPrOH_WO$_3$, i.e. 1.4 ns, compared to other samples (0.56, 0.72 and 0.83 ns for BuOH_WO$_3$, EtOH_WO$_3$ and MeOH_WO$_3$, respectively) (Fig. 4b). It is important to note here, that in order to have efficient PEC performance, the amount of defects at the interfacial region of a semiconductor should be sufficient to facilitate charge separation, but not too large to impede PEC reactions due to trap-mediated recombination of electrons and holes [29]. As will be shown further, however, the efficiency of charge transfer in a photoelectrochemical systems depends to a large extent on the nature of hole-scavenging species in the electrolyte as well as on the electrode polarization mode (potentiodynamic vs potentiostatic), which is also a significant factor affecting the recombination rate of photoinduced charge carriers.

3.3. Photoelectrochemical performance of WO$_3$ layers

3.3.1. Comparison of PEC behaviour of WO$_3$ layers in 0.5 M H$_2$SO$_4$ and 0.5 M NaCl electrolytes: influence of the nature of hole scavenging species and morphology

Cyclic voltammograms of WO$_3$ films recorded in 0.5 M H$_2$SO$_4$ and 0.5 M NaCl solutions are shown in Fig. 5. Comparison of PEC responses reveals certain differences in the behaviour of the samples. In the case of sulphuric acid solution the highest photocurrent is observed for IsoPrOH_WO$_3$, whereas in chloride solution MeOH_WO$_3$ outperforms the others. It should be noted here, that the same electrodes were used for measurement in both electrolytes in order to avoid the influence of possible sample to sample variations in donor density, structure of defects, etc. The nearly symmetric oxidation/reduction peaks seen in the CVs of WO$_3$ samples at $E < 0.5$ V in 0.5 M H$_2$SO$_4$ (Fig. 5a) are illumination- independent and reflect reversible transition between W^{+6}/W^{+5} oxygen species [36]:

$$WO_3 + xe^- + xH^+ \leftrightharpoons H_xWO_3 \qquad (5)$$
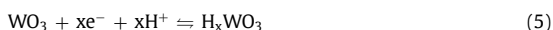
The area under these peaks can be considered as a relative measure of the electrochemically active surface area (EASA) of the films. Such method of EASA evaluation based on metal oxide reduction charge has been reported in other studies as well [37–39]. It can be seen from Fig. 5a that IsoPrOH_WO$_3$ and MeOH_WO$_3$ had significantly higher EASA than the other two electrodes, which also seems to be consistent with higher photocurrents of these samples in 0.5 M H$_2$SO$_4$. Interestingly, however, the arrangement of photocurrents of the very same electrodes in 0.5 M NaCl (Fig. 5b) was different and not consistent with EASA, implying that PEC activity of the films depends to a large extent on the nature of hole scavenging species in the electrolyte. It is evident from CVs in Fig. 5, that, in general, photocurrents in chloride solution were lower than those in sulphate medium for all electrodes, except MeOH_WO$_3$. The most drastic decrease in j_{ph} was observed for IsoPrOH_WO$_3$, which is composed of the largest plate-shaped particles (Fig. 1c). The latter observation suggests that chloride ions tend to suppress the photoelectrochemical activity of WO$_3$ layers and the extent of this suppression is morphology-dependent.

The illumination-independent region of voltammograms recorded in chloride medium (Fig. 5b, $E < 0.3$ V) is different in shape compared to that of CVs in 0.5 M H$_2$SO$_4$ (Fig. 5a, $E < 0.5$ V): the highest reduction current in chloride solution is observed for MeOH_WO$_3$. Moreover, the reduction currents were seen to increase proportionally to time the photoelectrode was polarised at 1.4 V under illumination (not shown in Fig. 5), which implies that there is a causal relationship between the photoanodic and subsequent cathodic processes. To investigate the origin of cathodic current increase in chloride solution at $E < 0.3$ V, additional experiments were performed with MeOH_WO$_3$ electrode. The sample was polarised for 5 min at 1.4 V under illumination and then the electrode potential was swept towards -0.2 V at different scan rates, v, ranging from 5 to 50 mV s^{-1}. The cathodic peak current densities, j_{peak}, were plotted against $v^{1/2}$ and the results are shown in Fig. 6. Linear dependence of peak current on $v^{1/2}$ (inset in Fig. 6) points to diffusion-controlled process, implying that cathodic current arises from the reduction of the products of photoanodic reaction, which are released to solution rather than adsorbed on the photoelectrode surface.

3.3.2. Analysis of the products and Faradaic efficiency of photoanodic reactions in 0.5 M H$_2$SO$_4$ and 0.5 M NaCl electrolytes

The products of PEC processes occurring on WO$_3$ surface, which were analysed in this study, were persulfate (S$_2$O$_8$$^{2-}$) in 0.5 M
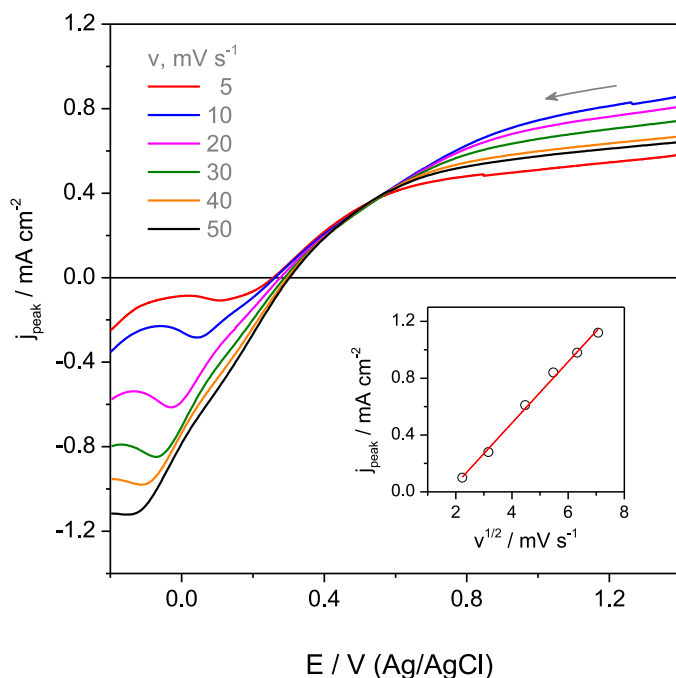
Fig. 6. Linear sweep voltammograms of MeOH_WO$_3$ electrode in 0.5 M NaCl recorded at different potential scan rates after polarizing the electrode at 1.4 V for 5 min under illumination (100 mW cm^{-2}). Inset: dependence of cathodic peak current on v$^{1/2}$.
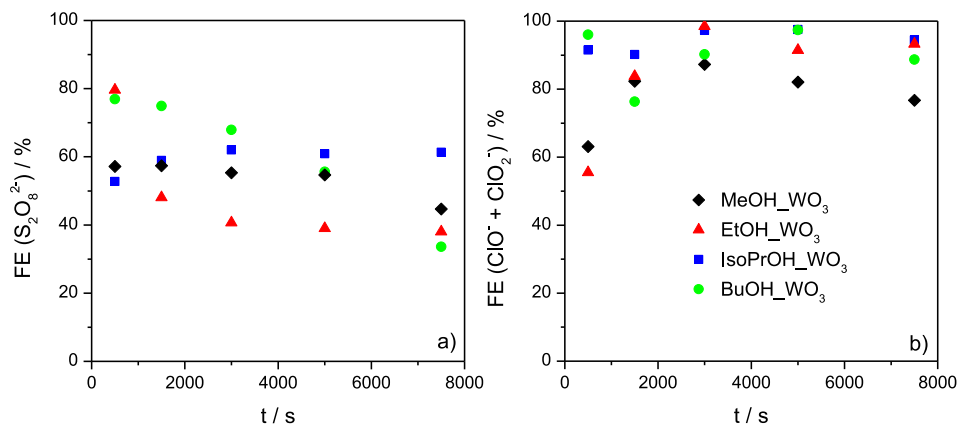

Fig. 7. Variation of Faradaic efficiency of photoelectrochemical generation of S$_2$O$_8{}^{2-}$ (a) and active chlorine species (ClO$^-$ + ClO$_2{}^-$) (b) on indicated WO$_3$ coatings during photoelectrolysis in solutions of 0.5 M H$_2$SO$_4$ and 0.5 M NaCl, respectively.

H$_2$SO$_4$ and active chlorine species (ClO$^-$ + ClO$_2{}^-$) in 0.5 M NaCl. Formation of Cl$_2$ was not considered based on the thermodynamic stability of various chloride oxidation products in neutral 0.5 M NaCl [36,40]. The values of Faradaic efficiency are summarised in Fig. 7 (variation of partial FEs of ClO$^-$ and ClO$_2{}^-$ formation is not analysed in this paper). Rather wide scattering of experimental points was observed in both solutions: FEs varied between 35 and 80% for S$_2$O$_8{}^{2-}$ (Fig. 7a) and between 50 and 99% for ACS (Fig. 7b). The remaining charge was assigned to oxidation of H$_2$O (to O$_2$ or H$_2$O$_2$). While no clear correlation of FE values with sample mor-

phology was observed, these results show that the competition between the photoanodic oxidation of anions and water molecules on the surface of WO$_3$ electrodes is significant. Overall, the contribution of anion oxidation into the total photocurrent was markedly higher in chloride medium with FEs reaching nearly 100% (Fig. 7b). Therefore the above discussed increase in cathodic current seen in voltammograms of WO$_3$ photoelectrodes in 0.5 M NaCl (Figs. 5b and 6) is most likely related with reduction of ACS, though the possibility of H$_2$O$_2$ reduction cannot be excluded.
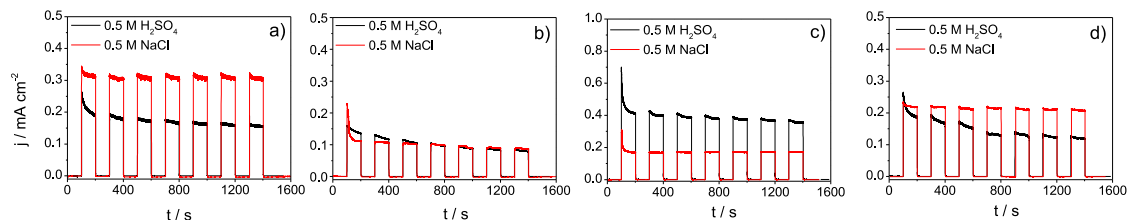
Fig. 8. Chronoamperograms of WO$_3$ photoanodes formed using MeOH (a), EtOH (b), IsoPrOH (c) and BuOH (d) as reductants, under chopped illumination in 0.5 M H$_2$SO$_4$ (black lines) and 0.5 M NaCl (red lines) at 0.7 V and 0.4 V, respectively; the same electrode was used in both solutions (note the different current density scale in c).

Another important observation is that in 0.5 M H$_2$SO$_4$ FE values were diminishing with increase in photoelectrolysis duration more significantly than in 0.5 M NaCl (Fig. 7). This was true for all samples except IsoPrOH_WO$_3$, which demonstrated the most stable performance in sulphuric acid with slightly increasing Faradaic efficiency of S$_2$O$_8$$^{2-}$ formation. There are several reasons, which can explain the decrease in FE of PEC generation of active species with time: i) persulfate ions can undergo a number of chemical as well as photolytic decomposition processes as shown explicitly in [41], ii) photoelectrochemically formed hypochlorite and chlorite ions can either be further oxidised to ClO$_3$$^-$ [42] or diffuse to the cathodic compartment of the cell where they can be reduced to chloride [43], iii) degradation of photoactive layer itself can influence the proportions of competing photoanodic processes. Dissolution of WO$_3$ during photoanodic reaction in sulphate medium has been experimentally evidenced in [44,45]. More insights regarding the competition between PEC oxidation of water vs anions on the surface of WO$_3$ photoanodes in sulphate and chloride electrolytes are presented further.

3.3.3. Comparison of photoelectrochemical behaviour of WO$_3$ layers in 0.5 M H$_2$SO$_4$ and 0.5 M NaCl electrolytes under potentiostatic conditions

Next, the photoelectrochemical activity of WO$_3$ samples in sulphate and chloride medium was compared in chronoamperometric measurements under potentiostatic conditions and chopped illumination. The potential of WO$_3$ photoanodes was set to 0.7 V in 0.5 M H$_2$SO$_4$ and 0.4 V in 0.5 M NaCl. These E values are close to the photocurrent onset potential and correspond to the rising part of CVs in Fig. 5, implying that under such conditions the electron-hole recombination is not fully suppressed by the applied bias, therefore the influence of morphology and/or presence of defects should be more pronounced (as opposed to the photocurrent saturation region, where practically all photogenerated holes reaching electrode/electrolyte interface participate in charge transfer reactions). Several key observations can be made from Fig. 8.

Firstly, the photocurrents in 0.5 M NaCl were higher (Fig. 8a, d) or almost equal (Fig. 8b) to those in 0.5 M H$_2$SO$_4$ for all samples except IsoPrOH_WO$_3$ (Fig. 8c), whereas in CV measurements the trend was opposite - saturation photocurrents in chloride medium were mostly lower as described above (Fig. 5). This illustrates the effect of electrode polarization mode on the recombination rate of charge carriers and hence the PEC response of WO$_3$ films. This should be taken into consideration when analysing the results of EIS measurements, which were obtained at the open-circuit potential of the system. In terms of morphology, MeOH_WO$_3$ and BuOH_WO$_3$ composed of small plates (Fig. 1a and d), exhibited higher PEC activity in chloride medium, whereas the photocurrent of IsoPrOH_WO$_3$ electrode with large-plate morphology was significantly higher in 0.5 M H$_2$SO$_4$. PEC activity of EtOH_WO$_3$ was almost the same in both electrolytes, which is consistent with intermediate dimensions of plate-like units forming the film.

Secondly, the photocurrents in 0.5 M NaCl were more stable, i.e. less decreasing with time, than those in 0.5 M H$_2$SO$_4$ for all WO$_3$ coatings investigated, implying that either charge transfer was more efficient in chloride medium with less recombination even at low values of applied external bias or the degradation of the photoelectrode was less. In literature, the decay in photocurrent of WO$_3$ electrodes is usually ascribed to formation and accumulation of peroxo species [5,12,46] in the process of photoanodic oxidation of water molecules. If so, the stability of j_{ph} implies that chloride ions in some way prevent the accumulation of peroxo species on the photoanode surface. The possible reasons behind this phenomenon are discussed further.

3.3.4. Photoelectrochemical investigations in mixed sulphate and chloride electrolytes: specific adsorption of Cl$^-$ ions

Comparison of CVs presented in Fig. 5a and b shows that the onset of photocurrent in 0.5 M NaCl is observed at ~0.3 V, whereas in 0.5 M H$_2$SO$_4$ - at ~0.6 V. The shift of the j_{ph} onset potential towards more negative values could be attributed to change in pH, because the flatband potential of an ideally behaving oxide electrode should shift 59 mV to the negative direction per pH unit as pH increases [5], however further PEC investigations in mixed sulphate-chloride electrolytes provided additional clues for understanding such behaviour. Cyclic voltammograms comparing photoelectrochemical responses of the four electrodes in sulphuric acid solution in the absence and presence of chloride ions are shown in Fig. 9. It is clearly seen that in chloride-containing electrolytes the onset of j_{ph} is shifted towards more negative potentials, though pH of 0.5 M H$_2$SO$_4$ should not be affected by addition of 0.5 M NaCl. Most likely, chloride ions adsorb specifically on the semiconductor surface [47,48] leading to an increase in the electric field strength within the semiconductor space charge layer, and, consequently, increase in band bending. This helps to suppress electron-hole recombination at semiconductor/electrolyte interface, therefore the onset of photoanodic current in chloride containing solution shifts towards lower E values compared with sulphuric acid medium.

Though addition of NaCl to sulphuric acid solution depolarised the onset of j_{ph}, it also led to a decrease in photocurrents for all the electrodes except MeOH_WO$_3$ (Fig. 9a). Similarly to results shown in Fig. 5, the most significant decrease was observed for IsoPrOH_WO$_3$, the photoelectrochemical activity of which in pure 0.5 M H$_2$SO$_4$ was the highest (Fig. 9c). This implies that addition of chlorides suppressed the rate of hole transfer, whereas the extent of this decrease in j_{ph} correlated with morphological features of WO$_3$ layers: the ratio of anodic photocurrents measured at 1.8 V in the solutions with and without chloride, j_{ph}^{Cl}/j_{ph}, increased consistently with decrease in dimensions of plate-shaped particles forming the films (Fig. S1).

3.3.5. Analysis of possible photoanodic processes

In order to understand the observed phenomena, possible photoanodic processes occurring in the system under investigation should be analysed. In mixed sulphate-chloride electrolyte
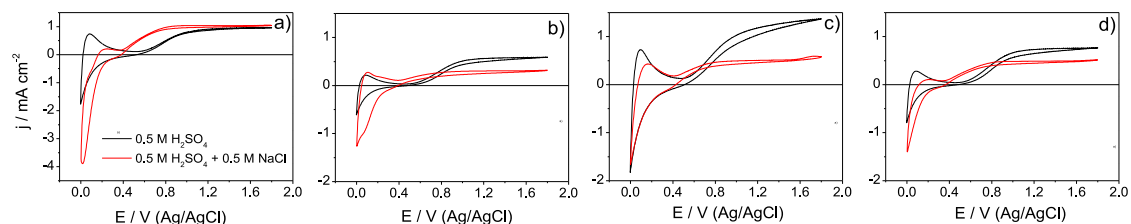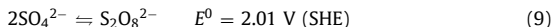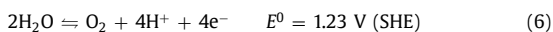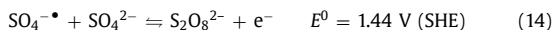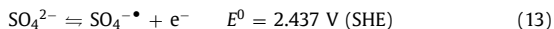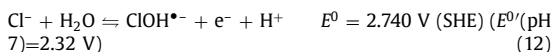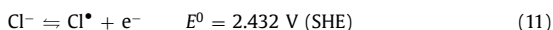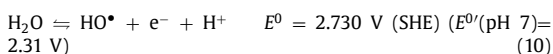
Fig. 9. Cyclic voltammograms of WO_3 photoanodes formed using MeOH (a), EtOH (b), IsoPrOH (c) and BuOH (d) as reductants in solutions of 0.5 M H_2SO_4 (black curves) and 0.5 M H_2SO_4 + 0.5 M NaCl (red curves), the same electrode was used in both solutions, illumination intensity 100 mW cm^{-2}, potential scan rate 50 mV s^{-1}.
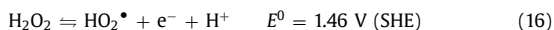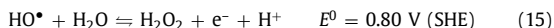
the species that can undergo photoanodic oxidation are H_2O molecules, Cl^- and SO_4^{2-} ions. The common approach is to compare the standard electrochemical potentials, E^0, of possible oxidation processes, which are as follows:

$$2H_2O \rightleftharpoons O_2 + 4H^+ + 4e^- \qquad E^0 = 1.23 \text{ V (SHE)} \tag{6}$$

$$2Cl^- \rightleftharpoons Cl_2 + 2e^- \qquad E^0 = 1.36 \text{ V (SHE)} \tag{7}$$

$$2H_2O \rightleftharpoons H_2O_2 + 2H^+ + 2e^- \qquad E^0 = 1.77 \text{ V (SHE)} \tag{8}$$

$$2SO_4^{2-} \rightleftharpoons S_2O_8^{2-} \qquad E^0 = 2.01 \text{ V (SHE)} \tag{9}$$

Thermodynamically, in accordance with the indicated values of E^0, the most favourable process is oxygen evolution reaction (OER) (eq. (6)). However, due to the complexity of OER mechanism involving transfer of four electrons, oxidation of chloride (eq. (7)) is known to have the kinetic advantage, especially in acidic medium [40], because the potential of OER shifts towards lower values as pH increases. The electrode potential, however, is a measure of the energy of electrons, whereas in photoanodic processes the photo-generated holes from the valence band play the key role and their energy depends on the nature of semiconductor. In the case of WO_3, potential of the valence band is around + 3.0 V (SHE) [4], which means that photoholes of tungsten (VI) oxide are strong oxidisers and have enough energy to drive the oxidation of solution species via pathways involving formation of highly reactive intermediates such as free radicals. There is a growing amount of scientific evidence which supports this assumption. It has been demonstrated recently [9,42,49,50], that hydroxyl radicals are formed during photoelectrocatalytic oxidation of water on WO_3. Generation of chlorine radical species on WO_3 photoanodes in chloride solutions was experimentally detected in [51,52]. Effective photoelectrochemical inactivation of various bacterial strains with WO_3 electrodes in chloride-containing medium was also ascribed to high bacteria killing power of photoanodically formed reactive chlorine radicals [43,53]. Photo-assisted formation of sulphate radicals, $SO_4^{-\bullet}$, was shown to be the main cause of degradation of refractory organics using WO_3 photoelectrode at pH 2 [54]. Therefore, the standard potentials of the reactions involving formation of radicals should, in fact, be considered when analysing the probability of one or another photoanodic reaction. According to [55] the E^0 values of hydroxyl, chlorine, hypochlorite and sulphate radicals formation are as follows:

$$H_2O \rightleftharpoons HO^\bullet + e^- + H^+ \qquad E^0 = 2.730 \text{ V (SHE)} \ (E^{0\prime}(\text{pH } 7) = 2.31 \text{ V}) \tag{10}$$

$$Cl^- \rightleftharpoons Cl^\bullet + e^- \qquad E^0 = 2.432 \text{ V (SHE)} \tag{11}$$

$$Cl^- + H_2O \rightleftharpoons ClOH^{\bullet-} + e^- + H^+ \qquad E^0 = 2.740 \text{ V (SHE)} \ (E^{0\prime}(\text{pH } 7) = 2.32 \text{ V}) \tag{12}$$

$$SO_4^{2-} \rightleftharpoons SO_4^{-\bullet} + e^- \qquad E^0 = 2.437 \text{ V (SHE)} \tag{13}$$

$$SO_4^{-\bullet} + SO_4^{2-} \rightleftharpoons S_2O_8^{2-} + e^- \qquad E^0 = 1.44 \text{ V (SHE)} \tag{14}$$

It is noteworthy that E^0 values of reactions (10) and (12) are pH-dependent (dE/dpH = −0.059 V), whereas those of processes (11), (13) and (14) are not. Such arrangement of E^0 values implies that in acidic medium formation of $Cl^\bullet$ and $SO_4^{-\bullet}$ is thermodynamically favoured over the formation of hydroxyl and hypochlorite radicals, whereas in neutral medium the latter processes have certain thermodynamic advantage. Moreover, formation of $HO^\bullet$ radical according to reaction (10) should not have kinetic limitations inherent to OER (Eq. (6)) as discussed above. Reaction of $HO^\bullet$ with another hydroxyl radical or water molecule can produce H_2O_2, whereas photoanodic oxidation of H_2O_2 can yield $HO_2^\bullet$ [55]:

$$HO^\bullet + H_2O \rightleftharpoons H_2O_2 + e^- + H^+ \qquad E^0 = 0.80 \text{ V (SHE)} \tag{15}$$

$$H_2O_2 \rightleftharpoons HO_2^\bullet + e^- + H^+ \qquad E^0 = 1.46 \text{ V (SHE)} \tag{16}$$

These intermediate compounds of water oxidation, most likely, are the peroxo species responsible for the above discussed degradation of WO_3 photoelectrodes.

Another important inference that can be drawn from the reactions (11) and (13) is that thermodynamically oxidation of chloride and sulphate anions is almost equally probable, therefore the competition between these two processes should be governed by the kinetic factors. Since photoanodic reactions are limited to the interface between the photoelectrode and electrolyte, adsorption of solution species should play an important role in determining the occurrence of one or another process. In general, the relative adsorption strength of chloride exceeds that of sulphate/bisulphate ions as was shown experimentally and by density functional theory calculations for various metal as well as oxide surfaces in recent studies [56–58]. Therefore, the above discussed shift of the onset of photocurrent to lower potentials upon addition of NaCl to 0.5 M H_2SO_4 means that holes primarily oxidise those species, which are adsorbed on the electrode surface, i.e. Cl^- ions, even though thermodynamic likelihood of SO_4^{2-} oxidation is the same. Specific adsorption of chloride ions also explains high Faradaic efficiencies of active chlorine species formation found in neutral 0.5 M NaCl (Fig. 7b), though oxidation of water molecules is the thermodynamically favoured process in this case (reaction (10) vs (11)).

3.3.6. Influence of WO_3 film morphology on PEC performance: potential-assisted photochemical approach

Further, the influence of WO_3 film morphology on the competition between photoanodic processes in the systems investigated is discussed. Though the dimensions of structural features of WO_3 films range between hundreds and thousands of nanometres and are by several orders of magnitude larger than anions and water molecules, the size of slits or cavities between the protruding
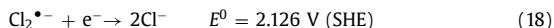
elements in oxide layer are roughly 10 - 100 times less, as can be inferred from the roughness plots in Fig. 1. Furthermore, the processes under investigation occur at rough electrified interfaces, where distribution of electric fields as well as the structure of electric double layer and the dynamics of water and ions are rather complex [59] and such parameters as electrolyte concentration, ion charge and size play an important role.

In the case of chronoamperometric experiment shown in Fig. 8, competition between the photoanodic oxidation of SO_4^{2-} *vs* H_2O or Cl^- *vs* H_2O should be considered. Since the electrode used for CA measurements was the same in both electrolytes, which implies no changes in N_D, structure of defects and morphology, the differences in stationary photocurrent should be attributed to loss of photogenerated charge carriers by recombination, which is affected by the solution species. The results obtained with samples MeOH_WO$_3$ and BuOH_WO$_3$ (Fig. 8a and d) show that recombination rate in 0.5 M H_2SO_4 is higher than in 0.5 M NaCl. Given the small-plate morphology of MeOH_WO$_3$ and BuOH_WO$_3$, the accessibility of the electrode/solution interface for bulkier, more strongly hydrated sulphate ions [60] should be lower. Sulphate ions compete with H_2O molecules for active sites to combine with holes on photoelectrode surface, thus altering the potential distribution as well as the electronic structure of the electrode at the interfacial region, which probably leads to situation that large fraction of photogenerated charge carriers is lost due to recombination. On the contrary, the large-plate morphology of IsoPrOH_WO$_3$ is more favourable for photoanodic reactions in 0.5 M H_2SO_4 than in 0.5 M NaCl (Fig. 5, 8c). Most likely, steric hindrance for sulphate ions in this case is lower and formation of persulfate proceeds according to reactions (13) and (14). Stability of Faradaic efficiency of photoelectrochemical generation of $S_2O_8^{2-}$ on IsoPrOH_WO$_3$ (Fig. 7a) corroborates this assumption. Rather low E^0 value of reaction (14) suggests that once sulphate radical is formed, its combination with another sulphate ion and further oxidation to persulfate is thermodynamically favoured over $S_2O_8^{2-}$ formation via combination of two $SO_4^{-•}$ radicals formed in reaction (13).

Lower photocurrents observed for IsoPrOH_WO$_3$ in the presence of chlorides (Figs. 5, 8c and 9c) can be understood considering the following possible processes. Photoanodically formed $Cl^•$ radicals are known to undergo rapid complexation by excess Cl^- ions [48,61–63] to form anion radicals:

$$Cl^• + Cl^- \rightarrow Cl_2^{•-} \tag{17}$$

The equilibrium constant of this reaction is $(1.4 \pm 0.2) \times 10^5$ M^{-1} [55], implying that product is strongly favoured over the reactants. Negatively charged $Cl_2^{•-}$ radicals should be electrostatically attracted to positively polarised WO$_3$ surface, thus blocking the access for water molecules or other anions. Moreover, these adsorbed species can act as surface recombination centres reacting with photogenerated electrons from the conduction band [55,61]:

$$Cl_2^{•-} + e^- \rightarrow 2Cl^- \qquad E^0 = 2.126 \text{ V (SHE)} \tag{18}$$

Chloride ions formed in the above process can again participate in hole scavenging. Thus the loop of reactions (11), (17) and (18) can account for lower photocurrents observed in the case of IsoPrOH_WO$_3$ in chloride containing electrolytes (Figs. 5, 8 and 9). Such surface-charge recombination mechanism or quenching of photogenerated charge carriers by chloride ions has been also suggested in [64] to explain the mechanism of photocatalytic degradation of 4-ethylphenol on TiO$_2$ surface. It is plausible that specific adsorption of Cl^- ions and $Cl_2^{•-}$ anion radicals prevents formation of peroxo species on WO$_3$ surface in chloride solutions, thus preserving the stability of WO$_3$ photoanodes in neutral medium. Stability of photocurrent of tungsten (VI) oxide anodes in chloride

solutions has been reported in other studies as well [5,8,65]. Larger contribution of photoanodic oxidation of water molecules in the photocurrent of WO$_3$ electrodes found in the case of 0.5 M H_2SO_4 electrolyte (Fig. 7a) leads to detrimental effects of hydroxo species and faster degradation of WO$_3$ films, even though thermodynamically their stability in acidic medium should be higher [36].

When the dimensions of plate-shaped particles forming WO$_3$ films are smaller, the conditions for adsorption of chlorine species become less favourable due to repulsive interactions between the adsorbates, what leads to a more dynamic exchange of ions or radicals with solution and lower contribution of recombination due to reaction (18). Morphology of EtOH_WO$_3$, which is intermediate between IsoPrOH_WO$_3$ and MeOH_WO$_3$ or BuOH_WO$_3$ in terms of size of plate-like units forming the coating, most likely, provides analogous conditions for the photoinduced charge transfer in both electrolytes (Fig. 8b). The above presented interpretation of possible reaction pathways invokes the mechanisms of photochemical processes, which to a certain extent are governed by the electrostatic interactions, conditioned by the electrode potential. Therefore, such treatment of photoelectrochemical processes can be termed as a potential-assisted photochemical approach.

To assess the effect of photoelectrolysis in chloride and sulphate electrolytes on the surface chemical composition of WO$_3$ samples, IsoPrOH_WO$_3$ and MeOH_WO$_3$ electrodes - as marginal cases in terms of morphology and PEC behaviour in the solutions investigated - were analysed by X-ray photoelectron spectroscopy. XPS spectra of WO$_3$ photoelectrodes which underwent 1 h-long photoelectrolysis in 0.5 M H_2SO_4 or in 0.5 M NaCl were compared with those of pristine samples. As can be seen from the survey spectra in Fig. S2, no incorporation of Cl or S species into the surface of the samples was observed. Spectra of W 4f electrons shown in Fig. S3 revealed that all investigated samples contained a small amount of W^{+5}, which varied between 2.5 and 5.5 at.%. O 1 s spectra (Fig. S4) were deconvoluted into three main peaks at binding energies of 530.5, 531.4 and 532.6 eV corresponding, respectively, to O^{2-} state in tungsten (VI) oxide, oxygen species in O^- ionization state and weakly adsorbed species O_{ads} [66]. The amount of O^- ranged between 8.5 and 13.3 at.% and was higher in the samples with higher content of W^{+5} (Table S1). This is consistent with the presence of oxygen vacancies as determined by PL measurements discussed above (Fig. 4). Though XPS investigations did not reveal any tangible changes in the surface chemical environment of IsoPrOH_WO$_3$ and MeOH_WO$_3$ samples after photoelectrolysis, these results highlight the importance of further studies, especially the application of in-situ/operando characterization techniques, which could deepen our understanding of photoelectrochemical phenomena.

Conclusions

WO$_3$ coatings composed of plate-like particles of similar shape but different sizes were formed by means of chemical solution deposition using methanol, ethanol, isopropanol and butanol as reductants. The coarsest morphology with the largest plate-shaped units (1 - 1.5 μm) was obtained with isopropanol and the finest plates (< 0.5 μm) were formed using methanol. The photoelectrochemical behaviour of WO$_3$ films in 0.5 M H_2SO_4, 0.5 M NaCl and mixture of these electrolytes was compared. It was found that the large-plate morphology of IsoPrOH_WO$_3$ was favourable for photoanodic reactions in 0.5 M H_2SO_4 and the photocurrent was significantly suppressed by the presence of chloride ions. On the contrary, the fine-plate morphology of MeOH_WO$_3$ ensured outstanding PEC performance in chloride-containing solutions, both neutral and acidic.

The morphology-dependent competition between the photoanodic oxidation of anions and water molecules was analysed taking

into consideration specific adsorption, electrostatic interactions as well as steric hindrance effects occurring at rough electrified photoelectrode/electrolyte interfaces. It was demonstrated that chloride ions tend to adsorb specifically on the surface of WO_3 electrodes. This provides them with a kinetic advantage over other solution species in the process of hole scavenging and leads to high Faradaic efficiencies (up to almost 100%) of photoelectrochemical generation of active chlorine species ($ClO^- + ClO_2^-$).

Potential-assisted photochemical approach, which takes into consideration hole-mediated formation of radical intermediates ($HO^\bullet$, $Cl^\bullet$, $Cl_2^{\bullet-}$, $SO_4^{-\bullet}$), was proposed to explain the photoelectrochemical performance of WO_3 coatings in the solutions studied. High PEC activity of IsoPrOH_WO₃ in 0.5 M H_2SO_4 medium was attributed to better accessibility of the surface with large plate morphology for bulky sulphate ions, resulting in effective hole scavenging and stable Faradaic efficiency of $S_2O_8^{2-}$ generation. Low photocurrent of IsoPrOH_WO₃ in chloride medium was explained by formation of surface-adsorbed anion radicals $Cl_2^{\bullet-}$, which can scavenge photogenerated electrons thus acting as surface traps or recombination centres:

$$Cl^- \xrightarrow{h^+} Cl^\bullet \xrightarrow{Cl^-} Cl_2^{\bullet-} \xrightarrow{e^-} 2Cl^-$$
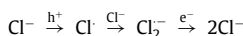
In the case of small plate morphology (MeOH_WO₃), this recombination loop is prevented by more dynamic exchange of ions or radicals with solution, because repulsive interactions between the adsorbed chlorine species (Cl^-, $Cl_2^{\bullet-}$) facilitate their removal from the surface, leading to enhanced photoelectrochemical performance of the samples in chloride medium.

Strong adsorption of chloride ions as well as the products of their photoanodic oxidation on WO_3 surface was suggested to prevent accumulation of peroxo species, thus contributing to higher stability of photoelectrodes in NaCl solutions as compared to H_2SO_4 electrolytes. Overall, the findings reported in this study can be helpful in engineering semiconductor/electrolyte interfaces for efficient photoelectrochemical generation of strong oxidants in advanced oxidation processes.

Credit author statement

M. Parvin: Original draft preparation, Visualization, Investigation **M. Petrulevičienė:** Investigation **I. Savickaja:** Investigation **B. Šebeka:** Investigation **R. Karpicz:** Investigation **A. Grigucevičienė**: Investigation **R. Ramanauskas:** Supervision **J. Juodkazytė:** Conceptualization, Writing- Reviewing and Editing, Visualization.

Declaration of Competing Interest

The authors declare that they have no known competing financial interests or personal relationships that could have appeared to influence the work reported in this paper.

Acknowledgement

Supplementary materials

Supplementary material associated with this article can be found, in the online version, at doi:10.1016/j.electacta.2021.139710.

References

[1] K. Sayama, Production of high-value-added chemicals on oxide semiconductor photoanodes under visible light for solar chemical-conversion processes, ACS Energy Lett 3 (2018) 1093–1101.

[2] J.D. García-Espinoza, I. Robles, A. Durán-Moreno, L.A. Godínez, Photo-assisted electrochemical advanced oxidation processes for the disinfection of aqueous solutions: a review, Chemosphere 274 (2021) 129957.

[3] S. Giménez, J. Bisquert, Photoelectrochemical Solar Fuel Production: From Basic Principles to Advanced Devices, Springer, 2016.

[4] C. Ros, T. Andreu, J.R. Morante, Photoelectrochemical water splitting: a road from stable metal oxides to protected thin film solar cells, J. Mater. Chem. A Mater. Energy Sustain. 8 (2020) 10625–10669.

[5] J.C. Hill, K.–S. Choi, Effect of electrolytes on the selectivity and stability of n–type WO_3 photoelectrodes for use in solar water oxidation, J. Phys. Chem. C 116 (2012) 7612–7620.

[6] J. Desilvestro, M. Grätzel, Photoelectrochemistry of polycrystalline n-wo3: electrochemical characterization and photoassisted oxidation processes, J. Electroanal. Chem. Interfacial Electrochem. 238 (1987) 129–150.

[7] S. Takasugi, Y. Miseki, K. Sayama, Photo-electrochemical production of IO4− from IO3− over a WO_3 semiconductor photoanode, Chem. Lett. (2021), doi:10.1246/cl.210094.

[8] A.G. Breuhaus-Alvarez, Q. Cheek, J.J. Cooper, S. Maldonado, B.M. Bartlett, Chloride oxidation as an alternative to the oxygen-evolution reaction on HxWO3 photoelectrodes, J. Phys. Chem. C 125 (2021) 8543–8550.

[9] M. Desseigne, N. Dirany, V. Chevallier, M. Arab, Shape dependence of photosensitive properties of WO3 oxide for photocatalysis under solar light irradiation, Appl. Surf. Sci. 483 (2019) 313–323.

[10] S. Wang, G. Liu, L. Wang, Crystal facet engineering of photoelectrodes for photoelectrochemical water splitting, Chem. Rev. 119 (2019) 5192–5247.

[11] E. Samuel, B. Joshi, M.-W. Kim, M.T. Swihart, S.S. Yoon, Morphology engineering of photoelectrodes for efficient photoelectrochemical water splitting, Nano Energy 72 (2020) 104648.

[12] S.S. Kalanur, D.Le Thai, H. Seo, Recent progress in photoelectrochemical water splitting activity of WO3 photoanodes, Topics in Catalysis 61 (2018) 1043–1076, doi:10.1007/s11244-018-0950-1.

[13] A.S. Hammad, H.M. El-Bery, A.H. El-Shazly, M.F. Elkady, Effect of WO3 morphological structure on its photoelectrochemical properties, Int. J. Electrochem. Sci. 13 (2018) 362–372.

[14] P. Dong, G. Hou, X. Xi, R. Shao, F. Dong, WO3-based photocatalysts: morphology control, activity enhancement and multifunctional applications, Environ. Sci. 4 (2017) 539–557, doi:10.1039/c6en00478d.

[15] Q. Zeng, J. Li, J. Bai, X. Li, L. Xia, B. Zhou, Preparation of vertically aligned WO3 nanoplate array films based on peroxotungstate reduction reaction and their excellent photoelectrocatalytic performance, Appl. Catal. B. 202 (2017) 388–396.

[16] T. Özdal, H. Kavak, Determination of crystallization threshold temperature for sol-gel spin coated Cu2ZnSnS4 thin films, Ceram. Int. 44 (2018) 18928–18934.

[17] S.K. Sen, T.C. Paul, S. Dutta, M.N. Hossain, M.N.H. Mia, XRD peak profile and optical properties analysis of Ag-doped h-MoO3 nanorods synthesized via hydrothermal method, J. Mater. Sci.: Mater. Electron. 31 (2020) 1768–1786.

[18] Z. Zhou, Z. Wu, Q. Xu, G. Zhao, A solar-charged photoelectrochemical wastewater fuel cell for efficient and sustainable hydrogen production, J. Mater. Chem. A Mater. Energy Sustain. 5 (2017) 25450–25459.

[19] C. Guo, S. Yin, M. Yan, M. Kobayashi, M. Kakihana, T. Sato, Morphology-controlled synthesis of W18O49 nanostructures and their near-infrared absorption properties, Inorg. Chem. 51 (2012) 4763–4771.

[20] Y. Xiong, Z. Zhu, T. Guo, H. Li, Q. Xue, Synthesis of nanowire bundle-like WO3-W18O49 heterostructures for highly sensitive NH3 sensor application, J. Hazard. Mater. 353 (2018) 290–299.

[21] H.G. Choi, Y.H. Jung, D.K. Kim, Solvothermal synthesis of tungsten oxide nanorod/nanowire/nanosheet, J. Am. Ceram. Soc. 88 (2005) 1684–1686.

[22] M. Mohsen-Nia, H. Amiri, B. Jazi, Dielectric constants of water, methanol, ethanol, butanol and acetone: measurement and computational study, J. Solution Chem. 39 (2010) 701–708.

[23] Y. Liu, Q. Li, S. Gao, J.K. Shang, Template-free solvothermal synthesis of WO3/WO3•H2O hollow spheres and their enhanced photocatalytic activity from the mixture phase effect, CrystEngComm 16 (2014) 7493–7501, doi:10.1039/c4ce00857j.

[24] J.-.M. Kim, H.-.T. Chung, Electrochemical characteristics of orthorhombic LiMnO2 with different degrees of stacking faults, J. Power Sources. 115 (2003) 125–130.

[25] T. Ungár, Microstructural parameters from X-ray diffraction peak broadening, Scr. Mater. 51 (2004) 777–781.

[26] K. Song, Z. Ma, W. Yang, H. Hou, F. Gao, Electrospinning WO3 nanofibers with tunable Fe-doping levels towards efficient photoelectrochemical water splitting, J. Mater. Sci. 29 (2018) 8338–8346, doi:10.1007/s10854-018-8844-3.

[27] K.H. Ng, L.J. Minggu, M.B. Kassim, Gallium-doped tungsten trioxide thin film photoelectrodes for photoelectrochemical water splitting, Int. J. Hydrogen Energy. 38 (2013) 9585–9591.

[28] G. Wang, Y. Ling, H. Wang, X. Yang, C. Wang, J.Z. Zhang, Y. Li, Hydrogen-treated WO3 nanoflakes show enhanced photostability, Energy Environ. Sci. 5 (2012) 6180–6187.

[29] S. Corby, L. Francàs, A. Kafizas, J.R. Durrant, Determining the role of oxygen vacancies in the photoelectrocatalytic performance of WO3 for water oxidation, Chem. Sci. 11 (2020) 2907–2914, doi:10.1039/c9sc06325k.

[30] J. Wang, P.S. Lee, J. Ma, Synthesis, growth mechanism and room-temperature blue luminescence emission of uniform WO3 nanosheets with W as starting material, J. Cryst. Growth. 311 (2009) 316–319.

[31] J. Sungpanich, T. Thongtem, S. Thongtem, Large-scale synthesis of WO3 nanoplates by a microwave-hydrothermal method, Ceram. Int. 38 (2012) 1051–1055.

[32] S. Mohammed Harshulkhan, K. Janaki, G. Velraj, R. Sakthi Ganapathy, S. Krishnaraj, Structural and optical properties of Ag doped tungsten oxide (WO3) by microwave-assisted chemical route, J. Mater. Sci.: Mater. Electron. 27 (2016) 3158–3163.

[33] C. Yang, Q. Zhu, S. Zhang, Z. Zou, K. Tian, C. Xie, A comparative study of microstructures on the photoelectric properties of tungsten trioxide films with plate-like arrays, Appl. Surf. Sci. 297 (2014) 116–124.

[34] C. Yang, Q. Zhu, T. Lei, H. Li, C. Xie, The coupled effect of oxygen vacancies and Pt on the photoelectric response of tungsten trioxide films, J. Mater. Chem. 2 (2014) 9467–9477.

[35] P.Kaur Kriti, S. Kaur, D. Arora, K. Asokan, D.P. Singh, Influence of defect structure on colour tunability and magneto optical behaviour of WO 3 nanoforms, RSC Adv 9 (2019) 20536–20548.

[36] M. Pourbaix, Atlas of Electrochemical Equilibria in Aqueous Solutions, National Association of Corrosion Engineers, 1974.

[37] U.P. Do, F. Seland, E.A. Johannessen, The real area of nanoporous catalytic surfaces of gold and palladium in aqueous solutions, J. Electrochem. Soc. 165 (2018) H219.

[38] S. Zhao, H. Yu, R. Maric, N. Danilovic, C.B. Capuano, K.E. Ayers, W.E. Mustain, Calculating the electrochemically active surface area of iridium oxide in operating proton exchange membrane electrolyzers, J. Electrochem. Soc. 162 (2015) F1292.

[39] F.P. Lohmann-Richters, B. Abel, Á. Varga, In situ determination of the electrochemically active platinum surface area: key to improvement of solid acid fuel cells, J. Mater. Chem. A Mater. Energy Sustain. 6 (2018) 2700–2707.

[40] F. Dionigi, T. Reier, Z. Pawolek, M. Gliech, P. Strasser, Design criteria, operating conditions, and nickel-iron hydroxide catalyst materials for selective seawater electrolysis, ChemSusChem 9 (2016) 962–972.

[41] C. Lee, H.-.H. Kim, N.-.B. Park, Chemistry of persulfates for the oxidation of organic contaminants in water, Membr. Water Treat. 9 (2018) 405–419.

[42] X. Li, M. Kan, T. Wang, Z. Qin, T. Zhang, X. Qian, Y. Kuwahara, K. Mori, H. Yamashita, Y. Zhao, The ClO• generation and chlorate suppression in photoelectrochemical reactive chlorine species systems on BiVO4 photoanodes, Appl. Catal. B. 296 (2021) 120387.

[43] J. Juodkazytė, M. Petrulevičienė, M. Parvin, B. Šebeka, I. Savickaja, V. Pakštas, A. Naujokaitis, J. Virkutis, A. Gegeckas, Activity of sol-gel derived nanocrystalline WO3 films in photoelectrochemical generation of reactive chlorine species, J. Electroanal. Chem. 871 (2020) 114277.

[44] J. Knöppel, S. Zhang, F.D. Speck, K.J.J. Mayrhofer, C. Scheu, S. Cherevko, Time-resolved analysis of dissolution phenomena in photoelectrochemistry – A case study of WO3 photocorrosion, Electrochem. Commun. 96 (2018) 53–56.

[45] J. Knöppel, A. Kormányos, B. Mayerhöfer, A. Hofer, M. Bierling, J. Bachmann, S. Thiele, S. Cherevko, Photocorrosion of WO3 photoanodes in different electrolytes, ACS Phys. Chem. Au. (2021), doi:10.1021/acsphyschemau.1c00004.

[46] J.A. Seabold, K.-.S. Choi, Effect of a cobalt-based oxygen evolution catalyst on the stability and the selectivity of photo-oxidation reactions of a WO3 photoanode, Chem. Mater. 23 (2011) 1105–1112.

[47] P. Singh, R. Singh, R. Gale, K. Rajeshwar, J. DuBow, Surface charge and specific ion adsorption effects in photoelectrochemical devices, J. Appl. Phys. 51 (1980) 6286–6291.

[48] J. Moser, M. Grätzel, Photoelectrochemistry with colloidal semiconductors; Laser studies of Halide oxidation in colloidal dispersions of TiO2and α-Fe2O3, Helv. Chim. Acta. 65 (1982) 1436–1444.

[49] A.D. Proctor, B.M. Bartlett, Hydroxyl radical suppression during photoelectrocatalytic water oxidation on WO3|FeOOH, J. Phys. Chem. C. 124 (2020) 17957–17963.

[50] V. Cristino, S. Marinello, A. Molinari, S. Caramori, R. Carli, R. Boaretto, R. Argazzi, L. Meda, C.A. Bignozzi, Some aspects of the charge transfer dynamics in nanostructured WO3 films, J. Mater. Chem. A 4 (2016) 2995–3006, doi:10.1039/c5ta06887h.

[51] Y. Ji, J. Bai, J. Li, T. Luo, L. Qiao, Q. Zeng, B. Zhou, Highly selective transformation of ammonia nitrogen to N2 based on a novel solar-driven photoelectrocatalytic-chlorine radical reactions system, Water Res. 125 (2017) 512–519.

[52] Y. Zhang, J. Li, J. Bai, X. Li, Z. Shen, L. Xia, S. Chen, Q. Xu, B. Zhou, Total organic carbon and total nitrogen removal and simultaneous electricity generation for nitrogen-containing wastewater based on the catalytic reactions of hydroxyl and chlorine radicals, Appl. Catal. B 238 (2018) 168–176.

[53] M.S. Koo, X. Chen, K. Cho, T. An, W. Choi, Situ photoelectrochemical chloride activation using a WO3 electrode for oxidative treatment with simultaneous H2 evolution under visible light, Environ. Sci. Technol. 53 (2019) 9926–9936.

[54] J. Zheng, J. Li, J. Bai, X. Tan, Q. Zeng, L. Li, B. Zhou, Efficient degradation of refractory organics using sulfate radicals generated directly from WO3 photoelectrode and the catalytic reaction of sulfate, Catalysts 7 (2017) 346.

[55] D.A. Armstrong, R.E. Huie, W.H. Koppenol, S.V. Lymar, G. Merényi, P. Neta, B. Ruscic, D.M. Stanbury, S. Steenken, P. Wardman, Standard electrode potentials involving radicals in aqueous solution: inorganic radicals (IUPAC Technical Report), Pure Appl. Chem. 87 (2015) 1139–1150.

[56] K. Berkesi, D. Horváth, Z. Németh, K. Varga, L. Péter, T. Pintér, Comparative study of the adsorption of SO42-/HSO4- and Cl– anions on smooth and rough surfaces of noble metal electrodes by in situ radiotracer thin gap method, J. Electroanal. Chem. 712 (2014) 151–160.

[57] R. Cheng, M. Shi, Sulfate-induced electrochemical instability in the transpassive region during the electrooxidation of Na2S on Pt, J. Solid State Electrochem. 23 (2019) 1523–1531.

[58] C.D. Taylor, S. Li, A.J. Samin, Oxidation versus salt-film formation: competitive adsorption on a series of metals from first-principles, Electrochim. Acta. 269 (2018) 93–101.

[59] M. Jia, C. Zhang, J. Cheng, Origin of asymmetric electric double layers at electrified oxide/electrolyte interfaces, J. Phys. Chem. Lett. 12 (2021) 4616–4622.

[60] T. Sata, Ion Exchange Membranes: Preparation, Characterization, Modification and Application, Royal Society of Chemistry, 2007.

[61] M. Krivec, R. Dillert, D.W. Bahnemann, A. Mehle, J. Štrancar, G. Dražić, The nature of chlorine-inhibition of photocatalytic degradation of dichloroacetic acid in a TiO2-based microreactor, Phys. Chem. Chem. Phys. 16 (2014) 14867, doi:10.1039/c4cp01043d.

[62] Y. Lei, X. Lei, P. Westerhoff, X. Zhang, X. Yang, Reactivity of chlorine radicals (Cl• and Cl2•−) with dissolved organic matter and the formation of chlorinated byproducts, Environ. Sci. Technol. 55 (2021) 689–699.

[63] K. Zhang, K.M. Parker, Halogen radical oxidants in natural and engineered aquatic systems, Environ. Sci. Technol. 52 (2018) 9579–9594.

[64] R. Brüninghoff, A.K. van Duijne, L. Braakhuis, P. Saha, A.W. Jeremiasse, B. Mei, G. Mul, Comparative analysis of photocatalytic and electrochemical degradation of 4-ethylphenol in saline conditions, Environ. Sci. Technol. 53 (2019) 8725–8735.

[65] M. Jadwiszczak, K. Jakubow-Piotrowska, P. Kedzierzawski, K. Bienkowski, J. Augustynski, Highly efficient sunlight-driven seawater splitting in a photoelectrochemical cell with chlorine evolved at nanostructured WO 3 photoanode and hydrogen stored as hydride within metallic cathode, Adv. Energy Mater. 10 (2020) 1903213, doi:10.1002/aenm.201903213.

[66] J.-.C. Dupin, D. Gonbeau, P. Vinatier, A. Levasseur, Systematic XPS studies of metal oxides, hydroxides and peroxides, Phys. Chem. Chem. Phys. 2 (2000) 1319–1324.

4$^{\text{th}}$ publication

WO$_3$ coatings for photoelectrochemical synthesis of persulfate: efficiency, stability and applicability

Petruleviciene, M., **Parvin, M.**, Savickaja, I., Gece, G., Naujokaitis, A., Pakstas, V., Pilipavicius, J., Gegeckas, A., Gaigalas, G. and Juodkazyte, J.

ORIGINAL PAPER

WO₃ coatings for photoelectrochemical synthesis of persulfate: efficiency, stability and applicability

Milda Petruleviciene[1] · Maliha Parvin[1] · Irena Savickaja[1] · Gintare Gece[1] · Arnas Naujokaitis[1] · Vidas Pakstas[1] · Jurgis Pilipavicius[1] · Audrius Gegeckas[2] · Gediminas Gaigalas[2] · Jurga Juodkazyte[1]

Abstract

Light-assisted electrochemical processes have the potential to replace energy-intensive electrosynthesis technologies, especially in the area of strong oxidant production. The efficiency of photoelectrochemical (PEC) synthesis relies mainly on the properties of a photoanode. PEC reaction as a multistep process, involving light absorption, charge carrier generation, separation, transport and transfer across electrode/electrolyte interface, is strongly dependent on the morphology, crystallinity and structural properties of the semiconductor layer. In this study, light-sensitive tungsten (VI) oxide, WO₃, films were formed applying a simple chemical solution deposition technique. Formation conditions were modified by using four different alcohols (methanol, ethanol, isopropanol and butanol) as reductants and different annealing temperatures. Detailed morphological, structural and compositional characterization of WO₃ samples was performed by X-ray diffraction, scanning electron microscopy, thermogravimetric analysis and Fourier transform infrared spectroscopy. Significant differences in surface morphology and crystallinity of the films were observed. PEC activity of the synthesized coatings was evaluated in sulfuric acid solution, where photocurrent stability and variation of Faradaic efficiency of persulfate generation were investigated. Possible causes of photocurrent decay and WO₃ surface passivation are discussed. Applicability of the system for deactivation of *Bacillus* spp. bacteria under visible light illumination is demonstrated.

Keywords Tungsten (VI) oxide · Photoelectrochemistry · Photoanode · Passivation · Persulfate · Disinfection

Introduction

Artificial photosynthesis, which directly converts photon energy into chemical energy, is regarded as a promising route to harness renewable solar energy for sustainable production of hydrogen as well as other important chemicals, especially strong oxidants (HClO, H_2O_2, $H_2S_2O_8$, etc.). These materials can inactivate bacteria and viruses, therefore, are of great interest for disinfection purposes [1–5] and water treatment [6, 7]. Photoelectrochemical (PEC) generation of strong oxidants is an attractive technology because it can be arranged in a way that disinfectants are produced at the

point-of-use without the need to handle hazardous chemicals. The efficiency of PEC processes strongly depends on the properties of semiconductor photoelectrodes. Tungsten (VI) oxide attracts the interest of researchers due to its moderate band gap (2.6–2.8 eV) and ability to absorb up to 12% of the solar spectrum [8], relatively large hole-diffusion length (~ 150 nm) as well as deep valence band position, rendering high oxidizing power to photogenerated holes. Photoelectrochemical reactions are complex multistep processes, which include light absorption, electron–hole pair generation, separation, transport and transfer across electrode/solution interface. Therefore, phase purity, crystallinity and morphology of the photocatalysts play a crucial role in determining the kinetics and efficiency of these processes [9]. It is well known that the structure and morphology of semiconductor layers can be controlled by synthesis route, additives and annealing conditions [10, 11]. Various techniques have been used to grow WO₃ thin films including chemical bath deposition [12], sol–gel [13], hydrothermal [14, 15], metal organic chemical vapour deposition [16], pulsed laser deposition [17]

✉ Jurga Juodkazyte
jurga.juodkazyte@ftmc.lt

[1] Center for Physical Sciences and Technology, Sauletekio av. 3, LT-10257 Vilnius, Lithuania

[2] Department of Microbiology and Biotechnology, Institute of Biosciences, Life Sciences Center, Vilnius University, Sauletekio av. 7, LT-10257 Vilnius, Lithuania

and magnetron sputtering [18]. Careful optimization of synthesis conditions is often required in order to achieve excellent performance of semiconductor photoelectrodes. There are several reports on the influence of alcohols on WO_3 phase formation in the sol–gel synthesis route. Orsini et al. [19] compared the effect of butanol and tert-butanol on the formation of mesoporous WO_3. The nature of alcohol as well as the composition of the alcohol mixture was shown to affect the porosity of the final product. Zeng et al. [20] synthesized vertically aligned WO_3 nanoplate array films by means of peroxotungstate reduction reaction. Excellent PEC performance was achieved using ethanol as a reductant. Yang et al. prepared tungsten trioxide layers with controlled morphology and strong photocatalytic activity using isopropanol alcohol as a stabilizer in sol–gel synthesis [21]. All mentioned works reported that alcohols influence the porosity, surface area and thickness of WO_3 coatings. However, a systematic study on how alcohols with different lengths of carbon chain effect the formation of tungsten (VI) oxide coatings has not been performed so far.

In this work, we studied how methanol, ethanol, isopropanol and butanol used as reductants in chemical solution deposition influence the crystallization of the WO_3 phase and shape the morphology of the coatings. Crystalline structure, composition and morphology of the films were investigated using X-ray diffraction (XRD), scanning electron microscopy (SEM) and Fourier transform infrared spectroscopy (FTIR). Phase evolution of WO_3 during the annealing process was studied using thermogravimetric analysis (TGA). The photoelectrochemical activity of the layers was evaluated by means of cyclic voltammetry (CV) in sulfuric acid solution. Significant influence of annealing temperature on PEC performance of the films was observed. Faradaic efficiency of photoanodic formation of persulfate species was evaluated and stability of the coatings under conditions of photoelectrolysis was investigated. Possible causes of deterioration of PEC activity were identified. The studied system was applied for deactivation of *Bacillus* spp. suspended in a neutral sulfate medium.

Experimental section

Synthesis of tungsten (VI) oxide layers

All chemicals used in this study were of analytical grade. Sodium tungstate dihydrate ($Na_2WO_4 \cdot 2H_2O$) (Carl Roth), ammonium oxalate ((NH_4)$_2C_2O_4$ (Chempur)), hydrochloric acid (HCl) (Chempur), hydrogen peroxide (H_2O_2) (Chempur), methanol (CH_3OH) (Reachem), ethanol (C_2H_5OH) (Merck), isopropanol (C_3H_7OH) (Reachem) and butanol (C_4H_9OH) (Reachem) were used as received from suppliers without further purification.

WO_3 thin films on fluorine-doped tin oxide (FTO) substrates were prepared using a slightly modified procedure described in detail in [13, 20]. FTO (5–7 Ω/sq) substrates were cut into 1×2.5 cm slides and washed under ultrasonication in acetone, ethanol and deionized water for 15 min in each. $Na_2WO_4 \cdot 2H_2O$ and (NH_4)$_2C_2O_4$ were dissolved in deionized water and HCl was added under continuous stirring at 40 °C. Next, H_2O_2 was added to form peroxotungstic acid (PTA) and, subsequently, methanol (MeOH) was added as a reductant. Ten minutes later, cleaned conducting glass substrates were dipped into the prepared mixture with FTO side facing down and kept for 140 min. Deposition was performed at 85 °C constant temperature in a water bath. Coated slides were rinsed in distilled water for 1 min to remove any remaining by-products of the synthesis (NaCl, oxalic acid, etc.) and dried in the drying oven at 40 °C for 10 h. The same synthesis procedure was followed for the preparation of WO_3 films using other reductants, i.e. ethanol (EtOH), isopropanol (IsoPrOH) and butanol (BuOH). Isopropanol was chosen instead of propanol, because coatings with propanol had poor adhesion to FTO substrate and synthesis was not reproducible. Finally, to investigate the effect of annealing conditions on phase purity, crystallinity, morphology and PEC performance of the films, WO_3 samples were annealed either at $T_{anneal} = 400$ °C or at 500 °C for 2 h in ambient atmosphere; the heating rate was 1 °C min^{-1} and the starting temperature was 20 °C. For the sake of brevity, the following notation of the samples was adopted in the paper: "reductant_WO_3_annealing temperature". The same synthesis procedure was applied to obtain WO_3 powders, which were used in TG and FTIR analysis described below. Powders used in TG analysis were not annealed.

Structural, morphological and optical characterization of tungsten (VI) oxide samples

XRD patterns of tungsten oxide films on FTO substrate were recorded using an X-ray diffractometer SmartLab (Rigaku) equipped with a 9-kW rotating Cu anode X-ray tube. The grazing incidence (GIXRD) method was used in 2θ range 20–80 °C. An angle between a parallel beam of X-rays and a specimen surface (ω angle) was adjusted to 0.5 °C. Phase identification was performed using Match software and Crystallography Open Database (COD).

The surface morphology and thickness of the tungsten oxide layers on FTO substrate were investigated using Helios NanoLab dual-beam workstation equipped with X-Max 20-mm^2 energy dispersion spectrometer (Oxford Instruments).

Phase evolution of the tungsten oxide upon heat treatment was studied using thermogravimetric analysis (TGA) (PerkinElmer STA6000) and differential thermal analysis (DTA) (PerkinElmer STA6000). Samples were annealed at

temperature from 30 to 500 °C with 10 °C min^{-1} heating rate. Air flow was 20 cm^3 min^{-1}.

The phase composition of WO_3 powders was investigated by Fourier transform infrared spectroscopy using a Perkin Elmer spectrophotometer with a resolution of 4 cm^{-1} over a wavenumber range of 450–4000 cm^{-1}.

The diffuse reflectance spectra of WO_3 films were measured in the spectral range from 300 to 1100 nm using the Avantes spectrometer (AvaSpec- HS-TEC) equipped with an integrating sphere (Labsphere). Avantes xenon lamp (AvaLight-XE) was used as the light source for sample excitation.

Photoelectrochemical measurements

Cyclic voltammetric measurements were performed using three-electrode cell and potentiostat/galvanostat AUTOLAB 302 (Eco Chemie). WO_3 films on FTO substrates, Ag/AgCl/ sat. KCl and Pt plate (1×1 cm^2) were used as working, reference and counter electrodes, respectively. All potential values in the text are reported vs Ag/AgCl scale unless noted otherwise. The surface of working electrodes was illuminated with a high-intensity discharge Xe-lamp with 6000 K spectrum and calibrated with a silicon diode to simulate AM 1.5 illumination (100 mW cm^{-2}) at the sample surface. The same illumination conditions were used throughout the study. Experiments were performed in the solution of 0.5 M H_2SO_4. Current density values were calculated based on the geometric area of the working electrode.

Photoelectrolysis experiments were performed in a two-electrode configuration using WO_3_400 samples as photoanodes and Pt plate as cathode. Photoelectrolysis with a certain photoanode was performed in 0.5 M H_2SO_4 solution under cell voltage of 1.8 V and illumination for the periods of 500, 1000, 1500, 2000 and 2500 s consecutively. After each period, the electrolyte from the anodic compartment of the cell was collected and subjected to redox titration with $FeCl_2$ and $K_2Cr_2O_7$ to determine the amount, m_{exp} (g), of photoelectrochemically formed $S_2O_8^{2-}$. The theoretical amount, m_{theor}, was calculated according to Faraday's law on the basis of electric charge, Q (C), passed through the cell during photoelectrolysis assuming two electron transfer in oxidation of SO_4^{2-} to $S_2O_8^{2-}$. The Faradaic efficiency, FE (%), of the photoelectrochemical $S_2O_8^{2-}$ generation was evaluated as the ratio $m_{exp}/m_{theor} \times 100$.

Evaluation of the antimicrobial effect of PEC system with WO_3 photoanode

Bacillus sp. AA2 strain was selected as the biological object to evaluate the antimicrobial effect of photoelectrochemical persulfate generation with the selected WO_3 sample. The procedure used in the experiments was analogous to the one reported in our previous study [22]. The bacterial strain was incubated in Lysogeny broth at 37 °C for 6 h on a rotary shaker with shaking of 180 RPM. The cells were collected by centrifugation at $1500 \times g$ for 15 min. The supernatant was then discarded and the cells were washed twice with 0.9% NaCl. After centrifugation, cells were collected again and then suspended in 50 cm^3 of 0.1 M Na_2SO_4. A fresh bacterial culture of the test strain was prepared for each experiment following the same procedure. Samples of 10 cm^3 were taken for bacterial disinfection experiments, which were conducted under photoelectrochemical (electrolysis under illumination), electrolytic (electrolysis without illumination), photolytic (illumination without electrolysis) and chemical oxidation conditions as described further.

The experiments were performed in a two-compartment quartz cell with a Millipore membrane filter (0.22 μm pore size) between the anode and cathode sections, Pt cathode and IsoPrOH_WO_3_400 sample as photoanode. The cathodic compartment of the cell was filled with pure 0.1 M Na_2SO_4 solution, whereas the anodic one was filled with suspension of cells in 0.1 M Na_2SO_4. Photoelectrolysis was performed at 1.6 V and illumination until charge of 0.5 C was passed through the system. In the case of electrolytic treatment, the same voltage with no illumination was applied, whereas under photolytic conditions just illumination without external bias was used. The duration of photolytic and electrolytic experiments was the same as that of photoelectrochemical one. The chemical impact of persulfate on bacteria species was tested by adding the calculated amount of potassium persulfate, which was equivalent to the amount of $S_2O_8^{2-}$ that would be produced photoelectrochemically after the passage of 0.5 C assuming 100% FE of persulfate formation. After each experiment, 1.5-cm^3 aliquots were acquired for the analysis of bacterial survival. Serial dilutions were made using 0.9% NaCl and 0.1 cm^3 was spread on plate count agar plates. The plates for microorganism were incubated at 37 °C overnight (16 h) and the colony-forming units (CFU) were enumerated. The CFU were counted before and after the disinfection experiments.

Results and discussion

Effect of synthesis conditions on crystalline structure, morphology and optical properties of WO_3 films

The crystalline structure of tungsten (VI) oxide coatings was characterized using XRD analysis. Figure 1 shows XRD patterns of coatings synthesized with methanol, ethanol, isopropanol and butanol and annealed at 400 °C (Fig. 1a) and 500 °C (Fig. 1b). It is evident that different reductants and annealing temperatures influence the crystallinity of the
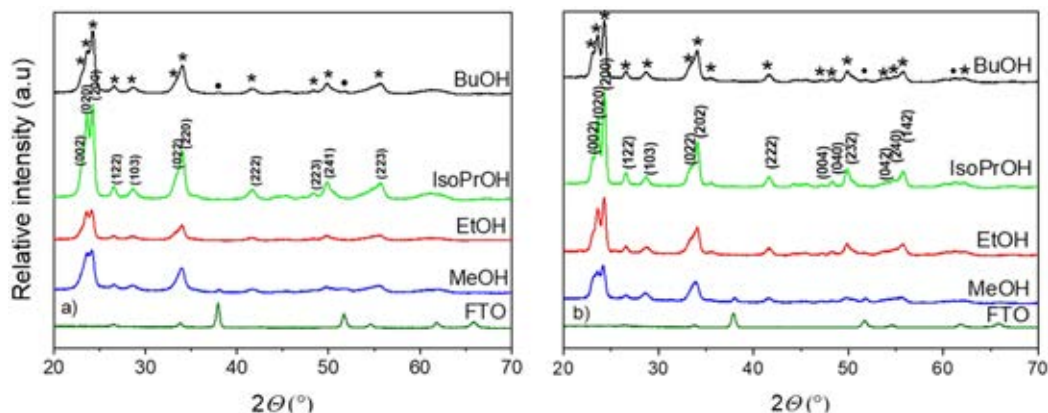
Fig. 1 XRD patterns of FTO substrate and WO₃ thin films deposited using methanol, ethanol, isopropanol and butanol as reductants and annealed at 400 °C **a**) or 500 °C **b**) Notations: *-WO₃ [COD: 2311041], ●-SnO₂ [COD: 2101853]

samples. All diffractograms have clusters of three peaks at $2\theta = 23.20°$, $23.60°$ and $24.29°$, which are, respectively, attributed to (002), (020) and (200) facets of monoclinic tungsten trioxide (COD: 2311041). The results of annealed samples indicate preferential growth of WO₃ along (020) and (200) crystal planes. The narrowest diffraction peaks corresponding to (020) and (200) facets are observed in the samples synthesized with IsoPrOH, implying that the crystallinity of these WO₃ coatings is the highest. Due to lower crystallinity, all samples annealed at 400 °C (Fig. 1a) have slightly broader peaks compared to their counterparts heated at 500 °C (Fig. 1b).

It is well known that solvents and additives in the synthesis reaction mixture can substantially influence the ultimate shape of the crystals by tuning their growing rate and orientation [9]. Normally, if preferred growth occurs along certain crystal plane, corresponding peak intensity in the XRD

spectrum will be higher compared to the same material with random distribution of crystallites [23]. It is noteworthy that peaks at $2\theta = 23.20°$, which correspond to facet (002), are not clearly expressed in all the coatings investigated (Fig. 1). Very low intensity of these peaks implies perpendicular position of the facet with respect to the substrate, whereas higher intensity of (020) and (200) peaks suggests parallel to substrate orientation of the facets. Preferential growth of (200) and (020) planes (Fig. 2) in the synthesis adopted in this study can be explained by preferential adsorption of oxalate ion as a capping agent onto (002) plane. Indeed, $C_2O_4^{2-}$ as an electron-rich organic ion is known to form hydrogen bonds with the interlayer H₂O molecules in orthorombic $WO_3 \cdot H_2O$ on (002) facet. This leads to restriction of the growth along [002] direction and formation of laminar structure [20]. In accordance with theoretical calculations reported in [24], a surface energy order of the facets is as

Fig. 2 Dominant **a**) (200) (red plane) and **b**) (020) (green plane) facets and growing directions of monoclinic WO₃ forming under different synthesis conditions used in this study; the position of facet (002) (blue plane) is perpendicular to the substrate
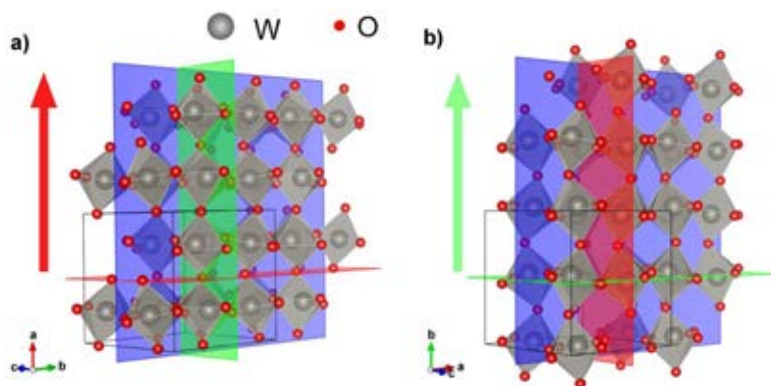
follows: 1.56 J m^{-2} (002) > 1.54 J m^{-2} (020) > 1.43 J m^{-2} (200), implying that (200) is the most stable and (002) is the most unstable. Thus, the synthesis conditions used in this study are favourable for the formation of thin films with preferential growth of the more stable crystal facets of monoclinic WO$_3$ with orientation parallel to the substrate. An additional phase of tin oxide from the FTO substrate was also observed in the XRD patterns of the samples (Fig. 1).

SEM images of the surface morphology and cross-sections of WO$_3$ coatings formed in four different solutions and annealed at different T_{anneal} are shown in Fig. 3. The

main difference between the morphology of WO$_3$ films, deposited using different alcohols as reductants, consists in the size and shape of the particles forming the coating. MeOH_WO$_3$ layers are composed of 100–700-nm circle-shaped plates. EtOH_WO$_3$ and IsoPrOH_WO$_3$ films consist of rather large 1000–1500-nm and 1000–2000-nm rectangular-shaped plates, whereas BuOH_WO$_3$ – of the finest 100–500-nm square-shaped particles. The influence of annealing temperature is more vivid in SEM images of EtOH_WO$_3$ and BuOH_WO$_3$ films, where a considerable increase in particle size after annealing at 500 °C can be

Fig. 3 Top view and cross-sectional (insets) SEM images of WO$_3$ samples formed using methanol (**a**, **b**), ethanol (**c**, **d**), isopropanol (**e**, **f**) and butanol (**g**, **h**) as reductants and annealed at 400 °C (**a**, **c**, **e**, **g**) or 500 °C (**b**, **d**, **f**, **h**)
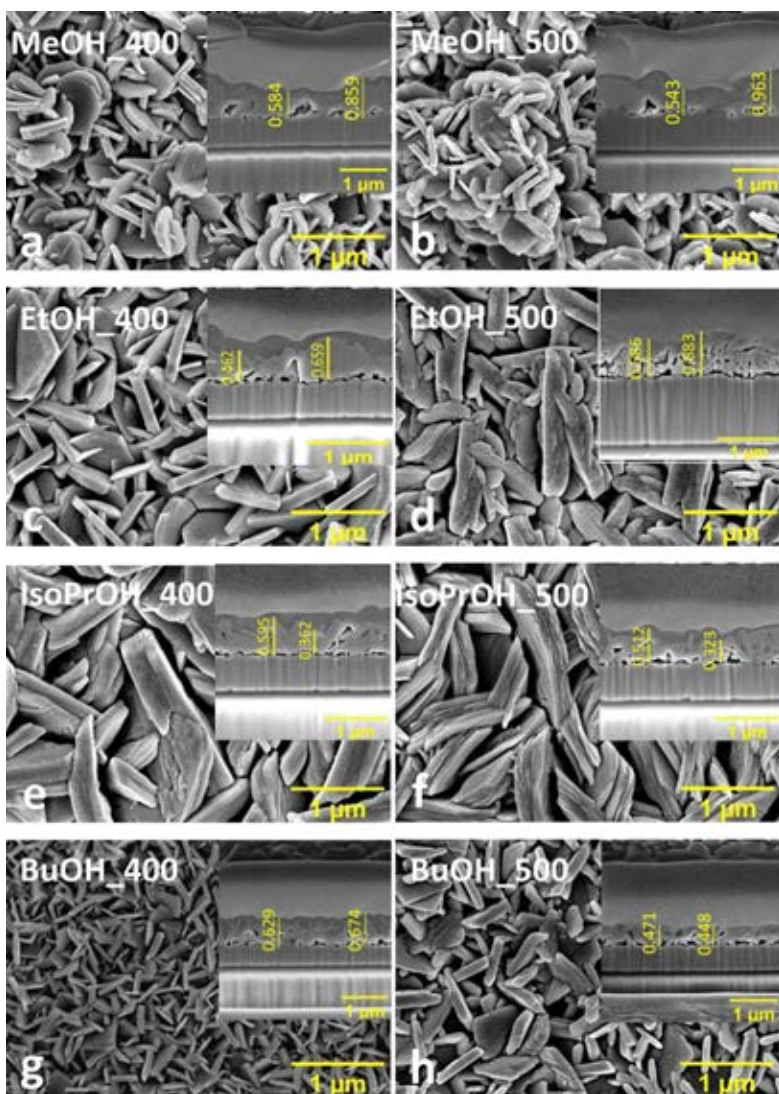
observed (Fig. 3c, d, g, h). Cross-sectional SEM images of the coatings, shown as insets in Fig. 3, reveal that the thickness of the layers varies between 0.5 and 0.7 μm and is practically independent of the reductant and T_{anneal}.

Significant differences in the morphology of WO_3 films can be explained considering the colloidal stability of the oxide particles in different solvents as well as the reducing ability of primary alcohols. The latter is known to increase with decreasing carbon chain length, due to higher electron density on the hydroxyl group of alcohol [25]. In the synthesis, stronger reductant should initiate faster reduction of PTA, leading to lower stability of solution and precipitation of $WO_3 \cdot nH_2O$ particles. In general, addition of alcohols with lower dielectric constant, κ, to aqueous solution leads to supersaturation and precipitation of dissolved substances because of a decrease in their solvation energy [26]. Moreover, dielectric constant is temperature dependent — it decreases with an increase in T and this is why precipitation occurs faster at higher temperatures. On the other hand, the energy barrier which inhibits the agglomeration of the particles is known to be directly proportional to κ of the liquid medium and the surface potential [27]. In the reduction process, when the dielectric constant of the solution is relatively high, the energy barrier between a particle and solution is high enough. Therefore, the primary oxide particles precipitated from such solution are stable and do not agglomerate, what leads to the formation of smaller units. Dielectric constants of water and alcohols used in the synthesis are listed in Table 1. The trend of increasing size of plate-shaped particles with a decrease in κ of alcohol is clearly observed in series: $MeOH\_WO_3 < EtOH\_WO_3 < IsoPrOH\_WO_3$. $BuOH\_WO_3$ coatings are composed of small particles (Fig. 3g, h) and do not follow the tendency. This could be explained by the lowest reduction ability of butanol among the alcohols-reductants investigated and, consequently, sluggish kinetics of the process. Moreover, steric barriers related with dimensions of 1-butanol and its oxidation products such as butyralaldehyde or butan-1-carboxylic acid can play a crucial role in the formation of $WO_3 \cdot nH_2O$ colloids with oxalate anion. Most likely, all these factors contribute to the formation of small particles.

Table 1 Dielectric constant κ values of water and alcohols used in the synthesis

Solvent	Boiling point, °C	κ at 20 °C	κ at 80 °C	Reference
Water	100	80.37	60	[59, 60]
Methanol	64.5	32.35	28.24	[59, 61–64]
Ethanol	78.3	25.0	19.45	[59, 61, 63, 64]
Isopropanol	82.2	18.62	11.82	[64, 65]
Butanol	117.6	17.43	11.4	[59, 62–64]

Due to considerable light scattering by the microstructured WO_3 surface, absorbance of the films was evaluated from diffuse reflectance spectra measured with an integrating sphere and the results are presented in Fig. 4. One can see that the absorption edge of the coatings is located at about 470 nm irrespective of the reductant used in the synthesis and annealing temperature. This corresponds to a bandgap of 2.6 eV, which is a typical value for WO_3 [28, 29].

Effect of alcohols-reductants on thermal decomposition of $WO_3 \cdot H_2O$ powders

The structural evolution of $WO_3 \cdot H_2O$ powders synthesized with methanol, ethanol, isopropanol and butanol was investigated by means of thermogravimetric-differential thermogravimetric (TG-DTG) analysis. The TG curves show weight loss during the annealing, whereas DTG profiles reflect the thermal processes. As can be seen from Fig. 5, weight loss and differential thermogravimograms differ significantly depending on the composition of the powder. DTG patterns of MeOH_WO₃ and EtOH_WO₃ show peaks
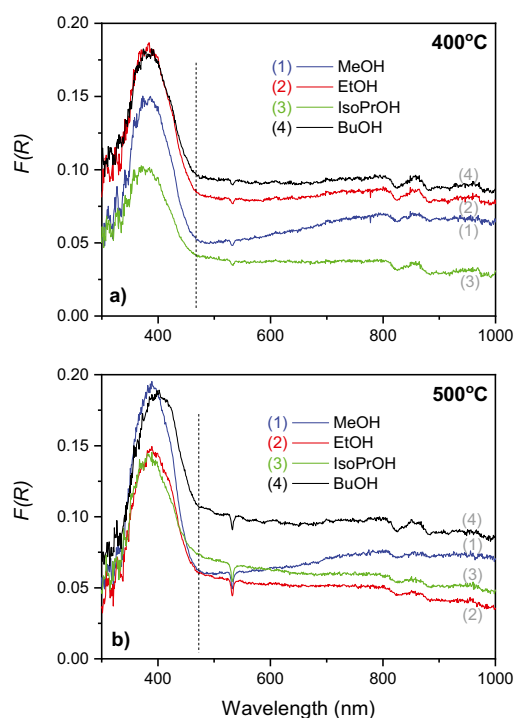

Fig. 4 Diffuse reflectance spectra of WO_3 coatings formed with methanol (1), ethanol (2), isopropanol (3) and butanol (4) as reductants and annealed at **a)** 400 °C and **b)** 500 °C
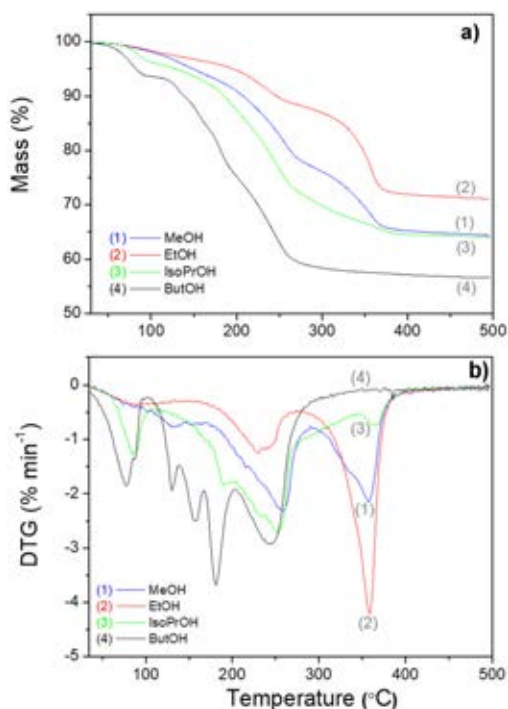
Fig. 5 Results of thermogravimetric **a**) and differential thermogravimetric **b**) analysis of $WO_3 \cdot nH_2O$ powders obtained using methanol, ethanol, isopropanol and butanol as reductants

at the same positions but of different intensity as well as two weight loss steps, whereas the profiles of IsoPrOH_WO$_3$ and BuOH_WO$_3$ powders display more endothermic peaks and weight loss steps at different ranges of temperature. Total weight losses of tungsten oxide hydrate synthesized with MeOH, EtOH, IsoPrOH and BuOH are 35%, 28%, 28% and 45%, respectively. During the first step, MeOH_WO$_3$ and EtOH_WO$_3$ powders slowly lose 22% and 10% of weight, respectively, as temperature rises from 25 to 260 °C (Fig. 5a). The first endothermic peak at ~ 125 °C (Fig. 5b) is mainly attributed to the desorption of the surface water and decomposition of organic compounds (aldehydes and carboxylic acid) [30]. However, in the samples synthesized with IsoPrOH and BuOH, this step is divided into two steps. The first one at 75 °C (Fig. 5a) is related with the removal of physically absorbed water molecules from the surface (4% and 6% of total mass, respectively). The second step within 100–260 °C with a corresponding weight loss of 26% and 41%, respectively, and larger number of endothermic peaks compared to MeOH_WO$_3$ and EtOH_WO$_3$ powders, can

be attributed to the decomposition of organic compounds, which are formed during the synthesis process. Isopropanol oxidation can yield acetone, propylene and, in some cases, small amounts of isopropyl ether [31]. Butanol oxidation produces aldehydes, carboxylic acids, olefins and unsaturated alcohols, which are removed below 260 °C. This can explain significant weight loss and endothermic peaks at 75 °C, 125 °C, 160 °C and 180 °C observed in the DTG profile (Fig. 5b). The endothermic peak at 255 °C seen in DTG curves of all samples in Fig. 5b is ascribed to the removal of structurally bonded water molecules and the beginning of formation of anhydrous WO$_3$ [32, 33]. This peak shows that structure of WO$_3$ starts to change from orthorhombic WO$_3 \cdot H_2O$ to monoclinic WO$_3$ [34–36]. Furthermore, the slight weight loss in 250–500 °C range and endothermic peaks at 360 °C, seen in DTG patterns of all samples except BuOH_WO$_3$, might be caused by continuing transition to monoclinic phase. In the case of butanol, this process takes place at 250 °C, probably due to low reducing power and formation of smaller WO$_3 \cdot H_2O$ colloids, what leads to faster phase transformation [33, 37]. Analysis of DTG results shows that the crystalline monoclinic WO$_3$ phase is already formed at 400 °C, because there are no more thermal processes within 400–500 °C (Fig. 5b). These results correlate well with XRD data witnessing the formation of crystalline structure of tungsten oxide at 400 °C. In the range between 400 and 500 °C, growth of crystals and some final arrangement of the structure occurs, which is also reflected in diffractograms by an increase in the intensity of the peak which corresponds to (002) facet (Fig. 1).

Structural investigations using FTIR spectroscopy

To confirm the structural composition and the purity of the annealed WO$_3$ powders formed using different alcohols, Fourier transform infrared spectroscopy measurements were performed. The results are presented in Fig. 6. The broad absorption peaks at < 1000 cm^{-1} indicate the characteristic lattice vibrations of tungsten oxide. The bands at 645 cm^{-1} and 619 cm^{-1} of the samples annealed at 400 °C and 500 °C, respectively, are attributed to W–O vibration mode [33]. Bands at 799 cm^{-1} (400 °C) and 807 cm^{-1} (500 °C) are related with the inter-bridge stretching of O–W–O and those at 739 cm^{-1} (400 °C) and 753 cm^{-1} (500 °C) — with the corner-sharing mode W–O–W [38, 39]. The broad, less intensive band at 3400 cm^{-1} can be attributed to O–H stretching mode and the peak at 1625 cm^{-1} corresponds to W–OH bending vibration mode of H$_2$O molecules adsorbed on the surface of the powder [33, 40, 41], because chemically bonded water is finally removed at 360 °C, as discussed above (Fig. 5). Moreover, it should be noted that W=O vibrational mode at 980 cm^{-1}
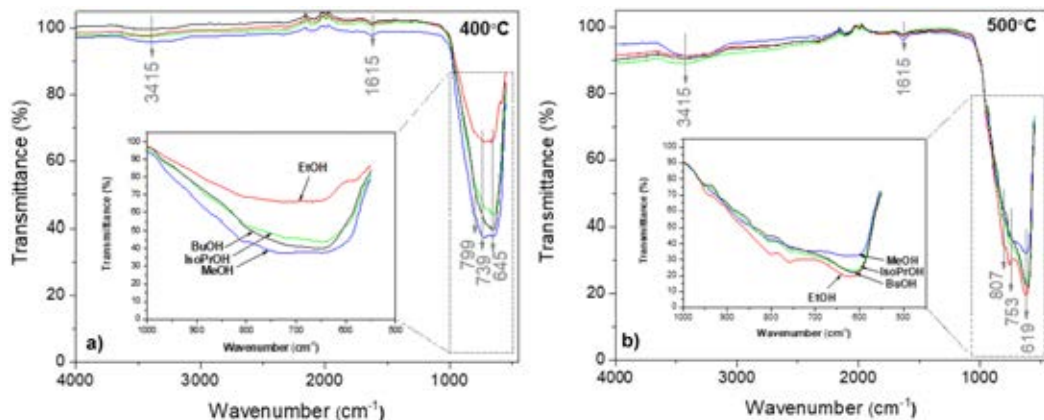
Fig. 6 FTIR spectra of WO$_3$ powders prepared using methanol, ethanol, isopropanol or butanol and annealed at 400 °C **a**) or 500 °C **b**)

is not seen in the FTIR spectra of the samples, implying that anhydrous WO$_3$ is formed [42]. Kanan et al. [43] have shown that there are two types of adsorbed water on the surface of tungsten oxide: the major part is weakly bound and can be eliminated with evacuation at room temperature, whereas the second type of adsorbed H$_2$O can be eliminated only after evacuation at 400 °C [43]. It can be seen that within 500–1000 cm^{-1} range peaks of powders annealed at 500 °C are sharper, which could be due to the higher crystallinity of WO$_3$ [44]. These results are in agreement with XRD data showing more distinguished (200) and (020) peaks as well as emerging peak of (002) plane after annealing at 500 °C.

Photoelectrochemical performance of WO$_3$ films formed

The photoelectrochemical activity of WO$_3$ films deposited on FTO substrate was characterized using cyclic voltammetry in the solution of 0.5 M H$_2$SO$_4$ in dark and under illumination. The results are presented in Fig. 7. The voltammetric response of WO$_3$ coatings can be divided into two parts as described further. Within the E range below 0.5 V, the electrochemical behaviour of the electrode is illumination independent, as can be seen from the comparison of CVs recorded in dark and under illumination (Fig. 7). Nearly symmetric anodic and cathodic peaks observed here
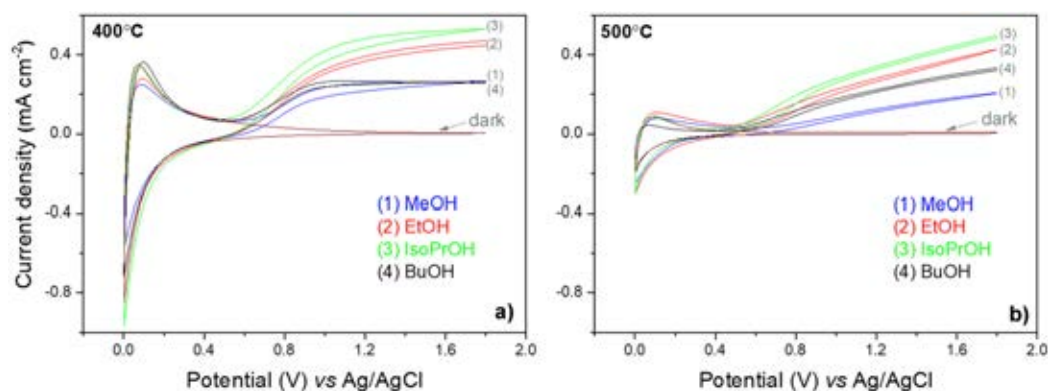

Fig. 7 Cyclic voltammograms of WO$_3$ coatings formed with methanol (1), ethanol (2), isopropanol (3) and butanol (4) as reductants and annealed at **a**) 400 °C and **b**) 500 °C. Solution 0.5 M H$_2$SO$_4$, poten-
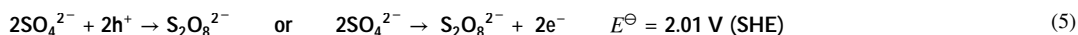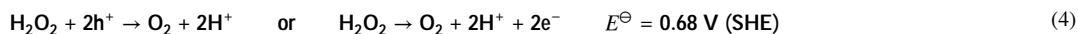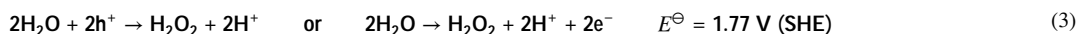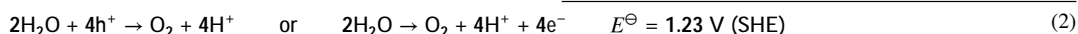
tial scan rate 50 mV s^{-1}, intensity of illumination ~100 mW cm^{-2}. Curves recorded in dark are those of samples prepared with isopropanol

correspond to reversible redox transition between W (VI) and W (V) oxygen species:
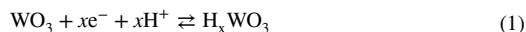
$$WO_3 + xe^- + xH^+ \rightleftarrows H_xWO_3 \tag{1}$$

This electrochemical process, involving participation of protons from the solution, takes place at the electrode/electrolyte interface as well as in the bulk of the oxide layer [45, 46]. The kinetics of this process depends on the diffusivity of protons within film, which, in turn, is dependent on the structural and morphological characteristics of WO_3 layers. Consequently, the area under the voltammetric peaks within 0–0.5 V, which is equivalent to charge consumed in reaction (1), can be treated as a relative measure of electrochemical activity of WO_3 films.

The region above 0.5 V is the range of photocurrent, where no electrochemical reactions occur in dark (zero current), whereas under illumination, anodic current is observed. Such behaviour is consistent with the n-type conductivity of WO_3 layers. The photoanodic current results from the interaction of solution species with photogenerated holes, which form in the valence band of the semiconductor. Possible processes can be described by the following reactions:

This is the reason why various hole-mediated processes are actually observed at potentials significantly lower than thermodynamically predicted values. Photogenerated electrons in the conduction band of semiconductor are driven to cathode, where they participate in reduction reactions. In the case of Pt cathode in sulfuric acid solution, hydrogen evolution reaction should be the main cathodic process.

It can be seen in Fig. 7 that all synthesized coatings were photoelectrochemically active; however, certain differences in their behaviour are observed. In general, samples annealed at 400 °C (Fig. 7a) exhibit significantly faster increase and saturation of photocurrent, j_{ph}, than those annealed at 500 °C (Fig. 7b). This implies more efficient generation, separation, transport and transfer of the photogenerated charge carriers in the films annealed at lower temperature. In accordance with j_{ph} values and the reductant used in synthesis, WO_3 coatings can be aligned into the following sequence: IsoPrOH_WO_3 > EtOH_WO_3 > BuOH_WO_3 > MeOH_WO_3. A very distinct feature of the coatings annealed at 500 °C is a significant decrease in illumination-independent currents at $E < 0.5$ V (Fig. 7). It means that rearrangement of the crystalline structure of WO_3, which takes place during annealing in the range of temperature between 400 and 500 °C as

$$2H_2O + 4h^+ \rightarrow O_2 + 4H^+ \quad \text{or} \quad 2H_2O \rightarrow O_2 + 4H^+ + 4e^- \quad E^\ominus = \textbf{1.23 V (SHE)} \tag{2}$$

$$2H_2O + 2h^+ \rightarrow H_2O_2 + 2H^+ \quad \text{or} \quad 2H_2O \rightarrow H_2O_2 + 2H^+ + 2e^- \quad E^\ominus = \textbf{1.77 V (SHE)} \tag{3}$$

$$H_2O_2 + 2h^+ \rightarrow O_2 + 2H^+ \quad \text{or} \quad H_2O_2 \rightarrow O_2 + 2H^+ + 2e^- \quad E^\ominus = \textbf{0.68 V (SHE)} \tag{4}$$

$$2SO_4^{2-} + 2h^+ \rightarrow S_2O_8^{2-} \quad \text{or} \quad 2SO_4^{2-} \rightarrow S_2O_8^{2-} + 2e^- \quad E^\ominus = \textbf{2.01 V (SHE)} \tag{5}$$

where $E^\ominus$ stands for standard potential. Due to deep valence band position in WO_3 (> 3 V (SHE) [47]), holes have enough energy to drive oxidation of water and anions via formation of highly reactive intermediates such as hydroxyl (OH•) and sulfate ion radicals (SO_4^{2-}•) [48]:

$$H_2O \rightarrow OH^\cdot + e^- + H^+ \qquad E^\ominus = \textbf{2.730 V (SHE)} \tag{6}$$

$$SO_4^{2-} \rightarrow SO_4^{-\cdot} + e^- \qquad E^\ominus = \textbf{2.437 V (SHE)} \tag{7}$$

which can yield H_2O_2 and $S_2O_8^{2-}$ through combination reactions ($2OH^\cdot \rightarrow H_2O_2$ and $2SO_4^{-\cdot} \rightarrow S_2O_8^{2-}$). It is noteworthy that the potential of the electrode, which is measured in CV experiments (Fig. 7), corresponds to the electrochemical potential of the electrons in the semiconductor (Fermi level), whereas photoanodic reactions involve participation of holes, which have different energy as discussed above.

revealed by XRD and FTIR investigations (Figs. 1, 6), leads also to a decrease in the electrochemical activity of the oxide films. The total charge corresponding to cathodic and anodic current peaks within E range from 0 to 0.45 V (Fig. 7) is compared in Fig. 8. It can be seen that upon annealing at 500 °C charge values decreased from 2 to 3 times (cf. Figure 8a and b). This points to a significant restructuring of WO_3 layers, as a result of which the insertion and extraction of protons according to reaction (1) becomes hindered. This correlates with the increase in particle size observed in SEM images of EtOH_WO_3 and BuOH_WO_3 (Fig. 3) and explains the degradation of photoelectrochemical performance, because these structural rearrangements hamper the movement of photoinduced charge carriers as well. Similar effect of sintering accompanied by deterioration of PEC activity with increase in annealing temperature of tungsten oxide films was reported in [49]. It should be noted,

Fig. 8 Influence of annealing temperature on electrochemical activity of WO$_3$ films prepared using different alcohols: charge under anodic and cathodic voltammetric peaks within 0–0.45 V range (see Fig. 6) is taken as a relative measure of electrochemical activity of coatings annealed at 400 °C **a**) and 500 °C **b**)
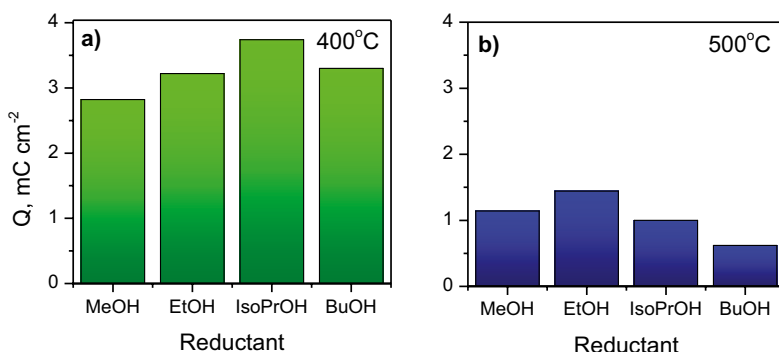
however, that the optimal annealing temperature depends on the synthesis method used. Though the majority of the studies report that annealing of WO$_3$ at 500 °C gives the best results in terms of PEC activity, our findings demonstrate that in the case of synthesis adopted in this study, heat treatment at 400 °C was the most optimal in terms of crystallinity and morphology of the coatings.

To evaluate the Faradaic efficiency (FE) of PEC generation of persulfate species as well as long-term stability of WO$_3$ samples, photoelectrolysis experiments in a two-electrode cell in 0.5 M H$_2$SO$_4$ solution were performed with MeOH_WO$_3$_400, EtOH_WO$_3$_400, IsoPrOH_WO$_3$_400 and BuOH_WO$_3$_400 photoanodes. Samples annealed at 400 °C were chosen for this experiment because of higher electrochemical activity (Fig. 8) and optimal PEC performance (Fig. 7). Cell voltage was set to 1.8 V, because such conditions ensured the highest achievable photocurrent, while the dark current was still negligible. On the basis of CVs shown in Fig. 7, it can be reasonably presumed that

the potential of WO$_3$ photoanode during photoelectrolysis stayed within the range between 1.0 and 1.8 V. Chrono-amperograms (CAs) showing the variation of j_{ph} during 5 consecutive periods of electrolysis with increasing duration are presented in Fig. 9 together with the values of Faradaic efficiency of photoelectrochemical S$_2$O$_8^{2-}$ formation determined in each experiment. It should be noted that the same sample was used in all 5 experiments in order to assess the deterioration of PEC activity. A characteristic feature of all CAs in Fig. 9 is the initial spike in photocurrent observed when light is turned on, which is followed by an exponential decay of j_{ph} mostly due to recombination of photoinduced charge carriers till some equilibrium between the charge transfer and recombination processes is attained. Kinetics of recombination depends mostly on the crystallinity (degree of structural order) of the materials as well as on the presence of the so-called surface states, which act as traps and recombination centres for the photoinduced electrons and holes [50, 51].
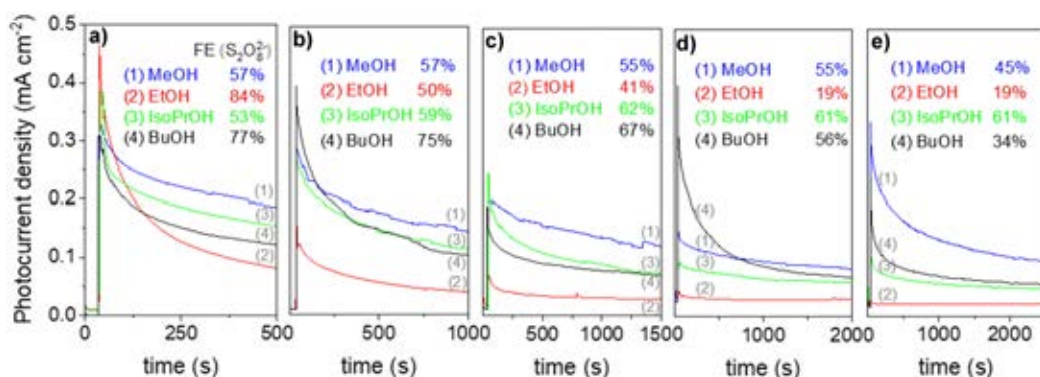

Fig. 9 Chronoamperograms of WO$_3$_400 films prepared using different alcohols. CAs were recorded during five consecutive photoelectrolysis experiments with increasing duration (**a–e**), 0.5 M H$_2$SO$_4$, cell voltage 1.8 V, intensity of illumination ~ 100 mW cm^{-2}. Values of Faradaic efficiency of photoelectrochemical S$_2$O$_8^{2-}$ generation determined after each experiment are indicated in the figures
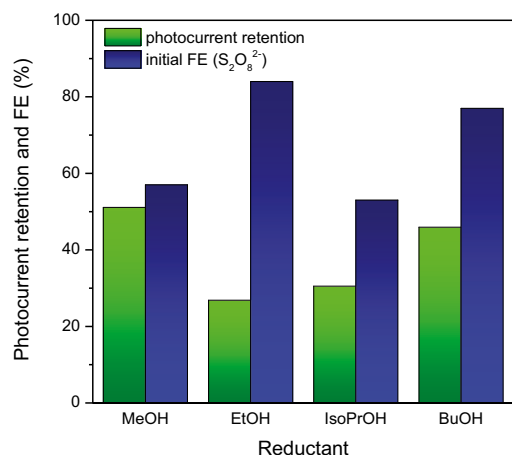
Fig. 10 Comparison of initial Faradaic efficiency (Fig. 8a) and photocurrent retention values (Fig. 8a vs e) of WO_3 coatings prepared using different alcohols

It can be seen from Fig. 9 that stability of photocurrent and FE of $S_2O_8^{2-}$ generation strongly depended on the photoanode. FE values were decreasing with the duration of photoelectrolysis for all samples except IsoPrOH_WO_3_400, for which even a slight increase in FE from 53 to 61% was observed. The most significant diminishing of FE — from 84 to 19% — was determined in the case of EtOH_WO_3_400, which was also accompanied by the most significant decrease in photocurrent (Fig. 9a vs e). The fact that Faradaic efficiency was lower than 100% implies that the rest of the photogenerated charge was consumed in the photooxidation of water molecules, which is the main competing reaction in aqueous electrolytes. As mentioned above, H_2O_2 can also be formed as an intermediate product of H_2O oxidation (Eq. 3) and its presence would distort the results of chromatometric $S_2O_8^{2-}$ determination. Therefore, permanganometric analysis, which is selective for H_2O_2 in the presence of persulfate, was performed in an attempt to detect the formation of this product. However, no H_2O_2 was found, or its amount was below the limit of detection of this analysis technique. It is highly probable that hydrogen

peroxide, once formed, undergoes fast further oxidation to O_2 according to reaction (4).

It is noteworthy that higher initial values of Faradaic efficiency of $S_2O_8^{2-}$ formation correlated with a faster decrease in j_{ph} for all samples except IsoPrOH_WO_3_400 as shown in Fig. 10, where the values of initial FE and photocurrent retention of all samples are compared. Retention of j_{ph} (in %) was evaluated from the data shown in Fig. 9 as the ratio of initial and final values of stationary photocurrent taken from Fig. 9a at $t = 500$ s and Fig. 9e at $t = 2500$ s, respectively. These results imply that higher activity of the sample in PEC formation of persulfate is related with more significant deterioration of PEC activity of WO_3 layer. The latter can be ascribed either to photocorrosion/dissolution or to surface passivation of the photoactive layer. Dissolution of WO_3 during photoanodic reactions in H_2SO_4 has been evidenced recently in [52–54]. The mechanism of this process is still unclear. Since tungsten in WO_3 is in its highest oxidation state, formation of surface peroxo species, induced by H_2O_2 and $HO\cdot$ as by-products of the water oxidation, is considered to be the main cause of material degradation [54]. The results of our study suggest that photocurrent decay is also significant when oxidation of SO_4^{2-} (not H_2O) is dominating photoanodic reaction (Fig. 10). In [55], the degradation of H_xWO_3 photoelectrodes was explained by recombination of holes with W^{5+} donors, which can be prevented by efficient hole scavenging by solution species. We hypothesize that holes, which are not scavenged by solution species, can destructively oxidize WO_3 to more soluble and photoelectrochemically inactive surface peroxotungstate compounds as shown in Fig. 11. Oxidative cleavage of W–O–W bond with formation of surface peroxo species can also occur as a result of light-induced interaction of WO_3 with radical species ($SO_4^{\bullet-}$ or $OH^\bullet$) leading to the deterioration of PEC activity of the samples. XRD and FTIR characterization of WO_3 photoelectrodes after photoelectrolysis did not, however, reveal any tangible changes in the crystalline structure of the layers (Figs. S1 and S2), what points to the necessity of application of in situ and operando techniques for investigation and profound understanding of PEC processes.

Overall, the results presented herein show that the kinetics of charge transfer and photocurrent stability as well as selectivity of photoanodic reaction is strongly influenced by the morphology of WO_3 films; therefore, careful engineering of

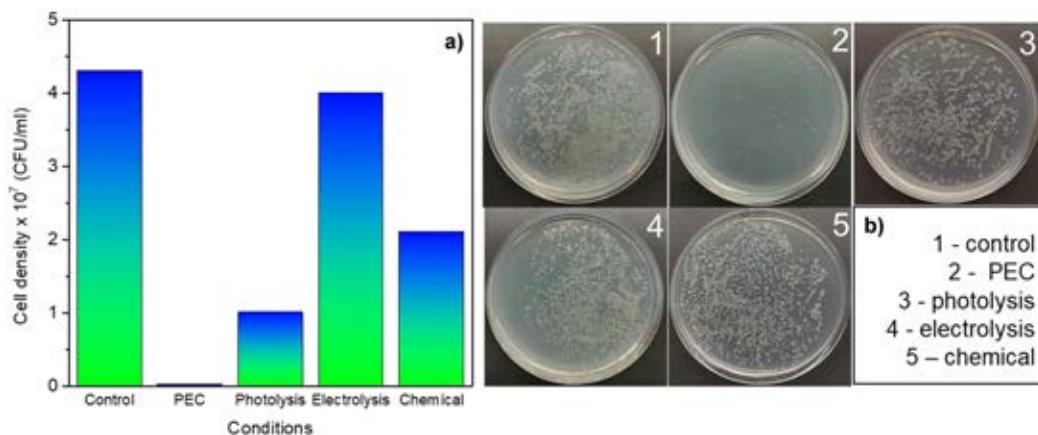**Fig. 11** Mechanism of hole-induced formation of peroxo species on the surface of WO_3 film

Fig. 12 **a**) Comparison of disinfection efficiencies under photoelectrochemical (100 mW cm^{-2}, 1.6 V), photolytic (100 mW cm^{-2}, 0 V), electrolytic (0 mW cm^{-2}, 1.6 V) and chemical oxidation conditions in the case of *Bacillus* spp. suspensions in 0.1 M Na$_2$SO$_4$; **b**) optical microscope images of microbial CFUs before and after indicated treatments at 10^{-3} dilution

the photoelectrode/electrolyte interface is essential in order to achieve efficient light-to-chemical energy conversion.

Antimicrobial effect of light-assisted formation of persulfate on WO$_3$ photoelectrode

Furthermore, applicability of photo-assisted generation of persulfate species on WO$_3$ photoelectrode for deactivation of *Bacillus* spp. suspended in 0.1 M Na$_2$SO$_4$ solution was investigated. IsoPrOH_WO$_3$_400 was chosen as photoanode because of the most stable FE of S$_2$O$_8$$^{2-}$ generation (Fig. 9). In Fig. 12, results of photoelectrochemical, photolytic, electrolytic and chemical impact on the viability of microorganisms are compared. It can be seen that the most significant decrease in cell density by a factor of ∼ 240 is observed in the case of PEC treatment. Photolytic treatment was more effective than the chemical one. It was reported in [56] that persulfate alone had almost no effect on *Bacillus subtilis* spores, but in combination with UV irradiation better results were achieved. The effect of UV illumination is most likely related with photolytic decomposition of persulfate leading to the formation of radical species, which have high bacteria-killing power [57]. Sulfate radical, SO$_4$$^{\bullet-}$, is known to be capable of quickly decomposing most of the organic pollutants and biological toxins in water [58]. In the system investigated herein, higher disinfection efficiencies obtained in the case of light-assisted treatments should also be attributed to the formation of highly active radical species as a result of interaction of photogenerated WO$_3$ holes with water molecules and sulfate ions (Eqs. (6, 7)). Most importantly, inactivation of bacteria in these experiments was achieved using visible light. These findings suggest that WO$_3$ photocatalysts

are promising candidates to be used in green energy systems for water disinfection or pollutant degradation.

Conclusions

Photoelectrochemically active tungsten (VI) oxide layers were formed using the chemical solution deposition technique and four different alcohols — methanol, ethanol, isopropanol and butanol — as reductants. Deposits consisting of plate-shaped particles of different sizes (100–2000 nm) and crystallinity were obtained, depending on reductant and annealing temperature. Differences in the morphology of WO$_3$ layers were explained in terms of different reducing power of alcohols along with different stability of colloidal particles in the reaction mixture, which is strongly influenced by dielectric constants of the reductants themselves as well as their oxidation products.

Significant influence of annealing temperature on the photoelectrochemical performance of the films was observed: treatment of WO$_3$ coatings at 500 °C resulted in inferior photoelectrochemical activity compared to samples annealed at 400 °C. The latter effect was ascribed to restructuring and agglomeration of WO$_3$ crystallites as revealed by FTIR and cyclic voltammetric measurements. These structural transformations also led to increased concentration of defects, which impeded the transport of photoinduced charge carriers.

Faradaic efficiency of the photoelectrochemical generation of persulfate was found to be WO$_3$ layer morphology-dependent as well. Large plate morphology of WO$_3$ formed with isopropanol ensured the highest and most stable FE

of $S_2O_8^{2-}$ formation of about 60%; however, a significant decrease in photocurrent during prolonged photoelectrolysis was observed for all coatings investigated. Formation of photoelectrochemically inactive surface peroxo species, induced by oxidative cleavage of W–O–W bonds either by photogenerated holes or solution-present radicals ($SO_4^{\bullet-}$ or $OH^{\bullet}$) was suggested as the possible cause of deterioration of WO_3 PEC performance.

Efficient deactivation of *Bacillus* spp. bacteria suspended in a neutral sulfate medium was achieved with tungsten (VI) oxide photoelectrode under visible light illumination. The reported findings serve as a guide for understanding the synthesis-dependent evolution of WO_3 structure and can be useful for tailoring the properties of this material in order to achieve efficient PEC energy conversion. Photoelectrochemical systems with WO_3 can find application in visible light-assisted advanced oxidation processes in the areas of water disinfection and organic pollutants degradation.

Supplementary information The online version contains supplementary material available at https://doi.org/10.1007/s10008-022-05144-8.

Declarations

Competing interests The authors declare no competing interests.

References

1. Sayama K (2018) Production of high-value-added chemicals on oxide semiconductor photoanodes under visible light for solar chemical-conversion processes. ACS Energy Lett 3:1093–1101
2. Ahn SH, Zhao J, Kim JH, Zheng X (2017) Effect of interfacial blocking layer morphology on the solar peroxydisulfate production of WO3 nanoflakes. Electrochim Acta 244:184–191
3. Juodkazytė J, Šebeka B, Savickaja I, Petrulevičienė M, Butkutė S, Jasulaitienė V, Selskis A, Ramanauskas R (2019) Electrolytic splitting of saline water: durable nickel oxide anode for selective oxygen evolution. Int J Hydrogen Energy 44:5929–5939
4. Zeng X, Wang Z, Wang G, Gengenbach TR, McCarthy DT, Deletic A, Yu J, Zhang X (2017) Highly dispersed TiO2 nanocrystals and WO3 nanorods on reduced graphene oxide: Z-scheme photocatalysis system for accelerated photocatalytic water disinfection. Appl Catal B Environ 218:163–173
5. Ghasemian S, Asadishad B, Omanovic S, Tufenkji N (2017) Electrochemical disinfection of bacteria-laden water using antimony-doped tin-tungsten-oxide electrodes. Water Res 126:299–307
6. Kusmierek E (2020) Semiconductor electrode materials applied in photoelectrocatalytic wastewater treatment — an overview. Catalysts 10:439
7. Garcia-Espinoza JD, Robles I, Dur A, Godínez LA (2021) Photo-assisted electrochemical advanced oxidation processes for the disinfection of aqueous solutions: a review. Chemosphere 274:129957
8. Syrek K, Zych M, Zaraska L, Sulka GD (2017) Influence of annealing conditions on anodic tungsten oxide layers and their photoelectrochemical activity. Electrochim Acta 231:61–68
9. Dong P, Hou G, Xi X, Shao R, Dong F (2017) WO3-based photocatalysts: morphology control, activity enhancement and multifunctional applications. Environ Sci Nano 4:539
10. Supothina S, Seeharaj P, Yoriya S, Sriyudthsak M (2007) Synthesis of tungsten oxide nanoparticles by acid precipitation method. Ceram Int 33:931–936
11. Zhang T, Paulose M, Neupane R, Schaffer LA, Rana DB, Su J, Guo L, Varghese OK (2020) Nanoporous WO3 films synthesized by tuning anodization conditions for photoelectrochemical water oxidation. Sol Energy Mater Sol Cells 209:110472
12. Nwanya AC, Jafta CJ, Ejikeme PM, Ugwuoke PE, Reddy MV, Osuji RU, Ozoemena KI, Ezema FI (2014) Electrochromic and electrochemical capacitive properties of tungsten oxide and its polyaniline nanocomposite films obtained by chemical bath deposition method. Electrochim Acta 128:218–225
13. Petruleviciene M, Juodkazyte J, Parvin M, Tereschenko A (2020) Tuning the photo-luminescence properties of WO 3 layers by the adjustment of layer formation conditions. Materials (Basel) 13:2814
14. Wei S, Zhao J, Hu B, Wu K, Du W, Zhou M (2017) Hydrothermal synthesis and gas sensing properties of hexagonal and orthorhombic WO3 nanostructures. Ceram Int 43:2579–2585
15. Han L, Chen C, Wei Y, Shao B, Mu X, Liu Q, Zhu P (2016) Hydrothermal deposition of tungsten oxide monohydrate films and room temperature gas sensing performance. J Alloys Compd 656:326–331
16. De Los AT, Cwik S, Milanov AP, Gwildies V, Parala H, Wagner T, Birkner A, Rogalla D, Becker HW, Winter J, Ludwig J, Fischer RA, Devi A (2012) Influence of process parameters on the crystallinity, morphology and composition of tungsten oxide-based thin films grown by metalorganic chemical vapor deposition. Thin Solid Films 522:11–16
17. Mehmood A, Long X, Haidry AA, Zhang X (2020) Trends in sputter deposited tungsten oxide structures for electrochromic applications: a review. Ceram Int 46:23295–23313
18. Basyooni MA, Zaki SE, Ertugrul S, Yilmaz M, Eker YR (2020) Fast response of CO2 room temperature gas sensor based on mixed-valence phases in molybdenum and tungsten oxide nanostructured thin films. Ceram Int 46:9839–9853
19. Orsini G, Tricoli V (2011) Facile nonhydrolytic sol–gel route to mesoporous mixed-conducting tungsten oxide. J Mater Chem 21:14530–14542
20. Zeng Q, Li J, Bai J, Li X, Xia L, Zhou B (2017) Preparation of vertically aligned WO 3 nanoplate array films based on peroxo-tungstate reduction reaction and their excellent photoelectro-catalytic performance. Appl Catal B, Environ 202:388–396
21. Yang B, Barnes PRF, Zhang Y (2007) Tungsten trioxide films with controlled morphology and strong photocatalytic activity via a simple sol – gel route. Catal Lett 118:280–284
22. Juodkazytė J, Petrulevičienė M, Parvin M, Šebeka B, Savickaja I, Pakštas V, Naujokaitis A, Virkutis J, Gegeckas A (2020) Activity of sol-gel derived nanocrystalline WO3 films in photoelectrochemical generation of reactive chlorine species. J Electroanal Chem 871:114277
23. Ramadan AA, El-Mongy AAA (2009) El_Shabiny AM, Mater AT, Mostafa SH, El-Sheheedy EA, Hashem HM. Addressing difficulties in using XRD intensity for structural study of thin films 116:111–116
24. Chem JM, Xie YP, Liu G, Yin L, Cheng H (2012) Crystal facet-dependent photocatalytic oxidation and reduction reactivity of monoclinic WO 3 for solar energy conversion. J Mater Chem 22:6746–6751
25. Patil VB, Adhyapak PV, Suryavanshi SS, Mulla IS (2014) Oxalic acid induced hydrothermal synthesis of single crystalline tungsten oxide nanorods. J Alloys Compd 590:283–288

26. Moon YT, Park HK, Kim DK, Kim CH (1995) Preparation of mono-disperse and spherical zirconia powders by heating of alcohol_aqueous salt solutions. J Am Chem Soc 78:2690–2694

27. Do W, Sun J, Cao X, Zhu Y, Wang Q, Wang G, Han Y, Lu G, Pang G, Shouhua F (2013) High-performance gas sensing achieved by mesoporous tungsten oxide mesocrystals with increased oxygen vacancies. J Mater Chem 1:8653–8657

28. Sánchez-Martínez D, Martínez-De La Cruz A, López-Cuéllar E (2013) Synthesis of WO3 nanoparticles by citric acid-assisted precipitation and evaluation of their photocatalytic properties. Mater Res Bull 48:691–697

29. Farhadian M, Sangpout P, Hosseinzadeh G (2015) Morphology dependent photocatalytic activity of WO3 nanostructures. J Energy Chem 24:171–177

30. Miecznikowski K, Kulesza PJ (2011) Activation of dispersed PtSn / C nanoparticles by tungsten oxide matrix towards more efficient oxidation of ethanol. J Power Sources 196:2595–2601

31. Kulkarni D, Wachs IE (2002) Isopropanol oxidation by pure metal oxide catalysts: number of active surface sites and turnover frequencies. Appl Catal A Gen 237:121–137

32. Thanomkiat O, Noonuruk R, Kahattha C (2018) Sol-gel derived tungsten oxide thin films deposited by spin coating technique using tungsten powder as starting material. Thai J Nanosci Nanotechnol 3:1–6

33. Kim CY, Kim BS, Wook J, Choi DK, Lim T-Y (2004) Fabrication of WO3 thin film by sol-gel dipcoating method. J Ceram Soc Japan 247:244–247

34. Lu S, Wang C, Wang H, Liu J, Yan H (2017) Excellent electrochromic properties of tungsten oxide films with a mesoporous structure. J Mater Sci Mater Electron 28:10049–10055

35. Hu W, Han G, Dong B, Liu C (2015) Facile synthesis of highly dispersed WO3·H2O and WO3 nanoplates for electrocatalytic hydrogen evolution. J Nanomater 2015:1–6

36. Chacon C, Rodriguez-Perez M, Oskam G, Rodriguez-Gattorno G (2015) Synthesis and characterization of WO3 polymorphs: monoclinic, orthorhombic and hexagonal structures. J Mater Sci Mater Electron 26:5526–5531

37. Yuan J, Zhang Y, Le J, Song L, Hu X (2007) New templated method to synthesize electrochromic mesoporous tungsten oxides. Mater Lett 61:1114–1117

38. Imran M, Sulthan S, Abdul A, Rashid H, Sabri Y, Motta N, Tesfamichael T, Sonar P, Shafiei M (2019) Template based sintering of WO3 nanoparticles into porous tungsten oxide nanofibers for acetone sensing applications. J Mater Chem C 7:2961–2970

39. Baitoul RHM (2019) Nanostructured tungsten trioxide (WO3): synthesis, structural and morphological investigations. J Phys Conf Ser 1292:12014

40. Shen Y, Wang W, Chen X, Zhang B, Wei D, Gao S (2016) Nitrogen dioxide sensing using tungsten oxide microspheres with hierarchical nanorod-assembled architectures by a complexing surfactant-mediated hydrothermal route. Mater Chem A 4:1345–1352

41. Kumar VB, Mohanta D (2011) Formation of nanoscale tungsten oxide structures. Bull Mater Sci 34:435–442

42. Shen Y, Wang W, Chen X, Zhang B, Wei D, Gao S (2016) Nitrogen dioxide sensing using tungsten oxide microspheres with hierarchical nanorod-assembled architectures by a complexing surfactant-mediated hydrothermal route. J Mater Chem A 4:1345–1352

43. Kanan SM, Lu Z, Cox JK, Bernhardt G, Tripp CP (2002) Identification of surface sites on monoclinic WO3 powders by infrared spectroscopy. Langmuir 18:1707–1712

44. Farjood M, Zanjanchi MA (2019) Template-free synthesis of mesoporous tungsten oxide nanostructures and its application in photocatalysis and adsorption reactions. Anal Chem 4:3042–3046

45. Subrahmanyam A, Karuppasamy A (2007) Optical and electrochromic properties of oxygen sputtered tungsten oxide (WO3) thin films. Sol Energy Mater Sol Cells 91:266–274

46. Inamdar AI, Kim YS, Jang BU, Im H, Jung W, Kim DY, Kim H (2012) Effects of oxygen stoichiometry on electrochromic properties in amorphous tungsten oxide films. Thin Solid Films 520:5367–5371

47. Ros C, Andreu T, Morante JR (2020) Photoelectrochemical water splitting: a road from stable metal oxides to protected thin film solar cells. J Mater Chem A 8:10625–10669

48. Armstrong DA, Huie RE, Koppenol WH, Lymar SV, Merenyi G, Neta P, Ruscic B, Stanbury DM, Steenken S, Wardman P (2015) Standard electrode potentials involving radicals in aqueous solution: inorganic radicals (IUPAC Technical Report). Pure Appl Chem 87:1139–1150

49. Ng C, Iwase A, Amal R (2013) Influence of annealing temperature of WO 3 in photoelectrochemical conversion and energy storage for water splitting. ACS Appl Mater Interfaces 5:5269–5275

50. Gimenez S, Bisquert J (2016) Photoelectrochemical solar fuel production: from basic principles to advanced devices. Springer

51. Berkesi K, Horváth D, Németh Z, Varga K, Péter L, Pintér T (2014) Comparative study of the adsorption of SO42- and Cl- anions on smooth and rough surfaces of noble metal electrodes by in situ radiotracer thin gap method. J Electroanal Chem 712:151–160

52. Knöppel J, Kormányos A, Mayerhöfer B, Hofer A, Bierling M, Bachmann J, Thiele S, Cherevko S (2021) Photocorrosion of WO 3 photoanodes in different electrolytes. ACS Phys Chem Au. https://doi.org/10.1021/acsphyschemau.1c00004

53. Knöppel J, Zhang S, Speck FD, Mayrhofer KJJ, Scheu C, Cherevko S (2018) Time-resolved analysis of dissolution phenomena in photoelectrochemistry – a case study of WO3 photocorrosion. Electrochem Commun 96:53–56

54. Le HV, Pham PT, Le LT, Nguyen AD, Tran NQ, Tran PD (2021) Fabrication of tungsten oxide photoanode by doctor blade technique and investigation on its photocatalytic operation mechanism. Int J Hydrogen Energy 46:22852–22863

55. Breuhaus-Alvarez AG, Cheek Q, Cooper JJ, Maldonado S, Bartlett BM (2021) Chloride oxidation as an alternative to the oxygen-evolution reaction on H xWO3 photoelectrodes. J Phys Chem C 125:8543–8550

56. XiaoLing L, Hai Y, Cheng Y (2017) UV and sodium persulfate combined disinfection enhanced inactivation of microbe in drinking water. Genomics Appl Biol 36:4716–4721

57. Moreno-Andrés J, Rios Quintero R, Acevedo-Merino A, Nebot E (2019) Disinfection performance using a UV/persulfate system: effects derived from different aqueous matrices. Photochem Photobiol Sci 18:878–883

58. Sabeti Z, Alimohammadi M, Yousefzadeh S, Aslani H, Ghani M, Nabizadeh R (2017) Application of response surface methodology for modeling and optimization of Bacillus subtilis spores inactivation by the UV / persulfate process. Water Sci Technol Water Supply 17:342–351

59. Amiri H, Jazi B (2010) Dielectric constants of water, methanol, ethanol, butanol and acetone : Measurement and computational. J Solut Chem 39:701–708

60. Malmberg GC , Maryott AA (1956) Dielectric constant of water from 0 to 100 C. J Res Natl Bur Stand 56:1–8

61. Shirke RM, Chaudhari A, More NM, Patil PB (2001) Temperature dependent dielectric relaxation study of ethyl acetate-Alcohol mixtures using time domain technique. J Mol Liq 94:27–36

62. Lone B, Madhurima V (2011) Dielectric and conformal studies of 1-propanol and 1-butanol in methanol. J Mol Model 17:709–719

63. Bezman RD, Casassa EF, Kay RL (1997) The temperature dependence of the dielectric constants of alkanols. J Mol Liq 74:397–402

64. Wang P, Anderko A (2001) Computation of dielectric constants of solvent mixtures and electrolyte solutions. Fluid Phase Equilib 186:103–122

65. Wang P, Anderko A (2001) Computation of dielectric constants of solvent mixtures and electrolyte solutions. Fluid Phase Equilib 186:103–122